Plasma deposited thin layers of amorphous hydrogenated carbon (a-C:H) on selected biodegradable polymer films

-

Layer thickness and substrate dependent carbon hybridisation and its effect on layer stability

von

Torben Schlebrowski
aus Gelsenkirchen, Deutschland

Angenommene Dissertation zur Erlangung des akademischen Grades eines
Doktors der Naturwissenschaften
Fachbereich 3: Mathematik/Naturwissenschaften
Universität Koblenz-Landau

Gutachterinnen und Gutachter:
Prof. (UM6P) Dr. Christian B. Fischer
Prof. Dr. Barbara Hahn

Prüfungskommission:
Prof. (UM6P) Dr. Christian B. Fischer
Prof. Dr. Barbara Hahn
Prof. Dr. Wolfgang Imhof

Tag der mündlichen Prüfung: 29. Juni 2020

Abstract in englisch

The three biodegradable polymers polylactic acid (PLA), polyhydroxybutyrate (PHB) and polybutylene adipate terephthalate (PBAT) were coated with hydrogenated amorphous carbon layers (a-C:H) in the context of this thesis. A direct alignment of the sample surface to the source was chosen, resulting in the deposition of a robust, r-type a-C:H. At the same time, a partly covered silicon wafer was placed together with the polymers in the coating chamber and was coated. Silicon is a hard material and serves as a reference for the applied layers. Due to the hardness of the material, no mixed phase occurs between the substrate and the applied layer (no interlayer formation). In addition, the thickness of the applied layer can be estimated with the help of the silicon sample.

The deposition of the layer was realized by radio frequency plasma enhanced chemical vapor deposition (RF-PECVD). For the coating the samples were pre-treated with an oxygen plasma. Acetylene was used as precursor gas for the plasma coating. Coatings with increasing thickness in 50 nm steps from 0-500 nm were realised.

The surface analysis was performed using several techniques: The morphology and layer stability were analyzed with scanning electron microscopy (SEM) measurements. The wettability was determined by contact angle technique. In addition, the contact angles provide macroscopic information about the bond types of the carbon atoms present on the surface. For microscopic analysis of the chemical composition of the sample and layer surfaces, diffuse reflectance Fourier transform infrared spectroscopy (DRIFT) as well as synchrotron based X-ray photon spectroscopy (XPS) and near edge X-ray absorption fine structure spectroscopy (NEXAFS) were used.

All coated polymers showed several cases of layer failure due to internal stress in the layers. However, these were at different layer thicknesses, so there was a substrate effect. In addition, it is visible in the SEM images that the coatings of PLA and PHB can cause the applied layer to wave, the so-called cord buckling. This does not occur with polymer PBAT, which indicates a possible better bonding of the layer to the polymer. The chemical analyses of the layer surfaces show for each material a layer thickness dependent ratio of sp^2 to sp^3 bonds of carbon, which alternately dominate the layer. In all polymers, the sp^3 bond initially dominates, but the sp^2 to sp^3 ratio changes at different intervals. Although the polymers were coated in the same plasma, i.e. the respective layer thicknesses (50 nm, 100 nm, ...) were applied in the same plasma process, the respective systems differed considerably from each other. A substrate effect is therefore demonstrably present. In

addition, it was found that a change in the dominant bond from sp^3 to sp^2 is an indication of an upcoming layer failure of the a-C:H layer deposited on the polymer. In the case of PLA, this occurs immediately with change to sp^2 as the dominant bond; in the case of PHB and PBAT, this occurs with different delay to increased layer thicknesses (at PHB 100 nm, at PBAT approx. 200 nm).

Overall, this thesis shows that there is a substrate effect in the coating of the biodegradable polymers PLA, PHB and PBAT, since despite the same coating there is a different chemical composition of the surface at the respective layer thicknesses. In addition, a layer failure can be predicted by analyzing the existing bond.

Abstract auf Deutsch

Die drei biologisch abbaubaren Polymere Polylactidsäure (PLA), Polyhydroxybutyrat (PHB) und Polybutylenadipat-Terephthalat (PBAT) wurden im Rahmen dieser Thesis mit hydrogenisierten amorphen Kohlenstoffschichten (a-C:H) beschichtet. Es wurde hierbei eine direkte Ausrichtung der Probenoberfläche zur Quelle gewählt, was die Abscheidung einer robusten r-typ a-C:H zur Folge hat. Gleichzeitig wurde mit den Polymeren eine teils abgedeckte Scheibe Siliziumwaver zusammen mit den Polymeren in die Beschichtungskammer eingebracht und beschichtet. Silizium ist ein hartes Material und dient als Referenz für die aufgebrachten Schichten. Dazu tritt durch die Materialhärte keine Mischphase zwischen dem Trägermaterial und der aufgebrachten Schicht auf (keine Interlayerbildung). Zudem kann mit Hilfe der Siliziumprobe die Dicke der aufgebrachten Schicht festgestellt werden.

Das Aufbringen der Schicht wurde mittels der Radiofrequenz-Plasmaunterstützten chemischen Gasphasenabscheidung (RF-PECVD) realisiert. Für die Beschichtung wurden die Proben zuvor mit einem Sauerstoffplasma vorbehandelt. Als Precursorgas für die Plasmabeschichtung wurde Acetylen verwendet. Es wurden Schichten mit steigender Dicke von 0-500 nm in 50 nm Schritten realisiert.

Die Realisierung der Oberflächenanalyse erfolgte mit mehreren Techniken: Die Morphologie und Schichtstabilität wurde mit Rasterelektronenmikroskopie (REM) Messungen analysiert. Die Benetzbarkeit wurde mittels Kontaktwinkelmessungen durchgeführt. Zudem liefern die Kontaktwinkel eine makroskopische Information über die an der Oberfläche vorliegenden Bindungstypen der Kohlenstoffatome. Zur mikroskopischen Analyse der chemischen Zusammensetzung der Proben- und Schichtoberflächen wurden sowohl die Diffuse Reflexions Fouriertransformations Infrarotspektroskopie (DRIFT) als auch die röntgenbasierten Röntgenphotonenspektroskopie (XPS) als auch die Nahkanten-Röntgenabsorption Feinstruktur Spektroskopie (NEXAFS) verwendet.

Bei allen beschichteten Polymeren konnten mehrere Fälle von Schichtversagen aufgrund von internen Stress in den Schichten festgestellt werden. Diese lagen jedoch bei unterschiedlichen Schichtdicken, ein Substrateffekt liegt also vor. Zudem ist in den REM Aufnahmen sichtbar, dass bei den Beschichtungen von PLA und PHB ein Aufwellen der aufgebrachten Schicht auftreten kann, dass so genannte (telephone) Cord Buckling. Beim polymer PBAT tritt dies nicht auf, was auf eine mögliche, bessere Bindung der Schicht an das Polymer hinweist. Die chemischen Analysen der Schichtoberflächen zeigen für jedes Material ein schichtdickenabhängiges Verhältnis von sp^2

zu sp^3 Bindungen des Kohlenstoffs, welche die Schicht wechselnd dominieren. Bei allem Polymere dominiert zwar zunächst diesp^3 Bindung, allerdings kippt das sp^2 zu sp^3 Verhältnis unterschiedlich schnell. Obwohl die Polymere im selben Plasma beschichtet, also die jeweiligen Schichtdicken (50 nm, 100 nm, ...) im selben Plasmaprozess aufgebracht wurden, unterschieden sich die jeweiligen Systeme deutlich voneinander. Ein Substrateffekt liegt also nachweislich vor. Zudem konnte festgestellt werden, dass ein Wechsel der dominierenden Bindung von sp^3 zu sp^2 ein Indiz für ein kommendes Schichtversagen der auf dem Polymer abgeschiedenen a-C:H Schicht ist. Bei PLA tritt dieses sofort mit Wechsel zu sp^2 als dominierender Bindung auf, bei PHB und PBAT geschieht dies mit einem je unterschiedlichen Verzug zu erhöhten Schichtdicken hin (bei PHB 100 nm, bei PBAT ca. 200 nm).

Insgesamt wird in dieser Arbeit gezeigt, dass bei der Beschichtung von den biologisch abbaubaren polymeren PLA, PHB und PBAT ein Substrateffekt vorliegt, da trotz gleicher Beschichtung eine unterschiedliche chemische Zusammensetzung der Oberfläche bei den jeweiligen Schichtdicken vorliegt. Zudem kann durch die Analyse der vorliegenden Bindung ein Schichtversagen vorhergesagt werden.

Contents

1 Introduction

Polymer materials have become an important resource for many different aspects of modern life. Due to their advantages such as formability, elasticity, low weight, good usability in a wide range of working temperatures and chemical resistance, there are a large number of applications [1, 2]. Examples are plastic packaging for food, medical implants or even automotive applications [3, 4, 5, 6, 7, 8, 9]. However, a common feature of most polymers is that they are based on crude oil. Considering the constantly growing demand for plastic raw materials, not only the consumption of shrinking oil reserves is increasing, but also the need for disposal. This leads to a negative impact on the environment, as these polymers are usually not (bio)degradable within a reasonable time. There are therefore major disposal and raw material problems [10, 11, 12]. However, an adequate exchange of materials is often not possible or useful due to the advantageous properties of polymers.

Nevertheless, it should be mentioned that polymers cannot be used for every application because of their poor mechanical properties, such as low hardness or insufficient resistance to surface abrasion [2]. To further adapt the material to the desired applications, these polymers are often coated with amorphous hydrogenated carbon layers (a-C:H) [13, 14, 15]. These a-C:H layers consist of hydrogen and sp^2- (σ and π), and sp^3-hybridised carbons, with the sp^2 clusters being limited to short chains embedded in an sp^3 matrix of carbon and hydrogen [16, 17, 18]. The properties of the a-C:H layers are strongly dependent on the precursor gas used and the resulting ratio between the sp^2 and sp^3 hybridisation of the carbon atoms and the amount of hydrogen atoms in the plasma that crosslink the underground region of the layer [16, 17, 18]. For example, a high sp^3-to-sp^2 ratio results in a layer with diamond-like properties such as high hardness, chemical inertness or high electrical resistance [19]. An increase in the sp^2/sp^3 ratio results in a graphite-like layer that is softer and has improved electrical conductivity [19]. This change in chemical composition also influences the overall wettability and thus the contact angle behaviour of the deposited carbon layer [20]. Such a-C:H layers are usually deposited by chemical vapour deposition (CVD). These layer deposition can be further improved by the use of RF plasma (radio frequency plasma enhanced chemical vapor deposition; RF-PECVD) [20, 19, 21, 15]. As an advantage this technique can also be used for non-conductive materials at low temperatures, making it usable for materials such as polymers [19, 13, 22]. The ratio of carbon hybridisation or bonding states and the hydrogen content can be controlled by adjusting the plasma parameters that determine the physical properties of the resulting layer [15, 18, 23, 24]. Unfortunately, this coating and the resulting adaptation to further

applications leads to a further increase in use and further drives forward the problems of disposal and raw materials.

One possible approach to solving the disposal situation is to switch from classical polymers to those that are biodegradable. If these polymers can additionally be obtained from renewable raw materials, the resource problem is also solved. Such candidates for biodegradable polymers are, for example, polylactic acid (PLA) [12, 25], polyhydroxybutyrate (PHB) [26] or polybutylene adipate terephthalate (PBAT) [27]. PLA and PHB are also based on renewable raw materials (PLA is mainly based on corn starch and sugar[12, 25], PHB can be obtained from renewable raw materials through fermentation processes [26]). Although these polymers also have the poor properties of the classical polymers, they most likely can also be modified and adapted for special applications by depositing an a-C:H layer.

In this thesis, a:C:H layers deposited on the biopolymers PLA and PHB and on the biodegradable polymer PBAT are realised and analysed. The carbon-containing layers were produced by RF-PECVD technique with acetylene plasma. Different analytical techniques were used for the sample evaluation: The surface morphology of these deposited carbon layers was examined ex-situ by scanning electron microscopy (SEM). Surface sensitive X-ray based techniques such as X-ray photoelectron spectroscopy (XPS) and near-edge X-ray absorption fine structure (NEXAFS) were used to study the chemical composition of the deposited layers. Additionally diffusive reflectance infrared Fourier transform (DRIFT) have been perfomed for the analysis of the chemical composition of the layer surface. Contact angle measurements (CA) were performed to evaluate the relationship between sp^2/sp^3 ratios and macroscopic physical aspects such as wettability.

2 Fundamentals of carbon bindings and plasma physics

In the following section the basics of atoms and the position of their electrons are explained. The concept of molecules is also introduced. Afterwards, in particular the carbon atom and its bonding possibilities with other atoms are presented, since these are of great importance for the a-C:H layers applied on polymers in this thesis. Finally, the fundamentals of plasma physics are discussed in detail, since the polymers were both pretreated and coated with plasma.

2.1 Atoms and molecules

In this section, atoms are presented which are chemically the smallest building blocks of matter that cannot be further dismantled, as well as molecules which represent a concatenation of atoms. An atom can be divided into two areas: the positively charged, massive nucleus in the center of the atom, which consists of protons and neutrons, and the atomic shell around the nucleus, which consists of electrons. The regions in which the electrons are located in the atom are described by the orbital model of quantum mechanics. Here it is indicated with which probability an electron is in a certain space range [28, 29]. The respective state is described by the main quantum number n, the angular momentum l, the magnetic quantum number m and the spin s. The electron is then in a spatial region around the nucleus, which is limited and described by the four quantum numbers. In the orbital model, the notation for the K-shell (the innermost electron shell) is 1s, for example. 1 is the main quantum number and s stands for the angular momentum 0. Beside the s-orbital there is also the p-orbital, the d-orbital etc. [28, 29]. The main quantum number also indicates the respective shell. For the quantum numbers and their restrictions the rules given in table 1 apply. The orbitals correspond to certain energy levels of the respective electrons. In the orbital model, an atom can be described by its electron distribution on the different orbitals. In the ground state of the atom, these are filled up by the energetically most favourable orbital (1s) upwards in a successive manner. However, it should be noted that the Pauli principle, which states that no two electrons in a quantum mechanical system may be in the same state, must be observed [28, 29]. So any allowed combination of n, l and m represents an orbital. Since the spin can only assume two different values, each orbital can only be occupied by a maximum of two electrons. Atoms in the ground state are electrically neutral to the environment; they have the same number of protons in the nucleus as electrons in the shell [28, 29].

It is possible to move these electrons from the ground state of the atom into an excited state

Table 1: List of the four quantum numbers, the restrictions for their values and the naming for the respective values.

Name	Quantum number and rules	Value separation
main quantum number	$n = 1, 2, 3, ...$	1: K-shell
		2: L-shell
		3: M-shell
		...
angular momentum	$l = 0, 1, 2, ... < n$	0 = s (sharp state)
		1 = p (principal state)
		2 = d (diffuse state)
		3 = f (fundamental state)
		...
magnetic quantum number	$m = -l, ..., -1, 0, 1, .., l$	For low values letters as indices
		l=0 and m=0 nothing
		l=1, m = $0, \pm 1$ p_x, p_y, p_z
		...
spin	$s = \pm\frac{1}{2}$	spin up, spin down

by supplying energy to this atom or the respective electrons. Electrons can even receive enough energy to leave the electron shells of the atom and move into space. If this is the case, so-called free electrons and a remaining ion, which is an atom with more positive than negative charge carriers, are obtained [28, 29].

Molecules are particle compounds consisting of at least two, but often more atoms. These atoms are chemically coupled by a covalent bond and are also electrically neutral. They bond with each other to fill incompletely filled shells by dividing electrons. Molecules can be composed of atoms of a single type. Examples would be O_2, N_2 or H_2. However, many molecules, such as water (H_2O) and acetylene (C_2H_2), are made up of different types of atoms. Their physical properties, such as boiling point or melting point, are determined by the forces acting between the individual atoms of the molecules [28, 29]. Very large molecules are also called macromolecules. Polymers such as (high-density) polyethylene (HDPE) and polylactic acid (PLA) are made up of such macromolecules [30].

2.2 Carbon bindings

The carbon atom has six electrons. In the orbital model, two electrons occupy the inner 1s shell. The 2s orbital also contains two of the six electrons. The last two electrons are in the $2p_x$ and $2p_y$ orbitals. The 2s and the 2p orbital form the second electron shell. Only the four outer electrons of the second shell are responsible for the chemical bonding of the carbon [19]. In a p-orbital, the distribution of the electrons is anisotropic and has an dumbbell shape with the nucleus of the atom in the center. So each orbital has two opposing orbital spheres. Along the x-axis there is one half to the left of the center and the other half to the right. The p_y- and p_z orbitals (along the y- and z-axis) are perpendicular to it [19]. For the bond with other atoms, the 2s and the different 2p obritals hybridise to form the so-called sp^3, sp^2 and sp^1 bonds. These three types of carbon bonds are presented in the following:

- **Single bond diamond structure (sp^3)** The diamond structure is a consequence of the hybridisation of the 2s orbital of carbon with its three 2p orbitals. One of the electrons changes from the 2s orbital to the previously free 2p orbital. As a result, the four energies of the orbitals of the second shell are aligned. The space on which their probability of residence is mapped now has the shape of four elongated, asymmetrical drops. The probability of the electron being located in the respective orbital is much greater in one lobe on one side than in the other, which almost completely disappears. These four orbitals orient themselves with the greatest possible distance to each other in space. The resulting structure is that of a tetrahedron with an angle of 109.5° to each other. If this orbital of the sp^3 structure of the carbon atom overlaps with those of other atoms, these atoms can form solid covalent bonds. Each electron (or electron orbital) binds to another adjacent carbon atom. The structure of the connected carbon atoms is also tetrahedral and is called diamond structure, because pure diamonds consist of carbon atoms, which are only sp^3 -like bound [19].

- **Double bond graphite structure (sp^2)** If only two of the three available 2p orbitals are involved in the hybridisation of the 2s orbital, the so-called sp^2 bond is formed. The third p orbital remains in its original state. Again, each of the orbitals is occupied by one electron. The resulting hybrid orbitals have the same form as in sp^3 hybridisation, but they are divided differently by the different number and location of the regular p orbitals. These are in a plane with a distance of 120° to each other. Here, too, the probability of the electron being located in an orbital is much higher on one side than on the other, and one orbital lap is much more

pronounced than the other, which almost completely disappears. Carbon atoms which are sp^2 hybridised can form covalent bonds with each other, which then are in the same level and form a trigonal structure. This is the structure of graphite. The part of the bond of the atoms located in the level of their hybridised orbitals forms the $sp^2\,\sigma$ bond. The bond that runs through the unhybridised p orbital is the $sp^2\,\pi$ bond. The π bonds have a much lower energy than the σ bond. Due to the two electrons involved in the bonding with the same atom, this is called a double bond, which is also written as C=C [19].

- **Triple bond** (sp^1) The last bond presented is the triple bond of the carbon atom. Here the s-orbital hybridises with only one of the p-orbitals. There are two linear π binding lobes which are perpendicular to the other p-orbitals. Two sp^1-hybridised carbon atoms can form a triple bond with each other, whereby then three of the electrons of each atom bind with the neighboring atom (C $\equiv$ C) [19].

Overall, it can be said that sp^3 bonds form three-dimensional structures, sp^2 form two-dimensional planes and sp^1 bonds form only one-dimensional (linear) chains. The different carbon binding types are drawn in fig 2.1.

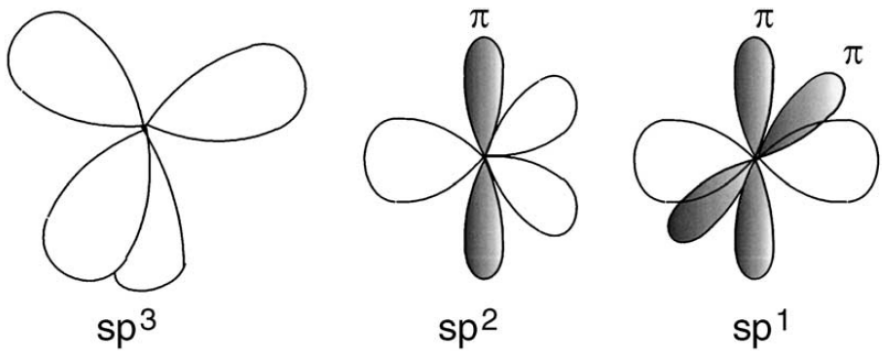

Figure 2.1: The three different types of carbon hybridisation: sp^3, sp^2 and sp^1. The image is taken from ref [19].

2.3 Plasma

2.3.1 Definition

A plasma is matter in the so-called fourth state [31, 32, 33]. It is said that nearly 99 % of the matter in the universe are in the plasma state. Examples for such plasmas on earth are lightnings, the *"Aurora Borealis"* or neon lights. In space the stars or gaseous nebulas are matter in the plasma state [32]. The Saha equation (2.1) describes whether matter is present in the plasma state or it is still referred to as a gas. This equation shows the degree of ionization as a function of the temperature of the gas in thermal equilibrium.

$$\frac{\mathrm{n_i}}{\mathrm{n_n}} \approx 2,4 * 10^{21} \frac{\mathrm{T}^{\frac{3}{2}}}{\mathrm{n_i}} \mathrm{e}^{\frac{-\mathrm{U_i}}{\mathrm{k_B T}}} \tag{2.1}$$

Here are n_i and n_n the density (number per m^3) of ionised and neutral atoms, T is the gas temperature in °Kelvin, k_B the Boltzmann´s constant and U_i the ionisation energy of the gas [33, 32]. Physically, the Saha equation states that the thermal energy of the atoms in a gas is Boltzmann distributed and only the atoms whose electrons have a thermal energy higher than the ionization energy are ionised. If an atom meets an impact partner, which has a sufficient energy, an electron can be released as the lightest component of an atom. For a cold gas, this case is very unlikely because the ionization energy is higher than the mean energy of the particles. In order to ionise a particle, energy must first be transferred in the form of several impacts to the impact partner, so that it can accumulate enough (kinetic) energy. As the temperature of the gas increases, the velocity of the atoms increases, too. Excited atoms remain in this state until they encounter an electron and recombine with them [32]. Therefore the recombination is directly dependent on the electron density. This is equal to the density of the ionised particles $\mathrm{n_i}$. For ordinary air at room temperature for example the fractional ionisation is low: $\frac{\mathrm{n_i}}{\mathrm{n_n}} \approx 10^{-122}$ [32]. If $\frac{\mathrm{n_i}}{\mathrm{n_n}}$ raises abruptly due to increasing temperature the matter is transferred into the plasma state. This is achieved by continuing to supply energy to an enclosed gas. The term plasma goes back to Erwin Langmuir [31, 32, 33]. A very compact definition for plasmas is:

> "A plasma is a quasineutral gas of charged and neutral particles which exhibits collective behavior." [32]

A plasma contains electrons, positive and negative ions, neutral atoms, neutral and charged molecules, and other radicals. Therefore that plasmas contain both free charge carriers and neutral

particles. The densities of the different species differ depending on the degree of ionization of the plasma. This ranges from 1 % for weakly ionised plasmas to 100 % for fully ionised plasmas. The quasineutrality is fulfilled as long as the observed area is larger than the so-called Debye length [31, 32, 33]. This is the shielding wavelength to which a local excess charge drops to a factor of $\frac{1}{\mathrm{e}}$ times. In the immediate vicinity of a charge carrier there are more particles with an opposite than the same charging. This is due to the electrostatic repulsion. These opposite charges now shield the charge in the center. Due to the thermal movement of the particles, this shielding is attenuated to short distances with the Debye length [31, 32, 33, 34]. The Debye length λ_D is defined by:

$$\lambda_{\mathrm{D}} = \left(\frac{\epsilon_0 \mathrm{k_B T_e}}{\mathrm{n_e e^2}} \right)^{\frac{1}{2}} \tag{2.2}$$

Here are ϵ_0 the electric field constant, n_e the density (number per m^3) of electrons, T_e is the electron temperature in °Kelvin, k_B the Boltzmann´s constant and e the elementary charge. For a plasma, the number of particles within the Debye sphere (the Debye length here is the radius) must be way larger then one [31, 32, 33]. Plasmas behave differently depending on their particle densities, temperatures, gas composition and the fields acting in them (magnetic and electric fields). For example, they can behave like a normal gas. For a complete description, however, transport equations, radiation losses and, in the case of reactive plasmas, plasma chemistry must also be taken into account, which becomes very complex due to the very extensive plasma system.

Towards the outside, a plasma is electrically neutral. The number of ions as well as the number of electrons is approximately in equilibrium, which leads to the fact that the net charge of the plasma is relatively small compared to the electron and ion density. This is only violated in areas with the size of the Debye length as well as in zones such as the rand sheath [31, 32, 33, 34]. The rand sheath builds up in the border areas of the plasma to the walls. As the electrons are much faster than the ions due to their lower mass at the same temperature, they leave the plasma quickly and get lost in the wall. Since this violates quasineutrality, a zone of electrically negative charge builds up, which reflects the electrons back into the plasma and accelerates the ions towards the wall [31, 32, 33]. In an acetylene plasma, for example, these ions can be used to deposit a carbon layer on a specimen [16, 19, 21, 35]. The deposition rate and the speed at which the ions leave the plasma can be increased by applying an external voltage to the electrode below the sample (BIAS voltage, see section 4.4).

2.3.2 Plasma parameters

Several parameters are necessary to describe a plasma. One of these parameters is the temperature. In the case of plasmas, however, there is not only one temperature [34]. In order to determine the temperature, firstly the energy distribution of the particles have to be considered. If there is enough time and (elastic) shocks in the plasma, this can be described by the Maxwell distribution [31, 32, 33], which is a distribution of maximum entropy and can be normalied in two ways. First, it can be normalised to one and then indicates the probability of finding a particle in a velocity interval. The other possibility is to specify the particle density n equal in the velocity interval. If the distribution is normalized, the mean energy $< E >$ of the particles can be determined by equation 2.3 [32]:

$$< \mathrm{E} >= \frac{\int \frac{1}{2}\mathrm{mv}^2\mathrm{f(v)d}^3\mathrm{v}}{\int \mathrm{f(v)d}^3\mathrm{v}} = \frac{3}{2}\mathrm{k_B T} \tag{2.3}$$

However, the concept of a uniform temperature can only be used if the temperatures of the individual charge carriers can be adjusted by enough impacts. This is referred to as a thermal equilibrium ($\mathrm{T_e} = \mathrm{T_i}$). Since the masses of the two charge carriers differ greatly, a large number of impacts are required to balance the temperatures. However, the concept of temperature can also be used without this large number of impacts if a distinction is made between the temperatures of the individual species [32]. The electron temperature can be measured by the usage of a Langmuir probe [33].

It can also be used to measure the next parameter to be introduced: the electron density (or the resulting charge carrier density). The charge carrier density indicates how many free charge carriers are present in a volume. It can be used to draw conclusions about the degree of ionization of the plasmas (see eq. 2.1; $n_e \approx n_i$). The concept of Debye shielding is only valid if the number of load carriers within the Debye sphere is high enough [31, 32, 33]. Some single particles within these would not result in a valid system, as there would be no outwardly electrically neutral sphere [32, 33]. The number of particles N_D in the Debye sphere can be calculated as follows:

$$\mathrm{N_D} = \mathrm{n}\frac{3}{4}\pi\lambda_\mathrm{D}^3 = 1,38 * 10^6 \frac{\mathrm{T}^{\frac{3}{2}}}{\mathrm{n}^{\frac{1}{2}}} \tag{2.4}$$

With $\lambda_\mathrm{D} \ll \mathrm{L}$, where L is the dimension of the system. A collective behaviour of the system (a stable Debye shielding) aquires $\mathrm{N_D} \ggg 1$. So the density of the particles in the Debye sphere must

be high [32, 33].

Finally, the plasma frequency (of the electrons) is introduced. Due to the large mass differences between the ions and the electrons, the ions can be assumed to be dormant for the following movement. Once the electrons have been removed from the atoms, they are subjected to the Coulomb force, which attempts to restore the homogeneous charge distribution [31, 32, 33]. The fast electrons now move again in the direction of the ions, but fly past the ions due to their high speed and miss the electrically neutral position. They are now decelerated by the Coulomb force and again accelerated in the direction of the ion. This leads to a periodic oscillation of the electrons around the ions [31, 32, 33]. The frequency at which the electron density oscillates around the electrically neutral position is known as the plasma frequency ω_p. It can be calculated as follows [31, 32, 33]:

$$\omega_{\mathrm{p}} = \left(\frac{\mathrm{n_e e^2}}{\epsilon_0 \mathrm{m}} \right)^{\frac{1}{2}} \tag{2.5}$$

Waves that penetrate the plasma can excite this oscillation and can therefore be absorbed or reflected [32, 33]. The only non-constant quantity occurring in the plasma frequency is the plasma density. Since it depends only on this quantity, it is a fundamental parameter to describe a plasma. Due to the small size of the electron mass, the plasma frequency is normally very high and within the microwave range. Therefore, microwaves can be used to heat plasmas [31, 32, 33].

In order to qualify a gas as a plasma, the movement of the particles must be driven by electromagnetic forces. This is not the case in very weakly ionised gases. Here the particle motion can be described by the equations of hydrodynamic forces. For a plasma, however, the product of the plasma frequency and the mean collision time of the charge carriers with neutral atoms must be greater than 1 in order to indicate a plasma-like behaviour [31, 32, 33].

Therefore three conditions have to be fulfilled for the plasma state [31, 32, 33]:

1. $\lambda_{\mathrm{D}} \ll \mathrm{L}$
2. $\mathrm{N_D} \ggg 1$
3. $\omega\tau > 1$

2.3.3 Transport mechanism

Transport processes determine the quality of the confinement of a plasma. The particles in the plasma and the energy are driven by a density gradient as well as by electric fields. If magnetic fields are added, the direction perpendicular to them is almost suppressed [32]. So the transport in a plasma is driven by two mechanisms: The drift caused by the adjacent fields and the diffusion caused by a density gradient. In order to calculate the transport properties of plasmas, the fluid equation is used, which takes the collision of particles into account and which is valid for all species [32]:

$$\mathrm{mn}\frac{\mathrm{dv}}{\mathrm{dt}} = \mathrm{mn}\left[\frac{\mathrm{dv}}{\mathrm{dt}} + (\mathrm{v}\cdot\nabla)\mathrm{v}\right] = \pm\mathrm{enE} - \nabla\mathrm{p} - \mathrm{mn}\nu\mathrm{v} \tag{2.6}$$

The plus-minus shows the charge dependence of the equation. Assuming an equilibrium state (leading to $\frac{\partial \mathrm{v}}{\partial \mathrm{t}}$) and that v is very small (or ν very large), it can be assumed that a fluid element does not move within the collision time to another region with a deviating E and ∇p, the equations for drift and diffusion can be derived [32]. The drift is described by the so-called mobility:

$$\mu = \frac{\mid \mathrm{q} \mid}{\mathrm{mv_m}} \tag{2.7}$$

The diffusion constant D (measured in $\frac{\mathrm{m}^2}{\mathrm{s}}$) is calculated as follows [32]:

$$\mathrm{D} = \frac{\mathrm{k_b T}}{\mathrm{mv_m}} \tag{2.8}$$

These two variables are linked by the Einstein relation [32]:

$$\mu = \frac{\mid \mathrm{q} \mid}{\mathrm{k_b T}}\mathrm{D} \tag{2.9}$$

The diffusion of the different species in a plasma is a random walk process in which the flow of denser particles into less dense regions is only carried by more particles starting in a dense region than in a less dense region [32]. This results in the flow being directly proportional to the gradient of the density. This flow can be expressed as follows:

$$\mathrm{J_e} = \mathrm{nv_e} = -\mu_\mathrm{e}\mathrm{nE} - \mathrm{D_e}\nabla\mathrm{n} \tag{2.10}$$

for the electron flux and

$$J_i = nv_i = -\mu_e nE - D_i \nabla n \tag{2.11}$$

for the flux of the ions [32]. The first part of the flux is the drift driven by the electric field and the second part is the diffusion driven by the density gradient. If the electric filed E equals zero or the particles observed are uncharged (leading to $\mu = 0$) the Fick´s law as a special case of the diffusion is received [32]:

$$J = -D\nabla n \tag{2.12}$$

Since an electrical neutrality towards the outside must be fulfilled for the plasma state, the flow of electrons and the flow of ions or the electron and ion density must correspond.

For a better understanding, the example of a plasma in a closed container is now discussed. Due to the diffusion-driven movement to the walls, it begins to decay, because as soon as an electron or ion reaches the wall, it recombines there [32]. This leads to a density of almost zero in the vicinity of the walls and feeds this process continuously [32]. Due to their lower mass and the resulting higher speed of the electrons, these reach the walls earlier than the ions. This would result in the flow of electrons greater than that of ions [32]. However, since a plasma requires quasineutrality over lengths greater than the Debye lengths, there must be a process that prevents this. If more electrons than ions leave the plasma, a positive net charge remains. This generates a field which prevents the electrons from leaving the plasma by a repulsive force and enhancing the ions motion [32]. The flow of electrons and ions out of the plasma to the walls is equal. This compensation is also called ambipolar drift with the ambipolar drift coefficient [32]:

$$D_a = \frac{\mu_i D_e + \mu_e D_i}{\mu_i + \mu_e} \tag{2.13}$$

Equating the flux J_e (eq. 2.10) and the flux J_i(eq. 2.11) and replaces n_e and n_i by n, the resulting equation can be changed according to the electric field E generating the repulsing force. ∇n is the total concentration gradient. We receive:

$$E = \frac{D_i - D_e}{\mu_i - \mu_e} \frac{\nabla n}{n} \tag{2.14}$$

If a plasma is now used to coat surfaces, this surface is exposed to the plasma and bombarded with particles from the plasma. This results in a flow of charged particles onto the sample, which generate a current density j [36]. First, due to their greater mobility, more electrons reach the surface and charge the surface negatively. This leads to a repulsive field for electrons, which prevents them from continuing to flow onto the surface. Ions, on the other hand, are accelerated towards the surface by this field and ensure that the sample is electrically neutral again after some time and that the electron and ion flux are aligned. Thus the sample remains neutral during the coating process, apart from the beginning of the coating, and the current density j becomes zero [36].

There are various variants for the case of drift. Which drift is responsible for the movement in the plasma depends primarily on the shape, direction and strength of the magnetic and electric fields present. An example of a drift would be the $\mathrm{E} \times \mathrm{B}$ drift [32, 31]. Here, a temporally constant magnetic field is superimposed with a temporally constant electric field. This leads to the following equation of motion:

$$\mathrm{m}\frac{\mathrm{dv}}{\mathrm{dt}} = \mathrm{q}(\mathrm{E} + \mathrm{v} \times \mathrm{B}) \tag{2.15}$$

Other possibilities are the gravitational drift (driven by the gravitation) or the diamagnetic drift with a motion of the guiding centers perpendicular to B [32, 31].

2.3.4 Plasma generation

The necessary energy can be supplied to the gas thermally (by impact ionisation), chemically (by an exothermic reaction such as a cutting torch) or through external fields (electrostatic or electromagnetic fields). The samples investigated in this thesis were deposited by using the RF-assisted plasma enhanced chemical vapour deposition. The heating of plasmas with a high-frequency RF signal is based on the absorption of waves in plasmas. Waves below the plasma frequency (eq. 2.5) cannot penetrate completely into the plasma and are reflected at the plasma [31, 32, 33]. A part, however, can penetrate and is attenuated by the plasma. The penetration depth, also called skin depth, is the distance the wave travels until its amplitude drops to $\frac{1}{\mathrm{e}}$ of its original value. The skin depth δ can be calculated using the following expression (assuming $\omega < \omega_\mathrm{p}$) [34]:

$$\delta = \frac{\mathrm{c}}{\omega_\mathrm{p}} = \left(\frac{\epsilon_0 \mathrm{mc}^2}{\mathrm{ne}^2}\right)^{\frac{1}{2}} \tag{2.16}$$

This is called the normal skin effect. If the penetration depth is also frequency-dependent, it is called the abnormal skin effect and the penetration depth is calculated as follows [34]:

$$\delta = \left(\frac{2\epsilon_0 \mathrm{c}^2}{\omega \sigma_\mathrm{DC}}\right)^{\frac{1}{2}} \tag{2.17}$$

In both cases delta scales approximately with $\delta \propto \mathrm{n}^{\frac{1}{2}}$. The absorbed power depends directly on the absorbing volume (the volume into which the electromagnetic wave can penetrate) and thus on the skin depth. Two cases have to be distinguished for the vessel dimension [37]:

$\delta > \mathrm{d}$ If the electron density is very low, the skin depth is greater than the vessel dimension. The wave can penetrate deeply. However, the low electron density limits the plasma's ability to absorb energy [37].

$\delta < \mathrm{d}$ If the electron density is very high, a small skin depth follows. Due to the large number of charge carriers, however, the entire energy can be carried into the plasma. But the heated volume is very limited [37].

The power loss in the plasma scales with the electron density. This is adjusted in such a way that absorbed and dissipated power is balanced. RF discharges normally operate in a frequency range of $\mathrm{f} = \frac{\omega}{2\pi} \backsimeq 1..100\,\mathrm{MHz}$, which means that the associated wavelengths ($\lambda = 300 - 3\,\mathrm{m}$) are much larger than the dimensions of the plasma vessel [37]. Microwave plasmas as another example usually use the frequency of 2.45 GHz. The associated wavelength of 12.24 cm is about the same as the dimensions of a plasma reactor [37]. The electric field between the electrodes ionizes the gas in between. The now free electrons are accelerated by the electric field and can release further secondary electrons through collisions with the neutral gas. If the field is strong enough, secondary electrons are released like an avalanche and the gas becomes electrically conductive due to the large number of free charge carriers.

A plasma ignited in a reactor chamber with a coil as electrode, can be used in two modes of operation: The inductive and the capacitive mode [37].

- **capacitivly coupled discharge (CCP, so called "E-Mode"):** At low coupled energies the system is in capacitive mode. Here the plasma is ignited between the coil, which is the upper electrode, and the lower, earthed electrode. The current flows directly from electrode to electrode through the plasma. In a reactor in which one of the electrodes is realised by a coil, this method of driving a plasma is called capacitive (E-) mode [37]. With an RF alternating current, much higher power and charge carrier densities can be obtained than with a DC discharge (direct current). In this case, there is a displacement current between the two electrodes which tries to follow the field and thus heats the plasma. The percentage of the ohmic current is only small. As a result of the displacement current, the plasma volume oscillates between the two electrodes. The lower electrode can also be assigned with an arbitrary bias, but this only changes the vertical position of the plasma to the electrodes. This can be seen more clearly in the case of DC discharge. The frequency of the displacement current is typically 13.56 MHz [37]. Since this structure corresponds to the capacitive element of a circuit, it is referred to as a capacitive plasma. In a plasma operating in CCP mode, the electrodes can be made of two circular disk-shaped electrodes that are seperated by a distance of a few cm. The electron density is rather low [37].
- **inductivly coupled discharge (ICP, so called "H-Mode"):** With an inductive plasma, an alternating magnetic field is applied via a current-carrying coil. This alternating field generates an electric field in the plasma, which leads to a current in the plasma. A displacement current is also generated here, but it runs parallel to the surface and not vertically as in the capacitive case. This current accelerates the electrons, which in turn heats the plasma. It can be imagined as a transformer system in which the plasma is a secondary coil with only one winding. An advantage compared to capacitive discharges is that the electrons are not accelerated towards the plates, but move parallel to them. In the capacitive case the fast electrons are lost. The inductive case has a much higher electron energy and electron density (up to two magnitudes) than the capacitive case. ICPs can have very high electron densities at comparatively low ion energies [37].

At low powers, however, the capacitive case is initially realised by the charge of the coil and the grounded lower electrode, since the inductive power coupling here is not yet effective enough to dominate. If the power is increased, this system switches to inductive (H) mode [37]. Plasmas used to coat the samples in this thesis were based on a source called COPRA. It is a single-turn inductively coupled rf discharge which is operated at a frequency of 13.56 MHz and additionally

superimposed with a static transverse magnetic field. The ion current density, the ion energy and the degrees of dissociation and ionization of the working gas can be controlled independently. A more detailed description of the source used can be found in the references [38, 39].

2.3.5 Plasma chemistry

In the case of reactive plasmas such as coating plasmas, a wide variety of processes can take place in the plasma due to the large number of particles present. Plasma contains neutral particles, radicals, electrons, simple to multiple ionised ions as well as fragments of partly or fully dissociated molecules [40]. There are many particles which are in the chemically active state and thus lead to a multitude of possible chemical reactions in the plasma. The rates of chemical reactions depend strongly on the concentration and energy distribution of the reaction partners [40]. Since electrons have the lowest mass and highest velocity and thus the greatest mobility, many reactions in reactive plasma can be traced back to electron collisions. General chemical reaction equations determine the concentration of the different reaction partners [40]:

- $e + AB \rightarrow AB^+ + 2e$ electron-ion pair production
- $e + AB \rightarrow A + B + e$ radical production
- $e + AB \rightarrow A^- + B$ negative ion production
- $A + A \rightarrow C + D$ gas phase chemical reactions
- $J_i = -D_a \nabla n_i$ ion transport to surface
- $J_A = -D_A \nabla n_A$ radical transport to surface
- $A(g) + B(s) \rightarrow C(g)$ surface- gas-phase reactions

The energy absorbed by these reactions must be supplied by the plasma. Considering these possible processes, chemical reactions in plasmas generate free charge carriers (electrons and ions) during ionization processes. The electrons have several possibilities: They can lead to other ionization reactions or recombine with positive ions. It is also possible to combine them with neutral species leading to the generation of negatively charged particles in the plasma [40]. In addition, electrons are able to dissociate or excite neutral molecules. This is done by an energy transfer

that leads to transitions between oscillation, rotation or electron states (orbital transitions). Also charges between the different plasma species can be transferred to the respective partner. All these reactions take place in coating plasmas and influence the coating process of surfaces [40].

3 Film growth

The coating of surfaces is realised in most cases by the deposition of a layer. Depending on the application, the layer thicknesses of these films range from a few nanometers to a few micrometers. Due to their large industrial application, the layer growth behaviour has been increasingly investigated and developed in recent decades in order to adapt the layers obtained to the desired application. The following chapter explains how films are deposited on surfaces. Deposition takes place in six consecutive sub-steps before the complete film is deposited on the surface. The first step is the adsorption of the incident atoms and molecules on the surface, which is followed by diffusion of the deposited particles over the surface. The third step is the incooperation of the particles into the film, which is expressed by the reaction of the deposited particles with each other and with the free binding sites of the surface atoms. The now bound particles begin to grow in a step called nucleation. Here, the effective growth of the film starts. In the fifth step the structure of the layer surface develops, including its surface and its bulk region, until in step six diffusion takes place between the coated substrate and the bulk of the layer [41]. The steps listed here are now described in more detail. In the first subsection, the early steps of the particles on the surface up to their incorporation are described.

3.1 Surface adsorption - physisorption and chemisorption

Figure 3.1 shows the first steps of the film growth beginning with the approach of the species deposited from the plasma to the surface up to their incorporation. Considering these atoms or molecules approaching the surface from the plasma, they begin an attraction within a few atomic distances from the surface due to the interaction with the surface [41]. This is because the bonds of the surface atoms adjacent to the incoming species create a potential that attracts the incoming species. The incoming species thus moves along the curve of a potential well until it passes its minimum and is repelled by the mutual repulsion of the nucleus. If the incoming species has dissipated enough of its perpendicular component of momentum at this time by releasing it at the surface during the interaction, it will not be able to escape the potential well after it has been repelled [41]. Nevertheless, it is not too strongly bound to the corresponding surface atoms and can still move over the surface (diffusion). This weakly adsorbed state is also called physisorption or physical adsorption ($E_{\text{physisorption}} \sim 0,25\,\text{eV}$ [36]). The particle is bound to the surface by the Van-der-Waals force. It is here in the first potential minimum (see fig 3.2 **A**). However, if the

particle was not able to dissipate sufficient energy during the approach, it is reflected back from the surface into the plasma [36, 41].

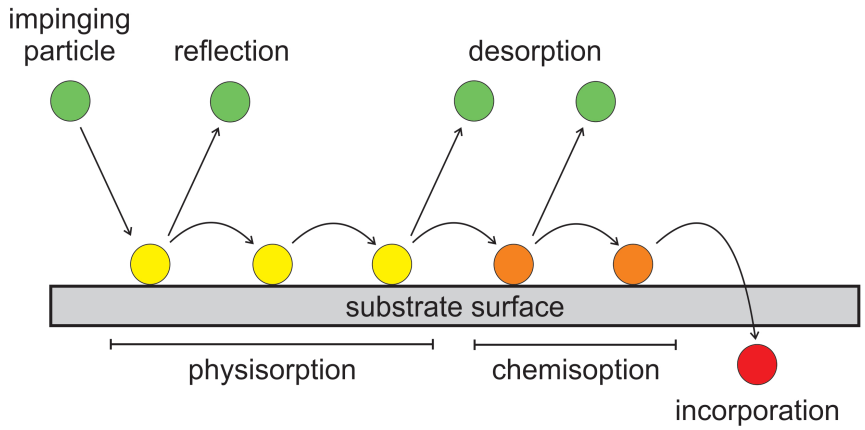

Figure 3.1: Representation of the impinging of a particle incident from the plasma onto the substrate surface. Shown are the possible reflection of the particle, its physisorption, chemisorption, desorption and incorporation. The green particles are unbound, the yellow ones are physisorbed (weakly bound), the orange ones are chemisorbed (strongly bound) and the red ones are incorporated into the film. The figure is based on ref [41].

As already mentioned, the particles bound by physisorption are only weakly bound and can move between the atomic sites on the surface by diffusion. There are now two possible results: they can gain enough energy and desorb from the surface or they can form a chemical bond with the surface atoms by further interaction with the surface. This state is called chemisorption. In contrast to physisorption, in which the particles are only bound by dipole interactions, chemisorption involves sharing of electrons of the surface atoms and the incident atoms in new molecular orbitals. This binding is many times stronger than physisorption ($E_{chemisorption} \sim 1 - 10\,eV$ [36]). If both physisorption and chemisorption exist in the process, the physisorption is also referred to as the precursor state. As shown in Figure 3.2, the minimum of the potential well in chemisorption is much lower than in physisorption and the state is more stable as a result. The desorbed as well as the refracted particles can hit the surface again out of the plasma and be physisorbed and/or chemisorbed here as well. Next, the previously chemisorbed particles are incorporated into the now growing film with a continuous deposition process [41, 36].

In the following figure 3.2, the potential energy of such a particle from the plasma approaching the substrate is plotted. Here the potential energy is plotted against the distance to the surface

and the physisorbed and chemisorbed states following from the potential curve are shown. The chemisorbed state is the energetically lower potential minimum of the curve. Since it is energetically lower, it is more stable than the physisorbed state, which is represented by the not quite so low potential minimum. If a particle is to change from the physisorbed state to the chemisorbed state, it must first overcome the intermediate potential barrier [41]. The height of the potential barrier depends on the degree to which the bonds must be strained both within the precursor and within the surface from their relaxed state before new bonds can be formed between the precursor and the surface. Figure 3.2 **B** shows the diffusion of a particle on the surface, which moves through the potential curves of the different bond states. The top of the barriers is also called the "transition state" of the particle. At motion, the particle changes from a physisorbed state to a physisorbed state until it finally lands in a deep potential minimum and is chemisorbed [41].

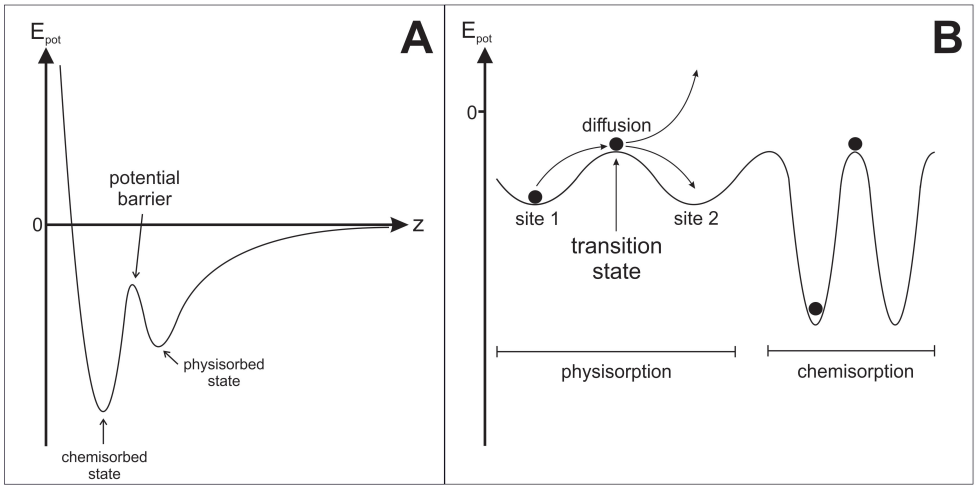

Figure 3.2: The potential energy of a particle approaching the surface from the plasma is applied against the distance z. Both the chemisorbed and the physisorbed state, as well as the potential barrier separating the two, are visible. The figure is based on ref [41].

Is the molar quantity of molar potential energy of the arriving vapour is high enough, direct chemisorption can occur without the precusor state. For surface chemistry the direct reaction between incoming species and the surface site is also called the Eley-Rideal mechanism while a reaction among the surface species (with the physisorption as precursor state) is called the Langmuir-Hinshelwood mechanism [41].

3.2 Nucleation and growth modes

With the incorporation of the particles into the film, the nucleation phase begins and with it the growth of the film. A determining force is the surface free energy γ. The surface energy exists because molecules in the condensed phase are attracted by each other and thus the condensation is caused [41]. If a surface is to be created, the free molecular contacts above the surface must be removed or saturated. For this purpose, bonds have to be broken and energy has to be used. The surface free energy always strives for a minimum and thus strongly influences the development of structures in the surface/film [41]. The minimization is achieved by surface diffusion. The free surface energy is thus the stored work per unit area, which was applied during the formation of the surface by the forces generated during this process. The unit of free surface energy is typically $\frac{\mathrm{J}}{\mathrm{m}^2}$ [36]. During layer growth, both the surface area and the surface free energy are variable. The surface area depends strongly on the surface topography while the surface free energy has several dependencies such as the chemical composition, the crystallographic orientation, the atomic reconstruction or the roughness on an atomic scale [41]. For materials without orientation dependency of a certain property, this property is considered isotropic [41].

If a film is deposited on a surface, three different surface energies have to be considered: those of the substrate to be coated γ_s, those of the substrate-film interface γ_i and those of the film free surface γ_f itself [41]. In the following two different cases have to be considered. If there is enough diffusion at the surface so that the deposited material is able to minimize its surface free energy on its own, then nucleation is not kinetically limited and there is an equilibrium growth mode. For this, the diffusion length Λ must be much larger than the atomic site distance a ($\Lambda >> \mathrm{a}$). In the opposite case ($\Lambda << \mathrm{a}$, e.g. if no diffusion takes place) sticks every atom directly where it lands and the growth behaviour is "quenched", which leads to a different characteristic film structure. This is also called non-equilibrium growth mode [41].

3.2.1 Equilibrium growth modes

In this section the equilibrium growth modes are introduced, so $\Lambda >> \mathrm{a}$, diffusion takes place and nucleation is not kinetically limited. The film can grow on the surface in three different ways as shown in figure 3.3. The favorite growth mode is determined by the sign of the surface free energy [41, 36, 42]:

$$\Delta\gamma = \gamma_{\mathrm{f}} + \gamma_{\mathrm{i}} - \gamma_{\mathrm{s}} \tag{3.1}$$

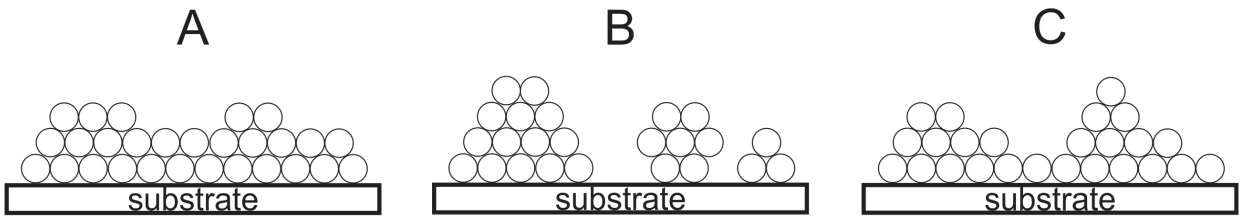

Figure 3.3: Equilibrium growth modes: **A** Frank-Van der Merwe (layer), **B** Volmer-Weber (island) and **C** Stranski-Krastanov. The figure is based on ref [41].

In Figure 3.3 **A** the film wets the substrate surface. This is possible because the following equation is valid for free energy:

$$\gamma_{\mathrm{s}} > \gamma_{\mathrm{f}} + \gamma_{\mathrm{i}} \tag{3.2}$$

As a result, the total surface energy is lower when the surface is wetted than when the substrate surface is bare [41]. From this growth mode follows a very smooth layer growth, which takes place layer by layer. For this a strong bond between depositing film and the substrate is necessary to reduce γ_{i}, therefore equation (eq. 3.2) holds. This growth mode is also called Frank-Van der Merwe growth mode [41].

The second possible case is that equation (eq. 3.1) results in the following surface free energy:

$$\gamma_{\mathrm{s}} < \gamma_{\mathrm{f}} + \gamma_{\mathrm{i}} \tag{3.3}$$

Here a wetting of the surface by the film always leads to an increase of the total surface energy [41]. Therefore, due to insufficient substrate bonding, the film begins to form three-dimensional (3D) islands on the surface instead of wetting the surface completely. Thus it reduces the contact with the surface. This growth mode, also called Volmer-Weber growth mode, is shown in Figure 3.3 **B** [41].

The third growth mode is a hybrid of the previously introduced modes and is called Stranski-Krastanov growth mode. It is shown in Figure 3.3 **C**. Here the growth changes from layer-to-layer

to 3D island growth after one or two monolayers of film have been deposited. Since the surface free energy can change with the completion of the very first monolayers, a change of the growth mode is caused [41, 36, 43]. Three-dimensional nucleation is mostly undesirable, as it leads to rough, non-uniform films. For solid-on-solid growth, the Stranski-Krastanov growth ist the most comon one [43].

3.2.2 Non-equilibrium growth modes

For a complete description of layer growth, the non-equilibrium growth modes must also be considered. However, if the reaction rates of individual species on the surface or their diffusion rates differ, for example, the system is driven away from the equilibrium state. If the state of equilibrium is to be reached, the forward and reverse reaction rates of reactants and products required for layer growth must be fast enough to become balanced within a given time frame. This time frame could be for example the time required to deposit a monolayer [41]. However, if, for example, the forward rate is so slow that the product concentration is unable to reach its equilibrium level within this time frame, then this product concentration is no longer determined by its free energies but by the forward rate. In this case the kinetics rather than the thermodynamics determine the growth and which growth mode dominates. However, the question of kinetics versus thermodynamics is not so easy to answer [41]. The main problem here is that the applicable rate constants k_k are mostly unknown or only very inaccurately defined. This is partly because it is a dynamic measurement and partly because they have to be performed in the absence of reverse reactions. Especially in the (PE-)CVD processes, where many different reactions take place, this is especially bothersome. The experimentalist has two essential parameters at his disposal to steer the system away from the state of equilibrium: The temperature and the pressure. Both the diffusion and the adsorption on the surface are controlled by the substrate temperature. The surface energy also depends on it. The (partial) pressure of the gas determines the impingement rate of the adsorbed atoms/molecules. Therefore, whether an equilibrium growth is present or not depends on these two parameters [43]. If the kinetic processes are the dominant and thus structure-determining factor during coating, the kinetic balance of several different surface processes must be investigated as shown in fig 3.4. Not only deposition occurs, but also nucleation of particles on the surface, terrace diffusion, accomodation of atoms at formed steps on the surface or diffusion accros these steps [43]. Energetically, only the step-down diffusion is kinetically significant, if the temperature of the system is not very high. This is because the particles are more strongly bound at the bottom of the steps and the

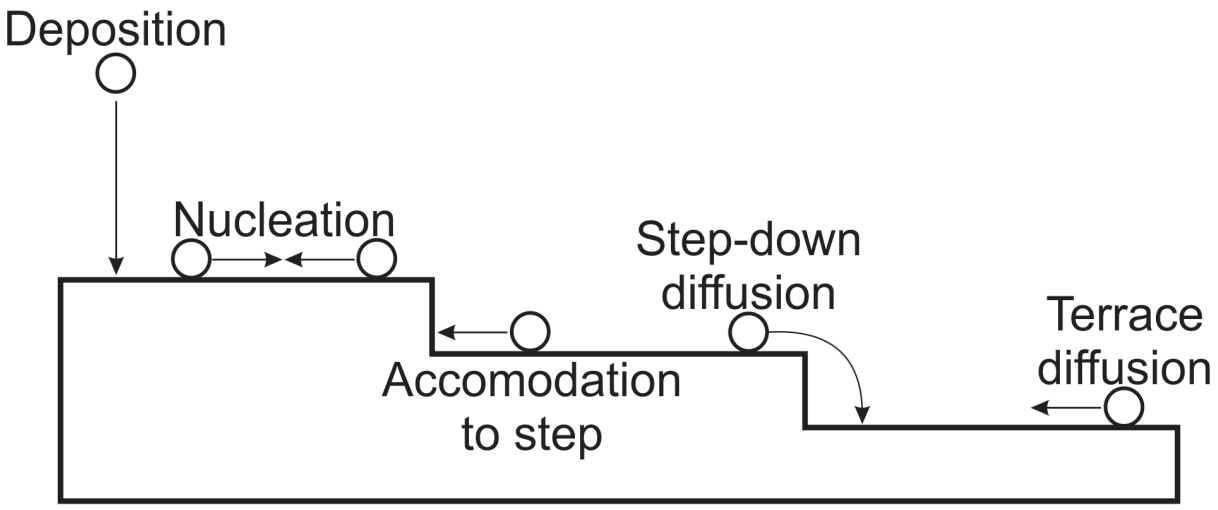

Figure 3.4: Surface processes involved in non-equilibrium film growth. The figure is based on ref [43].

energetic barrier to be overcome for step-up diffusion is therefore much larger. The relative rates of the different processes determine the growth mode and the film morphology [43].

If the non-equilibrium state is present, three distinct growth modes can also be distinguished here, which are illustrated in figure 3.5. If the system is close to equilibrium, step-flow growth is the predominant growth process (3.5 **A**). There is no transport of material across the terraces. The diffusion on the respective terraces is so rapid that all atoms reach a stage even before the nucleation of islands can begin. If, on the other hand, the system is far away from the state of equilibrium, the nucleation of islands is rapid. The growth mode is now determined by the transport over the terraces and between the steps [43]. In the limit of high transport, ideal 2D layer growth takes place. Here 2D islands grow on the surface and no nucleation takes place on top of them until the gaps between the islands are filled and the layer is completed. This growth mode is represented by figure 3.5 **B**. However, the ideal layer growth is commonly not achievable, since there is always a finite chance that further nucleation will take place on the existing islands before the layer is closed. This also leads to a roughening of the surface [43]. In the limit of no or only poor transport between the steps the nucleation of further islands begins on top of the uncompleted layer. This is the 3D multilayer growth (fig 3.5 **C**). The higher the deposited

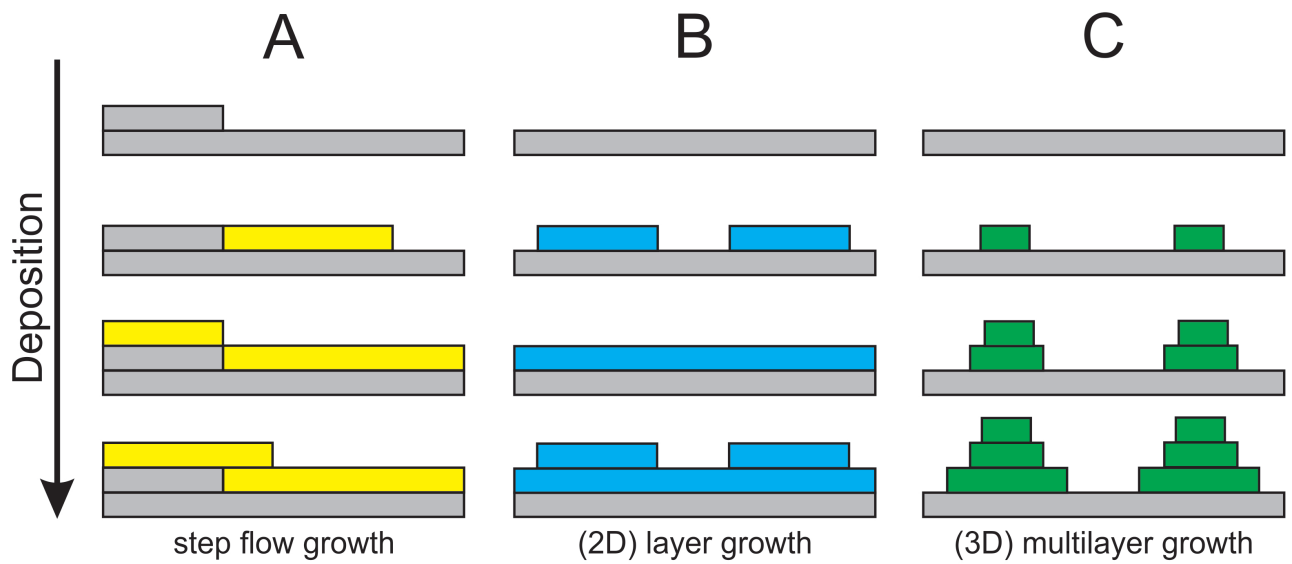

Figure 3.5: Non-equilibrium film growth modes. **A** the step-flow growth (yellow), **B** the (2D) layer growth by island coalescence (blue) and **C** (3D) multilayer growth (green). The deposition increases from top to bottom. This figure is based on ref [43]

amount, the greater the number of islands growing on islands. Regardless of which of the latter two processes occurs, once many layers are deposited, each far from equilibrium system becomes rough and tends to grow pyramid-like structures [43].

The difference between layer and multilayer growth can be considered quantitatively. For this, the critical coverage θ_c at which nucleation takes place on the top of the growing islands and the coverage θ_{coal} at which island coalescence takes place, which forms a completed layer, are considered. This allows the conditions for the growth modes to be specified as follows:

$$\Theta_c > \Theta_{coal} \Rightarrow \text{layer growth} \tag{3.4}$$

$$\Theta_c < \Theta_{coal} \Rightarrow \text{multilayer growth} \tag{3.5}$$

The value of θ_c is not constant and is typically $0.5 \leq \theta_c \leq 0.8$ [43]. It can be increased by either increasing the temperature or decreasing the deposition rate. As mentioned before, temperature and pressure are the decisive, variable parameters. If $T_s \to \infty$ and $r_{dep} \to 0$ apply, the equilibrium

is reached and step-flow growth can be observed. For $T_s \to 0$ and $r_{dep} \to \infty$, the transport between the layers stops and multilayer growth occurs due to the nucleation still proceeding. This means for high temperatures and low deposition rates the step-flow growth is the preferred growth mode and for low temperatures and high deposition rates the multilayer growth. Furthermore, the terrace diffusion length λ can also be used to express which growth mode takes place. This increases with increasing temperature T_s and decreases with increasing growth material flux J. If $\lambda \geq l$, step-flow growth occurs and if $\lambda < l$ then 2D layer growth is preferred [43].

3.2.3 Nucleation rate

Now the nucleation rate will be considered more closely. This expresses how many nuclei of critical size are formed on a substrate surface per unit area and time [36]. This is important because the formation of new phases is not possible without the existence of these nuclei. The nucleation processes are an indispensable prerequisite for the growth of thin layers and control further layer growth. The size of these nuclei is of particular importance, since both the surface energy and their thermodynamic stability depend on them. Small nuclei, also called sub nuclei, are not thermodynamically stable and cannot exist for a long time. In order to minimize the free energy change these nuclei disappear by shrinking [41]. Nuclei that are missing only one atom to overcome the critical size and to be thermodynamically stable are called critical nuclei. Only large nuclei whose radius exceeds the critical radius exist longer and can be used for further layer growth. Nucleation can take place spontaneously in the gas phase or anywhere on the homogeneous surface of the substrate. However, in almost all practical situations nucleation will take place predominantly at active sites such as steps or sinks, because the potential is more attractive here [41, 36]. Thus the density of these (critical) nuclei depends directly on the density of these active sites. The rate at which this critical nuclei then grows depends on the rate at which adsorbed adatoms attach to it. If adatoms land on the surface, they are discarded here for the time τ_s:

$$\tau_s = \frac{1}{\nu} \exp\left(\frac{E_{des}}{k_b T}\right) \tag{3.6}$$

ν here is the vibration frequency of the adatoms on the surface (typically $10^{13}\,\frac{1}{s}$) and E_{des} is their desorption energy [36, 44]. If these adatoms are not thermally adapted to the surface, they perform a random walk on the surface (diffusion). During their movement, they can form pairs with other atoms and combine then to form larger clusters or they can simply be captured by existing clusters.

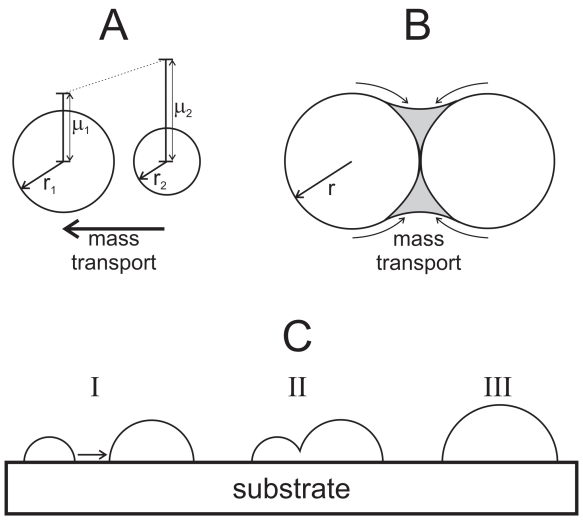

Figure 3.6: Coalescence phenomena of islands on the substrate surface. **A** Ostwald ripening, **B** sintering and **C** cluster migration. For more clarity the cluster migration is additionally divided into three steps: **I** cluster migration, **II** cluster collision, **III** merged cluster. The figure is based on ref [36].

Desorption of the adatoms is then very unlikely [36, 44]. The nucleation rate is decisive for the forming layer. A high nucleation rate results in fine-grained or even amorphous structures while a coarse-grained structure prefers to form at a low rate. The density of stable nuclei increases with time up to a maximum level. This number then decreases due to coalescence phenomena which are described in more detail in the next section.

3.2.4 Cluster coalescence and formation of grains

There are some characteristics that accompany the coalescence and growth of nuclei. There is a reduction in the total area covered by nuclei. In return, their height increases. The coalescence behaviour can be described partially liquid-like, with clusters merging and changing their shape according to the mode of movement of liquid droplets. It was also observed that the clusters move across the substrate surface before merging with others. This is also known as cluster-mobility coalescence. There are several mass transport mechanisms which have been proposed to be responsible for this coalescence phenomena. In the following they are presented [36].

Ostwald Ripening

Ostwald ripening begins with the presence of many islands of varied size. With time, the large ones begin to grow at the expense of the smaller ones (or "ripen"). This happens because the islands want to minimize their surface free energy. For better understanding, two isolated islands of different size and surface energy in close proximity as shown in figure 3.6 **A** are considered. For the simplified view it is assumed that these are spherical and their free energy G can be expressed as follows [36, 44]:

$$\mathrm{G_i} = 4\pi \mathrm{r_i^2}\gamma \tag{3.7}$$

with i=1,2. The number of atoms $\mathrm{n_i}$ bound in the islands can be calculated as follows [36]:

$$\mathrm{n_i} = \frac{4\pi \mathrm{r_i^3}}{3\Omega} \tag{3.8}$$

Here Ω is the volume of the respective atoms. The free energy per atom μ_i (or chemical potential $\frac{\mathrm{dG}}{\mathrm{dn_i}}$) then results [36]:

$$\mu_\mathrm{i} = \frac{\mathrm{d}(4\pi \mathrm{r_i^2}\gamma)}{\mathrm{d}\left(\frac{4\pi \mathrm{r_i^3}}{3\Omega}\right)} = \frac{8\pi \mathrm{r_i}\gamma\,\mathrm{dr_i}}{\frac{4\pi \mathrm{r_i^2}\,\mathrm{dr_i}}{\Omega}} = \frac{2\Omega\gamma}{\mathrm{r_i}} \tag{3.9}$$

If μ is large, then the effective atomic concentration is also high and the atoms are forced to migrate where μ is smaller [36]. If one now considers eq. 3.9 and assumes that $\mathrm{r_1} > \mathrm{r_2}$, then follows $\mu_2 > \mu_1$. As a result, atoms from cluster 2 begin to migrate over the surface to cluster 1, so cluster 2 shrinks as cluster 1 grows. It is therefore a transport mechanism that does not require direct contact between the partners. If it is multi-island arrays, then the kinetic analysis is a little more complicated, but ripening leads to the establishment of a quasi-steady-state island size distribution, which changes over time, but will never reach equilibrium during growth [36].

Sintering

The second coalescence process is the sintering, shown in figure 3.6 **B**. Here the clusters are in contact before the mass transfer takes place. During sintering, a neck forms between the two clusters at the contact point, which thickens with time as the atoms are transported to this region.

The driving force for the formation of the neck and the transport of the atoms is again the tendency to reduce the surface free energy γ of the system. Since the algebraic magnitude of μ for the atoms in the convex island surfaces ($r > 0$) is larger than for the atoms in the formed concave neck ($r < 0$), a concentration gradient develops between these two regions, which leads to an observable mass transfer into the neck region [36, 44].

Cluster Migration

The last coalescence process presented is based on the migration of whole clusters on the substrate surface. The coalescence takes place when two separate islands collide while performing random movements on the substrate surface. This process is shown in figure 3.6 **C** and is divided into three steps: 1) the movement of the clusters, 2) the collision of the clusters and 3) the resulting merged cluster. Electron microscopes have shown that clusters of up to 50-100 Å can move across the surface as a whole, provided the temperature of the substrate is high enough (at least 450 °K) [36]. Observations show that the clusters not only migrate, but can also rotate or even "jump" onto each other. Cluster migration takes place only in so-called conservative systems, which means that the amount of material deposited remains constant. It therefore only takes place after the deposition has ended and leads to a decreasing density of particles on the surface along with an increasing average volume of these remaining clusters. The surface migration of clusters with a projected radius r is described by an effective diffusion coefficient *D(r)* $\left[\frac{cm^2}{s}\right]$. This is given as follows [36]:

$$D(r) = \frac{B(T)}{r^s \exp\left(-\frac{E_c}{k_b T}\right)} \tag{3.10}$$

B(T) is here a temperature dependent constant and s a number between 1 and 3. Cluster migration is thermally activated by an energy E_c, which is related to the surface self-diffusion. It is faster for smaller clusters than for large ones. Experimentally, however, it is difficult to distinguish it from Ostwald ripening [36].

3.3 Film structure development

As the layer thickness increases, not only the processes leading to layer growth take place on the surface, but also the film bulk region begins to form within the layer. This is the previously

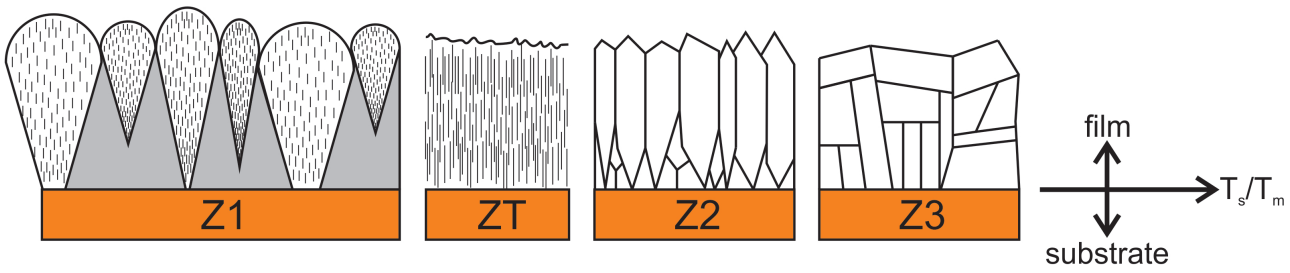

Figure 3.7: Representation of the four basic structural zones as a cross-section. The reduced temperature $\frac{T_s}{T_m}$, which is the ratio of the substrate temperature T_s and the melting temperature $T_m$of the film, increases with direction Z1 $\rightarrow$ ZT $\rightarrow$ Z2 $\rightarrow$ Z3. The figure is based on ref [36].

mentioned fifth step of the layer growth process. The decisive factor for the shape of this structure is the amount of thermally driven motion that takes place during film growth. This scales with the ratio $\frac{T_S}{T_m}$ of the substrate temperature T_s to the melting temperature T_m of the applied layer (in Kelvin), which is also called "homologous" or "reduced" temperature. The resulting structure is also determined by the amount of additional energy contributed to the growth surface. Fig 3.7 shows three structural zones (Z1, Z2 and Z3) and a transitional zone between Z1 and Z2. In the following these are described briefly [41].

Z1 If the ratio of the substrate temperature to the melting temperature is so low $\left(\frac{T_S}{T_m} < 0.3\right)$ that surface diffusion can be neglected and the nucleus diffusion length Λ is smaller than a (i.e. $\Lambda <$ a applies), then structure Z1 occurs. Here the structure consists of columns, which typically have a diameter of some ten nm. These are separated from voids with a size of a few nm. The crystallinity of these columns ranges from very small (many defects occur) to amorphous films. As the layers become thicker, a series of cones with larger voids between them is superimposed on this structure. At the surface, these cones terminate with domes, whose size grows with increasing layer thickness [41].

ZT ZT also occurs when surface diffusion processes are negligible ($\Lambda <$ a). Defected columns are also formed here, but ZT differs from Z1 in the point that voids and domes do not exist. The ZT structure normally occurs with energy-enhanced processes [41].

Z2 If the reduced temperature rises and exceeds the value of $\frac{T_s}{T_m} > 0.3$, surface diffusion can no longer be neglected. Once again, they consist of columns with very dense grain boundaries

between them. Their characteristic diameter increases with increasing $\frac{T_s}{T_m}$. The crystalline colums at Z2 contain less defects than at Z1 or ZT and are often facettet at the surface. The Z2 structure can also occur in amorphous films. In this case, however, the column boundaries are more flat reduced bonds than flat cristallographic discontinuity [41].

Z3 If the reduced temperature exceeds the value of $\frac{T_s}{T_m} > 0.5$, a considerable annealing of the bulks of the film begins during deposition. The Z3 structure has isotropic or equiaxed cristallite shapes and the grain boundaries can develop grooves at this structure. Film surfaces obtained with a value for $\frac{T_s}{T_m} > 0.5$ is smoother for both Z2 and Z3 [41].

It should be mentioned that it is not always possible to identify all four structures in materials. Especially the structure Z3 is rare to see. This is due to the high temperature required to raise the reduced temperature so that the Z3 structure can form [41]. Also the transition from one structure to another does not always take place abruptly with rising T. This is because the transition temperature in the systems is directly dependent on the substrate to be coated and the coating parameters such as ion energy, ion flow, surface energy anisotropy or the angle at which the coating is applied. In addition, the structure can change from Z3 to Z2 or ZT to Z1 when moving through different depths of the film. Amorphous layers only have such a structure if they are inhomogeneous because they do not have cristallographic patterns that would define the boundaries between the grains.

The structures Z1 and ZT result from growth processes in which the diffusion of the adsorbed metal can be neglected while the structures Z2 and Z3 form when the layers can thermally rearrange. Thus the reduced temperature is the determining factor for the predominant structure [41].

3.4 Theory of stress formation in layers

During the deposition of layers on a sample, the workpiece is subjected to a certain strain. This strain is generally referred to as stress, whereby two types of stress are distinguished. The first type of stress is tensile stress. If a layer is deposited on the workpiece, this sample will bend inwards under the pressure that the layer exerts on the material. The second type of stress is the so-called compressive stress. In order to maximize the surface of the applied layer, the sample bulges outwards and at the same time minimizes the surface of the sample that has come into contact with the layer [19]. Fig 3.8 below shows this curvature graphically for better understanding:

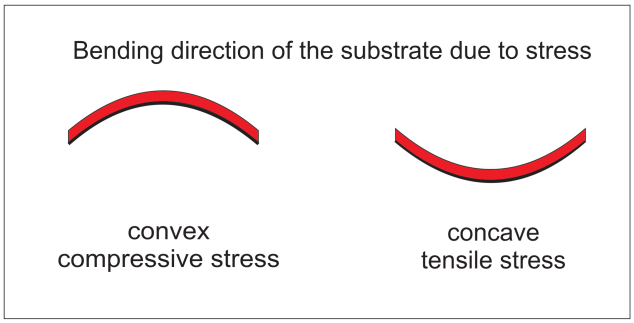

Figure 3.8: Bending direction of the substrate (black) coated with a-C:H layers (red). On the left compressive stress, on the right tensile.

This stress limits the possible layer thickness to values from several hundred to several thousand nm before the applied layers break open due to the stress and are detached from the substrate surface [16]. The force exerted by the stress must be absorbed by adhesive forces so that the layer adheres to the substrate surface. A modified form of the Stoney equation is used to study the influence of the stress applied by the coating on the sample. By measuring the radii of curvature of the sample before and after coating, this equation is able to calculate the stress produced in the sample by the applied layer [45].

$$\sigma_{\mathrm{f}} = \frac{\mathrm{Y}}{(1-\nu_{\mathrm{s}})}\frac{\mathrm{h_s^2}}{6\mathrm{h_f}}\triangle\mathrm{K} \tag{3.11}$$

The unit of stress is pascal.

It should be noted that $\triangle$K is the difference between the inverse of the radii of curvature of the coated and uncoated samples [45]. These radii can for example be obtained by measurements with a profilometer. The value for the biaxial modulus of elasticity Y can be taken from the literature for various materials. A further quantity occurring in this equation is the Poisson's ratio ν_s. This can also be taken from the literature. The size h_s occurring in the second term is the thickness of the substrate on which a layer with the thickness h_f is applied. The resulting stress from the layer applied to the substrate can be determined.

However, this equation can only be applied if some conditions are observed:

1. The specimen to be coated must have a rectangular shape (a < b). However, the small side must be much larger than the substrate thickness ($\mathrm{h_s} \ll$ a)[45].

2. The thickness of the applied layer must be much smaller than the thickness of the sustrate to be coated: $h_f \ll h_s$[45].

If the resulting result is negative, compressive stress is present, i.e. the substrate is curved outwards, if the obtained value is positive, the substrate will bulge inwards and tensile stress will be present.

In the following, a simple model developed by Davis [46] is presented in detail to explain the compressive stress in the layers. In this model it is assumed that the stress is caused by the ion bombardment of the layer. Atoms on the surface of the layer are hit by these ions and are transported deeper into the lattice by the transfer of energy. This way they reach places on the lattice of the growing film where they have less space than they would normally have. They form a kind of interstitial grid. For the atoms to be transported from the surface out of the atomic lattice somewhere into the layer, the incident ions must exceed a limit energy of E_{crit}, which depends on the structure, density and constituents of the deposited layer. The rate of atoms built into the interior of the layer per area depends directly on the number of ions incident (= ion current j_{ion}) and their energy [46].

In order to compensate these atoms in its interstitial lattice, the deposited layer on the surface of the substrate begins to spread into the volume of free space. Since this is not possible in the direction of the cross-section of the layer with the substrate, since the substrate limits the layer surface, the layer is stressed by the trapped atoms. Due to the thermal movement of the atoms trapped in the interstitial lattice, however, there is also a slight relaxation of the stress [46]. The energy required for this is also provided by impinging ions, since the impact of the ions converts part of their kinetic energy into heat. This heat is transferred to the surrounding particles, some of which may also be on an interstitial site by previous impact. The area that benefits from this thermal energy is also called the "thermal spike" [41]. If this energy is sufficient to exceed the excitation energy E_0, the atom can move away from its position into the normal atomic lattice of the layer and stress is reduced [46]. The number of atoms to which the energy is transferred when a particle deposits its energy in a "thermal spike" depends on the density of the particles located in this section of the surface as well as on the energy introduced and the excitation energy [46].

The rate of atoms relaxing per area then depends on the number of atoms n_{atom} supplied with a thermal energy greater than E_0 here, on the number of atoms moved from their lattice location in this area, and on the rate of ion bombardment. It can be expressed as follows [46]:

$$\mathrm{n_{relaxation}} = 0.016\rho\frac{\mathrm{n}}{\mathrm{N}}\mathrm{j}\left(\frac{\mathrm{Q}}{\mathrm{E_0}}\right)^{\frac{5}{3}} \tag{3.12}$$

Q is the energy deposited by a thermal spike, ρ is a material-dependent parameter in the order of 1, N the density of a structureless film, n the number of implanted atoms in the film and j the flux of the impinging ions. For energys below 1 kV it is assumed that every ion only generates one thermal spike, so the energy of the ions $\mathrm{E_{ion}}$ can be taken as the energy Q deposited in the thermal spike [46]. However, it is also true that not all atoms that have the necessary energy to move in the lattice can reach positions where they contribute to the reduction of stress. The rate of atoms built into the interstitial space is the difference between the implantation and relaxation rates. With the help of the rate $\mathrm{R}(\frac{\mathrm{n}}{\mathrm{N}})$, at which the implanted atoms per surface are incorporated into the film, a steady-state condition follows [46]:

$$\mathrm{n_{implanted}} - \mathrm{n_{relaxation}} = \mathrm{R}\frac{\mathrm{n}}{\mathrm{N}} \tag{3.13}$$

Here it is assumed that the rate of implanted atoms is constant over time. Now the proportion of the atoms implanted in the film can be calculated [46]:

$$\frac{\mathrm{n}}{\mathrm{N}} \propto \frac{\mathrm{E}^{\frac{1}{2}}}{\frac{\mathrm{R}}{\mathrm{j}} + 0.016\rho(\frac{\mathrm{E}}{\mathrm{E_0}})^{\frac{5}{3}}} \tag{3.14}$$

This model is able to explain the formation of compressive stress. However, there are some discrepancies between model and experiment. If the BIAS voltages are low, then the stress in the experiment is lower than predicted, whereas at high voltages it increases more than expected. One possible reason for this behaviour may be the layer density [46].

To explain tensile stress, the model developed and presented by Finegan and Hoffman is generally used [47]. In this model, it is assumed that the crystals/grains of the layer form small, isolated islands with no preferred orientation when coating surfaces. Due to the continued coating process and the associated further material input, these islands combine to form a single layer during the course of the coating process. Due to atoms and molecules deposited on the substrate from the gas phase, the islands increase in size over time [47]. If the distance between individual islands is very small at some point, forces acting between the atoms of one island can also act on atoms of other islands. These forces cause the islands to attract each other. This leads to a force being exerted on

the substrate and to a stress strain of the substrate through the layer [47]. This distance between the islands depends on the lattice and is about one to two times the lattice constant. Also the tensile stress can decrease already during the coating process, because due to the heating of the substrate by the ion bombardment a recrystallization occurs in the layer and these islands or these island networks align themselves energetically more favorably [47].

The stress that occurs in a layer can be influenced by a number of parameters. One possibility is to increase the pressure present during the coating process. This reduces the value of the stress. In contrast, by increasing the BIAS voltage, the stress present in the layer will be increased [16]. Considering eq. 4.2 (next section), it becomes apparent that both are decisive for the ion energy E_{impact}. If the BIAS voltage decreases, the energy available to the impacting ions also decreases and they cannot penetrate so deeply into the structure. If the pressure is increased, this energy also decreases. Thus the ion energy during the coating is a factor which influences the stress in the deposited film and can be used to control the stress. The ion energy is directly linked to the sp^3 content. A higher ion energy leads to more sp^3 bonds. Overall, it has to be noted that the sp^3 content of the layers is directly related to the prevailing stress. The higher the proportion of sp^3 bonds, the more rigid the network is and the greater the existing stress, until it can be reduced either by the thermal spikes already mentioned or by breaking the bonds and subsequently breaking the layer [46, 48, 49]. However, there are also cases in which the stress present in the layer decreases with increasing ion energy. It has to be considered that different gases have to be distinguished, because at the same average ionic energy different values for the stress in the layer can be determined. In addition, the proportion of hydrogen in the layer is also relevant and has a direct influence on the amount of stress. Stress can also be reduced by adding other chemical precursors to the plasma, such as nitrogen [16].

4 Amorphous hydrogenated carbon (a-C:H) films

This section describes how an a-C:H layer is deposited on polymeric materials and the influencing factors. After a more detailed description of the plasma through which the layer is deposited in chapter 2 and a general explanation of the layer growth in chapter 3, this section explicitly deals with the deposition of carbon layers and how this is realized on polymers. In addition, the coating process used for the polymer samples studied in this thesis is presented.

4.1 a-C:H coatings in general

Amorphous hydrogenated carbon layers are a metastable form of carbon. The material exhibits a great variability of crystalline and disordered structures. The basis for this are the three different hybridisation states of carbon: sp, sp^2 (graphite-like), sp^3 (diamond-like). In addition, an incooperation of hydrogen in the layer is also possible. The proportion of hydrogen can range from less than 10 % to 60 % for films applied by PE-CVD [50, 16, 19, 21]. Also, the hydrogen content is strongly responsible for the ratio of carbon atoms in the different coordinations. In the case of (almost) hydrogen-free films, these are also referred to as a-C films (amorphous carbon) [16]. The largest proportion of sp^3 bonds to date has been detected in a-C and was 90 % [21]. However, sp^2 bonds are always present, which is why "real amorphous diamond" is never deposited [21]. In general, the hydrogenated or hydrogen-containing a-C:H layers are also referred to as diamond-like carbon layers (DLC) and the hydrogen-free a-C layers are also referred to as tetrahedral amorhpous carbon (ta-C) [16]. What both film types have in common, however, is that they have diamond-like properties such as high hardness, a similar Young modulus, a wide band gap and are also chemically inert. The advantage over diamonds is that this can be achieved in disordered thin films, which is much cheaper than the production of diamonds [19]. The hardness of these a-C:H and a-C films is between 1000-3000 $\frac{\text{kg}}{\text{mm}^2}$, which is accompanied by a very low friction with values between 0.01 and 0.28 [50]. The respective values depend strongly on the hydrogen (and thus also on the sp^3/sp^2 ratio). Hydrogen is necessary to obtain the diamond-like properties of these materials. It influences the film structure, passivates the dangling bonds of the amorphous structures, and thereby controls the electrical and optical properties of the layer. The stress present in the film is also influenced by the hydrogen [16] - films with high densities and low content of hydrogen are the most stressed films [18]. Additionally the hydrogen influences the density and hardness of the film. This is caused by a rising structural disorder when the hydrogen content is reduced.

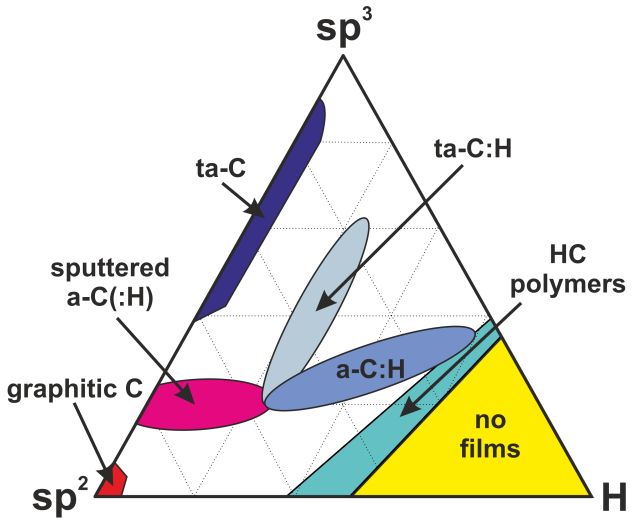

Figure 4.1: Ternary diagram of carbon based on Robertson's triangle. Here, the different categories of carbon films are classified based on their sp^2, sp^3 and hydrogen content. The figure is based on ref [19].

A common way to represent the different shapes of amorphous C-H alloys is the so-called ternary phase diagram of carbon, as shown in fig 4.1. This was first proposed by Jacob and Möller [51].

The placement of the different types of amorphous carbon films in the ternary diagram depends on their proportion of sp^3, sp^2 and hydrogen [19, 52, 21]. In the following, the different layer types are now presented with descending sp^3 content:

ta-C Tetrahedral amorphous carbon layers are the most sp^3 containing layers that are produced. They have a sp^3 content of up to 90 %. The density of these layers is about 3.1 $\frac{g}{cm^3}$. The high density is achieved by the high proportion of sp^3 bonds. This also gives the layers a large Young modulus with values between 500 and 800 GPa. Since the hardness of the film is about 10 % of the Young modulus, ta-C films have a hardness of 50-80 GPa. There are also sp^2 bonds, but these are limited to the grain boundaries [21, 19]. The hydrogen content of such films is less then 1 % [16].

ta-C:H represents the hydrogenated form of the ta-C layers. Due to the presence of hydrogen in the layer, they are softer than pure ta-C layers (their hardness is about 50 GPa). Typically their density is around 2.4 $\frac{g}{cm^3}$. The comparatively lower density also results in a lower Young modulus. This is about 500 GPa for these layers [21, 19].

a-C:H The amorphous hydrogenated carbon layers form one of the most hydrogen-containing layers presented in this section. Due to the high proportion of hydrogen, which can be between 25 % and 55 %, these layers have a very low density of only $1.2 - 1.6 \frac{g}{cm^3}$ for soft a-C:H layers and $1.6 - 2.2 \frac{g}{cm^3}$ for hard a-C:H layers. In this respect, their hardness is also not particularly high (below 10 GPa for soft and 10-20 GPa for hard layers). Their Young modulus is very low at less than 100 GPa [21, 19].

graphitic C Graphitic carbon has the largest proportion of sp^2 bonds and has practically no sp^3 or hydrogen bonds. Their density is approximately $2.25 \frac{g}{cm^3}$ due to the high carbon content [19, 21]. Their Young modulus is about 200-300 GPa which results in a hardness of 20-30 GPa [21]. As the name suggests, these structures are graphite-like, which means that they consist of sp^2 hybridised carbon atoms, which are arranged in six-folded rings and lie on top of each other in many finite layers. The six-fold rings are only interrupted by impurities such as open rings. The bonds between the layers are only weak. The **GLC** (graphite-like carbon films) or also **sputtered a-C(:H)** represents their hydrogenated form with slightly increased sp^3 content with a density of around $2.2 \frac{g}{cm^3}$ [21, 19].

HC polymers Hydrocarbon polymer (HC polymer) films form the films with the highest hydrogen content. Their content of sp^2 and sp^3 bonds is the lowest of the films presented here. These films consist of amorphous chains of carbon and hydrogen atoms, which are linked together. Due to the low content of C-C bonds, these layers are very unstable [21].

Finally, it should be mentioned that there are no stable films with a hydrogen content above 65 %. This region is located in the lower right corner of the ternary diagram of carbon [21].

4.2 The carbon network in a-C:H films

The structure of a-C:H films can best be illustrated by the cluster model [19, 21]. The material can be described as graphitic clusters consisting of sp^2 bound carbon in the form of six-fold rings embedded in a matrix of sp^3 bound carbon. Thus the clusters are limited to small groups of six-fold rings and short chains of sp^2 sites [21, 19]. In the hydrogenized films, hydrogen is also bound to the sp^3 hybridised carbon atoms in the surrounding matrix, thus terminating carbon bonds [18, 21, 16]. Furthermore, a part of the hydrogen atoms can be incorporated into the film as single atoms or in molecular form (in so-called voids). These voids can be jointly responsible

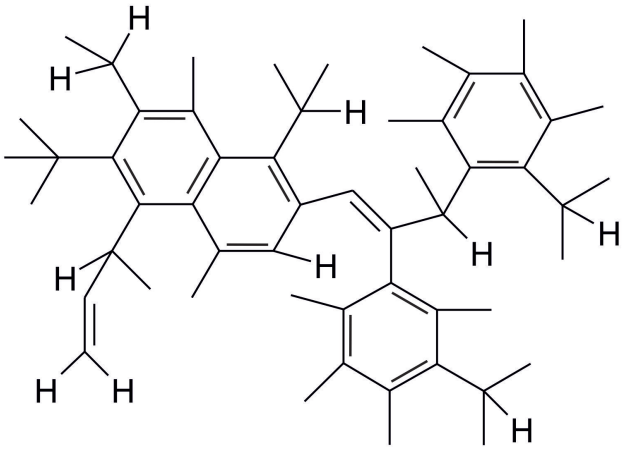

Figure 4.2: Schematic draw of the a-C:H film network following the cluster modell. sp^2 clusters are embedded in a sp^3 matrix consisting of C-C and C-H bonds. The figure is based on ref [19].

for the density and hardness of the layer. It has been observed that up to 50 % of the hydrogen incorporated in the layer is present in unbound form [16]. In fig 4.2 is a schematic sketch of the a-C:H network based on Robertsons cluster model [19].

In Robertson's cluster model, besides the short-range order, there is also a substantial degree of medium-range order, which is approximately in the order of ~ 1 nm. The structure is controlled by the $\pi -$ bonds of the sp^2 sites, which tend to cluster to maximize their energy [21, 52]. In addition, they can generate additional energy by forming planar six-fold aromatic rings and integrating them into larger graphitic clusters. However, the energy gain from increasing cluster size beyond pairing is comparatively small, so the clusters remain relatively small [52]. The size and distribution of the sp^2 clusters as well as the chemical organization of the sp^3 bonded carbon determine the film properties and its features. The sp^2 sites control the electronic properties as well as the optical gap of the film (their π states lie closest to the Fermi level) and the sp^3 matrix controlls the mechanical properties [19].

4.3 Deposition mechanism for a-C:H films

According to Robertson [21], the process responsible for the formation of sp^3 bonds is the so-called subplantation process. Only the high-energy ions are involved. Other species with low energies below 10 eV cannot penetrate the surface and remain attached to the top layer where they form sp^2

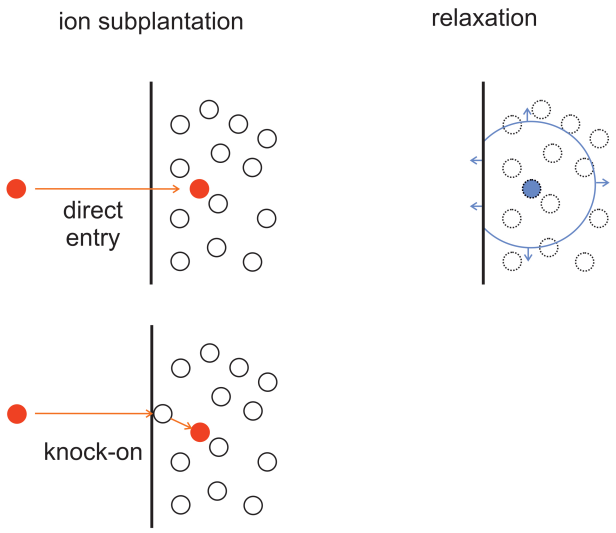

Figure 4.3: Schematic sketch of the subplantation and relaxation mechanisms which occur during a-C layer growth due to energetic ions. The figure is based on ref [21].

binding sites or are reflected back into the plasma depending on the sticking coefficient. Thus C^+ ions form sp^2 networks on the surface to lower their energy while H^+ ions set on the free dangling bonds and passivate them [21, 53]. Neutral hydrocarbon redicals are to large to penetrate the layer and can react therefore on the surface only [53]. High energetic (>10 eV) C^+ and H^+ ions can penetrate the outer atomic layers of the film and enter the subsurface region of the film. This penetration of the near-surface layers leads to local densification. Due to the densification, local sp^3 bonds begin to be generated in the area of the subsurface site. The higher the energy of the penetrating ions, the deeper they can penetrate into the material [21, 53].

As shown in figure 4.3, the subplantation process can take place in two different ways. One way is the direct penetration of the ions through the near surface layers into the subsurface. The second possibility is the knock-on. Here, the penetrating ions are not those coming directly from the plasma, but their impact partners in the near-surface region to which they release their energy. These can now penetrate deeper into the film and contribute to densification [21].

Both processes have in common that ions must release their energy in order to be integrated into the layer: this occurs by emitting phonons in the lattice (thermal dissipation) or in the form of impacts with lattice atoms and associated displacement damage of the film (knock-on) [53, 21]. A simple process that describes the energy loss of the ions are the so-called thermal spikes. Here a

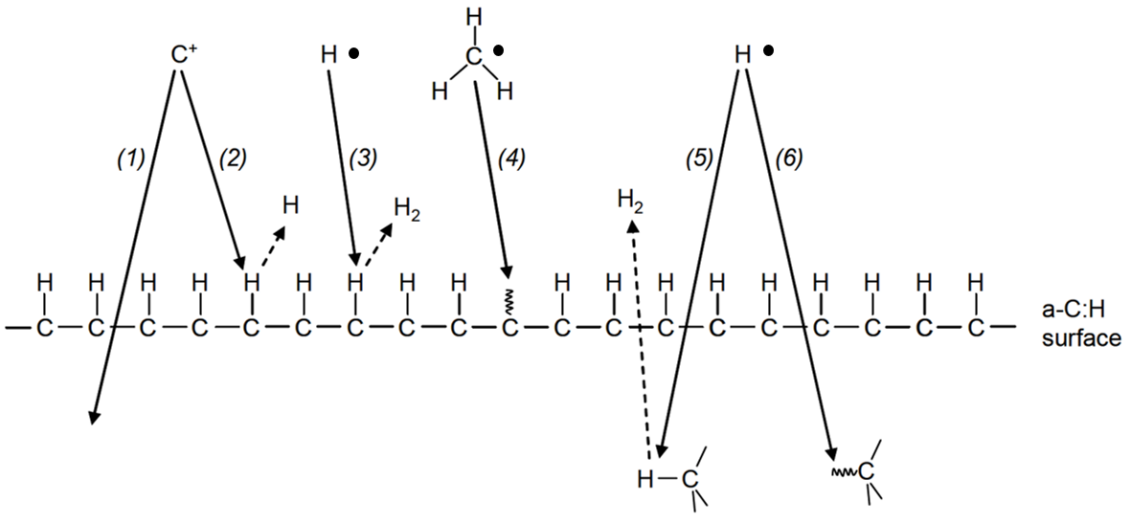

Figure 4.4: Deposition processes for the growth of a-C:H films: (1) Ion subplantation processes, (2) creation of surface dangling bonds by ion impacts, (3) creation of surface dangling bond by abstraction of hydrogen atoms, (4) passivation of surface dangling bonds by hydrocarbons, (5) hydrogen abstraction from the subsurface, (6) passivation of free dangling bonds in the subsurface by hydrogen. The figure is based on refs. [53, 19].

large part of the energy of the incoming ions is converted into heat within a very small volume. This expands the volume and cools it down, distributing the energy to all atoms within the volume. This local heating leads to thermal activated diffusion, which transports atoms from this region to the surface. This leads to two competing processes: densification and relaxation/diffusion. With an ion energy of about 100 eV the maximum density and the maximum sp^3 content is reached [21]. The processes of ion subplantation and of relaxation are shown in fig 4.3.

Considering the schematic representation of the a-C:H growth process after Neyts [53], as shown in figure 4.4, the ion subplantation ((1)) is not the only process that takes place during the coating process. Carbon ions, which hit the surface, can abstract hydrogen and create free dangling bonds ((2)). Similar is also possible for hydrogen ions, which remove the previously bound hydrogen in the form of a hydrogen molecule ((3)). Hydrocarbons such as CH and CH_3 are, as already mentioned, too large to penetrate the surface. However, they are able to passivate the previously generated free dangling bonds and thus adhere to the surface ((4)) where they create sp^2 binding sites. Finally, hydrogen ions can also penetrate the surface and reach the subsurface there. Here they have two possibilities: on the one hand they can abstract other hydrogen atoms and leave

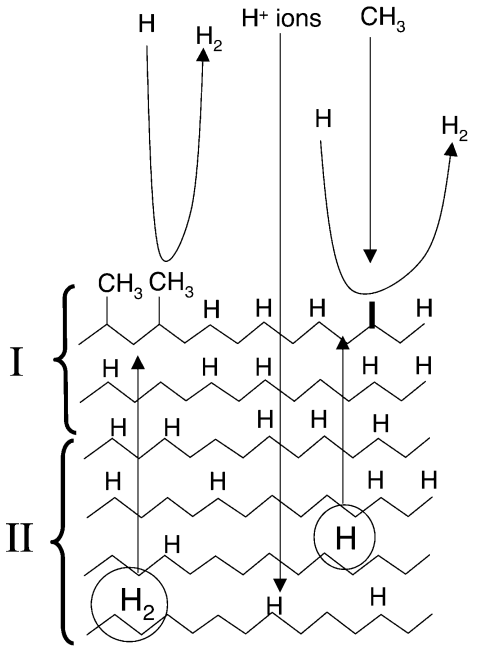

Figure 4.5: Schematic drawing of the surface of the growing film. In addition to the surface itself, the film structure is divided into two further regions: **I** the growth zone chemically dominated by atomic hydrogen, **II** the growth zone dominated by hydrogen ions in which the bulk processes take place. The figure is based on ref [54].

the layer again as H_2 molecule and thus produce free dangling bonds ((5)) or they can adhere to molecular chains and passivate free dangling bonds ((6)) [53].

Figure 4.5 shows a schematic drawing of the a-C:H growth mechanism. In addition to the surface of the film, whose properties are dominated by the reactions of the hydrocarbons as described above, the structure of the growing film is additionally divided into two zones [54]: Section **I** is a chemistry-dominated growth zone, which is dominated by reactions of atomic hydrogen and is about 2 nm thick [54]. It was directly detected in experiments [55]. The second (**II**), deeper zone is a growth zone dominated by hydrogen ions. Due to their low mass and charge, these can penetrate deepest into the a-C:H film and enable all processes that take place in bulk material [54].

4.4 BIAS voltage effect

The BIAS voltage directly influences the properties of the resulting layer. With this voltage, the energy with which the ions strike the surface can be changed. An increase in the BIAS voltage

leads to an increase in the energy of the ions and, as a result, to an increase in the proportion of sp^3 bonds in the layer structure that are important for the hardness of a layer [21]. The metastable structure of DLC films is due to the thermal and pressure spikes [50]. These are generated by impinging high-energy species during the coating process. The energy of a 100 eV ion is dissipated in a very small, near-surface volume by some angstroms, resulting in an energy dissipation of the order of some $\frac{\mathrm{W}}{\mathrm{cm}^3}$ [50]. These spikes live longer than the vibrational period of $2,6 \cdot 10^{-14}\,\mathrm{s}$ (valid for diamonds) and thus longer than required to allow bonding. Extremely high quenching rates of thermal spikes lead to the metastable structure [50].

But also other layer properties are changed by a variation of the BIAS voltage. Among other things, the coating rate is influenced by the fact that the surface is more strongly fragmented by increased bombardment with ions and the coating rate increases. With increasing BIAS, the refractive index of the applied layer is also increased. In return, the hydrogen concentration and the range of optical transmittance decrease [50, 15].

However, it should be noted that BIAS must be distinguished between an externally applied BIAS and a self-BIAS created by the plasma. Thus, the self-BIAS of a substrate in a reactor depends directly on the pressure prevailing in the chamber, the rf voltage applied from the outside and the geometry of the reactor [50]. If the self-BIAS is to be changed by varying the rf power applied, this variation not only affects the self-BIAS but also the chemistry prevailing in the plasma, since the fragmentation of the precursor gas is directly influenced here and other reaction products can become dominant. According to Catherine the self-BIAS of a substrate can be discribed as follows [16]:

$$\mathrm{V_{Bias}} \propto \left(\frac{\mathrm{P_{RF}}}{\mathrm{p}}\right)^{\frac{1}{2}} \tag{4.1}$$

Here P_{RF} are the rf power of the system and p the pressure in the reactor. The energy with which the ions impinge on the surface depends on the pressure in the chamber and, as already mentioned, on the BIAS present, whereby both external and self-BIAS must be taken into account here. High pressures lead to a high ion scattering due to collisions and therefore to a power loss and a distribution of ion energies lower than the applied BIAS [50, 56, 57]. The change can be calculated using the following equation:

$$\mathrm{E_{impact}} \propto \frac{\mathrm{V_{Bias}}}{\mathrm{p}^{\frac{1}{2}}} \tag{4.2}$$

To produce hard carbon layers, substrate BIAS voltages of more than 100 V are typically required to obtain the required energy E_{impact} [50]. However, a distinction must be made between different output gases: For example, using acetylene requires a lower BIAS voltage to obtain hard layers than cyclohexane [15].

4.5 a-C:H coatings on (soft) plastic materials

Plastic materials are used in everyday life in many sectors. This is mainly due to the low costs as well as their advantages such as deformability, elasticity, low weight and chemical resistance. Furthermore, they have good usability in a wide range of working temperatures [1, 2]. All these properties make them a readily used raw material. However, they are by far not suitable for all applications. In order to adapt these materials to other applications, coatings with a-C:H are one of the most frequently used and promising processes [13, 14, 15]. With these, the poor properties of the polymer, such as its low hardness, low abrasion resistance or poor mechanical qualities, which would otherwise greatly curtail its usability, can be achieved. Some examples for the use of coated polymers are food packaging, the medical sector or the automotive industry [3, 4, 5, 6, 7, 8, 9].

Many foods are now packaged in plastic. Plastic containers have the advantage that they are inexpensive and the customer can see the product. One problem, however, is that many plastic containers have an insufficient barrier effect against hydrogen and oxygen and therefore do not achieve the desired effect [3, 58, 4, 59]. To improve this, the packaging is coated with a-C:H layers, as these have excellent gas barrier properties and reduce the permeation rates of the various gases by at least one order of magnitude [3, 60, 59, 61]. This increases the shelf life of the products. Special attention is paid to the a-C:H coating of PET bottles in order to preserve the products packaged here for as long as possible [3, 60, 58, 4, 61]. This results in better food quality as the product stays fresh longer and is in the condition desired by the manufacturer [58, 4].

In the medical sector, there is a large number of artificial implants that are surgically inserted into patients. Some examples are artificial joints, coronal stents or artificial heart valves. The problem is that these plastic parts are not autologous and interact with the patient's body or its cells and fluids. This can lead to infections in the body or damage to the host tissue [7]. These implants are also affected by the body mechanisms of the patient and by time itself. If this is the case, the implants must be removed from the patient, which usually leads to a cost-intensive and for the patient resilient operation. Coating the implants with a-C:H layers results in a longer implant

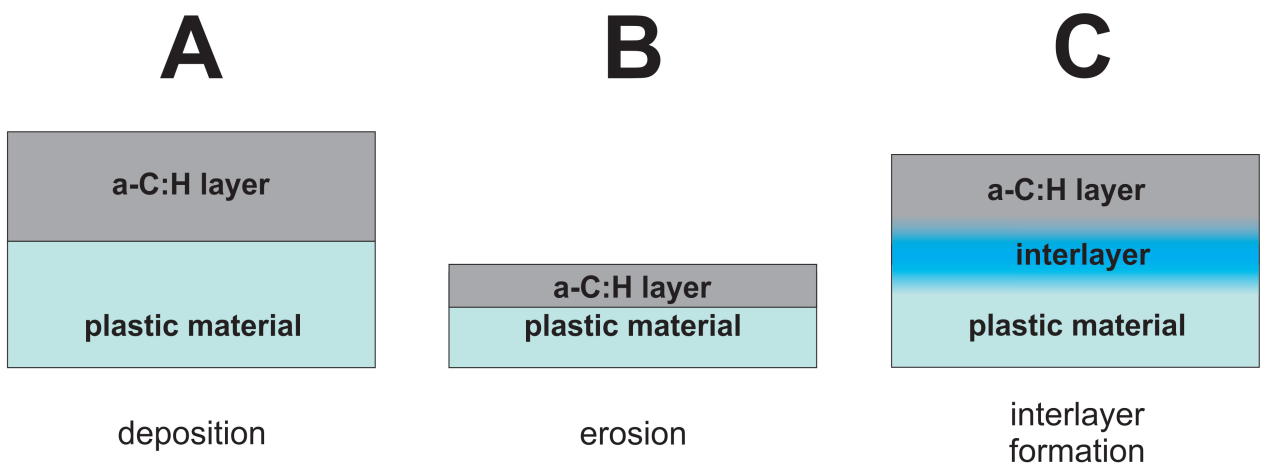

Figure 4.6: Presentation of the three possible ways in which the plasma can interact with the polymer during the coating process: **A** the direct deposition of the a-C:H layer on the polymer, **B** the erosion of the a-C:H layer and polymer during deposition, and **C** the formation of an interlayer between the polymer and the a-C:H layer. The figure is based on ref [22].

life and better biocompatibility with the human body [7]. The layers are bio-inert and lead to better adhesion of the implant to the tissue and reduced formation of biofilms on the implants, resulting in a lower risk of infection. Another application of a-C:H coated polymers in medicine is the medication dosing. The barrier effect of the a-C:H layer allows the drug release rate to be specifically controlled. Also the number of adherent platelets can be reduced by a power of ten compared to the currently used steel stents [62]. Dental medicine also benefits from the positive properties of a-C:H coatings. For example, dental prosthesis implants made of resin have a much higher resistance to material erosion through tooth brushing, which means a longer implant service life [7].

In the automotive industry, these coatings are used to reduce energy losses due to friction and thus lead to a better CO_2 balance and fuel savings [63]. Overcoming friction for engines, transmissions, tyres and brakes costs about 28 % of the fuel energy of a private car. This means that in 2009, 208,000 million litres of fuel (petrol and diesel) were consumed worldwide just to overcome friction. The aim of new technologies is to reduce this friction [64]. For example, valve spring retainers are coated with a-C:H layers for better performance [6]. Valve lifters are also coated with a-C:H layers to reduce friction and increase energy performance [65, 66].

As mentioned before, these a-C:H coatings are often applied by RF-PECVD technology. The mechanisms that work during coating, both chemical and physical, have been the subject of little research [67, 54, 68, 69, 70, 71, 13, 14, 72, 73, 74]. Especially the initial phase of the layer formation on the polymer is of great significance for the adhesion of the layer [73, 22]. There can be three different ways how the plasma interacts with the polymer during the coating process and how the a-C:H layer binds with the polymer [22]. The possible reactions are shown in fig 4.6. The easiest way for deposition of a-C:H layers on polymers is the pure coating on the substrate without further interaction (fig 4.6 **A**). The layer adheres simply to the polymer but does not form a direct bond and can therefore be easily removed [22, 73]. The second possibility of depositing a layer is during an erosion process on the surface of the polymer. During the plasma process, material is permanently eroded from the surface of the substrate. This happens due to the permanent impingement of plasma species on the surface. Due to the constant erosion, the coating only leads to a relatively thin layer on the substrate surface, which consists mainly of carbonization products. This process is shown in fig 4.6 **B** [22]. The last possible process is the formation of an interlayer region as shown in fig 4.6 **C**. Here, a gradual mixing phase of polymer is developed, which is eroded by the plasma and integrated into the deposited layer. This leads to a layer which is a combination of both materials. The growth of the interlayer continues until a pure a-C:H layer is formed [22]. This occurs when no further surface material of the polymer can be eroded because the overlying layer is thick enough to prevent impingement of the plasma species. In this process, a gradual change in the dominant material from the polymer substrate to the a-C:H film takes place on the new surface depending on the layer thickness. Overall, this process, as shown in fig 4.6 **C**, results in a lower thickness for the coating obtained [22].

In order to adapt the coatings to the requirements of the desired industrial application, a deeper understanding of the growth process on the respective polymer surfaces is necessary. The presence of an interlayer, for example, was detected for (HD-)PE [22] and determined to a thickness of about 40 nm [75]. For polyoxymethylene (POM), in contrast, no formation of an interlayer could be detected; the bonding of the layer with the polymer is only weak [73]. For industrial applications, the maximum thickness of the coating that can be applied is also important before it tears through internal stresses and becomes ineffective.

4.6 The coating process

The films for coating were cut into square pieces with a size of 10 x 10 cm and attached to vacuum-compatible, self-manufactured aluminum sample holders of similar dimensions. These were then placed in the coating chamber and a vacuum was created. Coatings of various thicknesses (50 to 500 nm, 50 nm steps) were then deposited on the material using radio frequency plasma enhanced chemical vapor deposition (RF-PECVD) [34]. The coating process was performed with a high frequency (RF, 13.65 MHz) plasma source (Copra DN 400, CCR GmbH, Troisdorf, Germany) installed in the high vacuum chamber. The process of coating was described in detail by Kleinen *et al.* and will be presented briefly in the following [5]:

The coating was carried out in two separate plasma processes. First, all samples were cleaned or prepared for suitable deposition by the action of an oxygen plasma at a pressure of 1 Pa, a flow of 65 sccm and a power of 200 W for a period of ten minutes. Secondly, the samples were then exposed to acetylene plasma at 0.65 Pa, a flow rate of 65 sccm and 107 W at room temperature in a second plasma process. By varying the coating time, different layer thicknesses could be achieved. The approximate layer growth speed was 10 nm/min [22].

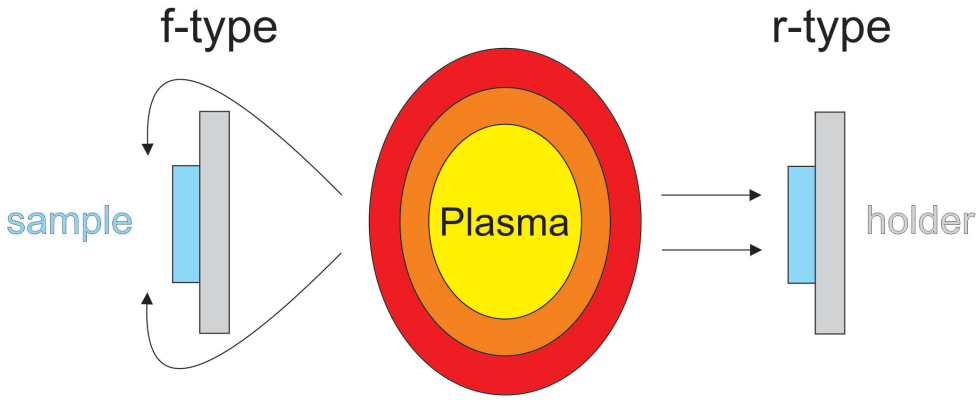

Figure 4.7: Schematic draw of the coating process. On the right the r-type deposition with the sample surface directly facing the plasma and on the left - for completion -the f-type a-C:H coating with the sample surface turned away from the plasma source.

During the entire plasma process, the polymer films mounted in the sample holder were placed at a distance of 275 mm from the front of the plasma source. Due to the direct alignment to the plasma, a variety of ion species with high kinetic energy hit the substrate surface and cause

a large amount of subplantation processes, resulting in a higher degree of cross-linked sp^3 carbon centers and therefore in the preferred r-type DLC coating (see fig 4.7). For the completeness, the f-deposition should be mentioned, where the samples are facing away from the plasma source, as shown in fig 4.7 [22]. However, these were not examined in this thesis.

To measure the layer thickness, silicon wafers (Silicon Materials, Kaufering, Germany), half covered with aluminum foil, were mounted on the aluminum sample holder. The partial cover allowed part of the wafer not to be coated and a layer edge to be formed. This made it possible to evaluate the applied layer thickness using a profilometer (Dektak 3, Veeco Instruments Inc., Plainview, NY, USA). A conformal analysis of thicker layers was not always possible for all coated polymer samples, as these layers were no longer stable on the sample, cracked and began to dissolve.

5 Experimental techniques

In the following, the analysis techniques are presented and explained, which were used in the context of the analyses in this thesis. Also the respective physical basics are explained for a better understanding. Finally, the polymers under investigation are introduced.

5.1 Scanning electron microscopy (SEM)

A scanning electron microscope (SEM) scans a surface with an electron beam. An image of the surface can be generated from the interaction of the electrons with the surface of the sample to be analysed. With these images it can be examined in the context of this work whether the applied layers are intact or whether they are detached. Here it has to be differentiated whether the layers are detached and break open, which means a layer failure, or whether they are detached but still remain intact and wavy (the so-called cord-buckling effect [76, 77]). For the morphological studies of the surface, a scanning electron microscope type SEM515 manufactured by Phillips at the University of Applied Sciences Koblenz, RheinAhrCampus Remagen, was used. In order to avoid charging effects due to the electron beam, a 7-10 nm thick gold layer was applied to the samples to compensate for the poor conductivity of the polymer samples. An acceleration voltage of 7 kV was used for the measurements, the distance to the sample is 20 mm. In the following, the functionality of an SEM is briefly explained:

A schematic illustration of an SEM is shown in fig. 5.1. An electron source, which is usually a tungsten heating wire that emits electrons when heated, generates free electrons. These are accelerated in an electric field with a voltage of several kV. With a lens system consisting of magnetic or electrostatic coils, the beam is then directed and focused onto the surface to be observed. As soon as the beam hits a surface, there can be different types of interaction between electrons and that surface. If these interaction processes are detected, this information can be used to determine the nature of the surface. Using the magnetic coils, the primary beam is then guided over the entire sample, which can then be scanned step by step [78]. After the sample has been completely examined, the scanning starts again. From the information of the interaction, the computer creates a grayscale image of the surface. On the one hand, information can be drawn from the secondary electrons, which have been released from the upper layers of the surface and have low energies. They provide information about the topography of the surface. On the other hand, information is obtained from the electrons reflected from the surface of the primary beam.

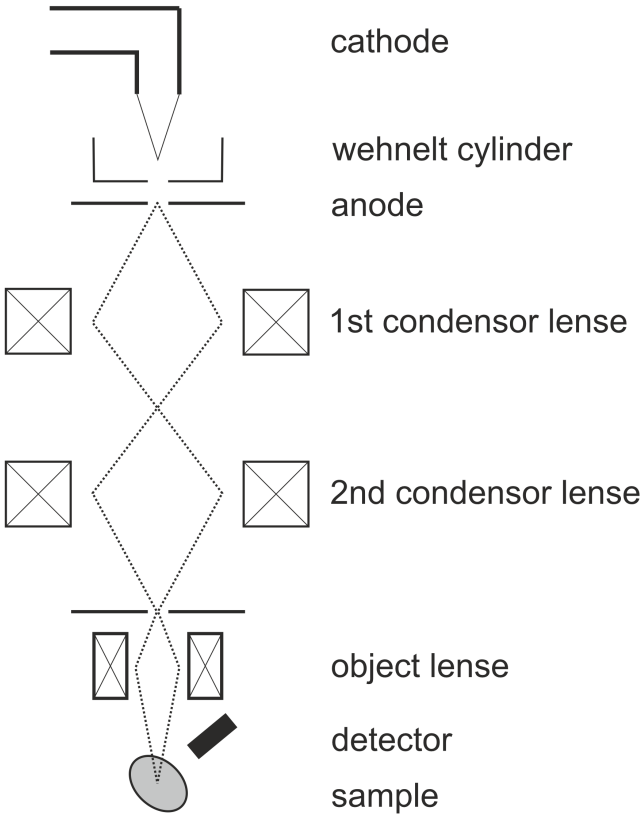

Figure 5.1: Schematic draw of the operating principles of a SEM. The figure is based on ref [78].

This can be observed especially with heavy particles of high atomic numbers. The problem with these methods is that the signal depends strongly on the position of the detector relative to the surface. If the surface is turned away from the detector, it appears darker than if it were turned towards it. The charging of the surface also causes different brightness levels in the grayscale image.

5.2 Contact angle measurement (CA)

The contact angle measurements shown in this thesis were performed using the sessile drop technique. Two different contact angle measurement devices have been used: The measurements for the PLA and PHB samples were performed on a contact angle goniometer type OCA 15 plus

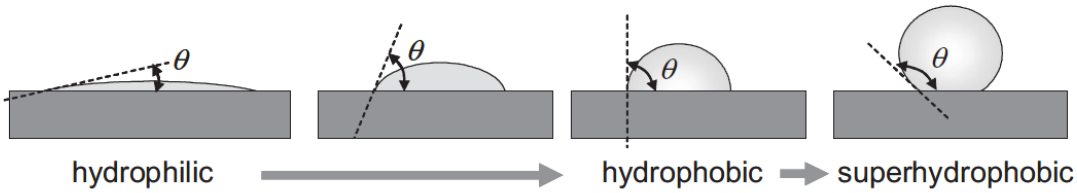

Figure 5.2: Schematic draw for different contact angles on a surface representing a variety of surface wettability. The image is taken from ref [79].

(DataPhysics Instruments GmbH, Filderstadt, Germany). For the measurements of the PBAT samples a contact angle goniometer type OCA 15EC (DataPhysics Instruments GmbH, Filderstadt, Germany) has been used. The measurements were carried out at room temperature and in ambient air. A drop of water (HPLC quality) with a volume of 1μl was automatically applied to the sample surface by a dispensing needle. At least five drops were placed at different points on the surface and analysed to ensure homogeneity. Contact angles were determined on the left and right sides of each drop and averaged for each sample. The measurement results obtained were then plotted using OriginPro 8.1G software (OriginLab Corporation, Northampton, MA, USA).

The wettability of surfaces can be determined by the angle between the liquid droplets and the surface. The description of surfaces distinguishes between hydrophobic (water-repellent surfaces) and hydrophilic (water-attracting surfaces) surfaces. The barrier between hydrophobic and hydrophilic is 90°. If the contact angle is lower, a surface is hydrophilic, if it is higher than 90°, it is hydrophobic. There is also the possibility of a very high contact angle of >150° [79]. These surfaces are also referred to as superhydrophobic, an example of this water-repellent behaviour is the lotus effect. All four examples are shown in Figure 5.2. Thomas Young defined the contact angle of liquids applied to a solid surface in a gas atmosphere as the angle at the phase boundary between the liquid, gaseous and solid phases. It is described by the Youngs equation:

$$\cos\theta = \frac{\gamma_{\mathrm{SG}} - \gamma_{\mathrm{SL}}}{\gamma_{\mathrm{GL}}} \tag{5.1}$$

Here γ_{SG} is the interfacial tension between the solid and the gase phase, γ_{SL} the one between solid and liquid and γ_{GL} between the gaseous and the liquid phase [79].

In general, the wettability of carbon-containing surfaces depends on three factors: the topography of the surface to be analysed [80, 81, 82], the chemical bonds present on the surface [83, 84, 85, 86],

and the different hybridisation states of the carbon atoms and their distribution on the surface [87, 88, 24]. If an oxygen-rich surface is present, the formation of functional oxygen groups leads to an increased attractiveness for water [86]. In contrast, if the free dangling bonds of the surface are saturated with hydrogen, a strong C-H bond is present, which inhibits further interaction between the sample surface and the liquid applied for the measurement [83, 84, 85]. These surfaces are more hydrophobic compared to less hydrogenated surfaces. The hybridisation of the carbon atoms on the surface influences the contact angles obtained by the different interaction of the bond types with water. A sp^3-rich surface has a reduced contact angle compared to a sp^2-rich surface. This is due to the high surface energy of the sp^3 hybridised carbon. This bond has a strong covalent character compared to the sp^2 bond, while the sp^2 dominated surface has only a weak polarity [19, 24]. Strong polarity leads to lower contact angles and increased hydrophilicity [89].

5.3 Infrared spectroscopy

The basis of infrared spectroscopy is the absorption of photons by atoms and molecules. Electrons are located in atoms in so-called quantum states (energy levels), which can be assigned to an atom dependent discrete energy. An electron can absorb a photon and change to a higher energy level if the energy of the photon $\mathrm{h} \cdot \nu$ corresponds exactly to the energy difference between the two energy levels. On the other hand, it emits a photon with exactly this energy when it changes from a higher to a lower energy level. The energy difference is calculated as follows:

$$\Delta \mathrm{E} = \mid \mathrm{E}_1 - \mathrm{E}_2 \mid = \mathrm{h} \cdot \nu \tag{5.2}$$

Here E_1 is the energy of the electron at the first level and E_2 is the energy at the second level. ν is the frequency of the photon and h is the Plancks constant. Therefore the electron levels are quantized and discribed by quantum numbers [90].

Molecules, on the other hand, consist of two or more atoms whose distance from each other in their resting position depends on the forces acting between these atoms. If these atoms now absorb photons, they can vibrate around their initial position. Also the vibration states are quantized like the electron states and can be described by quantum numbers. Therefore only certain photons can be absorbed [90]. A diatomic molecule can only perform a single vibrational motion. Molecules consisting of several atoms have more degrees of freedom for vibration. Each atom can vibrate in three spatial directions, but they do not detach from each other, but all move in the same direction,

simultaneously changing the common center of mass. These are the so-called translational motions of the molecules. In total, polyatomic molecules have $Z = 3N - 6$ degrees of freedom to vibrate [90]. However, if the molecules are linear, the number increases to $Z = 3N - 5$ degrees of freedom. The number of vibrations of the molecules calculated here is also called molecule´s normal modes of vibration. The possible energies are in the range of infrared radiation between 780 nm and 50 μm [90]. The change from a vibration state to a higher level is therefore accompanied by the absorption of a photon. If the energy of the absorbed photon is too low to convey the molecule into a higher vibration state, however, the rotation of the molecule can be stimulated. The simplest possible model to represent the vibration of a molecule are two point atoms with the masses m_1 and m_2, which are connected by a massless spring. The electrons of the atoms are neglected in this model, not least because of their low mass [90]. The vibration around the common center of mass can now be treated as a one-dimensional harmonic oscillator with the following frequency:

$$\omega = \sqrt{\frac{k}{\mu}} \tag{5.3}$$

μ is the reduced mass of the system and k the spring constant (depending on the binding energy) of the system. If the masses differ so that $m_1 \neq m_2$, they vibrate with a different amplitude. If this model is now transferred into quantum mechanics with the aid of operators and the Schrödinger equation as the solution of the system, the following discrete energy states with the energy Eigenfunction of the one-dimensional harmonic oscillator are obtained:

$$E_v = h\nu \left(v + \frac{1}{2} \right) \tag{5.4}$$

h is the Planck constant, v is the vibration quantum number and ν is the oscillation frequency from classical mechanics [90]. The vibration quantum number can assume all positive integers as well as 0, where 0 represents the ground state of the system. Only transitions where $\Delta v = \pm 1$ is valid are allowed. Fig 5.3 shows a sketch of the different vibration states of such a one-dimensional quantum mechanical oscillator and the corrosponding term scheme. However, it must be remembered that diatomic molecules consisting of the same atoms cannot be excited to vibrate by infrared radiation if they do not have a dipole moment. Such molecules are called IR-inactive [90]. Molecules consisting of different atoms can always interact with infrared radiation and are therefore called IR-active. If there is no dipole moment at the beginning of polyatomic molecules such as CO_2, they

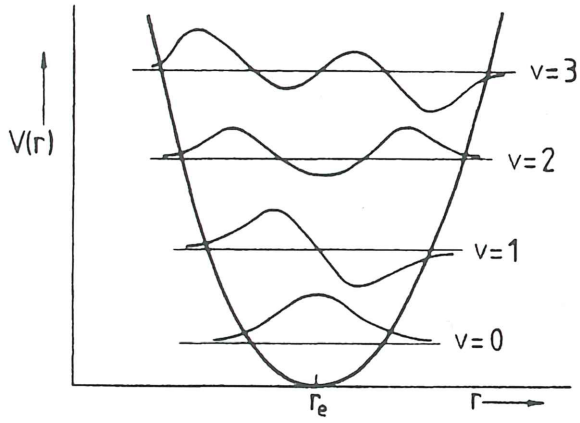

Figure 5.3: Sketch of the potential energy with the first discrete energy states and the corresponding Eigenfunction for a linear harmonic oscillator. The sketch is taken from [90].

can still be excited to vibrate. However, only the asymmetric oscillations can be excited here, since these lead to an asymmetric shift of the charge centre. A symmetrical oscillation would cause the negative charges (oxygen) to vibrate symmetrically around the positive charge (carbon) and the dipole moment would remain unchanged due to the stationary charge centre. The same applies to rotation, which can only be excited or raised to a higher level if the molecule has a dipole moment or if a dipole moment is generated by the vibration [90]. Fig 5.4 shows the dipole moment during vibration for three different molecules: **a)** Hydrogen chloride changes its dipole moment during the vibration, **b)** antisymmetric vibration for carbon dioxide with oscillating centers of charge (the negative center of charge of the oxygen and the positive center of the carbon), **c)** symmetric vibration of the carbon dioxide with a oscillation in phase of the positive and negative charge centers without the change of the dipole moment [90].

In IR spectra, at least the transmission or absorption of IR-radiation is plotted over the wavenumber. The wavenumber is calculated as follows:

$$\bar{\nu} = \frac{\nu}{\mathrm{c}} \tag{5.5}$$

and therefore is connected to the wavelength via $\bar{\nu} = \frac{1}{\lambda}\left[\frac{1}{\mathrm{m}}\right]$. Typical values for the wavenumber used in IR spectroscopy are between 200 cm^{-1} and 4500 cm^{-1} [90]. However, it must be mentioned

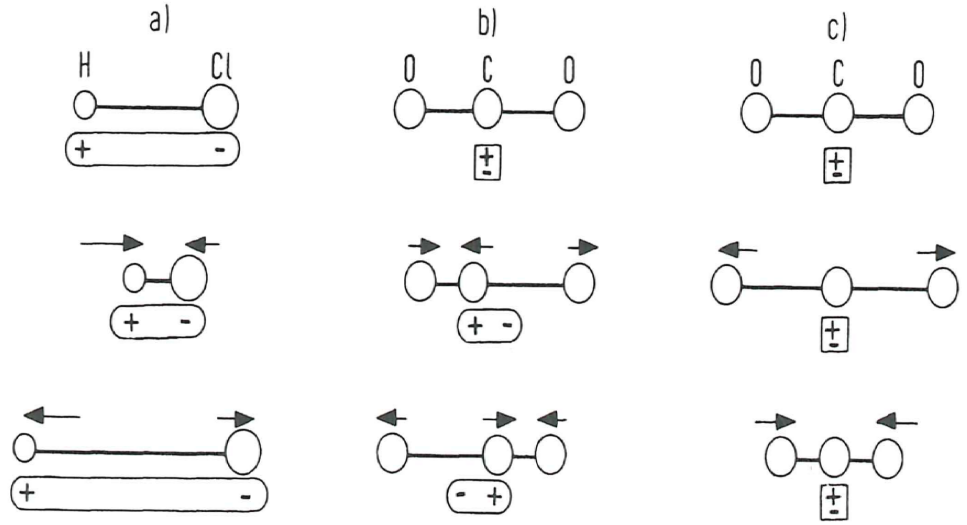

Figure 5.4: Dipole moment changing during the molecular vibrations: **a)** hydrogen chloride with a changing dipole moment, **b)** antisymmetric vibration for carbon dioxide with an oscillation of the positive and negative centers of charge and **c)** symmetric vibration for the carbon dioxide with a in-phase oscillation of the positive and negative centers of charge. The sketch is taken from [90].

that the assumption of a one-dimensional harmonic oscillator is only an approximation for the system. A more accurate assumption is the anharmonic oscillator. The most important difference between the two oscillators is that the selection rule for the anharmonic oscillator is given by $\Delta v = \pm 1, 2, 3, \ldots$. Therefore a system in the ground state $\Delta v = 0$ can not only be excited into the state $\Delta v = 1$, but also into states $\Delta v = 2$, $\Delta v = 3$ etc. These are so called overtones. The transition from the ground state to the first excited state is called fundamental vibration. The transition from the ground state to the second excited state is called first overtone, from the ground state to the third excited state second overtone, etc. A fundamental vibration can therefore not only be detected at its actual location, but also appears, due to the anharmonicity of the vibration, at two [$\Delta v = 2$] and three [$\Delta v = 3$] times the value of the wave number [90].

If the molecule is to change to a lower vibrational state, two possible processes are used: firstly by emitting a photon and secondly by transferring energy to the surrounding medium (e.g. by collision with other particles in a gas).

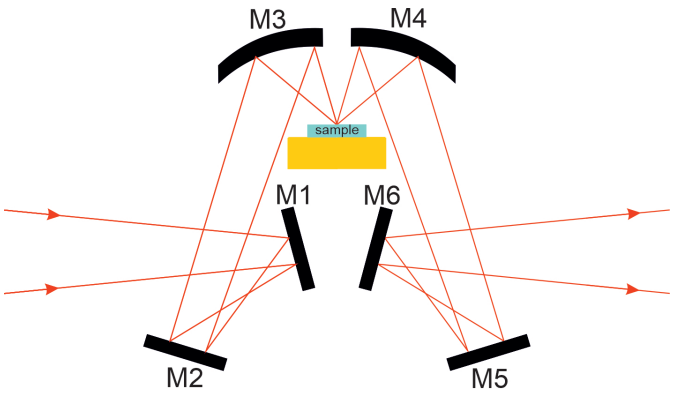

Figure 5.5: Sketch of the diffuse reflectance measurement unit. The sketch is based on ref [90].

5.3.1 Diffuse reflectance infrared Fourier transform (DRIFT) spectroscopy

For samples which consist of powder or have a very rough surface, diffuse reflection is often used. Therefore the Shimadzu Fourier transform spectrometer (IRPrestige-21, Shimadzu, Kyoto, Japan) used was equipped with the diffuse reflectance measuring apparatus DRS-8000 (Shimadzu, Kyoto, Japan). Here, an IR laser beam is divided by a beam splitter. One partial beam is directed onto the sample (analysis beam), another is used as a reference beam for later analysis. Fig 5.5 shows the structure of such a DRIFT unit (diffuse reflectance infrared Fourier transform spectroscopy) for the analysis beam. The system consists of several mirrors, which direct the laser beam onto the sample. In the sketch the laser beam comes from the left, hits mirror M1, is reflected by mirror M2 onto mirror M3 and finally hits the sample. The IR beam is then scattered and reflected at the sample. The resulting signal is collected by the mirror M4 and then passed through the mirrors M5 and M6 to the analyser (not shown here), where the signal is compared with the reference beam and the corresponding absorption spectrum is calculated by the software [90].

The diffuse light scattered on the sample consists of two different components: One part of the incoming beam is reflected directly by the roughness of the surface. Another part of the beam penetrates into the sample, is partially absorbed there or returns to the surface by scattering processes within the sample. The two beams can usually not be separated experimentally and are analysed as an overall signal [91]. In the literature this diffuse reflection is also called "Kubelka-Munk reflection", since these two have described the radiation transport in scattering media [90]. Here the diffuse reflection is described in a one-dimensional model in which the optical properties of the samples are only described by two relevant constants: the absorption coefficient and the

reflection coefficient. The Lambert-Beer law, which is normally used for transmission, is not directly applicable to DRIFT measurements [91]. In the following, the degree of reflection can be described by the following Kubelka-Munk equation:

$$\mathrm{f(R_\infty)} = \frac{(1-\mathrm{R_\infty})^2}{2\,\mathrm{R_\infty}} = \frac{\mathrm{K}}{\mathrm{S}} \tag{5.6}$$

R_∞ represents the degree of reflection for an infinite sample thickness, S is the scattering modulus and K is the absorption modulus (both in units of inverse length) [90, 91]. K can also be represented by the absorption coefficient a:

$$\mathrm{K} = 2\,\mathrm{a} \tag{5.7}$$

The absorption coefficient is directly proportional to the amount of absorbent material. However, the parameter S is difficult to determine and is not known for the a-C:H films applied to the examined samples. Kubelka and Munk circumvented the problem by assuming the sample to be examined to be infinitely thick, which reduced the transmission through the sample to zero and resulted in equation 5.7 [91]. However, it follows from the unknown value of the parameter S that the obtained spectra do not contain any information about the respective concentration and that these cannot be derived from the absorption coefficient a. Since equation 5.7 generally applies to powder samples, the software and measurement system are designed and calibrated for this type of sample [91]. It can also be assumed that no IR radiation reaches deeper regions of the samples to be examined and therefore only information about the functional active groups from the top-surface regions generates a measurement signal and thus only a low penetration depth is achieved. Overall, the DRIFT technique is particularly suitable for samples that cannot be measured in transmission.

The measurements were taken at room temperature in ambient air [91] and performed in two consecutive steps: First, the maximum measurable spectrum from 500 to 4000 $\mathrm{cm^{-1}}$ was recorded. A resolution of four wave numbers and 100 repetitions was chosen. With the help of this total spectrum it could be excluded whether other areas were also influenced by the different layer thicknesses. Subsequently, the most relevant spectral range of 2800-3100 $\mathrm{cm^{-1}}$, the so-called C-H-streching region [90, 35], was measured with a higher resolution of one wave number and an average of 300 repetitions. The measurements were based on three different points on the samples to prove the sample homogeneity and the correctness of the measurements. The reference for the

DRIFT measurements on a-C:H coated samples was the respective O_2 plasma treated polymer sample. The analysis of the obtained spectra was performed with the commercial IR solution - FTIR Control Software (software version 1.30, Shimadzu Corporation, Kyoto, Japan). The applied protocol only briefly: first a multi-point baseline insertion using the integrated manipulation tool, then fine tuning with the software integrated smoothing manipulation. These manipulations only change the appearance of the graph, but not the information contained in it. The spectra obtained were then plotted on the respective graphs using the software OriginPro 8.1G.

5.4 Near-edge X-ray absorption fine structure spectroscopy (NEXAFS)

The near edge X-ray absorption fine structure technique, or NEXAFS for short, was developed in the 1980s to analyse the structure of surface bound molecules. To perform this study, the K-edge of a single type of atom (e.g. carbon) is selected and the bonding with its neighbours within the molecule is evaluated. Information can also be obtained about the bond to neighbours outside the molecule (such as the atoms on the surface to which the molecule was deposited), although to a lesser extent. Thus, not only specific binding states are investigated (e.g. C-C, C=C, C-H etc.), but also information about the binding length of the intramolecular bonds and about the orientation of the molecules and functional groups can be obtained [92]. Within the framework of this thesis, the binding states of the a-C:H layers deposited on polymers were investigated using the NEXAFS technique with synchrotron radiation at the BESSY II in Berlin.

The spectroscopy of molecules bound on the top surface got two big problems. First of all the typical atomic density of around $10^{15}\,\frac{\text{atoms}}{\text{cm}^2}$ [92]. Since molecules cover the surface normally in a single layer this number corrosponds to the molecular number. Secondly the signal aquirred from the top layer is superimposed by a signal originated from the bulk material. Therefore it is necessary for the analysis of - especially very thin - layers to have a highly surface sensitive technique to perform these measurements [92].

In near-edge X-ray absorption fine structure spectroscopy, the energy of the incident photons is continuously varied over a certain energy range. The step size of the variation is usually not kept constant. Depending on the edge to be investigated, such as the C-edge or the O-edge, specific energy values occur at which absorption occurs. In these areas, the step size is reduced in order to obtain a better resolution. The optimum measuring range for this technique is for molecules

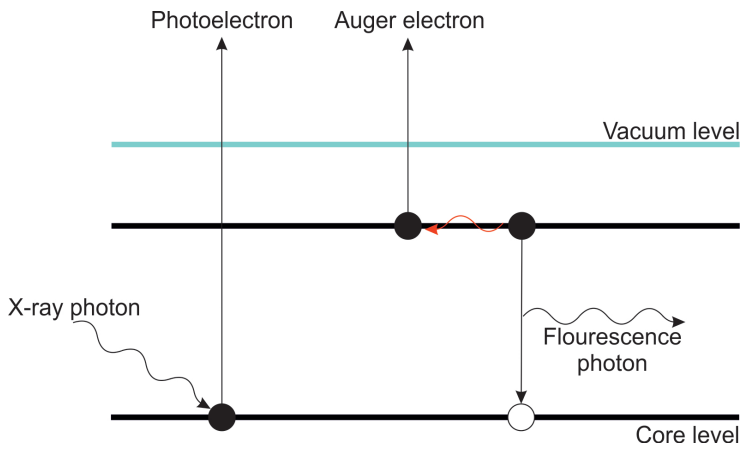

Figure 5.6: Schematic drawing of the photoabsorption with emission of a photoelectron. In addition, the occupation of the core hole is shown, which takes place either by emitting an Auger electron or a fluorescence photon. The Auger electron is used for NEXAFS studies, the photoelectron for XPS measurements. This figure is based on ref [92].

with a low atomic number Z and whose intense absorption edges are in the soft X-ray range between 100 and 700 eV. Since most organic molecules consist at least partially of light atoms like carbon, nitrogen or oxygen, this is not a strong restriction of the usability for surface analysis [92]. By standard, this technique is used to investigate the transition of electrons from the deepest shell in an atom, the so-called K-shell (hence the K-absorption edge), to unoccupied orbitals in this atomic/molecular system. Thus, this technique is not only useful to study intramolecular interactions at the substitution surface, but also to study the interaction between the adsorbed molecule and atoms of surrounding molecules or with atoms of the surface. A further advantage is the high selectivity of NEXAFS, as individual species are specifically examined for their binding states [92]. If NEXAFS is applied to insulating substrates such as diamond and polymers, there are also no charging effects which have to be compensated for in other techniques such as XPS. With NEXAFS, they are negligible because only the absorption of the incident photons is examined. The greatest advantage of the NEXAFS technique is the sensitivity of the chemical bonding systems. The C1s peak of the carbon atom and its bonds, for example, do not differ in single and double bonds by even one eV, which makes the deconvolution of the peak difficult. In NEXAFS, this separation is easier because not only the binding energy but also the final states into which the particle is lifted are considered. So the unoccupied $\sigma-$ and $\pi-$ orbitals of the double bond are several eV apart, which makes the detection of the double bonds very easy [92].

The easiest way to measure X-ray absorption would be to directly irradiate the sample with X-rays and measure the intensity before and after. However, the thickness of the sample is a limitation (only very thin samples could be measured) as well as the loss of surface sensitivity. Therefore, the method of measuring induced electrons is used. If the X-ray beam hits the surface of the sample and thus the molecules and atoms bound there (as can be seen in fig 5.6), free photoelectrons are generated as soon as the ionisation energy is reached, which leave the material. In addition, a core hole remains, which corresponds to an unoccupied, low-energy state. The resulting core hole is now filled by another electron, which was previously at a higher bond level [92]. To fill this core energy state it must release part of its energy. This happens either radiating through a fluorescence photon or radiation-free through the emission of an Auger electron [92]. The released energy is transferred to another electron in the system, which then leaves the atom/molecule as an Auger electron. These electrons then enter an electron multiplier and are then detected. A signal correlating with the absorption of the X-ray quants is generated. Both the fluorescence photons and the Auger electrons can be used for the detection of X-ray absorption. However, it is recommended to consider the Auger electrons for atoms with low nuclear charge numbers Z, such as carbon or oxygen, since the electron yield is much higher than the fluorescence yield [92]. In addition, the electron yield offers a higher surface sensitivity. This is due to the fact that the mean free path length of electrons in matter at this energy is only about 1 nm and therefore only electrons close to the surface can leave the material. The electron yield can be distinguished between total and partial electron yield [93, 92]. In total electron yield (TEY) all electrons are measured [92]. If the partial electron yield (PEY) is used, electrons with low kinetic energy are suppressed and thus only electrons from the region closest to the surface are measured. For the analysis of deeper layers, fluorescence analysis is recommended, since the X-ray photons emitted here can penetrate the material over a greater distance than the Auger electrons [92].

The NEXAFS measurements were performed at the HE-SGM beamline of the KIT in the Helmholtz-Zentrum Berlin. The measurement system used is described in detail elsewhere [94]. Due to the too high intensity of the radiation for the samples, the measurements were carried out during the low-alpha phase with a maximum ring current of 100 mA in decay mode. Furthermore, an integrated flood gun was used to reduce the loading effects on the samples during irradiation with X-ray. Both, the C K- and O K-edges of the samples were recorded. The C-edge was recorded at a minimum of two locations to ensure the accuracy of the measurements. The O-edges were used to detect the presence or absence of oxygen on the sample surface and are not discussed further

in this thesis. All measurements shown here were performed in partial electron yield (PEY) at a photon incidence angle of 55°, the so called "magic angle". In the PEY a counter voltage is applied and therefore not all electrons emerging from the material reach the measurement electronics. As a result, this technique is much more surface sensitive, since only the electrons of the near-surface regions have enough energy to reach the detector [94].

To analyse the measurements from the NEXAFS series, the spectra were first normalised after recording and synchronized to the ring current drop using OriginPro 8.1G. Background noise was also corrected. Finally, an adjustment was made to a gold edge to correct for grid contamination and mirror artifacts [93]. This gold edge for the corrections was recorded at the beginning of the measurement campaign on the analysis system itself. The corrected spectra were then smoothed and analysed. For the studies, the peak positions have been determined on the base of the work of other groups. The peaks analysed are C=C π (284.85 eV), C-H (286.15 eV), C-C (288.35 eV) and C=C σ (292.55 eV) [92, 95, 96, 97, 98]. The measured, normalised spectra were plotted using OriginPro 8.1G software. Here, the intensity was plotted against the photon energy.

5.5 X-ray photoelectron spectroscopy (XPS)

X-ray photoelecton spectroscopy (XPS) is a wide-spread technique for the investigation of the chemical composition of surfaces. It is a powerful technique for its ability to analyse the first atomic layers and assign the chemical states of the atoms detected. In the XPS analysis, the surface is bombarded with monochromatic soft X-rays and the resulting photoelectrons are measured. Here, the kinetic energy of the electrons is considered.

When the X-ray radiation impinges on the surface, electrons are released from the atoms according to the photoelectric effect and leave the material into the vacuum. There they reach the collector, which detects both the number and the kinetic energy of the electrons. The following equation can then be used to calculate the binding energy of the electrons and thus determine in which state they were bound in which type of atom [99]:

$$\mathrm{E_{kin,pe}} = \mathrm{h}\nu - \mathrm{E_{Binding}} - \Phi \tag{5.8}$$

where $E_{kin,pe}$ is the kinetic energy of the photoelectron, $h\nu$ the energy of the impinging X-ray photons, $E_{Binding}$ the binding energy of the electron in the atom and Φ the spectrometer work function [99]. Because each element has its own unique spectrum of binding energies, it is possible to de-

termine which element is present with XPS. In addition, the concentration of the corresponding elements on the surface can also be determined. Minor variation in the elemental binding energies can be attributed to differences in the chemical environment or to the polarization of the compounds. Thus, these shifts can be used to determine the chemical state of the investigated atoms. Since the accuracy of the results depends directly on the monochrony of the incident radiation (see formula 5.8), stable sources with a very narrow wavelength interval are necessary. Possible sources are for example the K_α radiation of magnesium (1253.6 eV) or aluminum (1486.6 eV), which are preferably used in in-house XPS instruments, or synchrotron radiation of an electron storage ring as in the measurements presented here [99, 94].

It should also be mentioned that a second process occurs during the measurement. If a photoelectron leaves its position in the atom, an Auger electron is additionally released from the atom with an offset of 10^{-15} seconds [92, 99]. Here an electron falls from an energetically higher level to the now free position and transfers its energy in the form of kinetic energy to a formerly adjacent electron, which then leaves the atom. Therefore two electrons are always emitted during the XPS measurement: The photoelectron, which is detected for the measurement, and an Auger electron, which has only relatively low energies [99]. These can be seen in the measurement of a survey starting with a binding energy of 700-650 eV (see fig 5.7). The sum of the kinetic energies of the emitted electrons cannot exceed the energy of the ionizing photons.

The high surface sensitivity is due to the different probabilities of the interaction of the existing species with matter. While the photons can penetrate several micrometers into matter, the free path length of the electrons is in the range of several nanometers [99]. Even if electrons are released deep in the material to be examined, they cannot reach the surface, because their energy loss becomes too great when crossing the material through interaction with it. These surface near electrons which can leave the surface an without energy loss are responsible for the peaks in the spectra and are used for the analysis.

In order to obtain a spectrum of the electrons emitted at the surface, an interval dE around the energy E is selected at the detector, whereby the electrons are detected and E is scanned over the relevant energy range. The energy filter used is usually either a hemispherical capacitor or a hemispherical electron energy analyser. Here, two electrodes arranged as concentric hemispheres generate an electrostatic field, which can only be passed by electrons with the so-called pass energy E_{pass}. The energy resolution dE is defined by slots at the input and output. A sketch of such an XPS can be seen in fig 5.8. The XPS measurements were performed at the HE-SGM beamline of the

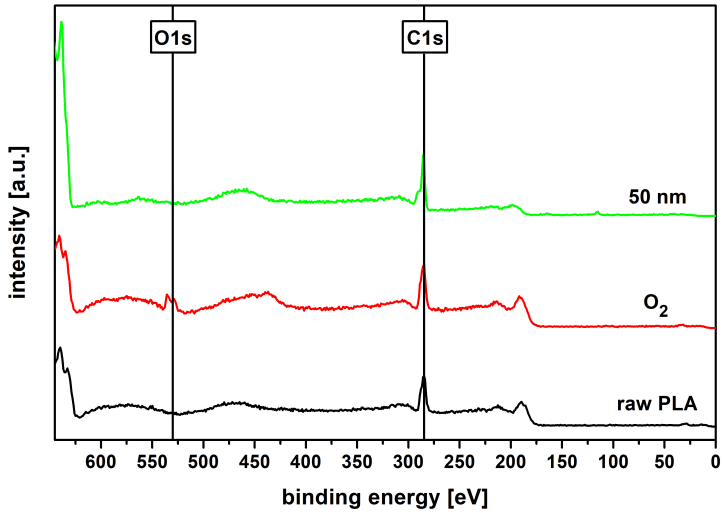

Figure 5.7: Examples for survey measurements of the raw polymer PLA (black), O_2 plasma treated PLA (red) and PLA coated with 50 nm a-C:H (green). The low energy electron peak on the left of the graph is cleary visible, the different element peak positions (for this system: O1s and C1s) are also visible. The graph is based on ref [100].

KIT at the BESSY II in the Helmholtz-Zentrum Berlin. The measurement system used is described in detail elsewhere [94]. A full survey spectrum of 700-0 eV and at least two measurements of the C1s peak (∼285 eV) were performed at different locations to ensure reproducibility and accuracy of the measurements. The spectra obtained were then analysed and evaluated with the CasaXPS software (software version 2.3.18, Casa Software Ltd., United Kingdom). Using the NIST database (https://srdata.nist.gov/xps/main_search_menu.aspx) and the work of other groups, the positions of the respective hybridisation states were determined [101, 102, 103]. The respective binding percentages were then plotted in the OriginPro 8G software.

5.6 Selected polymers for the coating

In the framework of this thesis different biodegradable polymers were coated with a-C:H layers. Polylactic acid (PLA) and polyhydroxybutyrate (PHB), which are also based on renewable raw materials (PLA is obtained from corn starche/potatoes or sugar [12, 25], PHB from a fermentive manufacturing process [26]), were used as well as the crude oil-based polybutylene adipate terephthalate (PBAT), which is also biodegradable [27]. PLA and PHB films have been obtained in industrial quality as sheets of 30×30 cm and 50 µm thickness (Goodfellow GmbH, Friedberg, Ger-

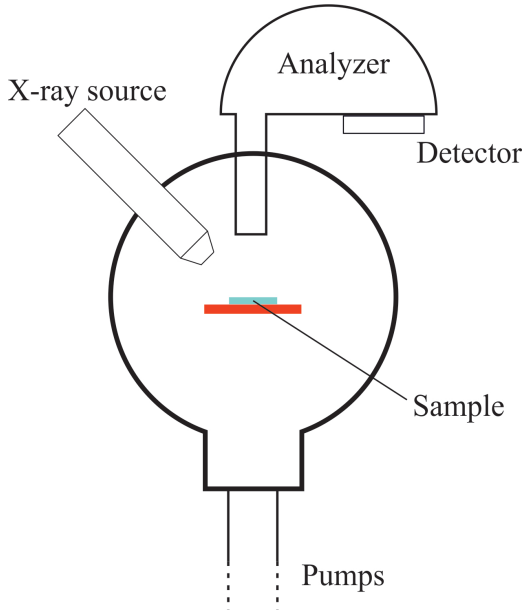

Figure 5.8: Sketch of an X-ray photoelectron spectroscopy analysis system. The figure is based on ref [94].

many), PBAT films were obtained by Dr. Lackner and also have a thickness of 50 µm (industrial quality, Lackner Ventures and Consulting GmbH, Vienna, Austria). The polymers PLA and PHB are used, among other things, for food packaging or in agriculture for mulch films. PLA and PHB also have good biocompatibility [104]. PBAT is furthermore used for composting bags or as foam [105, 106]. These polymers were chosen because they have a wide range of industrial applications. This could be further extended by the refinement with an a-C:H layer and thus replace classic, non-recyclable polymers and therefore help to solve the raw material/disposal problem. The respective polymer properties and the chemical composition are shown in table 2, the chemical structural formula is sketched in fig. 5.9.

However, in order for the respective polymers to be specifically adapted to the applications by coating them with an a-C:H layer, it must be examined how the layer grows on the respective polymer and whether it is stable. Furthermore, the different chemical structure of the polymers allows conclusions to be drawn about the effect of a changed carbon-oxygen ratio on the deposited layer. In addition to the polymers to be coated, silicon wafers from the company Silicon Materials were used during the coating processes to measure the thickness of the deposited layers (Silicon Materials, Kaufering, Germany). The wafers, which were delivered as wafer sheets with

Table 2: Overview of the substrates used in the thesis

substrate	Supplier	Tensile strength [MPa]	number of carbon/oxygen atoms
Polylactic acid	Goodfellow	53	3 : 2
Polyhydroxybutyrate	Goodfellow	40	4 : 2
Polybutylene adipate terephthalate	Lackner Ventures and Consulting GmbH	≥ 18	12 : 4 + 8 : 4
silicon (100)	Silicon Materials	-	-

a thickness of 0.5 mm thick, were cut into squared samples of 1 cm^2 of area (WGD WAFER & GLASSUBSTRATE DICING GmbH & Co. Kg, Linsengericht, Germany) by a laser procedure.

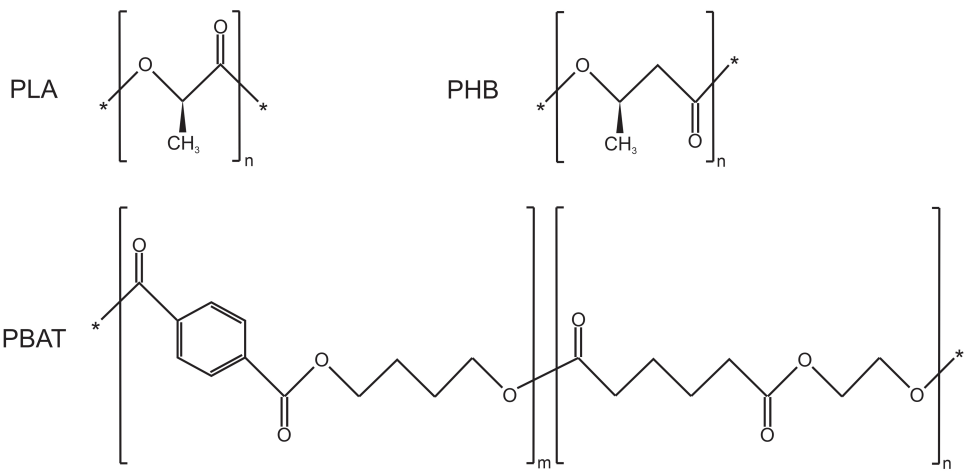

Figure 5.9: Structural formulas of the repeating chains for the polymers coated within the scope of this thesis: top line left polylactic acid (PLA), right polyhydroxybutyrate (PHB) and in the bottom line polybutylene adipate terephthalate (PBAT).

6 Results and Discussion

The results presented in this chapter of this thesis have been published in alltogether three publications. These are added to the end of this thesis and are refereed to as follows:

- T. Schlebrowski, L. Beucher, H. Bazzi, B. Hahn, S. Wehner, C.B. Fischer, Prediction of a-C:H layer failure on industrial relevant biopolymer polylactide acide (PLA) foils based on the sp^2/sp^3 ratio. Surface and Coatings Technology 2019, 368, 79–87, doi:10.1016/j.surfcoat.2019.03.069 [100]

- T. Schlebrowski, L. Beucher, H. Bazzi, B. Hahn, S. Wehner, C.B. Fischer, C.B. Changing Contents of Carbon Hybridizations in Amorphous Hydrogenated Carbon Layers (a-C:H) on Sustainable Polyhydroxybutyrate (PHB) Exhibit a Significant Deterioration in Stability, Depending on Thickness. C — Journal of Carbon Research 2019, 5, 52, doi:10.3390/c5030052 [107]

- T. Schlebrowski, H. Acharchi, B. Hahn, S. Wehner, C. B. Fischer Refinement of Sustainable Polybutylene Adipate Terephthalate (PBAT) with Amorphous Hydrogenated Carbon Films (a-C:H) Revealing Film Instabilities Influenced by a Thickness-Dependent Change of sp^2/sp^3 Ratio. Materials 2020, 13, 1077; doi:10.3390/ma13051077 [108]

The results presented in the following section are based on the publications listed here, no specific referencing is made. In addition, a further publication for the determination of interlayer thickness by means of X-ray spectroscopy was published, but the results obtained there are not presented in the context of this thesis.

- Schlebrowski, T.; Rouabeh, W.; Wehner, S.; Fischer, C.B. Specifying the interlayer turning point and dehydrogenation in a-C:H layers plasma deposited on high-density polyethylene with X-ray synchrotron techniques, Thin Solid Films 2019, 691, 137617, doi: 10.1016/j.tsf.2019.137617 [75]

Additionally, a publication on the basic coatability of fibre-reinforced biopolymers produced by the Materials Science, Energy and Nano-engineering Department of the Mohammed VI Polytechnic University in Ben Guerir, Morocco was also submitted and is currently under review:

- T. Schlebrowski, Z. Kassab, M. El Achaby, S. Wehner and C. B. Fischer, Influence of cellulose microfiber reinforcement for polyvinyl alcohol on the layer growth of plasma-deposited a-C:H, under review, Diamond and Related Materials, 2020

Some of the measures here presented are conducted during supervised bachelor/master thesis and projects as following (table 3):

Table 3: List of other persons' contributions to the results shown in this thesis (only measurements, no interpretation).

Name	Contribution	Project	Refrenz
L. Beucher:	Contact angle of PLA and PHB	project work	[100, 107]
H. Bazzi*	SEM for PLA and PHB	Bachelor Thesis: "Stabilitätsuntersuchungen an kohlenstoffbeschichteten, bioabbaubaren Kunststoffen"	[109]
H. Acharchi*:	SEM for PBAT	Bachelor Thesis: "Oberflächenuntersuchung von biologisch abbaubaren Polybutylenadipat -terephthalat- (PBAT)-Folien veredelt mit a-C:H-Schichten"	[110]

*University of Applied Sciences Koblenz - RheinAhrCampus, Remagen, Germany

The selection of the respective SEM images, their interpretation and the analysis of the contact angles was done by the author.

6.1 SEM

The following section presents the results of the SEM measurements for the biodegradable polymers PLA, PHB and PBAT coated with a-C:H films. The measurements of the reference and the O_2 plasma treated samples are also discussed in this section. Unless otherwise stated, the magnification rate is 442x. The edges of each image are 200 μm long.

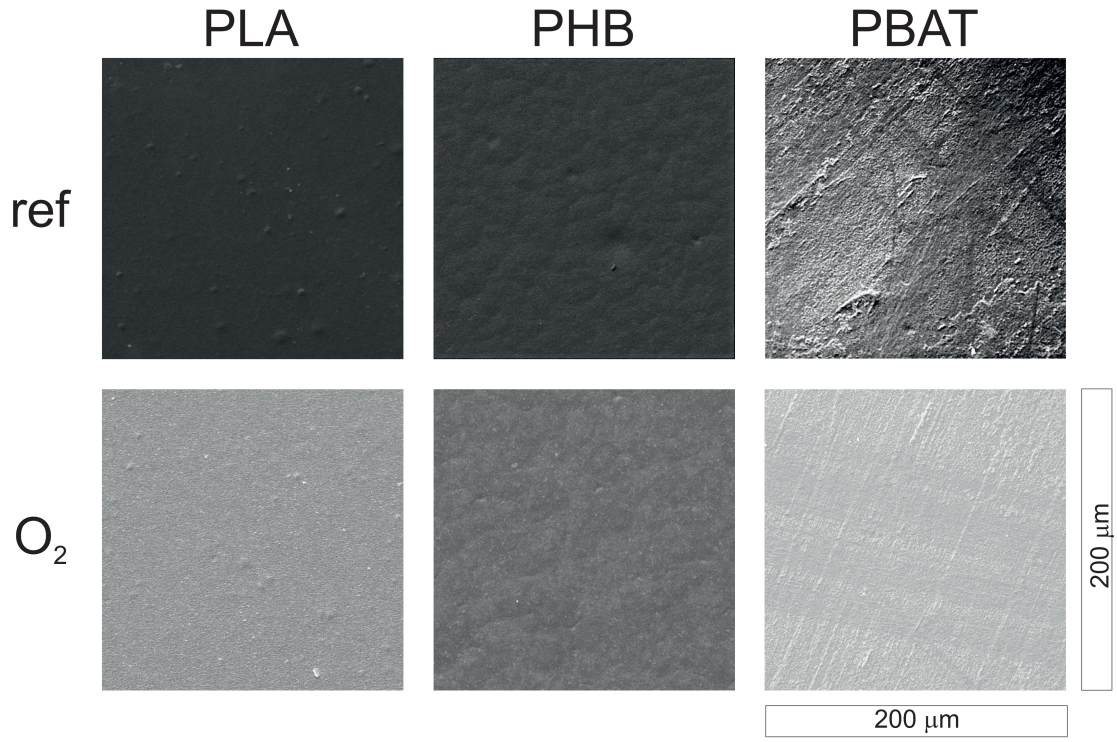

Figure 6.1: SEM measurements of the reference as well as the O_2 plasma treated PLA, PHB and PBAT samples.

The upper row of Figure 6.1 shows the SEM images of the raw polymers PLA, PHB and PBAT. The lower row shows the images of the O_2 plasma treated samples. The PLA raw polymer sample shows that some small particles are attached to the surface. In addition, unevenness in the form of smaller elevations is visible. After treatment with oxygen plasma, fewer particles are visible and the elevations are less pronounced. In addition, the surface appears roughened and more fragmented. The raw polymer sample from PHB shows clear granulate structures. With plasma treatment, this structure becomes weaker and the boundaries are less pronounced. For PBAT, a comparison of the sample treated with O_2 with the raw polymer shows that the previously present impurities

have disappeared. The surface also appears more constrictive and accentuated. The effects of the O_2 plasma treatment are mainly due to sputtering by the plasma. The use of O_2 plasmas results in a largely flat sample surface; only a few particles are visible on the sample surface. Possible sources of these particles are residues from the production and coating processes or dust particles from the ambient air during storage and transport of the films. In addition, the structures of the polymers become softer due to the removal of material.

Fig 6.2 **a)** show the SEM images for the O_2 treated PLA sample. Subsequently, the a-C:H coated samples are presented with increasing layer thickness. A comparison of the raw polymer sample and the O_2 treated sample shows that the surface is more pronounced and contrasted after treatment. This is mainly due to the sputtering process of the plasma. In addition, most of the particles on the surface are removed from the surface, leaving a smooth surface with few scattered particles. These particles can have several causes, such as dust from the ambient air or impurities from the production of the polymer itself or from in-house processes. Fig 6.2 **b)** shows a PLA sample with a 50 nm thick a-C:H layer. The resulting layer is uniform overall, which remains unchanged up to a thickness of 100 nm (fig. 6.2 **c)**). If the thickness of the carbon layer continues to increase, it is still closed, but shows strong visible crimps and waves. This effect is called "telephone cord buckling" [76, 77], which indicates stress release phenomena as seen at layer thicknesses of 150-250 nm and also at 450 nm and 500 nm. After further increasing the layer thickness to 300 nm, a clearly broken film can be seen in the SEM images (fig. 6.2 **g)**). The cracks run through the entire film and a broken surface is visible. As the a-C:H layer thickness increases, a uniform film is achieved again, as can be seen for the layer thicknesses of 350 and 400 nm. With a further increase of the layer thickness, the film starts to wave and crimp, as can be seen for the layer thicknesses of 450 nm and 500 nm. Again the cord-buckling effect occurs. In addition, a further film deposition leads to a detachment and rolling of the carbon film on the sample surface, as shown in the measurement for a layer thickness of 1000 nm in fig. 6.2 **l)**. The this sample was taken with a magnification of 225x was choosen becaue of the size of the failed layer area.

The SEM results obtained here show a change of the adhesion properties of the carbon coated PLA films with increasing thickness of the a-C:H layer. In the case of thin layers down to 100 nm, an apparently homogeneous and stable coating of the surface is achieved. However, structures such as imperfections of the base biopolymer are still visible. With increasing layer thickness, these structures are increasingly covered by the deposited carbon layer until they are no longer visible at a layer thickness of 250 nm. If the deposited layer exceeds a thickness of 150 nm, however, the cord

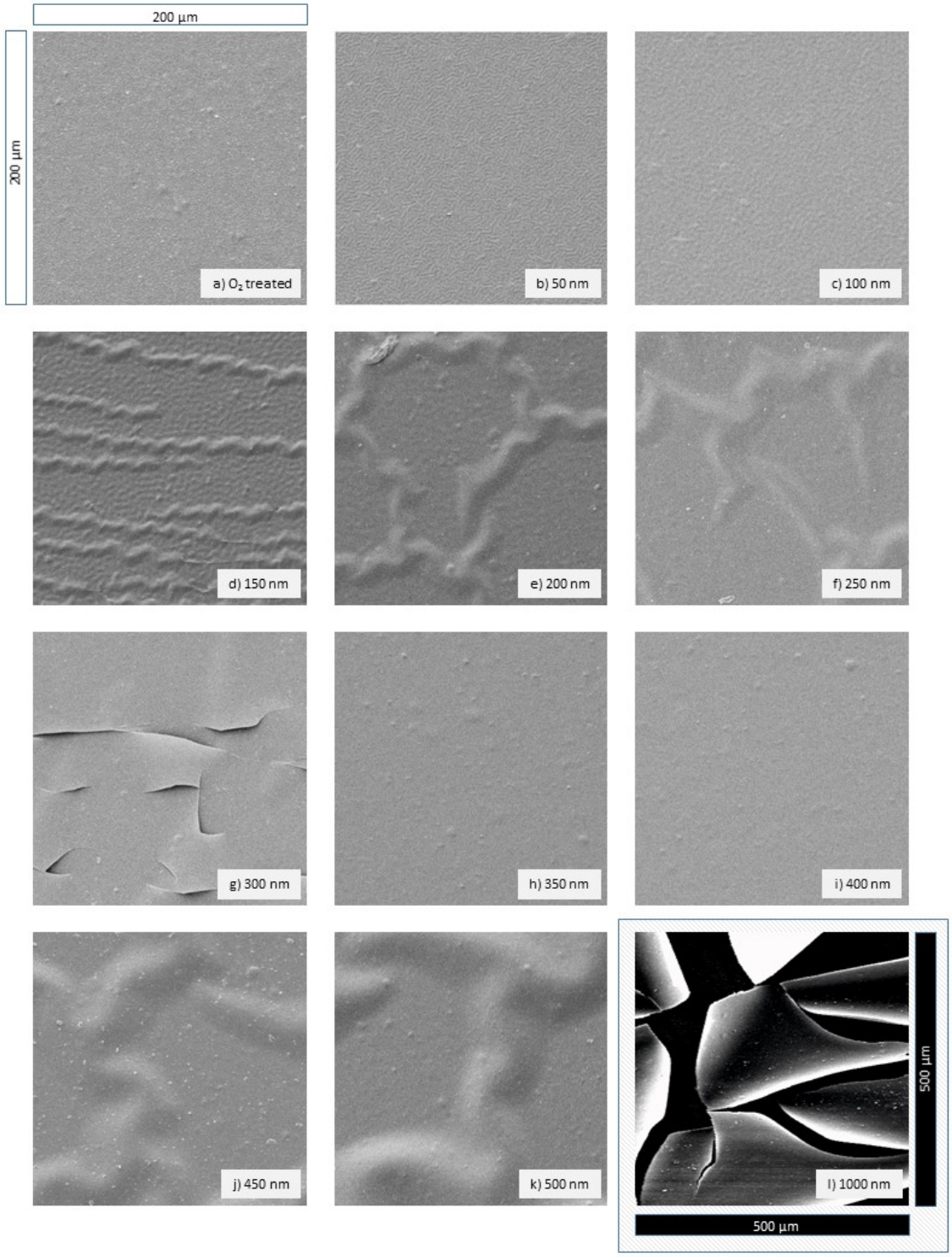

Figure 6.2: SEM images of PLA samples treated with an O_2 plasma **a)** and coated with a-C:H layers with increasing thickness **b)**-**k)**. The image magnification is 445x, the length of each side of the image equals 200 μm. Image **l)** shows the SEM picture for 1000 nm a-C:H thickness with a smaller magnification. The figure is based on ref [100].

buckling begins with a continuous detachment of the layer. These resulting crimp structures grow and begin to detach more and more from the base substrate. The film, however, is not broken open but remains stable and closed. With increasing thickness, the layer finally fails at a layer thickness of 300 nm and breaks open. This behaviour is repeated again with a higher layer thickness, even if homogeneous, closed layers have been obtained in the interim. The behaviour of the crimps and layer failure can be explained by the internal stress of the coating and substrate combination, which is apparently proportional to the layer thickness. Some reasons for these stresses may be: different expansion or material coefficients of both materials (PLA, a-C:H) or island formation of the a-C:H layer and interaction of these islands with each other in early growth phases as described in section 3.2.2. If this internal stress exceeds a critical value, the layer on the film begins to crimp (telephone cable bending effect), as can be seen with thicknesses from 150 nm up to 250 nm or at 450 nm. Increasing internal stress causes the a-C:H layers to continue to bend and detach from the polymer, but the layer remains closed at the beginning due to the stability of the carbon network. At a thickness of 300 nm the internal stress increased further and the film starts to crack. A relaxation of this internal stress is visible for layer thicknesses of 350 and 400 nm. Here the film is smooth and closed again until the internal stress rises again at a layer thickness of 450 nm leading to a total layer failure at a thickness of 1000 nm. Alltogether, the SEM images show three different possible results for the achieved a-C:H coating, dependent on the film thickness: **1)** two intervals of layer thickness of a-C:H coatings on PLA at which the film adheres stably after completion of the coating process (50, 100, 350, and 400 nm), **2)** coatings, which are still homogeneous and closed films on PLA, but with stress phenomena as bulges and crimp structures (150–250, 450, and 500 nm), **3)** complete layer failure at layer thicknesses of 300 and 1000 nm. Therefore, the film thickness is a critical value for the achivement of stable a-C:H layers on the polymer PLA as there are stable intervals of layer thickness.

Figure 6.3 shows the SEM images taken for the PHB sample series. Apart from the sample with a 500 nm a-C:H layer, for which 885x magnification was selected, all other images were taken with 442x magnification. The side edges of the images have a length of 200x200 μm or 100x100 μm for the 500 nm a-C:H coated sample. First the O_2 plasma treated sample is shown, followed by the a-C:H coated samples in order of increasing layer thickness. The treatment of PHB with the oxygen plasma results in a rougher surface compared to the reference sample, while impurities are removed. Again, as with the PLA, the sputtering of the plasma or plasma particles on the surface is responsible. If a 50 nm a-C:H layer is deposited on the polymer previously treated with O_2, it

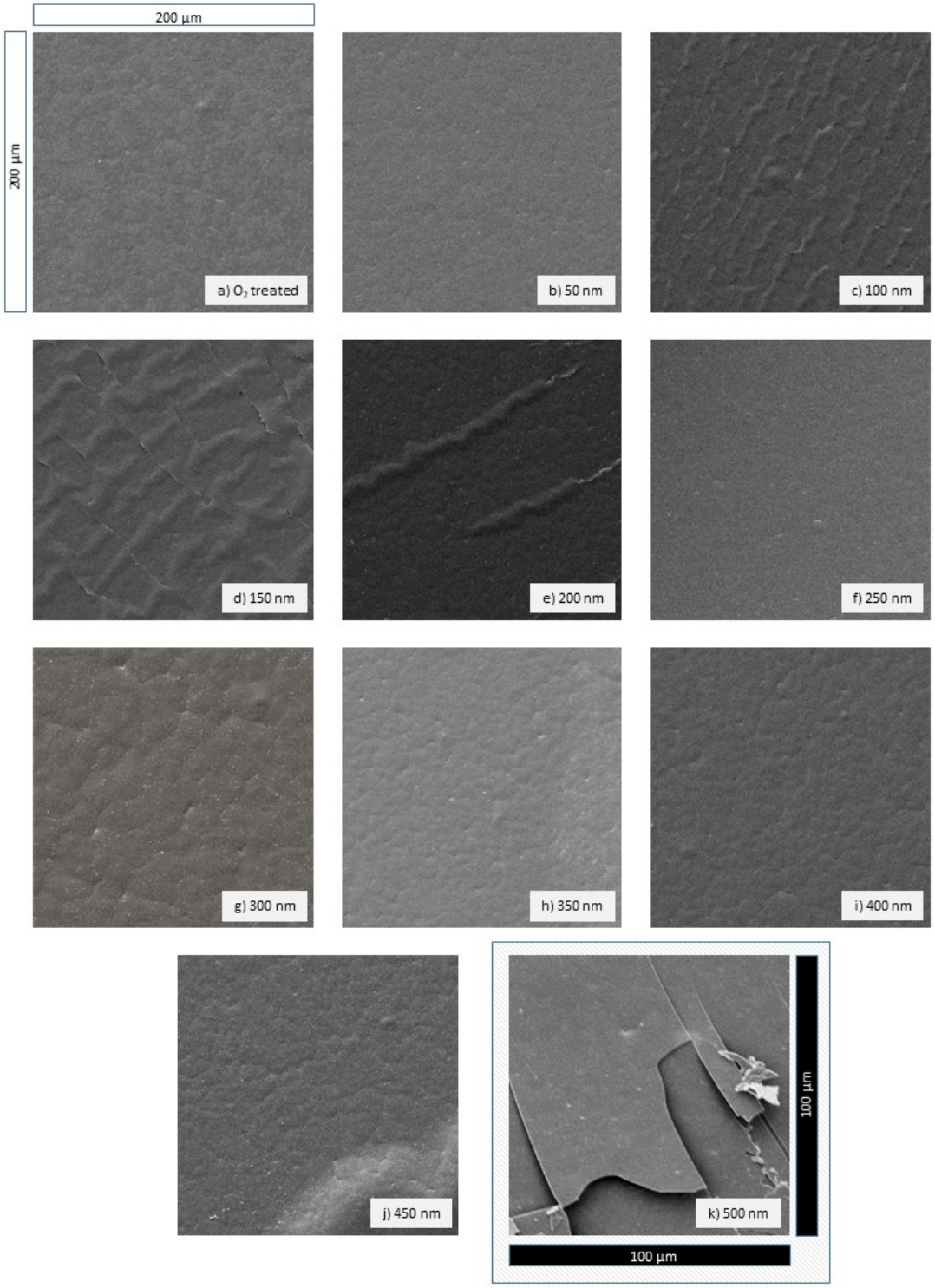

Figure 6.3: SEM images of PHB samples treated with an O_2 plasma **a)** and coated with a-C:H layers with increasing thickness **b)-j)**. The image magnification is 445x, the length of each side of the image equals 200 μm. Image **k)** was taken with a magnification of 885x to show evidence for the layer failure. The figure is based on ref [107].

forms a homogeneous layer. The surface roughness also decreases significantly compared to the O_2 plasma treated sample. When a 100 nm thick layer is applied, the SEM images show that the a-C:H film begins to peel off: The stress phenomena telephone cord buckling effect [76, 77] is also visible here, as with the PLA, but it already occurs at thinner layer thicknesses. At 100 nm the network is still strong enough to keep the film closed, but the stress increases with increasing layer thickness and the layer breaks open at a thickness of 150 nm. Even at a layer thickness of 200 nm these stress-related phenomena are still observable, the film is crimped and broken. Compared to the PLA, where film failure occurs at 300 nm film thickness, PHB is much earlier. A homogenous, closed film is present again after a layer thickness of 250 nm. Even with a further increase in film thickness, the film remains stable up to a film thickness of 400 nm. If an a-C:H layer thickness of 450 nm is applied to the PHB samples, the cord buckling effect occurs again. The layer begins to peel off and wave. With a layer thickness of 500 nm a-C:H on the PHB, the layer finally breaks up completely and a new layer failure occurs. Overall, the a-C:H coated PHB samples show a similar picture as the PLA samples. However, it should be mentioned that both cord buckling and breaking of the layer and thus layer failure in the case of PHB already occurs at lower layer thicknesses. Both events are due to stress phenomena and thus to the bonding of the layer on the polymer and the bonds of the carbon atoms in the respective layers to each other. Since both PLA and PHB were coated simultaneously in the same plasma process and thus the same plasma parameters are valid and the layers should be the same, this can only be attributed to a substrate effect of the polymers themselves. On the one hand, it may be due to different expansion coefficients of both materials (a-C:H layer and PHB substrate), as well as island formations of the a-C:H and their interaction with each other in the early growth stage on the other hand. A different attachment of the layer to the polymers provides a different basis for the following layers and can be a possible reason for different binding states in the top-most layer of the layers.

Once again, as with the PLA, several layer thickness intervals with intact, stable and unstable layers could be observed. Layer thicknesses of 50 nm as well as 250-400 nm provide a stable, homogeneous layer. A closed, but unstable and delaminated layer could be detected for the a-C:H layer thicknesses of 100 nm and 450 nm (cord buckling). Finally, there are also layer thickness intervals in which total layer failure occurs: 150-200 nm and 500 nm. It is noticeable that the cord buckling intervals are smaller compared to the PLA and layer failure occurs faster after the first stress-release phenomena.

Figure 6.4 shows the SEM measurements for the investigated PBAT films. Figure 6.4 **a)** is an

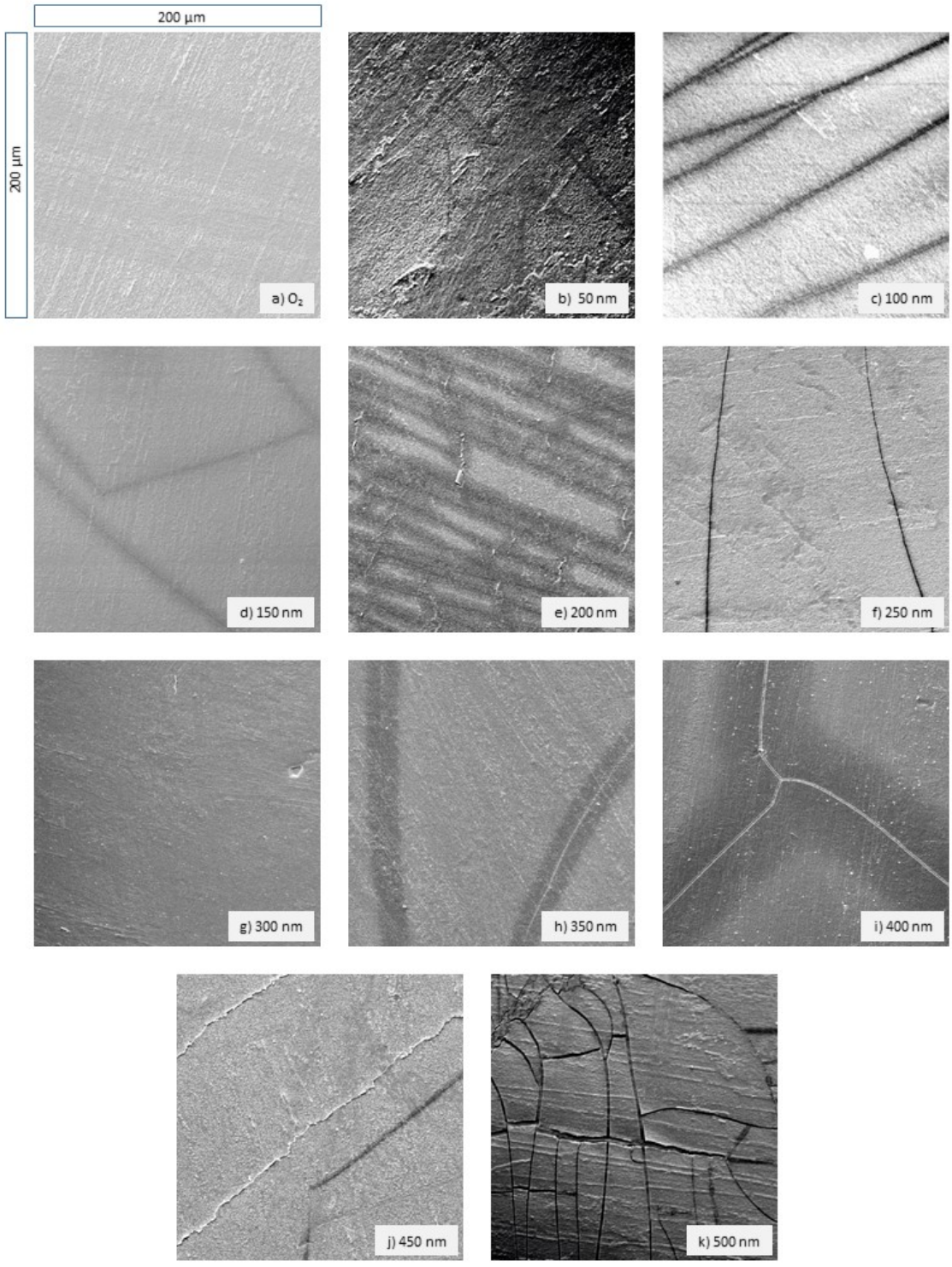

Figure 6.4: SEM images of PBAT samples treated with an O_2 plasma **a)** and coated with a-C:H layers with increasing thickness **b)-k)**. The image magnification is 445x, the length of each side of the image equals 200 μm. The figure is based on ref [108].

image of the O_2 plasma treated PBAT and afterwards images of the a-C:H coated samples are shown subsequently in ascending order (**b)-k)**). A 442x magnification was selected and the side edges of the images each cover a length of 200 μm. A comparison of the untreated PBAT film with the O_2 plasma treated film shows that before the plasma treatment existing impurities were successfully removed almost completely by the plasma and the associated sputtering. Only a few impurities are still visible, and the surface now appears smoother overall (see fig. 6.1). For the PBAT images, too, the particles on the surface probably originate either from the production or coating process itself, or they are dust particles that were deposited on them during storage or transport of the samples. In addition, vein-like granulate structures are visible on the O_2 plasma treated sample, which are arranged in linear patterns on the surface. Although these were also visible on the untreated PBAT sample, they are more prominent after plasma treatment. In the course of the SEM measurements, dark lines can be seen on many images (such as 100, 150, 200, 250, 350, 400 and 450 nm layer thickness). These are most likely due to a break-up of the gold film applied to the samples for the SEM measurements. It is conceivable that the samples were coated with gold long before they were measured in the SEM. Another possibility is that these structures are attributed to the nature of the foils. These are creased and wavy when delivered by the manufacturer. However, since these structures do not appear in all measurements, it is more likely that the gold film is broken.

For the PBAT sample, which was coated with 50 nm a-C:H, it can be seen that a homogeneous, closed layer is deposited. The structures of the polymer surface are still clearly visible. Even an increase of the layer thickness up to a value of 150 nm does not lead to any change. The layer remains homogeneous and closed, the surface structures visible. For the first time at a layer thickness of 200 nm (fig. 6.4 **e)**), a change in the layer surface occurs and small, locally isolated fractures become visible, but the layer itself remains adherent to the polymer. With the deposition of a 250 nm thick layer, a homogeneous, closed surface is again present. The two deep cracks are due to a failure of the gold layer and the resulting charging effects. Even a further increase of the layer thickness up to a value of 400 nm does not lead to any changes, a homogeneous and closed film is produced by the a-C:H coating. At a layer thickness of 450 nm, strong cracks occur in the a-C:H layer until complete layer failure occurs at 500 nm layer thickness (figs. 6.4 **j)** and **k)**). The cord buckling effect that has been occurred earlier for PLA and PHB samples coated the same way as the PBAT samples does not occur here. This is an indication for a good adhesion of the layer on the polymer and consequently for a pronounced interlayer. Likewise, the layer does not

roll up after breaking, but remains bonded to the polymer after the layer is torn open.

As with the polymers PLA and PHB, the layer failure is due to internal stress of the layer. If the residual stress exceeds a critical value, the layer begins to break. Up to this point, the layer on the polymer is stable and adheres well, except for the layer breaks in the dark areas. Cord buckling effects do not occur. Even if, as with PLA and PHB, stress is already present in the layers before breakage, a presumably good layer bonding to the polymer will prevent the layer from peeling off and waving. As a result, the layer thickness intervals for stable films are longer for PBAT than for PLA and PHB. As a result, only two different possibilities for the layer surface can be given for PBAT: **1)** a homogeneous, closed and completely intact layer which adheres to the polymer as can be seen with layer thicknesses of 50-150 nm or 250-400 nm and **2)** a break-up of the layer and associated layer failure (200 nm, 450-500 nm). However, it should be mentioned that the layer shows only slight damage at 200 nm. A substrate effect cannot be denied, since the a-C:H layer on the three polymers develops completely differently. While the layer failure in PLA only occurs at relatively high layer thicknesses (at the earliest at 300 nm) and is very quickly present in PHB and PBAT (at 150 resp. 200 nm layer thickness and 450/500 nm), the cord-buckling present in PLA and PHB does not occur in PBAT. While with PLA intact layers still form at 500 nm but influenced by the cord-buckling effect, with the other two polymers there are no intact layers left and the film is extensively damaged. Whether closed, homogeneous layers are produced again with increasing thickness must be clarified with further measurement campaigns. The results obtained from the SEM measurements are a strong indication that the layers of the different polymers not only bind differently, but also that the structure of the applied layer differs, since the stress on the different polymers only has an effect on the film at different layer thicknesses. This can be attributed to a more stable network in the layer or to different stress values. A chemical analysis of the layers can provide further answers. It is also noticeable that the applied a-C:H layer for the PBAT breaks at almost the same thickness as the PHB layer. Here, too, further methods must be used to check the extent to which the films resemble each other.

6.2 Surface wettability

Contact angle measurements were performed for the respective polymers to examine how the wettability of the surface changes with the respective layer thicknesses. In addition, to the contact angles on the layers, the contact angles of the O_2 plasma treatment were measured and used as new reference in the figures, since all coated samples were O_2 plasma pretreated..

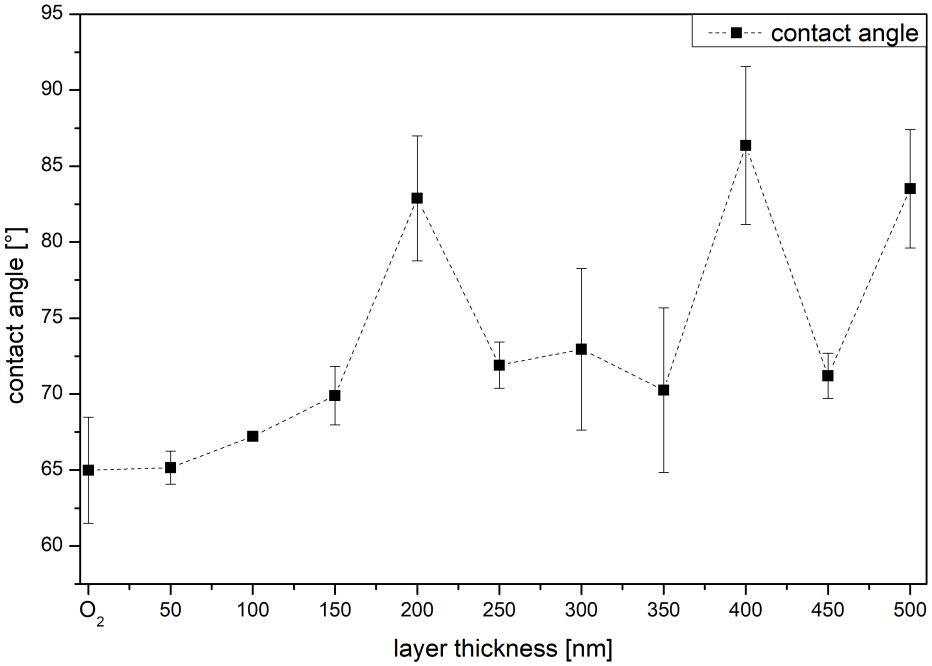

Figure 6.5: Contact angle results for a-C:H coatings on PLA with increasing thickness. The coatings were applied to samples previously treated with an O_2 plasma. The dashed line only indicates a trend of the values. The figure is based on ref [100].

Figure 6.5 shows the contact angles plotted against the layer thickness measured for the O_2 plasma treated and a-C:H film coated PLA samples of different thickness. The O_2 treated sample has a contact angle of 65°. With the application of an a-C:H layer, the contact angle increases with increasing layer thickness until it reaches its maximum at 200 nm a-C:H layer. If the layer thickness increases further to 250 nm, the contact angle decreases rapidly by more than 10°. In the further course, the measured contact angle remains almost constant at a value of about 72° up to a layer thickness of 350 nm. When an a-C:H thickness of 400 nm is reached, the contact angle increases rapidly again and reaches a value of 86°. The contact angle then collapses again and the values obtained fluctuate, which is due to the changing topography of the layer (compare with fig 6.2). The results of the contact angle measurements show large errors. However, this is due to the cord buckling effects and the repeatedly broken surface of the a-C:H applied. There is no uniform surface and especially with the 200 nm a-C:H layer and the thick layers there is no statistical distribution of the cracks, therefore the contact angle measurements scatter strongly and result in a wide range of errors. The constant change of the contact angles indicates a continuous change

of the sp^2/sp^3 ratio, which leads to a change of the surface free energy due to different chemical structures or bonds on the surface, as explained in section 5.2.

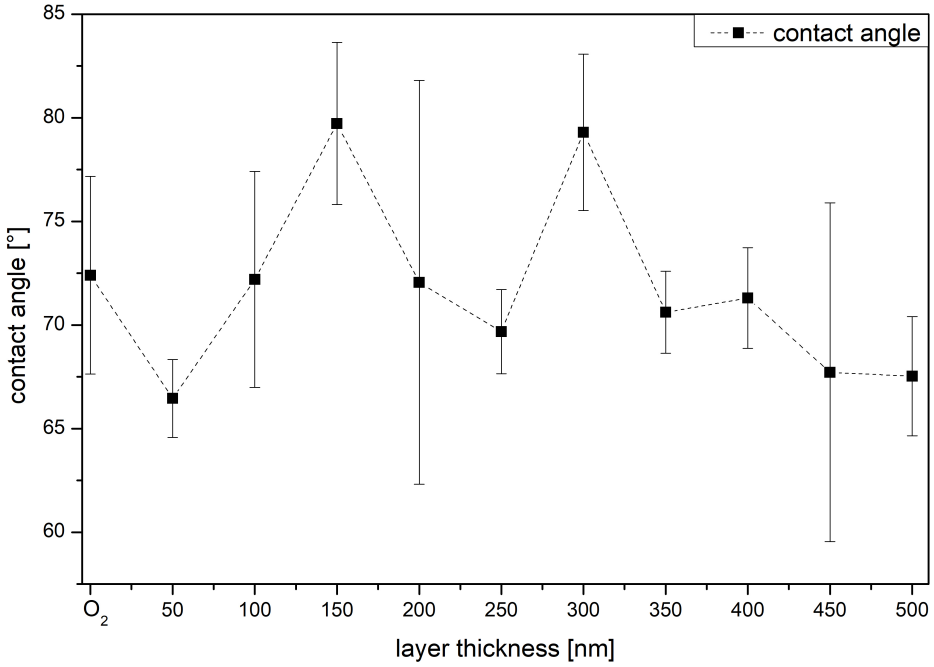

Figure 6.6: Contact angle results for a-C:H coatings on PHB with increasing thickness. The coatings were applied to samples previously treated with an O_2 plasma. The dashed line only indicates a trend of the values. The figure is based on ref [107].

In fig. 6.6 the contact angles are plotted over the different a-C:H layer thicknesses in increasing order for the material PHB. In addition, the O_2 plasma treated PHB sample is applied, which serves as a reference measurement and has a measured contact angle of 72°. With the application of an a-C:H layer of 50 nm, the contact angle with 67° is at its lowest value. This indicates a sp^3 hybridisation of the carbon atoms. Furthermore, it shows a reduced content of oxygen groups compared to the O_2 plasma activated sample, which is also expressed in the lower contact angle (see section 5.2). With increasing layer thickness, the contact angle also increases until it reaches its maximum value of 80° at a layer thickness of 150 nm. By increasing the layer thickness to 200 nm, the contact angle drops abruptly to 72°, but this measurement is accompanied by a large error. A comparison with the SEM images (fig 6.3) shows that the a-C:H layer is broken up here, which is probably due to stresses within the layer. With further increasing a-C:H thickness to 250 nm, the contact angle value decreases slightly and rises from 300 nm to 79° again. As the

process progresses, the contact angles decrease again and remain almost constant with a slight decrease in the higher layers. Since the entire deposition process has not been changed except for a longer coating time to obtain thicker layers, the hybridisation states must change with increasing layer thickness; increasing contact angles indicate an increased proportion of sp^2-hybridised carbon atoms, decreasing contact angles indicate an increased proportion of sp^3-hybridised carbon atoms (see section 5.2). The comparatively high contact angles at both 150 nm and 300 nm a-C:H layer thicknesses, which differ significantly from the surrounding values, indicate either a high content of sp^2 hybridised carbon, a strong hydration of the surface or a changed morphology. A comparison with the SEM images (fig. 6.3) shows that at 200 nm layer thickness there is a partially visible delamination of the layer, so that the morphology of the surface is responsible, which is also associated with the large errors. Cracks in the layers, such as are present at 200 nm and 450 nm layer thickness, are also responsible for fluctuating contact angles and large acompanied errors. A non-uniform surface makes the contact angle measurements here very error-prone, which is also indicated by the large error bars.

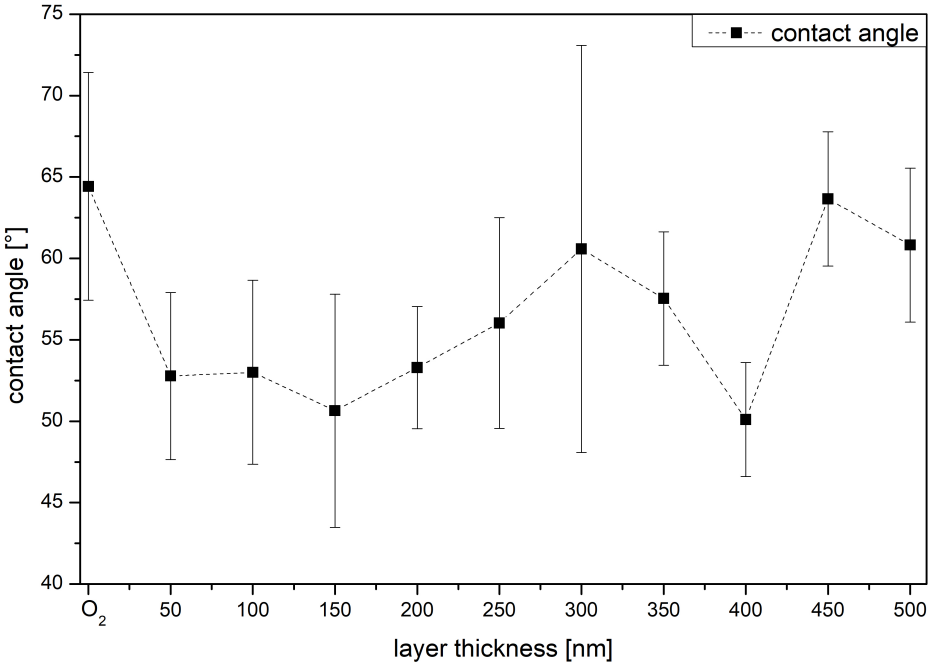

Figure 6.7: Contact angle results for a-C:H coatings on PBAT with increasing thickness. The coatings were applied to samples previously treated with an O_2 plasma. The dashed line only indicates a trend of the values. The figure is based on ref [108].

The contact angles used for an O_2 treated PBAT as well as other PBAT samples coated with a-C:H films of different thicknesses are shown in fig 6.7. Due to the wavy structure of the PBAT, the contact angle measurements are subject to very strong errors, however, a trend can be observed in the measurements. The contact angle of the O_2 treated sample is 64°. If a 50 nm a-C:H layer is applied, it drops to 52°. This change of contact angle is an indication of a relatively high content of sp^3 hybridised carbon or a reduced number of functional oxygen groups compared to the O_2 plasma treated sample (see section 5.2). Up to 200 nm layer thickness the contact angle remains nearly unchanged (in an interval of 51-53°) and assumes a minimum at 150 nm a-C:H layer. If the layer thickness continues to increase, the contact angle rises at a thickness of 250 nm and reaches its maximum at 300 nm. Up to a layer thickness of 350 nm, the contact angle remains almost constant again in an interval between 56° and 61°, until it drops back to a value of 50° when a layer thickness of 400 nm is reached. With a further increase of the layer thickness to 450 and 500 nm, the contact angle increases strongly (to 64° and 61° respectively). At this thickness a defect in the a-C:H layer can be seen in the SEM measurements (fig 6.4 **i)**). The change in the contact angle is due to the change in the surface free energy, which can be explained by different chemical structures or bonds, as discussed previously in section 5.2. Up to a layer thickness of 200 nm, the contact angles indicate a more sp^3 hybridised carbon bond. As the layer grows, the network reorganizes into a sp^2 hybridisation of the carbon bonds. In the further course of the coating at 350 nm the network is restructured again and the carbon on the surface is again rather sp^3 hybridised.

6.3 XPS

The XPS studies were performed to analyse the differences in carbon bonding states between the crude polymers and the coated polymers. The raw polymers were compared with the oxygen plasma purified and activated polymers, and the binding states of the carbon atoms on the surfaces of the coated polymers were analysed. For the analysis of the sp^2 and sp^3 hybridisation of carbon and C-O components, the percentages of the C1s peak obtained with the CasaXPS software were plotted over the respective layer thickness. Figure 6.8 shows the deconvolution of the C1s peaks of the raw polymers compared to the oxygen plasma activated polymers.

The shape of the C1s peak (284.80 eV) for the measurements of the untreated and O_2 plasma-treated PLA samples indicates a strong C-O bond leading to asymmetry on the left side of the peak. A comparison of the deconvolution of the C1s peak for the PLA reference with the O_2 oxygen plasma purified sample shows that the fraction of the sp^2 peak decreases. This is due to cleaning

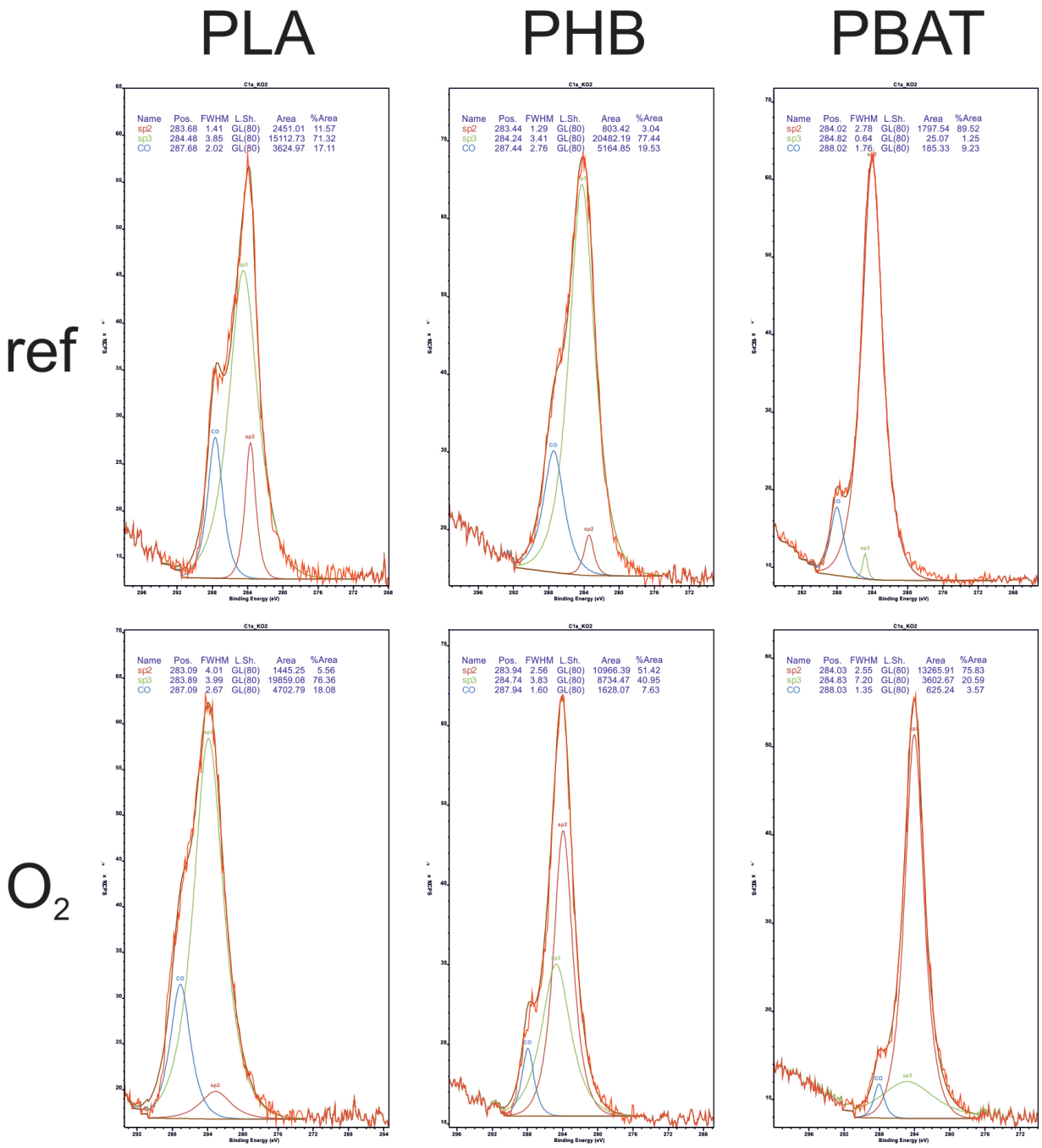

Figure 6.8: Deconvolution for the C1s peaks of the polymers PLA, PHB and PBAT. The upper line shows the raw polymers, the lower line the O_2 plasma treated samples.

of the surface of olefins and similar contaminations. The proportion of C-O compounds increases only slightly, oxygen enrichment by the oxygen plasma does not take place, the proportion of C-O bonds remains at about 17 %. With the plasma treatment, the left flank of the C1s peak (∼288 eV), which has been emphasized more so far, overlaps with the main peak, which, however, is due to the relative increase of the sp^3 content. This increase was expected due to the strong sp^3 binding in the polymer chain of the PLA (see section 5.6) as this has now been exposed.

The analysis of the PHB samples gives a different picture from that of the PLA samples. Although the superposition with the C-O peak at higher binding energies (288 eV) is visible again, the deconvolution of the C1s peak yields a very large proportion of sp^3 bonds, which is 78 % here. With the oxygen plasma treatment this proportion decreases to 40 %, also the amount of C-O bonds is more than halved (from 20 % to 8 %). In contrast, a large amount of sp^2 bonds is built up. This may be due to degradation or removal of the carbonyl group in PHB, resulting in a dangling bond, and therefore a free carbon position. Due to these changes in the bond ratio of the C1s peak it is sharper and the part of the peak belonging to the C-O bonds is more clearly separated from those of the sp^2 and sp^3 bonds.

The deconvolution of the C1s peak of the PBAT reference sample yields a fraction of almost 90 % of sp^2 bonds and 9 % of C-O bonds. sp^3 hybridised carbon is almost absent. If this is compared with the structural formula of PBAT (see section 5.6), it can be seen that there must be an impurity in the material (e.g. olefins on the surface, impurities from the manufacturing process). Sample treatment with an O_2 plasma reduces the proportion of sp^2 bonds to 75 % and that of C-O bonds to 3.5 %. Due to the structural formula of the PBAT, a much higher proportion of sp^3 bonds was to be expected. Possibly the plasma treatment of the PBAT samples leads to a restructuring of the surface which is accompanied by a change of the chemical environment. The abstraction of hydrogen atoms (see section 4.3) and a flipping of the free bonds to the adjacent carbon atom would be a possibility.

Fig 6.9 shows the XPS measurements for carbon coatings of different thicknesses applied to PLA polymer samples. The percentages of the sp^2, sp^3 and C-O bond of the C1s signal are plotted over the a-C:H layer thickness, starting at 50 nm. Here the sp^3 bond is the dominant bond with more than 50 % of the C1s peak. Up to a layer thickness of 150 nm this proportion increases strongly up to a value of 90 %, almost all carbon bonds on the coated surface belong to sp^3. Afterwards the sp^3 content decreases with increasing layer thickness until the sp^2 binding becomes dominant after 300 nm. A comparison with the SEM images from section 6.1 (fig 6.2) shows that this change of

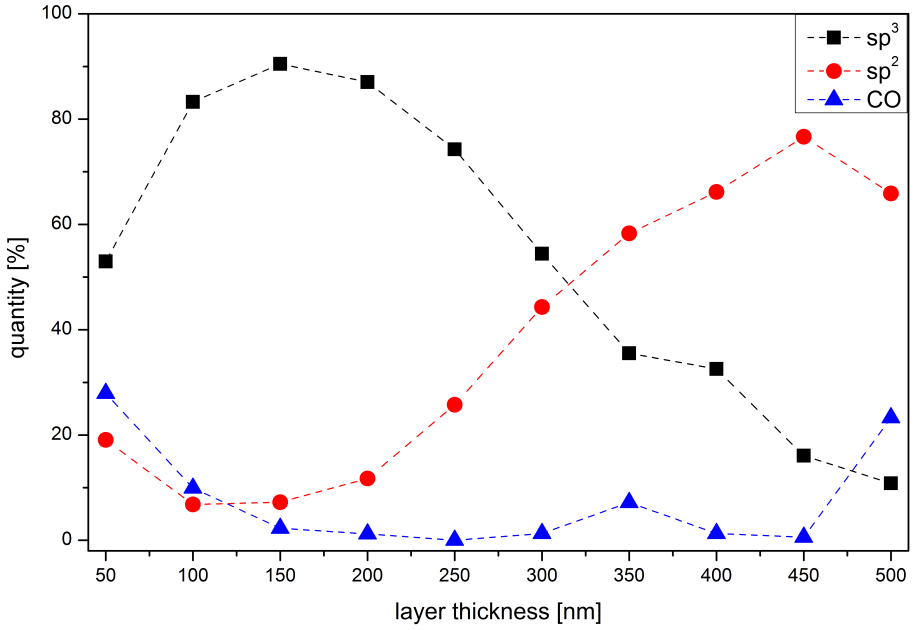

Figure 6.9: Quantification of XPS spectra for PLA samples coated with a:C-H layers of various thickness. Circles (red) present the specific amount of the sp^2 content, squares (black) the sp^3 content and triangles (blue) the C-O content (lines are just for better readability). The figure is based on ref [100].

the dominant binding from sp^3 to sp^2 is accompanied by layer failure (fig. 6.2 **g)**). The sp^2 content increases further up to a layer thickness of 450 nm, where the sp^2 bonds reach a maximum value of ∼77 %. The sp^3 content decreases continuously. With further growth to 500 nm film thickness, the sp^2 content decreases slightly while the proportion of C-O bonds, which was almost constant for smaller film thicknesses, increases here. Further exceptions for the C-O bond fraction are only the analysed layer thicknesses for 50-100 nm showing a continuous decrease from a value nearly 30 % to below 5 % with increasing thickness and an a-C:H layer thickness of 350 nm, where the proportion of C-O bonds increases slightly.

The decrease of the sp^3 content after 150 nm layer thickness can be attributed to a stress release. The proportion of sp^3 bonds was over 90 %. As a result, the bonds break due to excessive stress in the layer [49, 48]. Thus, the relaxation of the network introduced by Davis [46] is responsible for an increasing sp^2 content after a layer thickness of 150 nm. This occurs in conjunction with stress release due to layer failure. This layer failure, which occurs in the SEM images (fig 6.2 **g)**), is therefore most likely caused by such a bond break-up. The misalignment between the layer failure

and the maximum sp^3 content could be due to the fact that the entire network must be cracked before the breakage becomes visible. A beginning of this cracking of the network is indicated by the cord buckling effect (fig 6.2 **d)**).

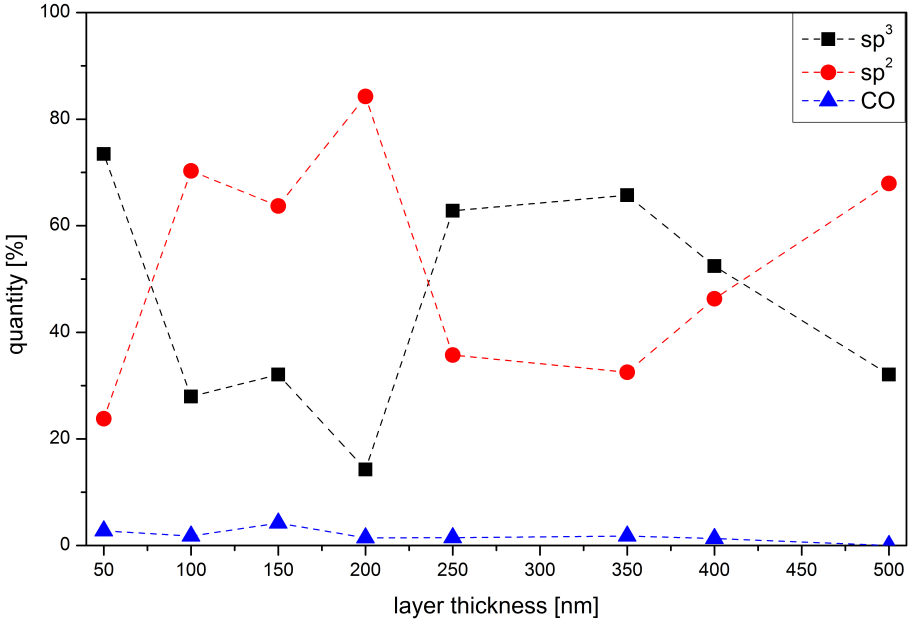

Figure 6.10: Quantification of XPS spectra for PHB samples coated with a:C-H layers of various thickness. Circles (red) present the specific amount of the sp^2 content, squares (black) the sp^3 content and triangles (blue) the C-O content (lines are just for better readability). The figure is based on ref [107].

The results of the percentages of carbon bonds from the XPS measurements for the a-C:H coated PHB samples are plotted in figure 6.10. Starting with a layer thickness of 50 nm a-C:H, the sp^3 bond is also the dominant one here, similar to the coated PLA samples, although it is more pronounced here with 75 %. If the applied layer thickness increases to 100 nm, the dominant bond changes in favor of the sp^2 bond. A comparison with the SEM images from section 6.1 (fig 6.3) shows that this is accompanied by an unstable layer, cord buckling occurs, but the layer is still closed. Layer failure occurs at a layer thickness of 150 nm. In contrast to the investigated PLA samples, there is a delay of around 100 nm between the change of the dominant bond from sp^3 to sp^2 and the resulting layer failure. The sp^2 bond remains dominant until the layer thickness exceeds 200 nm. With a layer thickness of 250 nm, the dominant bond changes back to the sp^3 bond. It is noticeable that the change from sp^2 to sp^3 as dominant bond does not lead to layer

failure in the SEM measurements (fig 6.3 **f)**). Up to a layer thickness of 400 nm the sp^3 bond remains dominant. Then a second change from sp^3 to sp^2 occurs as a favored bond in the carbon network of the surface. Once again, a comparison with the SEM images shows that cord buckling occurs with the change (fig 6.3 **j)**, 450 nm) and layer failure occurs with a delay of 100 nm layer thickness. The C-O bonds remain constant over all layer thicknesses in the lower percentage range. Overall, the change of the dominant bonds in PHB takes place already at lower layer thicknesses and also more frequently. Since both materials were coated simultaneously in the same plasma, a substrate effect can be seen. Again, as with PLA, a stress release of the sp^3 dominated network towards a sp^2 network is visible, which again is accompanied by a layer failure, even if it starts delayed. This is possibly due to a better cross-linking of the layer with the polymer, which is expressed in a better formed interlayer.

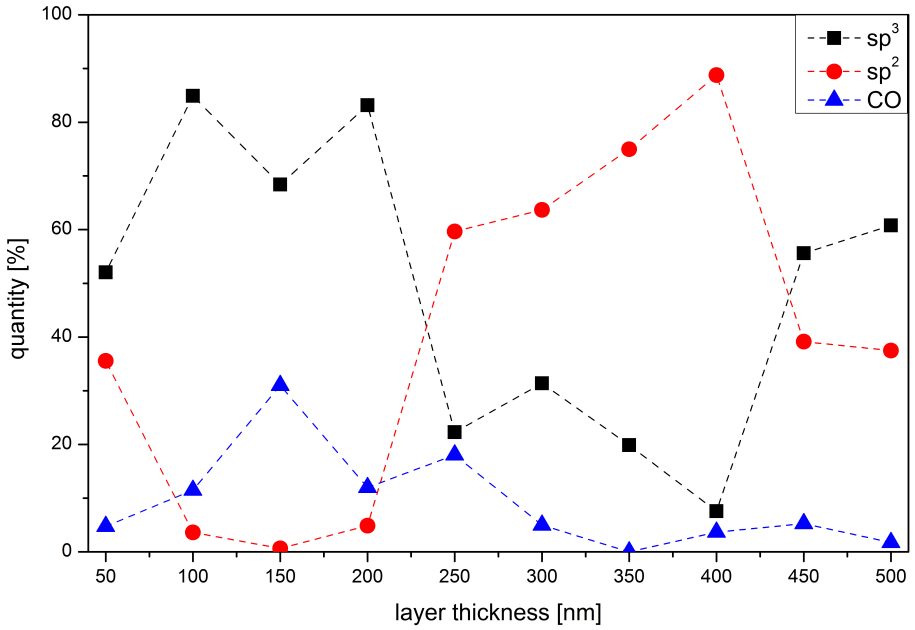

Figure 6.11: Quantification of XPS spectra for PBAT samples coated with a:C-H layers of various thickness. Circles (red) present the specific amount of the sp^2 content, squares (black) the sp^3 content and triangles (blue) the C-O content (lines are just for better readability). The figure is based on ref [108].

Figure 6.11 shows the results of the XPS measurements of a-C:H coated PBAT. At 50 nm a-C:H layer on the polymer the sp^3 bond is dominant as on PLA and PHB. Similar to the PLA, the value here is slightly above 50 % of the C1s peak. This dominance persists up to a layer thickness

of 200 nm. In the SEM measurements (fig 6.4 **e)**; section 6.1) small, isolated cracks appear in the film but the applied layer remains stable on the sample. These cracks are again traceable to the high stress caused by the rigid sp^3 network. The following increase in sp^2 bonds is again due to the thermal spikes according to Davis [46] and to the breaking of sp^3 bonds. If the layer thickness continues to increase up to 250 nm, the bond favored by carbon at the surface changes from sp^3 to sp^2, and the surface is closed again in SEM images. As the a-C:H thickness increases, the proportion of sp^2 bonds continues to increase until it reaches its maximum at 400 nm. Now the amount of sp^3 bound carbon increases again, but the sp^2 bond remains dominant. Only at a layer thickness of 500 nm is the sp^3 bond again the dominant bond. The comparison with the SEM images shows that when a layer thickness of 450 nm is reached there are pronounced cracks until finally at 500 nm a total layer failure occurs (fig. 6.4 **j)**, **k)**). However, the layer does not detach from the substrate and rolls up, but remains firmly attached to it. This is an indication for an accentuated interlayer between substrate and a-C:H layer, so that the layer is held on the substrate despite layer failure. In the case of PBAT, the C-O bond is much more variable in the first 300 nm layer thickness than in the measurements of PLA and PHB and reaches a maximum at a layer thickness of 150 nm after which it decreases again. This high oxygen content in the range of 100-200 nm layer thickness is possibly traceable to the extremely high sp^3 binding content. The high sp^3 content at the surface implies a high level of stress. Due to the mechanical loading when taking the samples or due to the temporal discharge of the stress during storage/transport, the bonds at the surface can be broken. Since the chamber is ventilated immediately after coating with ambient air and the samples are also stored under normal conditions, the oxygen contained in the ambient air can occupy the now free dangling bonds, so that a high oxygen content is obtained in the following ex-situ surface-sensitive measurements. After reaching a layer thickness of 300 nm, it remains constantly low below 5 %. The results found for the PBAT are only partially consistent with those of a-C:H coatings on PLA and PHB, which were coated simultaneously in the same process. In the case of PLA and PHB, layer failure is a consequence of the transition from sp^3 to sp^2 as the dominant bond. The change from sp^2 to sp^3 has no influence here. Furthermore, the layer breaks only after the change of binding from sp^3 to sp^2, so that with the change of binding an indication of imminent layer failure is given. In the case of PBAT, however, a layer failure occurs, which is followed by a change of the dominant bond: At 200 nm the layer in the SEM breaks up easily, from 200 nm to 250 nm the XPS shows a change from sp^3 to sp^2 as dominant bond and at 450 nm the layer breaks up in the SEM measurements and from 450 nm to 500 nm the XPS shows

a change from sp^2 to sp^3 as dominant bond. The direction of the binding change is not important here.

A substrate effect of the coated polymers, as already found in the "classic" crude oil-based polymers [72, 73, 74], is evident. While the layer thickness dependent bond change in PLA is still relatively slow, in PHB there are many changes of the dominant bond in this layer thickness interval. The behaviour of PBAT is between these two materials. In addition, the SEM images show a correlation between the change of the bond favored by the carbon at the surface and a layer failure. Also in the pure oxygen plasma treatment, a substrate effect is noticeable. In addition, the XPS measurements clearly show that the bonding conditions in the surface of the layer depend not only on the plasma parameters that predominate when the layer is deposited, but also on the layer thickness itself.

6.4 NEXAFS

Near edge X-ray absorption fine structure was used to study the binding states of carbon in the near-surface regions of the polymers and a-C:H layers. For this purpose the C K-edges were analysed and evaluated.

First, the measurements of the raw polymers (black) were compared with those of the oxygen plasma (red) treated. This can be seen in fig 6.12 for the three polymers PLA, PHB and PBAT. For the oxygen-treated PLA sample it is noticeable that the C-C peak is much more emphasized than in the reference sample. In both cases the C=C π peak is not present, which was to be expected due to the structure of PLA. In the case of PHB there is no change in the spectrum between the reference sample and the O_2 treated sample, so the plasma does not change the chemical environment of the polymer in the NEXAFS measurements. Considering the PBAT sample, however, it is noticeable that there is a change with the O_2 plasma treatment. While the C-C peak remains unchanged with the treatment, the C=C π peak decreases. The ratio of the two to each other changes, the surface is chemically changed. In the following the results of the a-C:H coated PLA, PHB and PBAT samples from the NEXAFS measurements are considered. The spectra are shown of in 100 nm steps and the O_2 sample was used as a new reference. For a better overview the spectra of the 50 nm intermediate steps were omitted, but the complete NEXAFS measurements are shown in the appendix.

Figure 6.13 shows the evaluated graphs of the NEXAFS spectra for PLA samples coated with a-C:H layers of different thickness. Figure **6.13 A** shows the full spectra, figures **B** and **C** detailed

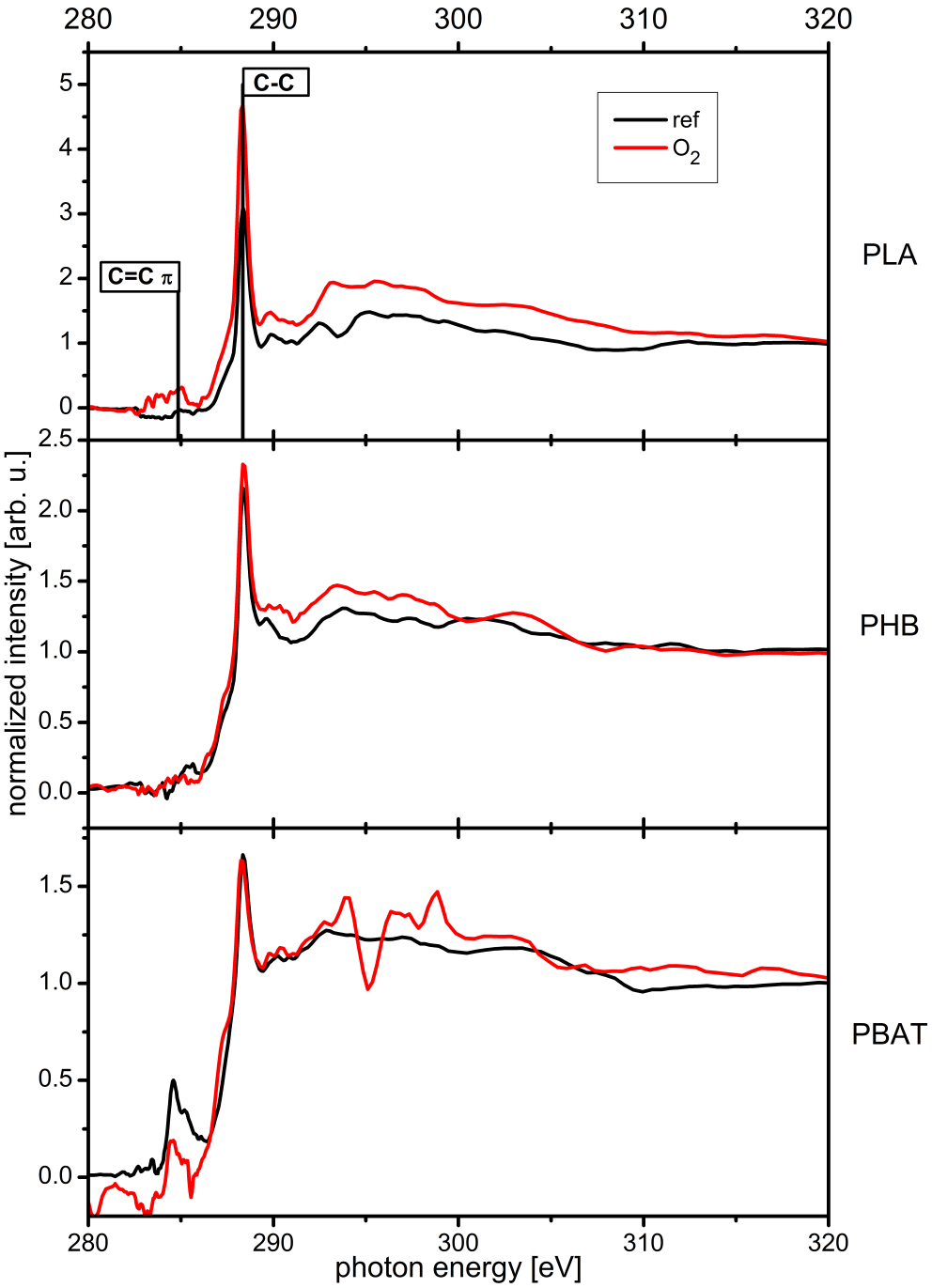

Figure 6.12: Comparison of NEXAFS results for the reference (black) and the oxygen plasma treated (red) samples. PLA on top, PHB in the middle and PBAT in the bottom.

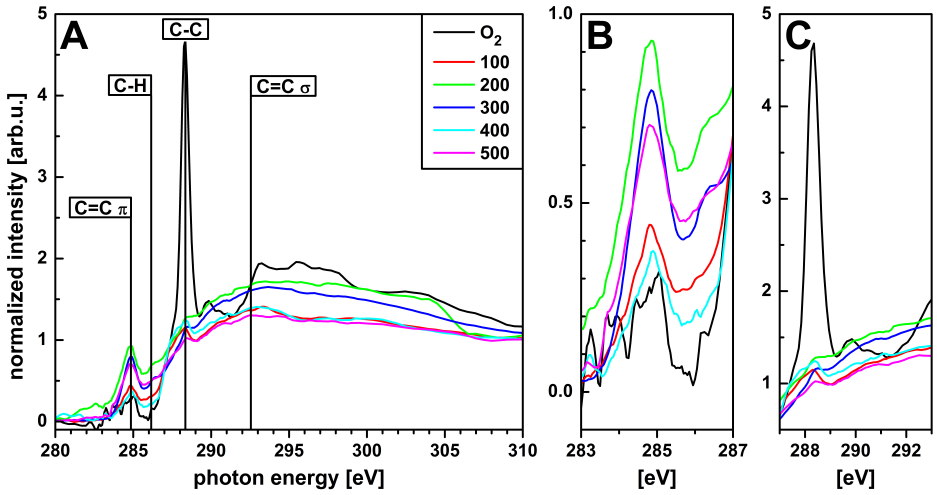

Figure 6.13: **A** Full NEXAFS spectra of selected a:C-H coatings on the biopolymer PLA including the O_2 plasma treated PLA as reference. Figures **B** and **C** show detailed photon energy intervals for carbon relevant peaks: **B** 283.00 to 287.00 eV for the C=C π peak (284.85 eV) and the C-H peak (286.15 eV); **C** 287.00 to 293.00 eV for the C-C and C=C σ (288.15 eV and 292.58 eV). Complete measurements for all thicknesses are shown in the appendix. The figure is based on ref [100].

photon energy intervals for carbon relevant peaks: **B** 283.00 to 287.00 eV for the C=C π peak (284.85 eV) and the C-H peak (286.15 eV); **C** 287.00 to 293.00 eV for the C-C and C=C σ (288.15 eV and 292.58 eV) [92, 95, 97, 98, 96]. For the O_2 treated PLA sample, as mentioned above, a dominant C-C peak at the position of 288.35 eV is visible. Other peaks are really weak (C=C σ) or not at all present (C=C π, C-H). With the application of an a-C:H layer (50 nm, see appendix), the C-C peak is only weakly emphasized, a dominant C=C π peak (284.85 eV) is formed. A C=C σ peak (292.55 eV) appears, but is only weakly emphasized. With increasing layer thickness (100 nm) the C-C peak emerges more strongly, the C=C π peak becomes slightly less pronounced. With a higher layer thickness, this stays this way until the C-C peak almost disappears again at a layer thickness of 200 nm. If the layer thickness continues to grow, it reappears at 250 nm thickness. At 300 nm a-C:H, the C=C σ peak develops more strongly. With increased layer thickness the C-C peak is again only weakly formed, the C=C π peak remains more dominant and the C=C σ becomes more pronounced. With a layer thickness of 400 nm, a slightly accentuated C-C peak is again formed, which, however, is only weak. Finally, when the layer thickness of 500 nm is reached, only the C=C π and the C=C σ peaks remains emphasized, the other peaks are only

weakly recognizable.

The NEXAFS measurements are consistent with the results of the XPS measurements (fig. 6.9). Up to 150 nm a strong C-C (sp^3) peak is visible, which subsequently decreases. An increase of the sp^2 content is visible by the C=C π peak and the C=C σ peak: With increasing thickness the sp^2 signal becomes stronger and a second sp^2 signal corresponding to the C=C σ bond occurs at 292.55 eV indicating a more polymer-like structure consisting mainly of sp^2 carbon double bonds. After reaching a layer thickness of 300 nm the C-C peak almost disappears, even if it is still visible at 400/450 nm a-C:H layer. The sp^2 associated peaks are dominant here. This can also be seen in the XPS measurements (fig. 6.9).

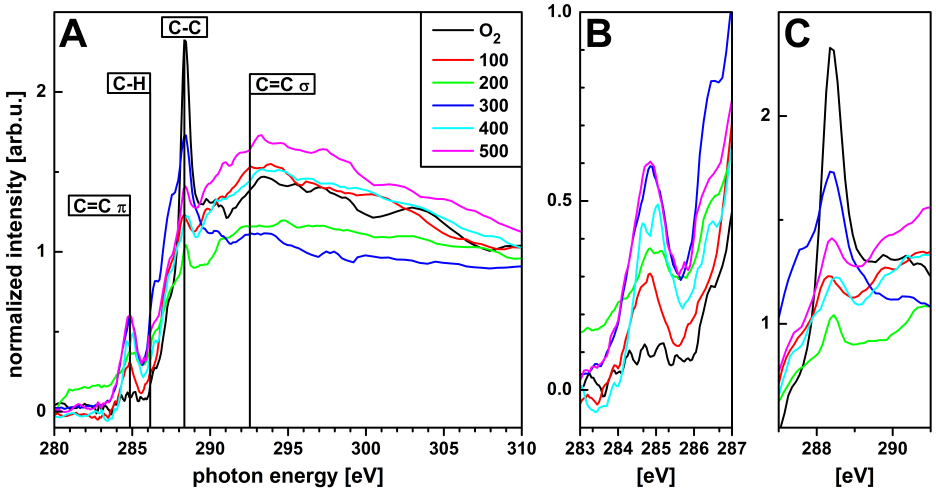

Figure 6.14: **A** Full NEXAFS spectra of selected a:C-H coatings on the biopolymer PHB including the O_2 plasma treated PHB as reference. Figures **B** and **C** show detailed photon energy intervals for carbon relevant peaks: **B** 283.00 to 287.00 eV for the C=C π peak (284.85 eV) and the C-H peak (286.15 eV); **C** 287.00 to 293.00 eV for the C-C and C=C σ (288.15 eV and 292.58 eV). Complete measurements for all thicknesses are shown in the appendix. The figure is based on ref [107].

In fig 6.14 the evaluated graphs of the NEXAFS spectra for the a-C:H coated polymer PHB are plotted. Figure **A** shows the full spectrum, figures **B** and **C** show detailed photon energy intervals for carbon relevant peaks: **B** 283.00 to 287.00 eV for the C=C π peak (284.85 eV) and the C-H peak (286.15 eV); **C** 287.00 to 293.00 eV for the C-C and C=C σ (288.15 eV and 292.58 eV). After the O_2 plasma treatment the C-C peak is dominant. With the deposition of an a-C:H layer of 50 nm both the C=C π and the C=C σ peak are formed (see appendix). The C-C peak is still visible,

but less dominant than before due to the presence of the two peaks belonging to the C=C bond. If the layer continues to grow to 100 nm, the C-C peak decreases further and the two C=C peaks become more pronounced. At a layer thickness of 200 nm the C=C σ peak decreases slightly, the C-C peak becomes more accentuated. If the a-C:H layer rises further, the C-C peak decreases again and the C=C σ peak forms more strongly. At 300 nm the C-C peak rises strongly and is strongly emphasized, also the C=C π peak grows. However, this only lasts up to a thickness of 350 nm (see appendix). Here the C-C peak decreases again and while the C=C π peak remains almost constant, the C=C σ peak increases again. From a layer thickness of more than 400 nm, the C=C π bond increases steadily, the C=C σ widens a little (becomes stronger) and the other two bonds decrease compared to the C=C π bond. At a layer thickness of 100 nm, the sp^2 bond is the dominant bond. This also continues at 200 nm. With a layer thickness of 300 nm, the sp^3 peak begins to dominate. At 400 nm, the sp^2 value determined in NEXAFS measurements increases again and the sp^3 content decreases slightly. At 500 nm, the values measured for sp^2 are again the dominant bonds.

The dominant sp^2 bond between 100 and 200 nm corresponds to the cord buckling effect visible in the SEM images (fig. 6.3 **c)-e)**). With increasing dominance of the sp^2 bonds from 100 to 200 nm, the wear of the a-C:H layers increases according to the SEM images. With the change from the sp^2 bond to the now stronger sp^3 bond, this effect disappears and the layer appears homogeneous again. After a repeated decrease in the dominance of the sp^3 bond and a further increase in the sp^2 content between 400 and 500 nm, cord buckling and layer defects occur again. The NEXAFS data therefore indicate a layer failure or defect if the sp^3 bond loses its dominant position in favour of the sp^2 bond. The results found here are consistent with the associated XPS results (fig. 6.10). Both the dominance of the sp^3 bond (C-C bond) at 50 nm and the increase of the sp^2 bond up to a layer thickness of 200 nm can be seen in the XPS and NEXAFS measurements. The increase of the C-C bond at 250 nm visible in the XPS measurements is also visible in the NEXAFS measurements, also the later increase of the sp^2 bond at 500 nm. Thus the measurements in NEXAFS correspond well with those in XPS and both techniques describe the same picture of a layer thickness dependent change of the bond states in the a-C:H layers.

Figure 6.15 shows the spectra of the NEXAFS analyses for a-C:H layers of different thicknesses deposited on the PBAT polymer. Figure **A** shows the full spectrum, figures **B** and **C** show detailed photon energy intervals for carbon relevant peaks: **B** 283.00 to 287.00 eV for the C=C π peak (284.85 eV) and the C-H peak (286.15 eV); **C** 287.00 to 293.00 eV for the C-C and C=C σ (288.15

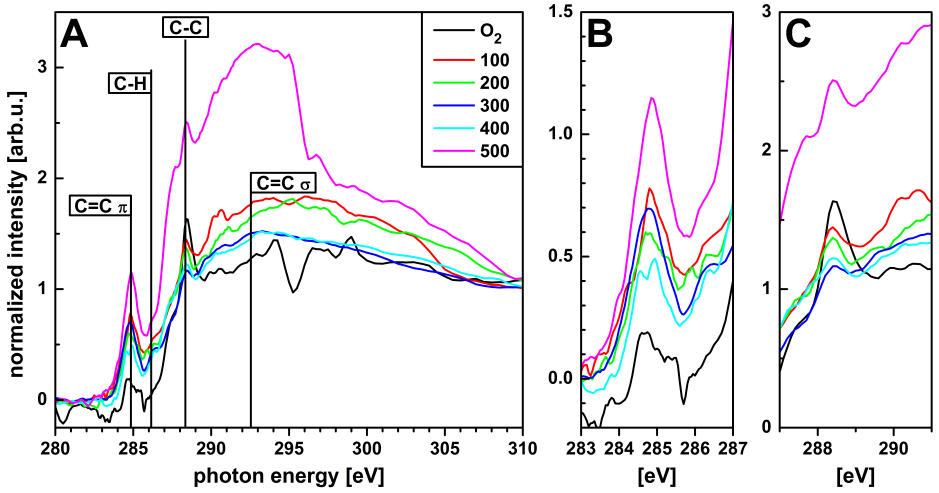

Figure 6.15: **A** Full NEXAFS spectra of selected a:C-H coatings on the biopolymer PBAT including the O_2 plasma treated PBAT as reference. Figures **B** and **C** show detailed photon energy intervals for carbon relevant peaks: **B** 283.00 to 287.00 eV for the C=C π peak (284.85 eV) and the C-H peak (286.15 eV); **C** 287.00 to 293.00 eV for the C-C and C=C σ (288.15 eV and 292.58 eV). Complete measurements for all thicknesses are shown in the appendix. The figure is based on ref [108].

eV and 292.58 eV). In the following, the binding peaks visible here and their layer thickness dependent development are examined in detail. With a 50 nm a-C:H layer, the two peaks for the C=C π (284.85 eV) and the C-C (288.35 eV) bond are visible (see appendix). Both peaks remain constant when an a-C:H layer with a thickness of 100 nm is deposited. A C-H peak is slightly indicated at 286.15 eV, but remains weak. When a layer thickness of 150 nm is reached, the C-C peak, which represents the sp^3 bond, decreases, while the C=C π bond becomes more dominant (see appendix). A comparison with the results of the XPS measurements (fig. 6.11), where a decrease of the sp^3 and an increase of the sp^2 content occurs at this layer thickness, shows a correspondence between the two techniques. At this thickness the C-H peak is more pronounced. With a layer thickness of 200 nm, the peak of the C-C bond increases again, while the C=C π peak weakens. Although the C-H peak and the C=C σ peak (292.55 eV) are emphasized more strongly here, they are only weakly developed in comparison with the C-C and the C=C π peak. This also corresponds to the results of the XPS investigations (fig. 6.11). With a further increase of the layer thickness to 250 nm, the C-C peak weakens strongly, while the C=C π peak continues to increase (see appendix). This behaviour continues over the layer thicknesses of 300 nm and 350 nm. After

exceeding the layer thickness of 400 nm the C=C π peak weakens again. This weakening behaviour continues with increasing layer thickness. When a thickness of 450 nm is reached, the C-C peak increases again and becomes more accentuated (see appendix). The peaks for the C=C σ and C-H binding are very weak and undefined throughout the measurement. Only for the C=C σ bond is a stronger or less pronounced behaviour recognizable, although it seems to almost disappear in some cases, as the surrounding signals increase. Even though its height remains almost unchanged, it widens a little when the C=C double bond is more strongly emphasized overall and narrows when this bond decreases. Thus, the measurement data obtained in NEXAFS correspond to those obtained in XPS and confirm these measurements.

A comparison of the results for the materials PLA, PHB and PBAT reveals a substrate effect for the a-C:H coating. The chemical surface composition for the three polymers differs despite the same layer thickness and the same coating process. In itself, the NEXAFS measurements are consistent with the results from XPS and thus also with the contact angle measurements for the respective polymers with different a-C:H coating thicknesses. Here, too, it is proven that the present bonding on the layer surface depends not only on the plasma parameters, but also on the thickness of the applied layer and the polymer itself.

6.5 DRIFT

For the further chemical analysis of the surface bonds diffuse reflectance infrared fourier transform (DRIFT) measurements were performed. Measurements were taken for all a-C:H layers of different thicknesses deposited on the different polymers to identify the specific C bond types. AnO_2 plasma pre-treated polymer sample was used as the base substrate for each of the coated samples and served as the reference spectrum since the layers were deposited on this pre-treated material. The DRIFT spectra are evaluated on the basis of the principles of infrared spectroscopy [90] according to the previous results of other groups [35, 73, 74, 111, 112, 113]. This section presents the results of the measurements for the C-H stretching region for the polymers PLA, PHB and PBAT coated with a-C:H layers of different thickness.

Fig 6.16 shows the measured DRIFT spectra in the range of 2800 - 3050 cm^{-1} of the a-C:H coated PLA samples with different thicknesses. As the coating process continues and the a-C:H layer grows on the surface, it undergoes several changes in the chemical configuration of the surface during the process. If an a-C:H layer thickness of 50 nm is deposited on the sample, two

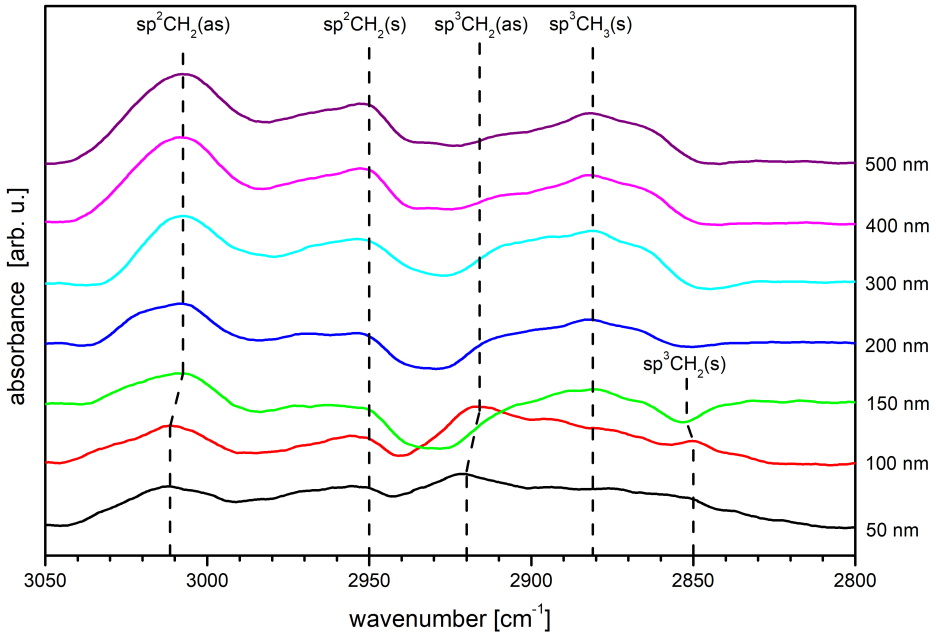

Figure 6.16: DRIFT measurements for a-C:H coatings on PLA with increasing thickness. The coatings were applied to samples previously treated with an O_2 plasma; a O_2 cleaned polymer sample was used as a reference sample for the measurements. The graph is based on ref [100].

peaks become visible. These peaks are at 2920 cm^{-1} and 3012 cm^{-1} , belonging to the sp^3 CH_2 asymmetric (as) (2920 cm^{-1}) vibration and to the sp^2 CH_2 (3012 cm^{-1}) vibration [113, 111, 35]. The formation of these CH_2 groups is due to the completion of the formation of the interlayer [73, 74]. Three dominant subplantation processes are responsible for the formation of an interlayer: First a complete unspecific etching of the surface by the different plasma species, followed by an introduction of C and H^+ ions into the sample and finally an absorption of plasma radical species to form new bonds at the surface. According to the latest results of Catena *et al.* [73, 74], the process of interlayer formation is for a-C:H coated polyethylene terephthalate (PET) and POM completed at a layer thickness of about 50 nm. The occurrence of $= CH_2$ bonds proves the end of interlayer formation. It is therefore concluded that with the occurrence of $= CH$ vibrations at a layer thickness of 50 nm, the formation of the interlayer is already complete and this interlayer is therefore also less than 50 nm. The CH_2 groups show a polymer-like a-C:H surface configuration, while the formation of $= CH_2$ indicates sp^2 formations according to the cluster model [19]. As the a-C:H layer thickness increases, these two peaks become more pronounced. In addition, a peak at 2850 cm^{-1} is visible, which can be assigned to the sp^3 CH_2 symmetric vibration [113, 111]. The

presence of sp^3 bound carbon indicates the presence of chain end groups. Thus some chains do not grow any longer at the place of the sp^3 bond within the a-C:H frame. With a thickness of 150 nm, the sp^3-linked vibration modes disappear in favor of a more sp^2-linked a-C:H structure. A peak at 2950 cm^{-1} appears, which is linked to the symmetrical vibration modes of $sp^2\,CH_2$ binding [113]. In addition, with a layer thickness of 150 nm, a peak shift of the $sp^2\,CH_2$ peak from 3012 cm^{-1} to 3007 cm^{-1} occurs. This shift to smaller wavenumbers indicates a lower carbon-hydrogen bond energy and thus a higher carbon-hydrogen bond distance for the $= CH_2$ group, as has already been demonstrated for PET and POM [74, 73]. Up to a layer thickness of 500 nm, the sp^2-linked vibration modes continue to grow at 2950 cm^{-1} and 3012 cm^{-1}. Only a small peak at 2880 cm^{-1}, which can be assigned to the sp^3 vibration [113, 111], increases further with increasing layer thickness. This indicates that a more polymer-like structure of the a-C:H film is achieved. From a layer thickness of 150 nm, the number of sp^3 bonds decreases in favour of sp^2 bonds. In addition, the increasing contact angles confirm this behaviour. The increase of the sp^2 parts from 150 nm at the expense of the sp^3 vibration is also visible in XPS and NEXAFS. The results of these three techniques therefore correspond and confirm the development of the chemical surface characteristics of the a-C:H coated PLA.

Figure 6.17 shows the DRIFT measurements for a-C:H coated PHB samples. The range of 3050-2800 cm^{-1} was plotted with the layer thickness increasing from bottom to top. Already with 50 nm CH_2 groups in the form of the $sp^3\,CH_2$ asymmetrical binding at 2932 cm^{-1} are recognisable. The presence of such CH_2 groups indicates the completion of the interlayer formation between polymer and a-C:H layer. Thus the interlayer formation stops at the latest with reaching a layer thickness of 50 nm with the formation of the $= CH_2$ bonds. For a more detailed investigation of the interlayer formation further analyses with layer thicknesses from 0 to 50 nm are necessary for all three polymers. A second bond visible at 50 nm is the $sp^3\,CH_3$ asymmetric bond at 2974 cm^{-1}. Therefore, the sp^3 bond dominates the DRIFT measurements for this layer thickness. The strong sp^3 vibrations are also visible in the XPS measurements for PHB (fig. 6.10). At 100 nm these vibrations are increased. In addition, the peak at 2974cm^{-1} widens in the direction of 2950 cm^{-1} towards its right flank, which is explained by a superposition with the $sp^2\,CH_2$ symmetrical peak, which is at about 2950 cm^{-1} and begins to form. A separate resolution of the two peaks was not possible, but the appearance of the sp^2 bond is also visible in the XPS measurements (fig. 6.10) and the NEXAFS measurements (fig. 6.14). A fourth peak is visible at 2876 cm^{-1}, which represents the $sp^3\,CH_3$ symmetrical bond. With a 150 nm a-C:H deposition the symmetrical

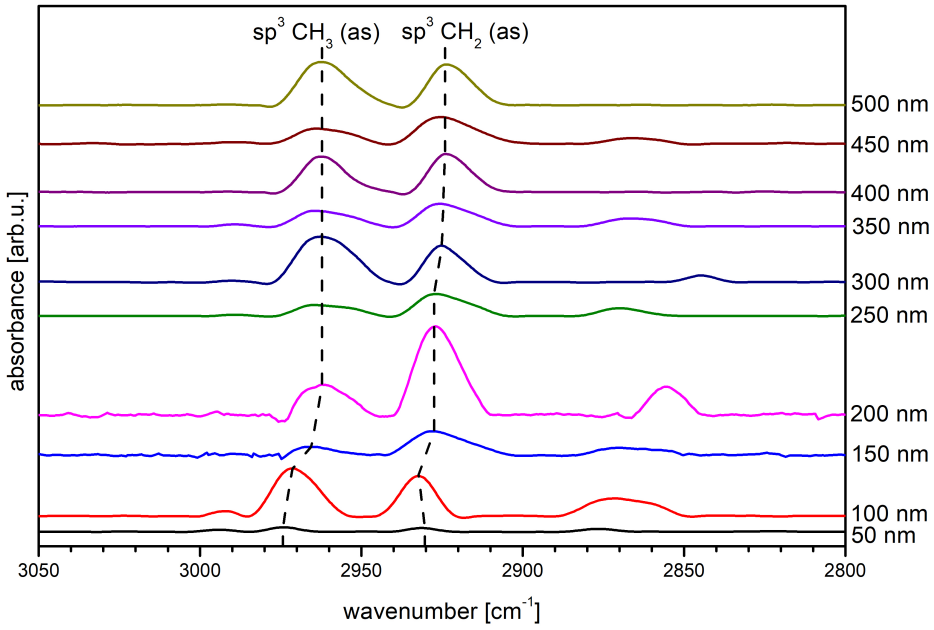

Figure 6.17: Results for the DRIFT measurements of a-C:H coatings on PHB with increasing layer thickness. The coatings were applied to samples previously treated with an O_2 plasma; a O_2 cleaned polymer sample was used as a reference sample for the measurements. The graph is based on ref [107].

sp^3 CH_3 peak at 2870 cm^{-1} disappears almost completely, as does the formerly dominant asymetric sp^3 CH_3 peak at 2974 cm^{-1}, which additionally shifts to 2965cm^{-1}. The asymetric sp^3 CH_2 peak at a wavenumber of 2932cm^{-1} shifts to a value of 2927 cm^{-1} and dominates the spectrum at this layer thickness. This shift of the wave number indicates a lower carbon-hydrogen bond energy and thus a higher carbon-hydrogen bond distance for the CH_3 and CH_2 groups. By increasing a layer thickness to 200 nm, the asymmetric sp^3 CH_3 peak is again more pronounced. In addition, a peak appears at 2855 cm^{-1} which is assigned to the sp^3 CH_2 symmetrical bond. The asymmetric sp^3 CH_2 peak at 2927 cm^{-1} is stronger again and becomes the dominant peak in the spectrum.

With application of a 250 nm a-C:H layer the spectrum changes again and is comparable with the previous one for 150 nm. The sp^3 CH_2 symmetrical peak disappears and the asymetrical sp^3 CH_3 decreases again. In addition, the symmetrical sp^3 CH_3 peak at 2870 cm^{-1} reappears. With 300 nm a-C:H film this dominance behaviour of the peaks is reversed again. The right flank of the sp^3 CH_3 asymmetric bond, which was formed by the superposition with the sp^2 CH_2 symmetrical peak, now drops more strongly, which is due to the fact that the sp^2 oscillation becomes weaker. The decrease

of the sp^2 bond at 300 or 350 nm is also visible in the XPS. At the layer thickness of 350 nm, the spectrum is comparable with 150 nm and 250 nm. At 400 nm layer thickness only two peaks are visible. Both the $sp^3\,CH_3$ asymmetric peak, which is 2962 cm^{-1} here, and the asymmetric peak $sp^3\,CH_2$ at 2924 cm^{-1} are almost balanced. The $sp^3\,CH_3$ asymmetric peak is still in superposition with the symmetrical $sp^2\,CH_2$ peak at 2950 cm^{-1}, but this has almost disappeared. The spectrum for 450 nm deposition is again comparable to that of 150, 250 and 350 nm. The 500 nm spectrum corresponds to the spectrum for 400 nm layer thickness. The similarities in the DRIFT spectra for 50, 150 and 250 nm depositions indicate that at a layer thickness greater than 250 nm a new layer growth of the carbon coating begins after an earlier layer failure. In addition, the similarities between the 200 and 300 nm layer thicknesses and for 150, 250 and 350 nm and their respective changes in the chemical environment indicate a layer thickness range that changes repeatedly in its chemistry between the bonding networks.

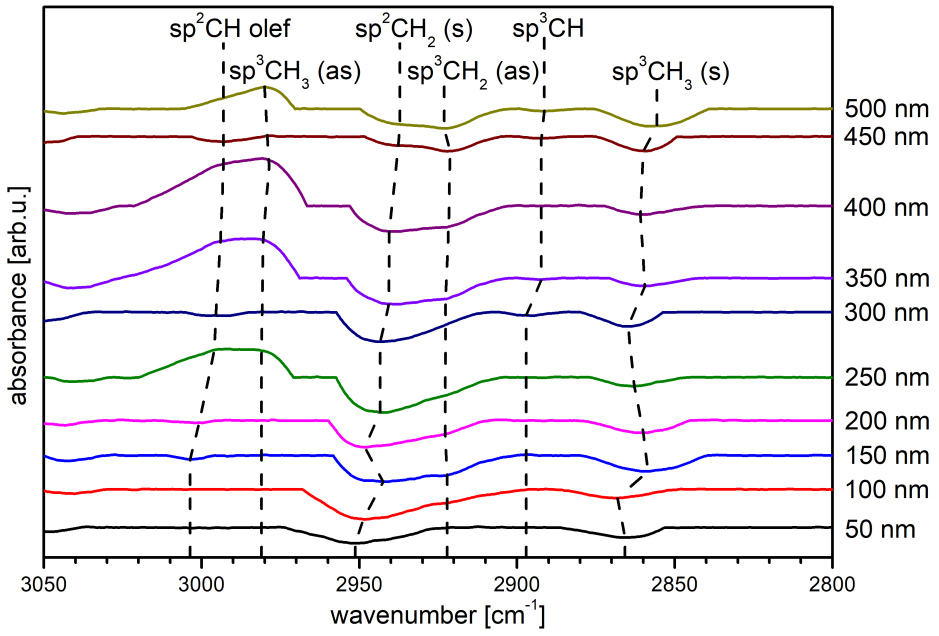

Figure 6.18: DIRFT spectra for a-C:H layers on PBAT with increasing thickness. The coatings were applied to samples previously treated with an O_2 plasma; a O_2 cleaned polymer sample was used as a reference sample for the measurements. The figure is based on ref [108].

Figure 6.18 shows the absorption spectra of the DRIFT measurements for the PBAT samples coated with a-C:H layers of different thicknesses. The measurements were performed with PBAT samples treated with O_2 plasma as reference. The sample coated with 50 nm a-C:H shows two

absorption peaks: the peak at 2951 cm^{-1} belonging to the symmetrical sp^2CH_2 bond and the peak at 2866 cm^{-1} belonging to the symmetrical sp^3CH_3 bond. The formation of CH_2 groups is, as before with PLA and PHB, an indication for the completion of interlayer formation. As the layer thickness increases to 100 nm, a third peak appears at 2920 cm^{-1}, which is, however, only weakly pronounced. This peak represents the asymmetric sp^3CH_2 bond. The peaks already visible at 50 nm are also still present, but the symmetrical sp^2CH_2 peak shifts with increasing layer thickness to lower wavelength values: This is due to a changing distance of the carbon-hydrogen bond. At 150 nm, a fourth, small peak is formed at 3003 cm^{-1}, which can be assigned to the sp^2CH- olefins. The shift of the symmetrical sp^2CH_2 bond, which begins at 100 nm, carries out a short backshift at 200 nm, which, however, is reversed with increasing layer thickness. In addition, this peak is more strongly accentuated with increasing layer thickness, which makes it very pronounced with a layer thickness of 250 nm. In addition, two further peaks appear at this layer thickness which overlap: the peak of the asymmetric sp^3CH_3 peak at 2982 cm^{-1} and again the sp^2CH- olefin peak which was previously at 3003 cm^{-1} and is now shifted to a value of 2995 cm^{-1}. However, these peaks are oriented in such a way that these bonds are less present compared to the O_2 plasma-treated PBAT sample. This reduction of the sp^3 bonds corresponds to the results obtained in the XPS (fig. 6.11). At 300 nm, the peaks occurring at 250 nm almost completely disappear again; only the sp^2CH- olefin peak remains, but this time as absorption peak. In addition, a peak at 2897 cm^{-1} becomes visible, which can be assigned to the sp^3CH bond. At 350 nm, the two peaks (asymmetric sp^3CH_3 peak at 2982 cm^{-1}, and sp^2CH- olefins at 2995 cm^{-1}) reappear and are oriented again as in the 250 nm measurement. Also the sp^3CH_2 asymmetric peak appears again. In addition, both the sp^3CH peak and the sp^3CH_3 symmetrical peak are shifted to smaller wave numbers. The peaks belonging to the sp^3 bond are also weaker here. This behaviour continues with increasing layer thickness. The results obtained are consistent with the XPS measurements, which predict the lowest fraction of sp^3 bonds here. If a layer thickness of 450 nm a-C:H is applied to the PBAT both the symmetrical sp^3CH_3 peak and also the sp^3CH_2 peak are more strongly formed again. The overlapping sp^2CH- olefins and the asymmetric sp^3CH_3 peaks now become absorption peaks. In addition, the balanced sp^2CH_2 peak is weakly emphasized at this layer thickness. This also corresponds to the XPS measurements (fig. 6.11), which predict a reduction of the sp^2 and an increase of the sp^3 content at this layer thickness. With a range of 500 nm a-C:H layer on PBAT, the sp^3 bonds continue to be strongly pronounced. It should be noted that the symmetric sp^3CH_3 peak has shifted to lower wavenumbers and the asymmetric sp^3CH_2 peak to higher wavenumbers.

While the symmetrical sp^3CH_3 peak is further strengthened, the asymmetrical sp^3CH_3 peak also appears again in the measured spectrum, but its orientation again indicates a weakening of this bond compared to the sample treated with O_2 plasma. Overall, the strengthening of the sp^3 bonds is again in line with the results of XPS, which predict the sp^3 bond as dominant. The peaks of the sp^2 bonds have almost disappeared.

A comparison of the DRIFT measurements for the three polymers PLA, PHB and PBAT shows that substrate effects are present when coated with a-C:H layers. The polmyers were coated simultaneously respectivly in the same plasma process, but the carbon atoms have different bonds on the layer surface. This is in line with the results obtained with the techniques presented above. In addition, it was once again proven that the bonds on the surface change with varying layer thickness and thus depend not only on the plasma parameters but also on the layer thickness.

The appearance of the CH_2 bonds at a layer thickness of 50 nm shows that interlayer formation has already been completed for all three polymers. The extent to which the thickness of this interlayer differs from material to material cannot be assessed with the samples examined here. For this purpose, further measurements with a thinner layer must be carried out.

A comparison of all the techniques used here provides a similar picture for the different polymers: XPS (figs. 6.9, 6.10 and 6.11), NEXAFS (figs. 6.13, 6.14 and 6.15) and DRIFT (figs. 6.16, 6.17 and 6.18) show an initially sp^3 dominated growth of the layer surface. This changes in favour of a sp^2-containing layer. This change takes place at different a-C:H layer thicknesses for the polymers. This is probably due to a stress release, as the rigid sp^3 network changes in favour of a more flexible sp^2 network. With this stress release the layer also breaks up, as the SEM (figs. 6.2, 6.3 and 6.4) images show. However, there is a polymer dependent delay in the break-up. This may be due to a differently pronounced interlayer formation and thus different level of binding. The PBAT samples do not show a cord-buckling effect (probably due to a good binding of the a-C:H layer on the polymer), but have the greatest delay (200 nm layer thickness) between the change from sp^3 to sp^2 to layer failure. The change from sp^2 to sp^3 as the dominant bond of the layer system shows no effect on the surface stability. Subsequently, the proportions of the sp^3 bonds increase again until the rigid network changes back to an sp^2 network due to the high internal stress. The contact angle measurements (figs. 6.5, 6.6 and 6.7) show a similar picture.

The better bonding of the layer with the polymer could be due to different carbon to oxygen ratios in the respective polymer backbones. These ratios were 3:2 for PLA, 4:2 for PHB and 12:4 and 8:4 for PBAT (see section 5.6), so the proportion of oxygen is lowest for PBAT. This may also explain

the results for POM, which the group obtained in earlier measurements and where no interlayer is present [73] and where the carbon to oxygen ratio is 1:1. HDPE, on the other hand, has no oxygen in the backbone and at 40 nm has a distinct interlayer and good layer retention [75]. To confirm this statement further measurements for thin a-C:H layers on the respective polymers have to be made.

7 Conclusion

The biodegradable polymeric PLA, PHB (both are also bio-based) and PBAT (produced on the basis of crude oils) were coated with an RF-PECVD acetylene plasma with a:C-H layers in different thicknesses. The surface of the raw polymer sample, O_2 plasma treated sample and the coated samples were analysed using several techniques: SEM for surface morphology and stability of the applied layers, contact angle measurements for wettability of the surface and macroscopic bonding ratios on the surface, DRIFT spectroscopy and NEXAFS and XPS X-ray based spectroscopy techniques were used to study the chemical composition of the surface.

The SEM images show areas of stable a:C-H coatings on the investigated samples: For PLA, the layer remains stable if the thickness of the layer is in the 0-300 nm and 350-450 nm intervals. PHB has stable a-C:H coatings providing their thickness is not between 100 and 200 nm or exceeds 450 nm. For PBAT, the deposited layer remains stable up to a thickness of 150 nm and for the range from 250 nm to at least 400 nm. It should also be mentioned that the so-called cord buckling effect for polymers PLA and PHB occurs in the SEM images. This is a detachment of the layer from the surface as well as a waviness of the same, but without a failure of the layer occurring. With both polymers the cord buckling precedes the breaking up and thus the failure of the layer. In the PBAT polymer, this effect does not occur, which indicates a very good bond between the a-C:H layer and the substrate. If the layer breaks open here, it still adheres stably to the polymer.

The chemical analysis of the surface using XPS shows that a shift in the dominant bond from sp^3 to sp^2 indicates an impending stress release in the layer, which leads to cracks and imminent layer failure. In PLA this occurs immediately when the dominant bond changes from sp^3 to sp^2, in PHB with a delay of 100 nm layer thickness and in PBAT with 200 nm.

Not only the XPS measurements, but also the NEXAFS and DRIFT results show that the chemical composition of the layer changes with increasing thickness. The sp^2 content increases with increasing layer thickness until this bond becomes dominant and a layer failure (delayed with PHB and PBAT) becomes visible in the SEM. The contact angle measurements also underline this trend and show an increasing error bar at the layer thicknesses at which layer failure occurs. In addition, the DRIFT studies show a shift in the positions of the absorption peaks, which means a change in the bond spacing. This shift underlines the changing chemical environment in the a-C:H layers. In addition, the DIRFT results reveal that CH_2 bonds have already formed for all three polymers at 50 nm layer thickness. This shows that if there is interlayer formation between the polymer and

the deposited a:C-H layers, this is already completed within the first 50 nm of the layer thickness.

The results obtained with the analytical techniques used in this thesis are largely consistent and show an almost identical picture of the growth behaviour of the a-C:H layers on the different polymers. Smaller deviations are caused on the one hand by the different penetration depths of the measuring techniques and on the other hand by the stress-induced damaged surface. The results show that the bonding ratios of the carbon atoms and the chemical environment depend not only on the plasma parameters used, but also on the resulting a-C:H layer thickness. This means that layers can also be adapted for specific applications by varying the layer thickness of a-C:H on the given polymer. Extensive analyses of the chemical environment of the a-C:H layers were performed and underline the significantly changed character of the a-C:H layers with increasing layer thickness.

For PLA it can be stated that the deposition of a stable a:C-H layer on the biopolymer is possible up to a thickness of 300 nm and for the range from 350 nm to at least 450 nm. Before layer failure due to internal stresses in the film occurs, cord buckling is formed, which later changes into cracks and ends in complete delamination at 1000 nm layer thickness. Stable a-C:H coatings are also possible for the polymer PHB. Exceptions, however, are layer thicknesses between 100 and 200 nm and thicknesses greater than 450 nm where the layers fail. For PBAT, a stable a-C:H layer on the polymer is possible if the thickness does not exceed 200 nm. The coating also remains stable on the polymer between 250 nm and 450 nm. It is also noticeable that layers with a thickness of 1000 nm were only possible for the material PLA.

Although all three polymers were coated in the same plasma process, the a-C:H layers applied have a different bonding ratio of carbon. This is a clear evidence for a substrate effect with an a-C:H coating of the three polymers. All three polymers have in common that a change from sp^3 to sp^2 as the dominant bond leads to a layer failure, the change from sp^2 to sp^3 has no consequences. There are differences in the delay of the failure as well as in the presence or absence of the cord-buckling effect, which in turn underlines a substrate effect. A possible reason for this are the different carbon to oxygen ratios in the polymer backbones. In summary, it is possible to deposit stable a-C:H layers with specific properties on the different biodegradable polymers even if the properties of the same layer thicknesses differ for the different polymers. To visualise the results in short form, the three graphical abstracts of the corresponding publications are attached in the appendix.

8 Acknowledgements

First and foremost I would like to thank my parents, who have always supported me and made my studies possible. Next, I would like to thank my supervisor, Prof. Dr. Stefan Wehner, who gave me the opportunity to do my doctorate at the university and who advised me on any problems that occured. I would also like to thank my supervisor Dr. Christian Fischer, who took over my direct supervision when Mr. Wehner was appointed Vice President. During my time at the University of Koblenz he directed my work and was always ready to conduct helpful discussions on the results obtained and their interpretation. Both of them taught me a lot about scientific work and teaching at a university. Next I would like to thank Prof. Dr. Barbara Hahn from the RheinAhrCampus of the University of Applied Sciences Koblenz, who agreed to be an reviewer for this thesis and without whom measurements with the SEM would not have been possible. I would also like to thank Dr. Alexei Nefedov from the Karlsruhe Institute of Technology (KIT), with whom we worked a lot in the XPS and NEXAFS measurements at the beamline HE-SGM of KIT at the Berlin electron storage ring for synchrotron radiation (BESSY) and where I could learn a lot about X-ray spectroscopy. I would also like to thank Dr. Michael Kunze, who taught me how to use the IR measuring instrument and how to evaluate the measurement data. I would also like to thank Prof. Dr. Joachim Scholz because he allowed me to take measurements at the Department of Chemistry at the University of Koblenz and made them possible in the first place. I would also like to thank Dr. Heinz Busch and Dr. Falk Bernsmann of NTTF coatings GmbH, who coated the samples examined here and also offered the opportunity to coat other samples for investigations by myself. In addition, we were allowed to use the contact angle measuring instrument for our measurements.

Furthermore I would like to thank my colleagues from the Department of physics. Here Dr. Merten Joost has to be mentioned in particular, who always helped me with computer and software problems. The two technical employees Thomas Knieper and Jürgen Schwaab helped me with every new device installation and operation and with the production of special components, which were necessary in the framework of some projects. Our secretary Mrs. Petra Kires, who assisted me with all kinds of bureaucratic work, and also Dr. Susanne Körsten, who I could always ask in case of problems. Last but not least I would like to thank all the other PhDs of the working group, as well as all the Bachelor and Master students of the working group for all the input and the numerous conversations and help and which made my time in the working group unique.

References

[1] Anthony L. Andrady and Mike A. Neal. Applications and societal benefits of plastics. *Philosophical transactions of the Royal Society of London. Series B, Biological sciences*, 364(1526):1977–1984, 2009.

[2] Luigia Sabbatini, editor. *Polymer surface characterization*. De Gruyter graduate. De Gruyter, Berlin and Boston, 2014.

[3] Hideyuki Kodama, Akira Shirakura, Atsushi Hotta, and Tetsuya Suzuki. Gas barrier properties of carbon films synthesized by atmospheric pressure glow plasma. *Surface and Coatings Technology*, 201(3-4):913–917, 2006.

[4] Masaki Nakaya, Akira Uedono, and Atsushi Hotta. Recent Progress in Gas Barrier Thin Film Coatings on PET Bottles in Food and Beverage Applications. *Coatings*, 5(4):987–1001, 2015.

[5] Lisa Kleinen, Ulla Böde, Karin Schenk, Heinz Busch, Jörg Bradenahl, Stefan C. Müller, Burkard Hillebrands, and Norbert Laube. Amorphous Carbon Coatings Inhibit Crystalline Biofilm Formation on Urological Implants. *Plasma Processes and Polymers*, 4(S1):S386–S391, 2007.

[6] Jeong-Uk Ahn, Seung-Kyun Ahn, and Jong-Dae Lim. Development of High Wear Resistant and Durable Coatings for Al Valve Spring Retainer. In *SAE Technical Paper Series*, SAE Technical Paper Series. SAE International400 Commonwealth Drive, Warrendale, PA, United States, 2007.

[7] Naoto Ohtake, Tomio Uchi, Toshiyuki Yasuhara, and Mai Takashima. Characteristics of Diamond-Like Carbon Films Deposited on Polymer Dental Materials. *Japanese Journal of Applied Physics*, 51:090128, 2012.

[8] Faris M. AL-Oqla and S. M. Sapuan. Natural fiber reinforced polymer composites in industrial applications: feasibility of date palm fibers for sustainable automotive industry: Journal of Cleaner Production, 66, 347-354. 2014.

[9] Alireza Ashori. Wood-plastic composites as promising green-composites for automotive industries! *Bioresource technology*, 99(11):4661–4667, 2008.

[10] Peter G. Ryan. A Brief History of Marine Litter Research. In Melanie Bergmann, Lars Gutow, and Michael Klages, editors, *Marine Anthropogenic Litter*, volume 2, pages 1–25. Springer International Publishing, Cham, 2015.

[11] Ray Smith. *Biodegradable polymers for industrial applications*. Woodhead, Cambridge and Boca Raton, Fla, 2005.

[12] L.-T. Lim, R. Auras, and M. Rubino. Processing technologies for poly(lactic acid). *Progress in Polymer Science*, 33(8):820–852, 2008.

[13] Magdalena Rohrbeck, Susanne Körsten, Christian B. Fischer, Stefan Wehner, and Barbara Kessler. Diamond-like carbon coating of a pure bioplastic foil. *Thin Solid Films*, 545:558–563, 2013.

[14] Magdalena Rohrbeck, Christian Fischer, Stefan Wehner, Jutta Meier, and Werner Manz. DLC-coated pure bioplastic foil. *Vakuum in Forschung und Praxis*, 26(2):42–47, 2014.

[15] A. Grill. Plasma-deposited diamondlike carbon and related materials. *IBM Journal of Research and Development*, 43(1.2):147–162, 1999.

[16] Alfred Grill. Diamond-like carbon: state of the art. *Diamond and Related Materials*, 8(2-5):428–434, 1999.

[17] A. Grill. Diamond-like carbon coatings as biocompatible materials—an overview. *Diamond and Related Materials*, 12(2):166–170, 2003.

[18] P. Couderc and Y. Catherine. Structure and physical properties of plasma-grown amorphous hydrogenated carbon films. *Thin Solid Films*, 146(1):93–107, 1987.

[19] J. Robertson. Diamond-like amorphous carbon. *Materials Science and Engineering: R: Reports*, 37(4-6):129–281, 2002.

[20] Shih-Chin Lee, Fong-Cheng Tai, and Che-Hung Wei. Correlation between sp2/sp3 Ratio or Hydrogen Content and Water Contact Angle in Hydrogenated DLC Film. *MATERIALS TRANSACTIONS*, 48(9):2534–2538, 2007.

[21] John Robertson. Plasma Deposition of Diamond-Like Carbon. *Japanese Journal of Applied Physics*, 50:01AF01, 2011.

[22] Christian B. Fischer, Magdalena Rohrbeck, Stefan Wehner, Matthias Richter, and Dieter Schmeißer. Interlayer formation of diamond-like carbon coatings on industrial polyethylene: Thickness dependent surface characterization by SEM, AFM and NEXAFS. *Applied Surface Science*, 271:381–389, 2013.

[23] Elham Mohagheghpour, Marjan Rajabi, Reza Gholamipour, Majid M. Larijani, and Shahab Sheibani. Ion beam energy dependence of surface and structural properties of amorphous carbon films deposited by IBSD method on Ni–Cu alloy. *Journal of Materials Research*, 32(07):1258–1266, 2017.

[24] R. Paul, S. N. Das, S. Dalui, R. N. Gayen, R. K. Roy, R. Bhar, and A. K. Pal. Synthesis of DLC films with different sp 2 /sp 3 ratios and their hydrophobic behaviour. *Journal of Physics D: Applied Physics*, 41(5):055309, 2008.

[25] Rathin Datta and Michael Henry. Lactic acid: recent advances in products, processes and technologies — a review. *Journal of Chemical Technology & Biotechnology*, 81(7):1119–1129, 2006.

[26] W. S. Ahn, S. J. Park, and S. Y. Lee. Production of Poly(3-hydroxybutyrate) by fed-batch culture of recombinant Escherichia coli with a highly concentrated whey solution. *Applied and environmental microbiology*, 66(8):3624–3627, 2000.

[27] U. Witt, T. Einig, M. Yamamoto, I. Kleeberg, W.-D Deckwer, and R.-J Müller. Biodegradation of aliphatic–aromatic copolyesters: evaluation of the final biodegradability and ecotoxicological impact of degradation intermediates. *Chemosphere*, 44(2):289–299, 2001.

[28] David Halliday, Robert Resnick, and Jearl Walker. *Physik*. Wiley-VCH Verlag GmbH & Co. KGaA, Weinheim, dritte, vollständig überarbeitete und erweiterte auflage edition, 2018.

[29] Paul A. Tipler and Dieter Gerlich, editors. *Physik*. Spektrum Lehrbuch. Spektrum Akad. Verl., Heidelberg, neuaufl. edition, 2004.

[30] Sebastian Koltzenburg, Michael Maskos, Oskar Nuyken, and Rolf Mülhaupt. *Polymere: Synthese, Eigenschaften und Anwendungen*. Springer Spektrum, Berlin, 2014.

[31] Robert J. Goldston, Paul H. Rutherford, and Timothy Striker. *Plasmaphysik: Eine Einführung*. Vieweg-Lehrbuch Physik. Vieweg, Braunschweig, 1998.

[32] Francis F. Chen. *Plasma physics*, volume / Francis F. Chen ; Vol. 1 of *Introduction to Plasma Physics and Controlled Fusion*. Springer US, New York, 2. ed., 5. printing edition, 2006.

[33] Michael Kaufman. *Plasmaphysik und Fusionsforschung*. Vieweg+Teubner Verlag, Wiesbaden, 2003.

[34] Michael A. Lieberman and Allan J. Lichtenberg. *Principles of plasma discharges and materials processing*. A Wiley Interscience publication. Wiley, New York, NY, 1994.

[35] P. Koidl, Ch. Wild, B. Dischler, J. Wagner, and M. Ramsteiner. Plasma Deposition, Properties and Structure of Amorphous Hydrogenated Carbon Films. *Materials Science Forum*, 52-53:41–70, 1991.

[36] Milton Ohring. *Materials science of thin films: Deposition and structure*. Academic Press, San Diego, Calif., 2. ed. edition, 2002.

[37] Achim von Keudell. Einführung in die Plasmaphysik II: Niedertemperaturplasmen. Wintersemester 2010/2011.

[38] N. A. Morrison, S. Muhl, S. E. Rodil, A. C. Ferrari, M. Nesládek, W. I. Milne, and J. Robertson. The Preparation, Characterization and Tribological Properties of TA-C:H Deposited Using an Electron Cyclotron Wave Resonance Plasma Beam Source. *physica status solidi (a)*, 172(1):79–90, 1999.

[39] M. Weiler, K. Lang, E. Li, and J. Robertson. Deposition of tetrahedral hydrogenated amorphous carbon using a novel electron cyclotron wave resonance reactor. *Applied Physics Letters*, 72(11):1314–1316, 1998.

[40] Alexander A. Fridman. *Plasma chemistry*. Cambridge University Press, Cambridge, 2012.

[41] Donald Leonard Smith. *Thin-film deposition: Principles and practice*. McGraw-Hill, Boston, Mass., internat. ed. edition, 1995.

[42] Hans Lüth. *Solid Surfaces, Interfaces and Thin Films*. Graduate Texts in Physics. Springer, Cham, 6th ed. 2015 edition, 2015.

[43] Kurt K. Kolasinski. *Surface Science: Foundations of Catalysis and Nanoscience*. Wiley, s.l., 3. aufl. edition, 2012.

[44] K. Oura, M. Katayama, A. V. Zotov, V. G. Lifshits, and A. A. Saranin. *Surface Science: An Introduction*. Advanced Texts in Physics. Springer, Berlin and Heidelberg, 2003.

[45] Claude A. Klein. How accurate are Stoney's equation and recent modifications. *Journal of Applied Physics*, 88(9):5487–5489, 2000.

[46] C. A. Davis. A simple model for the formation of compressive stress in thin films by ion bombardment. *Thin Solid Films*, 226(1):30–34, 1993.

[47] J. D. Finegan and R. W. Hoffman. Stress Anisotropy in Evaporated Iron Films. *Journal of Applied Physics*, 30(4):597–598, 1959.

[48] F. C. Marques, R. G. Lacerda, G. Y. Odo, and C. M. Lepienski. On the hardness of a-C:H films prepared by methane plasma decomposition. *Thin Solid Films*, 332(1-2):113–117, 1998.

[49] R. G. Lacerda and F. C. Marques. Hard hydrogenated carbon films with low stress. *Applied Physics Letters*, 73(5):617–619, 1998.

[50] Alfred Grill. *Cold plasma in materials fabrication: From fundamentals to applications*. IEEE Press and IEEE Xplore, Piscataway, New Jersey, 1994.

[51] W. Jacob and W. Möller. On the structure of thin hydrocarbon films. *Diamond and Related Materials*, 63(13):1771–1773, 1993.

[52] J. Robertson. Gap states in diamond-like amorphous carbon. *Philosophical Magazine B*, 76(3):335–350, 1997.

[53] E. Neyts, A. Bogaerts, and M. C. M. van de Sanden. Reaction mechanisms and thin a-C:H film growth from low energy hydrocarbon radicals. *Journal of Physics: Conference Series*, 86:012020, 2007.

[54] A. von Keudell, M. Meier, and C. Hopf. Growth mechanism of amorphous hydrogenated carbon. *Diamond and Related Materials*, 11(3-6):969–975, 2002.

[55] A. von Keudell and W. Jacob. Growth and erosion of hydrocarbon films investigated by in situ ellipsometry. *Surface and Coatings Technology*, 79(2):1092, 1996.

[56] Yves Catherine. Preparation Techniques for Diamond-Like Carbon. In Robert E. Clausing, Linda L. Horton, John C. Angus, and Peter Koidl, editors, *Diamond and Diamond-like Films and Coatings*, volume 266 of *NATO ASI Series*, pages 193–227. Springer US, Boston, MA, 1991.

[57] A. Rhallabi and Y. Catherine. Computer simulation of a carbon-deposition plasma in CH/sub 4. *IEEE Transactions on Plasma Science*, 19(2):270–277, 1991.

[58] Cinzia Casiraghi, John Robertson, and Andrea C. Ferrari. Diamond-like carbon for data and beer storage. *Materials Today*, 10(1-2):44–53, 2007.

[59] Y. Tachimoto, M. Noborisaka, A. Shirakura, C. Kuroyanagi, and T. Suzuki. Gas Barrier Properties of Diamond-like Carbon Films Synthesized by Using Remote Type Microwave Plasma CVD under Sub-ambient Atmospheric Pressure. *Journal of Physics: Conference Series*, 417:012043, 2013.

[60] Hideyuki Kodama, Masaki Nakaya, Akira Shirakura, Atsushi Hotta, Terumitsu Hasebe, and Tetsuya Suzuki. Synthesis of practical high-gas-barrier carbon films at low and atmospheric pressure for PET bottles. *New Diamond and Frontier Carbon Technology*, (16):107–119, 2006.

[61] Akira Shirakura, Masaki Nakaya, Yoshinori Koga, Hideyuki Kodama, Terumitsu Hasebe, and Tetsuya Suzuki. Diamond-like carbon films for PET bottles and medical applications. *Thin Solid Films*, 494(1-2):84–91, 2006.

[62] Kenta Bito, Terumitsu Hasebe, Shunto Maegawa, Tomoki Maeda, Tomohiro Matsumoto, Tetsuya Suzuki, and Atsushi Hotta. In vitro basic fibroblast growth factor (bFGF) delivery using an antithrombogenic 2-methacryloyloxyethyl phosphorylcholine (MPC) polymer coated with a micropatterned diamond-like carbon (DLC) film. *Journal of biomedical materials research. Part A*, 105(12):3384–3391, 2017.

[63] Makoto Kano. Overview of DLC-Coated Engine Components. In Sung Chul Cha and Ali Erdemir, editors, *Coating Technology for Vehicle Applications*, volume 254, pages 37–62. Springer International Publishing, Cham, 2015.

[64] Kenneth Holmberg, Peter Andersson, and Ali Erdemir. Global energy consumption due to friction in passenger cars. *Tribology International*, 47:221–234, 2012.

[65] Y. Mabuchi, T. Hamada, H. Izumi, Y. Yasuda, and M. Kano. The Development of Hydrogen-free DLC-coated Valve-lifter. *SAE Transactions*, (116):788–794, 2007.

[66] Yoshiteru Yasuda, Makoto Kano, Yutaka Mabuchi, and Sadayuki Abou. Research on Diamond-Like Carbon Coatings for Low-Friction Valve Lifters. In *SAE Technical Paper Series*, SAE Technical Paper Series. SAE International400 Commonwealth Drive, Warrendale, PA, United States, 2003.

[67] Achim von Keudell. Surface processes during thin-film growth. *Plasma Sources Science and Technology*, 9(4):455–467, 2000.

[68] J. Lackner, W. Waldhauser, A. Alamanou, C. Teichert, F. Schmied, L. Major, and B. Major. Mechanisms for self-assembling topography formation in low-temperature vacuum deposition of inorganic coatings on polymer surfaces. *Bulletin of the Polish Academy of Sciences: Technical Sciences*, 58(2):969, 2010.

[69] J. M. Lackner, S. Gumus, S. Polat, and W. Waldhauser. Nano-wrinkling of diamond-like carbon thin films on amorphous polycarbonate and semicrystalline polyethylene terephthalate. AIP Conference Proceedings, page 020064. AIP Publishing LLC, 2015.

[70] T. Hoshida, D. Tsubone, K. Takada, H. Kodama, T. Hasebe, A. Kamijo, T. Suzuki, and A. Hotta. Controlling the adhesion between diamond-like carbon (DLC) film and high-density polyethylene (HDPE) substrate. *Surface and Coatings Technology*, 202(4-7):1089–1093, 2007.

[71] Dai Tsubone, Terumitsu Hasebe, Aki Kamijo, and Atsushi Hotta. Fracture mechanics of diamond-like carbon (DLC) films coated on flexible polymer substrates. *Surface and Coatings Technology*, 201(14):6423–6430, 2007.

[72] Alberto Catena, Simonpietro Agnello, Liz M. Rösken, Helmut Bergen, Etienne Recktenwald, Falk Bernsmann, Heinz Busch, Marco Cannas, Franco M. Gelardi, Barbara Hahn, Stefan Wehner, and Christian B. Fischer. Characteristics of industrially manufactured amorphous hydrogenated carbon (a-C:H) depositions on high-density polyethylene. *Carbon*, 96:661–671, 2016.

[73] Alberto Catena, Michael R. Kunze, Simonpietro Agnello, Franco M. Gelardi, Stefan Wehner, and Christian B. Fischer. Amorphous hydrogenated carbon (a-C:H) depositions on poly-

oxymethylene: Substrate influence on the characteristics of the developing coatings. *Surface and Coatings Technology*, 307:658–665, 2016.

[74] Alberto Catena, Qiaochu Guo, Michael R. Kunze, Simonpietro Agnello, Franco M. Gelardi, Stefan Wehner, and Christian B. Fischer. Morphological and Chemical Evolution of Gradually Deposited Diamond-Like Carbon Films on Polyethylene Terephthalate: From Subplantation Processes to Structural Reorganization by Intrinsic Stress Release Phenomena. *ACS applied materials & interfaces*, 8(16):10636–10646, 2016.

[75] T. Schlebrowski, W. Rouabeh, S. Wehner, and C. B. Fischer. Specifying the interlayer turning point and dehydrogenation in a-C:H layers plasma deposited on high-density polyethylene with X-ray synchrotron techniques. *Thin Solid Films*, 691:137617, 2019.

[76] Haixia Mei, Rui Huang, Jun Young Chung, Christopher M. Stafford, and Hong-Hui Yu. Buckling modes of elastic thin films on elastic substrates. *Applied Physics Letters*, 90(15):151902, 2007.

[77] Alex A. Volinsky. Experiments with in-situ thin film telephone cord buckling delamination propagation. *MRS Proceedings*, 749:72, 2002.

[78] Wolfgang Demtröder. *Experimentalphysik*. Springer-Lehrbuch. Springer, Berlin, 4., überarb. aufl. edition, 2010.

[79] A. Tobias A. Jenkins, Holger Schönherr, and Renate Förch, editors. *Surface design: Applications in bioscience and nanotechnology*. Wiley-VCH, Weinheim, 2009.

[80] D. Banerjee, S. Mukherjee, and K. K. Chattopadhyay. Controlling the surface topology and hence the hydrophobicity of amorphous carbon thin films. *Carbon*, 48(4):1025–1031, 2010.

[81] W. Barthlott and C. Neinhuis. Purity of the sacred lotus, or escape from contamination in biological surfaces. *Planta*, 202(1):1–8, 1997.

[82] L. Feng, S. Li, Y. Li, H. Li, L. Zhang, J. Zhai, Y. Song, B. Liu, L. Jiang, and D. Zhu. Super-Hydrophobic Surfaces: From Natural to Artificial. *Advanced Materials*, 14(24):1857–1860, 2002.

[83] L. Ostrovskaya, V. Perevertailo, V. Ralchenko, A. Dementjev, and O. Loginova. Wettability and surface energy of oxidized and hydrogen plasma-treated diamond films. *Diamond and Related Materials*, 11(3-6):845–850, 2002.

[84] L.Yu Ostrovskaya. Studies of diamond and diamond-like film surfaces using XAES, AFM and wetting. *Vacuum*, 68(3):219–238, 2002.

[85] F. Piazza and G. Morell. Wettability of hydrogenated tetrahedral amorphous carbon. *Diamond and Related Materials*, 18(1):43–50, 2009.

[86] B.K Tay, D. Sheeja, S.P Lau, and J.X Guo. Study of surface energy of tetrahedral amorphous carbon films modified in various gas plasma. *Diamond and Related Materials*, 12(10-11):2072–2076, 2003.

[87] Y. Zhou, B. Wang, X. Song, E. Li, G. Li, S. Zhao, and H. Yan. Control over the wettability of amorphous carbon films in a large range from hydrophilicity to super-hydrophobicity. *Applied Surface Science*, 253(5):2690–2694, 2006.

[88] T. Werder, J. H. Walther, R. L. Jaffe, T. Halicioglu, and P. Koumoutsakos. On the Water−Carbon Interaction for Use in Molecular Dynamics Simulations of Graphite and Carbon Nanotubes. *The Journal of Physical Chemistry B*, 107(6):1345–1352, 2003.

[89] Alexander Bismarck, Witold Brostow, Rachel Chiu, Haley E. Hagg Lobland, and Kingsley K.C. Ho. Effects of surface plasma treatment on tribology of thermoplastic polymers. *Polymer Engineering & Science*, 48(10):1971–1976, 2008.

[90] Helmut Günzler and Hans-Ulrich Gremlich. *IR spectroscopy: An introduction*. Wiley-VCH, Weinheim, 2002.

[91] T. Armaroli, T. Bécue, and S. Gautier. Diffuse Reflection Infrared Spectroscopy (Drifts): Application to the in Situ Analysis of Catalysts. *Oil & Gas Science and Technology*, 59(2):215–237, 2004.

[92] Joachim Stöhr. *NEXAFS Spectroscopy*, volume 25 of *Springer series in surface sciences*. Springer, Berlin and Heidelberg, 1992.

[93] B. Watts, L. Thomsen, and P. C. Dastoor. Methods in carbon K-edge NEXAFS: Experiment and analysis. *Journal of Electron Spectroscopy and Related Phenomena*, 151(2):105–120, 2006.

[94] Alexei Nefedov and Christof Wöll. Advanced Applications of NEXAFS Spectroscopy for Functionalized Surfaces. In Gianangelo Bracco and Bodil Holst, editors, *Surface science techniques*, Springer series in surface sciences, pages 277–303. Springer, Berlin, 2013.

[95] Berit Brüster, Camilo Amozoqueño, Patrick Grysan, Inma Peral, Benjamin Watts, Jean-Marie Raquez, Philippe Dubois, and Frédéric Addiego. Resolving Inclusion Structure and Deformation Mechanisms in Polylactide Plasticized by Reactive Extrusion. *Macromolecular Materials and Engineering*, 302(12):1700326, 2017.

[96] O. Dhez, H. Ade, and S.G Urquhart. Calibrated NEXAFS spectra of some common polymers. *Journal of Electron Spectroscopy and Related Phenomena*, 128(1):85–96, 2003.

[97] J. Díaz, S. Anders, X. Zhou, E. J. Moler, S. A. Kellar, and Z. Hussain. Analysis of the π^* and ς^* bands of the x-ray absorption spectrum of amorphous carbon. *Journal of Physics D: Applied Physics*, 64(12):17, 2001.

[98] J. Diaz, O. R. Monteiro, and Z. Hussain. Structure of amorphous carbon from near-edge and extended x-ray absorption spectroscopy. *Surface and Coatings Technology*, 76(9):388, 2007.

[99] Klaus Wandelt, editor. *Surface and interface science: Volume 2: Properties of elemental surfaces*. Wiley-VCH, Weinheim, 2012.

[100] T. Schlebrowski, L. Beucher, H. Bazzi, B. Hahn, S. Wehner, and C. B. Fischer. Prediction of a-C:H layer failure on industrial relevant biopolymer polylactide acide (PLA) foils based on the sp2/sp3 ratio. *Surface and Coatings Technology*, 368:79–87, 2019.

[101] Paul M. Dietrich, Tim Horlacher, Pierre-Luc Girard-Lauriault, Thomas Gross, Andreas Lippitz, Hyegeun Min, Thomas Wirth, Riccardo Castelli, Peter H. Seeberger, and Wolfgang E. S. Unger. Adlayers of dimannoside thiols on gold: surface chemical analysis. *Langmuir : the ACS journal of surfaces and colloids*, 27(8):4808–4815, 2011.

[102] J. L. Solomon, R. J. Madix, and J. Stöhr. Orientation and absolute coverage of benzene, aniline, and phenol on Ag(110) determined by NEXAFS and XPS. *Surface Science*, 255(1-2):12–30, 1991.

[103] F. C. Tai, S. C. Lee, C. H. Wei, and S. L. Tyan. Correlation between ID / IG Ratio from Visible Raman Spectra and sp2/sp3 Ratio from XPS Spectra of Annealed Hydrogenated DLC Film. *MATERIALS TRANSACTIONS*, 47(7):1847–1852, 2006.

[104] Allan S. Hoffman. Hydrogels for biomedical applications. *Advanced Drug Delivery Reviews*, 54(1):3–12, 2002.

[105] Elizabeth Carvalho L. Cardoso, Marcus Vinicius S. Seixas, Helio Wiebeck, René R. Oliveira, Glauson Aparecido F. Machado, and Esperidiana A. B. Moura. Development of Bio-Based Foams Prepared from Pbat/Pla Reinforced with Bio-Calcium Carbonate Compatibilized by Electron-Beam Radiation. In Shadia Jamil Ikhmayies, Bowen Li, John S. Carpenter, Jiann-Yang Hwang, Sergio Neves Monteiro, Jian Li, Donato Firrao, Mingming Zhang, Zhiwei Peng, Juan P. Escobedo-Diaz, and Chenguang Bai, editors, *Characterization of Minerals, Metals, and Materials 2016*, volume 245, pages 637–644. Springer International Publishing, Cham, 2016.

[106] Hua Yuan, Zhiyong Liu, and Jie Ren. Preparation, characterization, and foaming behavior of poly(lactic acid)/poly(butylene adipate- co -butylene terephthalate) blend. *Polymer Engineering & Science*, 49(5):1004–1012, 2009.

[107] Torben Schlebrowski, Lucas Beucher, Hadi Bazzi, Barbara Hahn, Stefan Wehner, and Christian B. Fischer. Changing Contents of Carbon Hybridizations in Amorphous Hydrogenated Carbon Layers (a-C:H) on Sustainable Polyhydroxybutyrate (PHB) Exhibit a Significant Deterioration in Stability, Depending on Thickness. *C — Journal of Carbon Research*, 5(3):52, 2019.

[108] Torben Schlebrowski, Halima Acharchi, Barbara Hahn, Stefan Wehner, and Christian B. Fischer. Refinement of Sustainable Polybutylene Adipate Terephthalate (PBAT) with Amorphous Hydrogenated Carbon Films (a-C:H) Revealing Film Instabilities Influenced by a Thickness-Dependent Change of sp2/sp3 Ratio. *Materials (Basel, Switzerland)*, 13(5), 2020.

[109] Hadi Bazzi. Stabilitätsuntersuchungen an kohlenstoffbeschichteten, bioabbaubaren Kunststoffen, Bachelor-Thesis, University of Applied Sciences Koblenz - RheinAhrCampus, Remagen, Germany. 12.08.2016.

[110] Halima Aharchi. Oberflächenuntersuchung von biologisch abbaubaren Polybutylenadipatterephthalat- (PBAT)-Folien veredelt mit a-C:H-Schichten, Bachelor-Thesis, University of Applied sciences Remagen. 06.06.2017.

[111] M. Veres, M. Koós, and I. Pócsik. IR study of the formation process of polymeric hydrogenated amorphous carbon film. *Diamond and Related Materials*, 11(3-6):1110–1114, 2002.

[112] F. A. Miller. Chemical Applications of Infrared Spectroscopy. C. N. R. Rao. Academic Press, New York, 1963. xiv + 683 pp. Illus. $19.50. *Science*, 144(3625):1441, 1964.

[113] E. Tomasella, L. Thomas, M. Dubois, and C. Meunier. Structural and mechanical properties of a-C:H thin films grown by RF-PECVD. *Diamond and Related Materials*, 13(9):1618–1624, 2004.

List of Figures

List of Tables

Appendix

Graphical abstracts

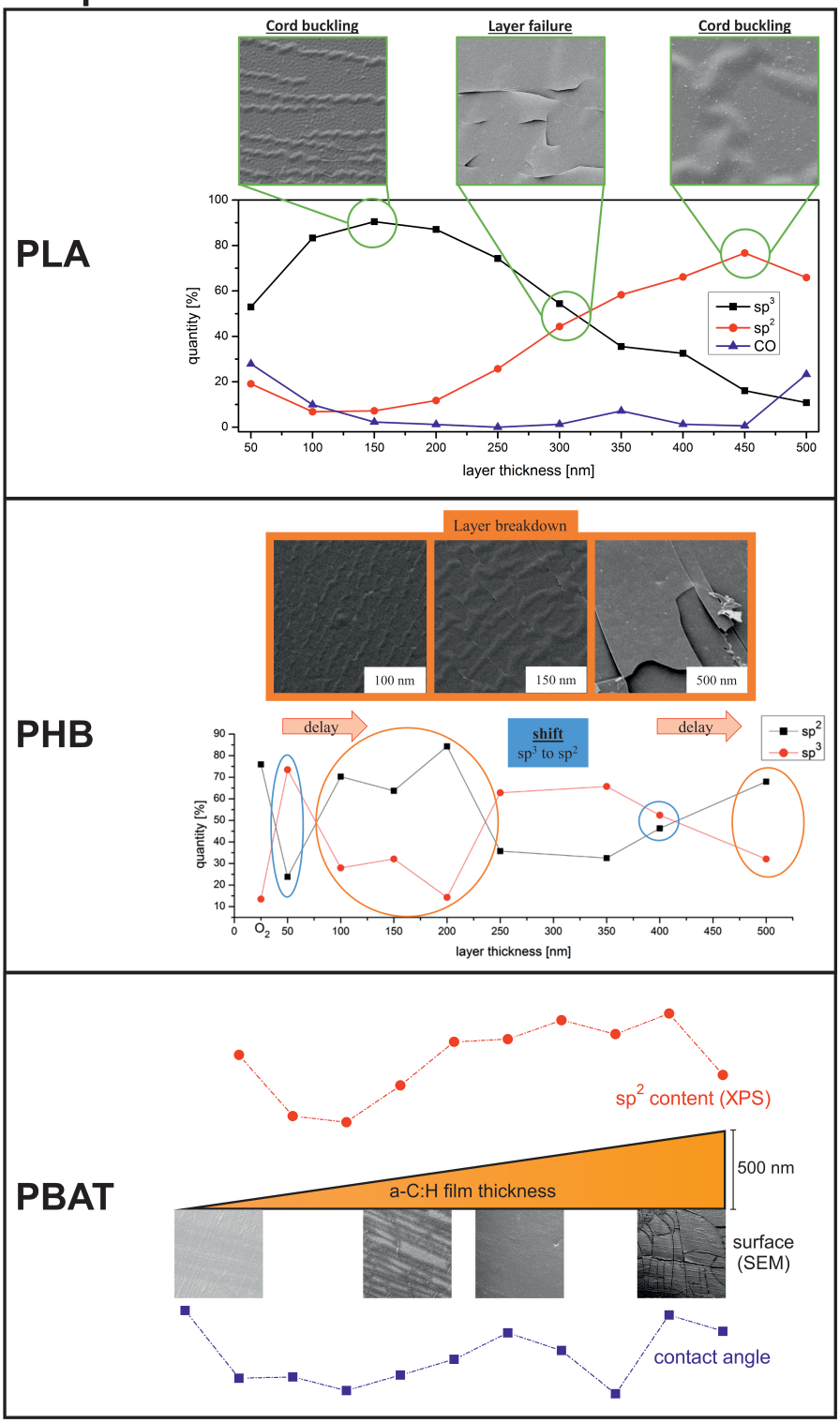

NEXAFS PLA

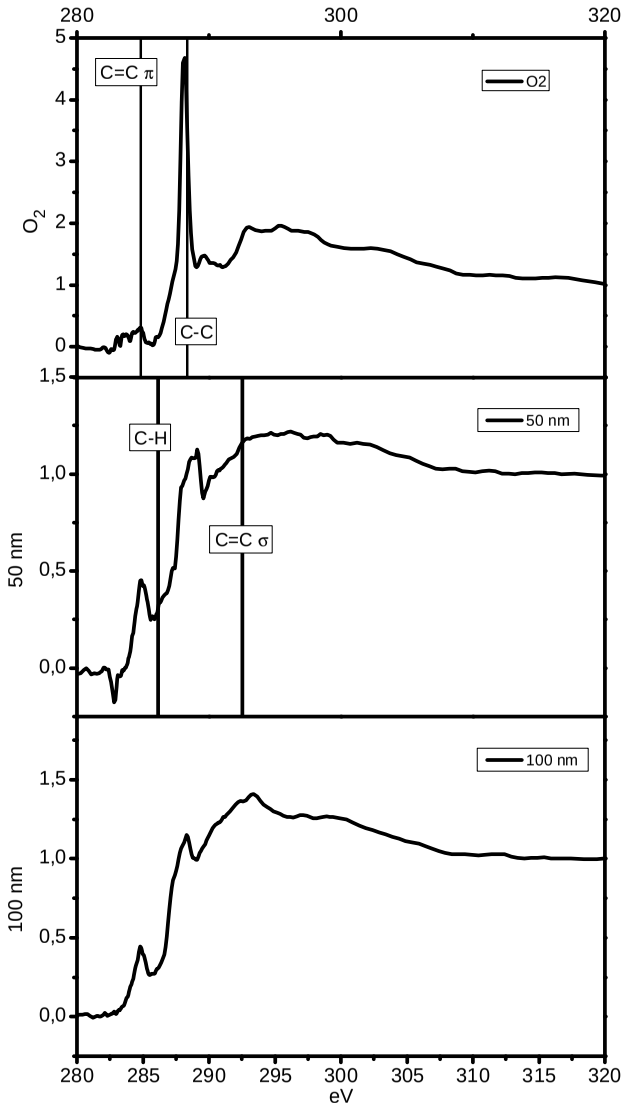
280
300
320
C=C π
O2
C-C
O_2
C-H
C=C σ
50 nm
100 nm
eV

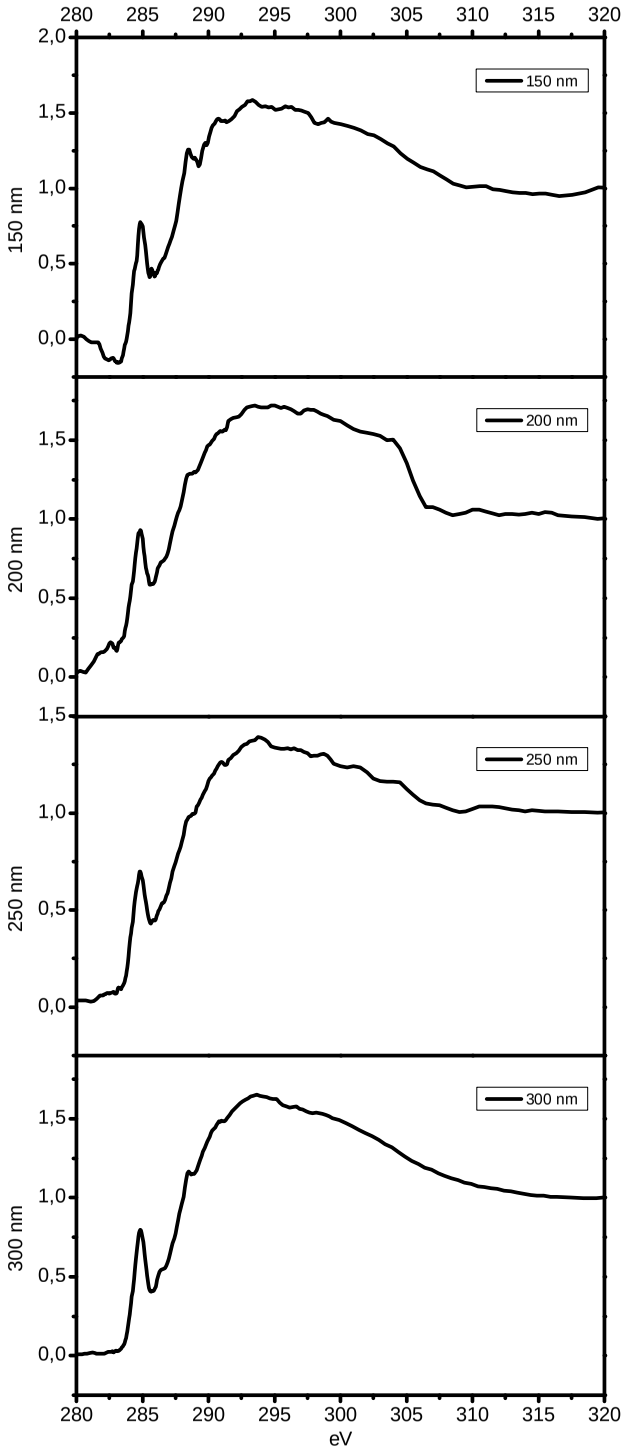
280 285 290 295 300 305 310 315 320
150 nm
200 nm
250 nm
300 nm
eV

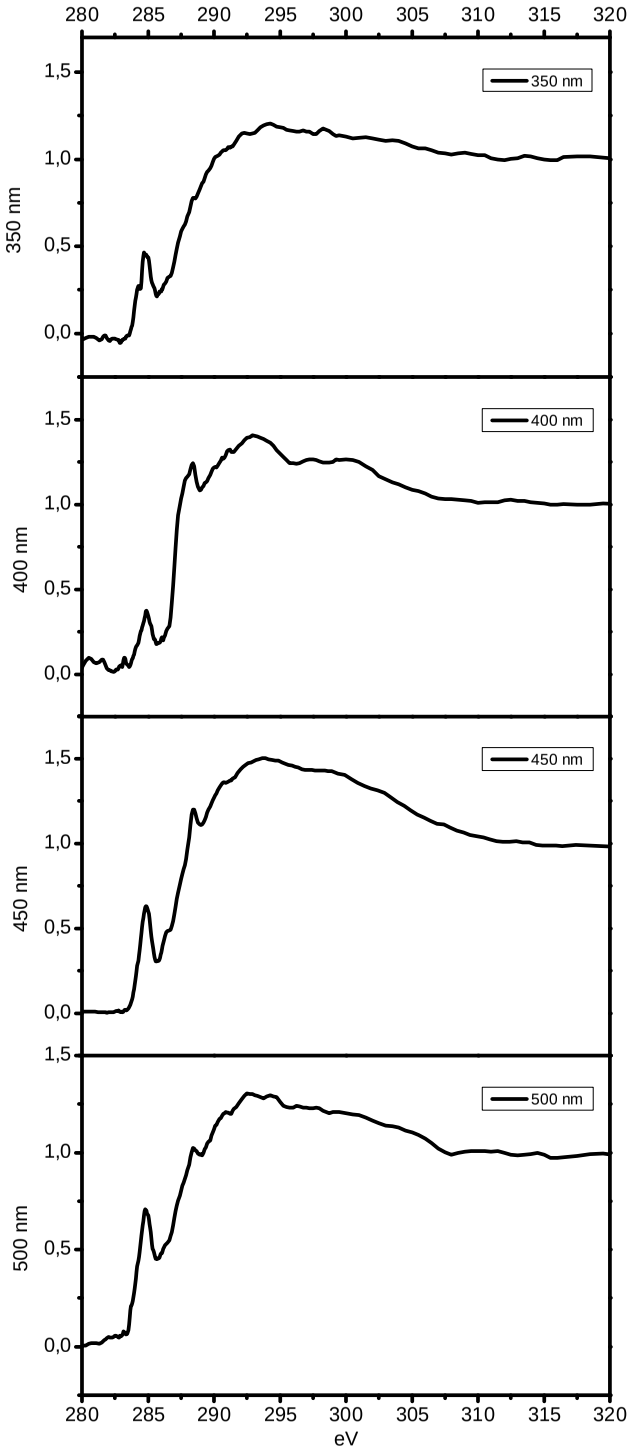
280 285 290 295 300 305 310 315 320
350 nm
400 nm
450 nm
500 nm
eV

NEXAFS
PHB

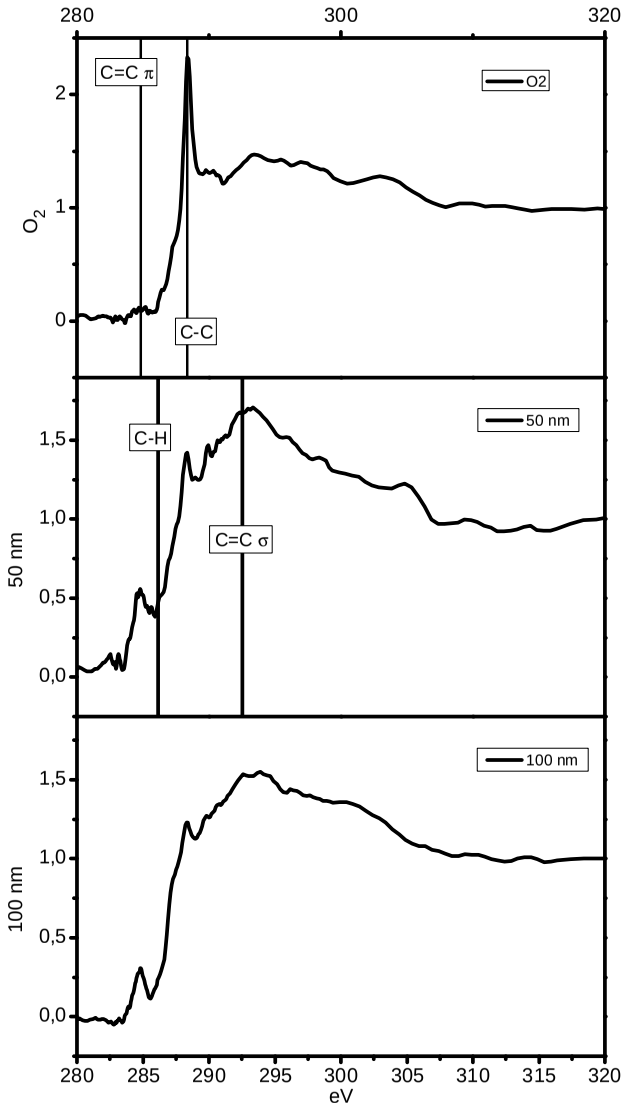
280
300
320
C=C π
O2
C-C
O_2
2
1
0
C-H
C=C σ
50 nm
1,5
1,0
0,5
0,0
100 nm
280 285 290 295 300 305 310 315 320
eV

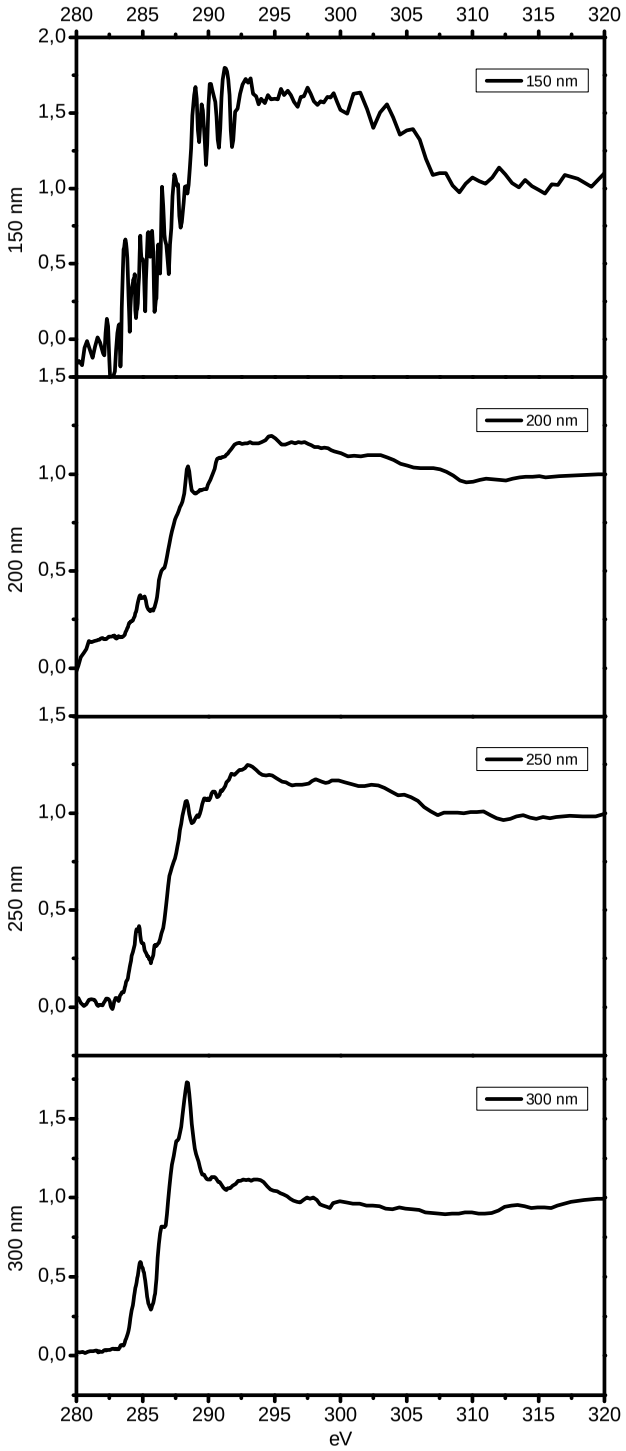
280 285 290 295 300 305 310 315 320
150 nm
200 nm
250 nm
300 nm
2,0
1,5
1,0
0,5
0,0
eV

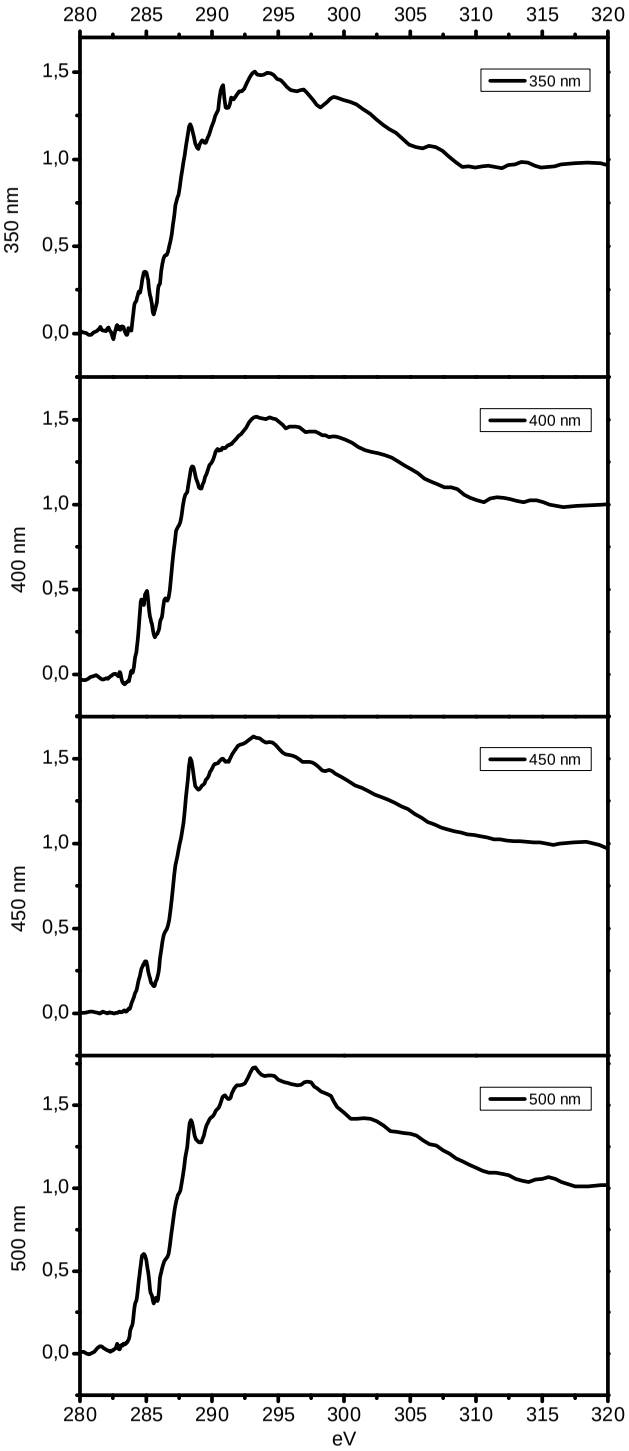
280 285 290 295 300 305 310 315 320
350 nm
400 nm
450 nm
500 nm
1,5
1,0
0,5
0,0
eV

NEXAFS
PBAT

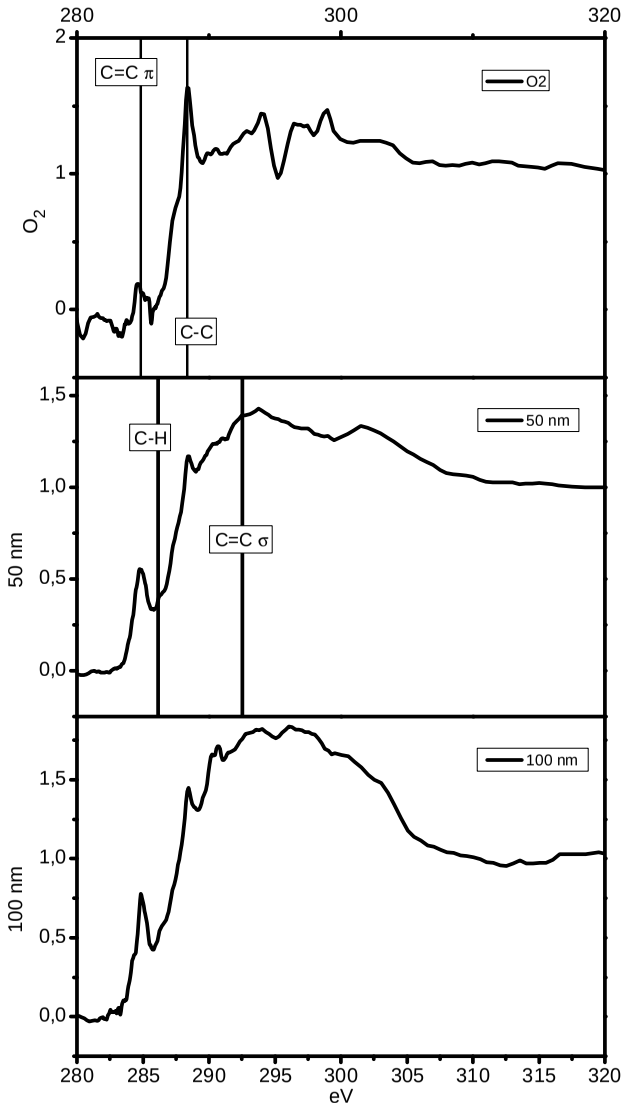
C=C π
C-C
O2
C-H
C=C σ
50 nm
100 nm
eV

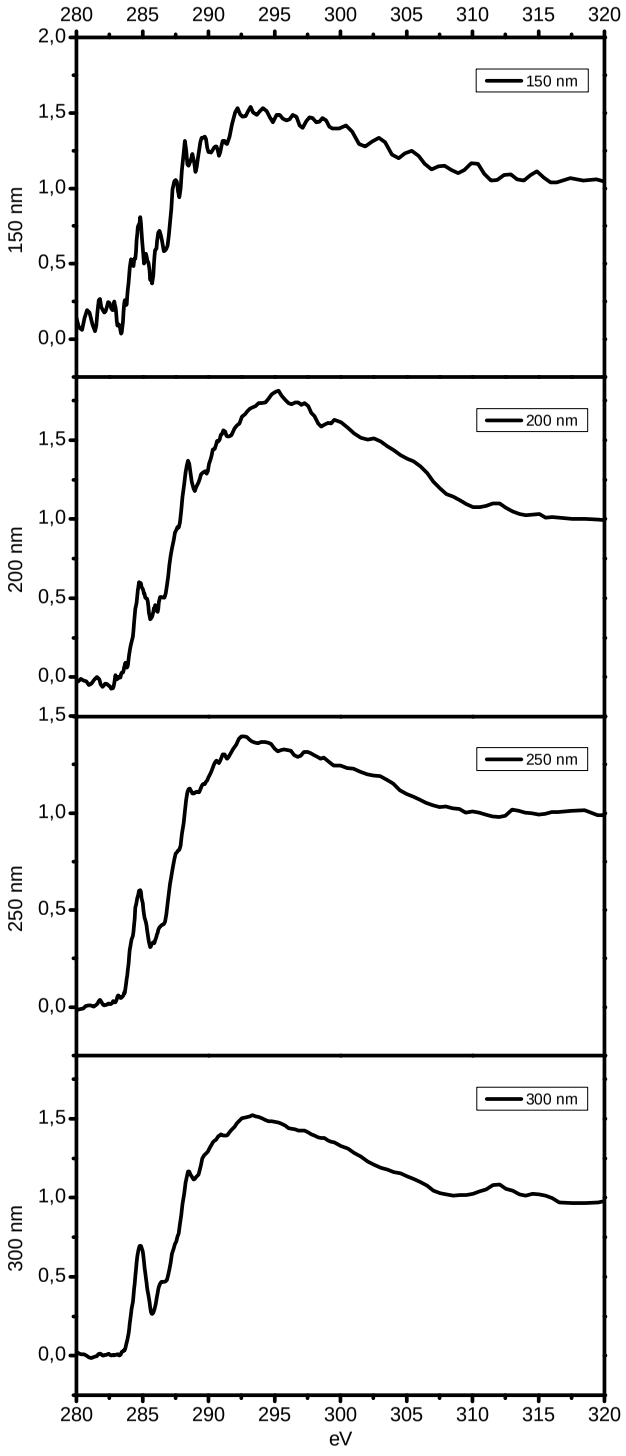
150 nm
200 nm
250 nm
300 nm
eV

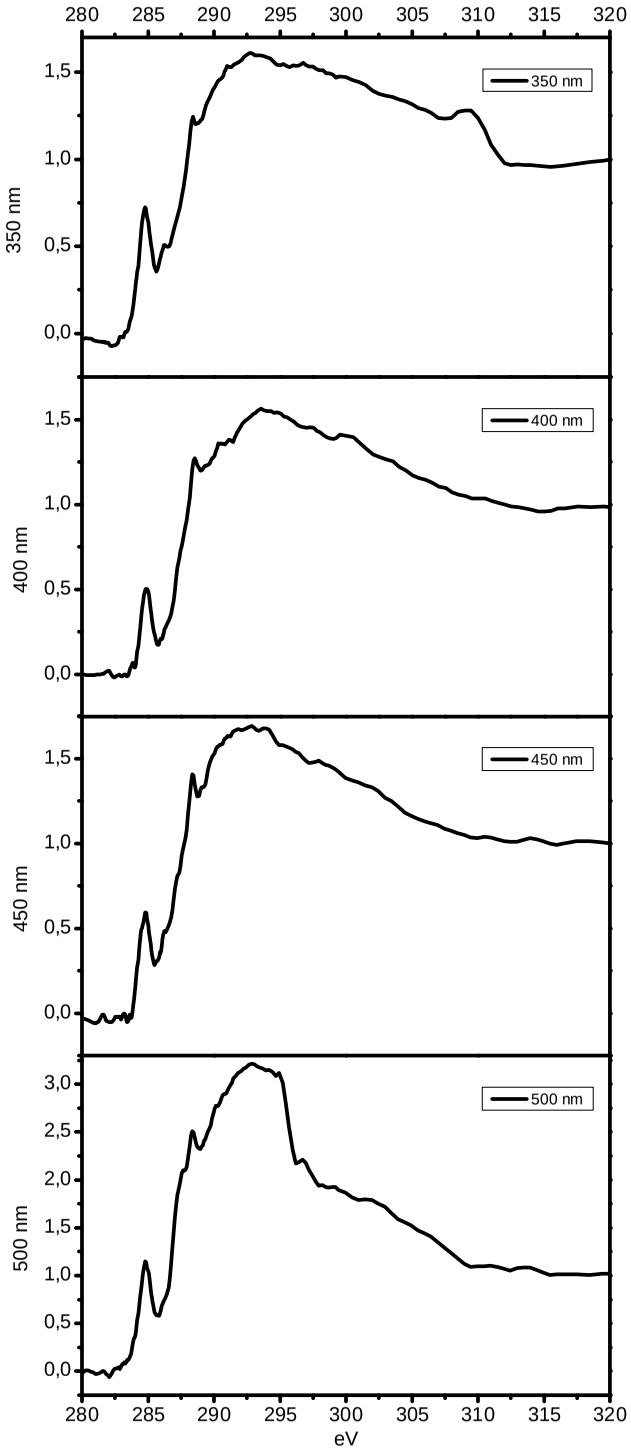
350 nm
400 nm
450 nm
500 nm
eV

Surface & Coatings Technology 368 (2019) 79–87

Contents lists available at ScienceDirect

Surface & Coatings Technology

journal homepage: www.elsevier.com/locate/surfcoat

Prediction of a-C:H layer failure on industrial relevant biopolymer polylactide acide (PLA) foils based on the sp^2/sp^3 ratio

T. Schlebrowski[a], L. Beucher[a], H. Bazzi[b], B. Hahn[b], S. Wehner[a], C.B. Fischer[a,c,*]

[a] Department of Physics, University Koblenz-Landau, 56070 Koblenz, Germany
[b] University of Applied Sciences Koblenz - RheinAhrCampus, 53424 Remagen, Germany
[c] Materials Science and Nano-engineering Department, Mohammed VI Polytechnic University, 43150 Ben Guerir, Morocco

ARTICLE INFO

Keywords:
Plasma coating
Gradual deposition of thin films
Synchrotron radiation
Wettability
Cord buckling

ABSTRACT

A common problem with most polymers is their crude oil-based production and hence their negative environmental impact. Therefore, changing to bio-based and biodegradable polymers like polylactide acide (PLA) as promising candidate could be a reasonable alternative. PLA is characterized by very good mechanical properties, but rather poor surface properties for functional applications. A material-friendly and frequently used technique for surface modification is the deposition of hydrogenated amorphous carbon (a-C:H) by plasma-enhanced chemical vapor deposition (PECVD) using acetylene. Here, a 50 µm thick PLA foil was coated with a-C:H layers of various thickness (50 nm up to 500 nm). Surface topography is analyzed with scanning electron microscopy (SEM), chemical composition by diffuse reflectance infrared Fourier transform (DRIFT), and wettability by contact angle. Additionally, layers were investigated by X-ray photoelectron spectroscopy (XPS) and near edge X-ray absorption fine structure (NEXAFS) at the synchrotron facility BESSYII resulting in thickness dependent changes of the sp^2-/sp^3-binding ratio. As the layer thickness increases, the topography also changes, showing internal stress-induced cord buckling and delamination phenomena for the carbon layers. Present results provide an improved understanding for the coating of the organic biopolymer PLA with the predominantly inorganic a-C:H via in situ growth.

1. Introduction

Plastic materials have become an important resource for several aspects of modern life. Due to their advantages such as deformability, elasticity, low weight, good usability in a wide range of working-temperatures and chemical resistance, widespread applications exist [1,2]. Disadvantages in contrast are for example low hardness, low abrasion resistance or poor mechanical qualities, which limit their usability considerably [2]. In addition, most of the polymers used have the increasingly important disadvantage that they are based on crude oil and are therefore usually only insufficiently or not biodegradable at all. This leads to a negative impact on the environment. The constantly growing demand for plastic raw materials not only increases the consumption of shrinking oil reserves, but also scales up the demand for disposal [3]. A possible alternative is the biodegradable polymer polylactide acide (PLA). PLA is based on corn starch and thus a sustainable and renewable raw material [4]. Nonetheless, it has the same poor material properties as other polymers.

A commonly used technique to improve the surface properties of polymers is the coverage with protective coatings such as hydrogenated amorphous carbon (a-C:H) films [5–7]. The chemical composition of these a-C:H layers consists of π- and σ-bonded sp^2 as well as sp^3 bonded carbons. The sp^2 clusters are limited to short chains embedded in a sp^3 matrix containing of carbon and hydrogen [5,8]. The sp^2/sp^3 ratio of the films as well as its hydrogen content and chemical composition can be determined by the plasma parameters [5,8–10]. Therefore physical properties can be controlled in order to tailor surface characteristics to necessary requirements such as high hardness, low friction or specific chemical inertness [5]. These properties depend strongly on the used gas and the resulting ratio between the sp^2 and sp^3 hybridization of the carbon atoms as well as the amount of hydrogen atoms in the plasma, which crosslink the subsurface region of the layer [5,11]. A high sp^3 to sp^2 ratio leads to a layer with diamond-like properties such as high hardness, chemical inertness or high electrical resistance [11]. An increase of the sp^2/sp^3 ratio leads to a more graphite-like layer, which is softer and shows improved electrical conductivity [11]. This change in the chemical composition also influences the overall wettability resp. the contact angle behavior of the deposited carbon layer [12]. Usually

* Corresponding author at: Department of Physics, University Koblenz-Landau, 56070 Koblenz, Germany.
E-mail address: chrbfischer@uni-koblenz.de (C.B. Fischer).

https://doi.org/10.1016/j.surfcoat.2019.03.069
Received 5 March 2019; Received in revised form 26 March 2019; Accepted 27 March 2019
Available online 09 April 2019
0257-8972/

these a-C:H layers are deposited by chemical vapor deposition (CVD), which additionally can be supported by the use of radio frequency induced plasmas (RF-PECVD) [5,11,13,14]. The RF-PECVD method has the advantage that it works at low temperatures and can also coat non-conductive substrates [6,11].

In the present study a:C-H layers deposited on biopolymer PLA samples are investigated. The carbonaceous films were produced by RF-PECVD technique with acetylene plasma. The surface morphology of these deposited carbon layers was studied ex-situ by scanning electron microscopy (SEM). Diffusive reflectance infrared Fourier transform (DRIFT) and surface sensitive X-ray based techniques such as near edge X-ray absorption fine structure (NEXAFS) and X-ray photoelectron spectroscopy (XPS) were used to investigate the chemical composition of the produced coatings on PLA. Additionally contact angle (CA) measurements were performed to evaluate the relation between the sp^2/sp^3 ratios to macroscopic physical aspects.

2. Materials and methods

2.1. Sample preparation and a-C:H deposition

Polylactide acide (PLA) foils have been obtained in industrial quality as sheets of 30 × 30 cm and 50 µm thickness (Goodfellow GmbH, Friedberg, Germany). The films were cut to quadratic pieces with a size of 10 × 10 cm and fixed on vacuum suitable, self-made aluminum sample holders of similar dimension. Coatings of various thickness (50 to 500 nm, 50 nm steps) have been deposited on the material. The coating process has been executed in a high vacuum chamber equipped with a radio-frequency (RF, 13.65 MHz) driven plasma source (Copra DN 400, CCR GmbH, Troisdorf, Germany) through plasma-enhanced chemical vapor deposition (RF-PECVD) [15]. Directly before subsequent carbon coating, all samples have been cleaned resp. prepared for a suitable deposition by exposure to an oxygen plasma at a pressure of 1 Pa, a flux of 65 sccm/min and a power of 200 W for a time period of 10 min [15–18]. Next the PLA samples have been exposed to an acetylene plasma at 0.65 Pa, a flux of 65 sccm/min and 107 W at room temperature [15–18]. Different film thicknesses are realized by coating time variation. For this purpose, the mounted samples have been placed in a distance of 275 mm from the plasma source during the entire plasma process [17]. The PLA samples to be coated were directly aligned to the plasma resulting in the preferred r-type DLC coating [15,16,18]. The coating process itself is described elsewhere [15]. In order to detect the coating thickness, silicon wafers (Silicon Materials, Kaufering, Germany) half covered with alumina foil, have been mounted additionally on the aluminum sample holders. This enabled the applied layer thickness to be determined with the aid of a profilometer (Dektak 3, Veeco Instruments Inc., Plainview, NY, USA). A conforming analysis of thicker layers was not always possible for all methods because these layers were no longer stable on the sample and became cracked and began to peel off.

2.2. SEM imaging

Scanning electron microscopy (SEM515, Phillips) was used for morphology studies. All samples had to be coated with a thin layer of gold (7–10 nm) to prevent charging effects caused by the electron beam and low conductivity of the polymer substrate. At least three repetitious measurements were done at different positions in order to ensure the correctness of the measure. The operating acceleration voltage was 7 kV at an average distance of 20 mm.

2.3. Contact angles

Contact angle (CA) measurements were conducted using the sessile drop technique performed on a contact angle goniometer (OCA 15 plus, DataPhysics Instruments GmbH, Filderstadt, Germany) at room temperature and in ambient air. A dispensing needle automatically deposited a drop of water (HPLC grade) with a volume of 1 µl on the sample surface. At least five drops were placed and analyzed at different locations on the surface to ensure homogeneity. The contact angles were determined at the left and the right side of each drop and averaged for each sample.

2.4. DRIFT spectroscopy

Infrared investigations of the coated samples were performed with diffuse reflectance for infrared Fourier transform (DRIFT) spectroscopy. A Shimadzu Fourier transform spectrometer (IRPrestige-21, Kyoto, Japan) equipped with the diffuse reflectance measuring apparatus DRS-8000 was used in ambient air and at room temperature [19,20]. First of all, an entire spectrum (500–4000 cm^{-1}) with a resolution of 4 wave numbers and 100 repetitions was recorded. The full spectra helped to rule out, if other sections are influenced by the different layer thicknesses. Measurements with a higher resolution of one wavenumber and an average of 300 repetitions were performed for the most relevant spectral range of 2800–3100 cm^{-1}, the C—H stretching region [14,21]. The measurements are based on three different points on the samples to prove the sample homogeneity and measurement correctness. The O_2-plasma cleaned PLA sample was used as reference for the following DRIFT measurements of a-C:H coated samples. The spectral analysis was done with the commercial IR Solution - FTIR Control Software (software version 1.30, Shimadzu Corporation, Kyoto, Japan). The applied protocol just briefly: firstly a multipoint baseline insertion via the integrated manipulation tool, then fine-tuning with software integrated smoothing manipulation. These manipulations only change the appearance of the graph but not the information contained.

2.5. Near edge X-ray absorption fine structure (NEXAFS)

The surface composition of the carbon depositions was examined by near edge X-ray absorption fine structure (NEXAFS) spectroscopy. Measurements were carried out at the NEXAFS instrument (HE-SGM) at Helmholtz-Zentrum Berlin. Due to the otherwise too high intensity for the samples, the measurements were carried out during the low alpha phase with a maximum ring current of 100 mA in decay mode. The measurement system itself is described in detail elsewhere [22]. To reduce charging effects on the samples during beam irradiation the integrated floodgun was used. Both the C-edge and O-edge of each sample was measured. All relevant measurements of C-edges presented here were repeated at a second location to ensure reproducibility and coatings' homogeneity. After recording the spectra were initially normalized and synchronized to the ring current decay with OriginPro software by OriginLab Corporation. Also a correction of the background noise was carried out. Finally, an adaptation to a gold edge was performed to correct the soiling of the grid and mirror artefacts [23]. The corrected spectra were then smoothed and analyzed by a homemade peak evaluation program. This program reads out the measured position of the C═C π and performs an energy correction by shifting the overall spectrum. Afterwards it derives the values for the analyzed peaks. The obtained ratios of the relevant bonds are normalized to the C═C π bond and subsequently plotted in Origin software.

2.6. X-ray photoelectron spectroscopy (XPS)

X-ray photoelectron spectroscopy was used additionally to verify the chemical environment of the a-C:H coatings. At first, a full survey spectrum between 700 and 0 eV was measured. Subsequently, the C1s peak was recorded at two different locations of the sample to ensure homogeneity and reproducibility. The O1s peak was measured separately to check its presence or absence. The C1s spectra were analyzed by the commercially available software CasaXPS (software version 2.3.18, Casa Software Ltd., United Kingdom). Thereby proportions of

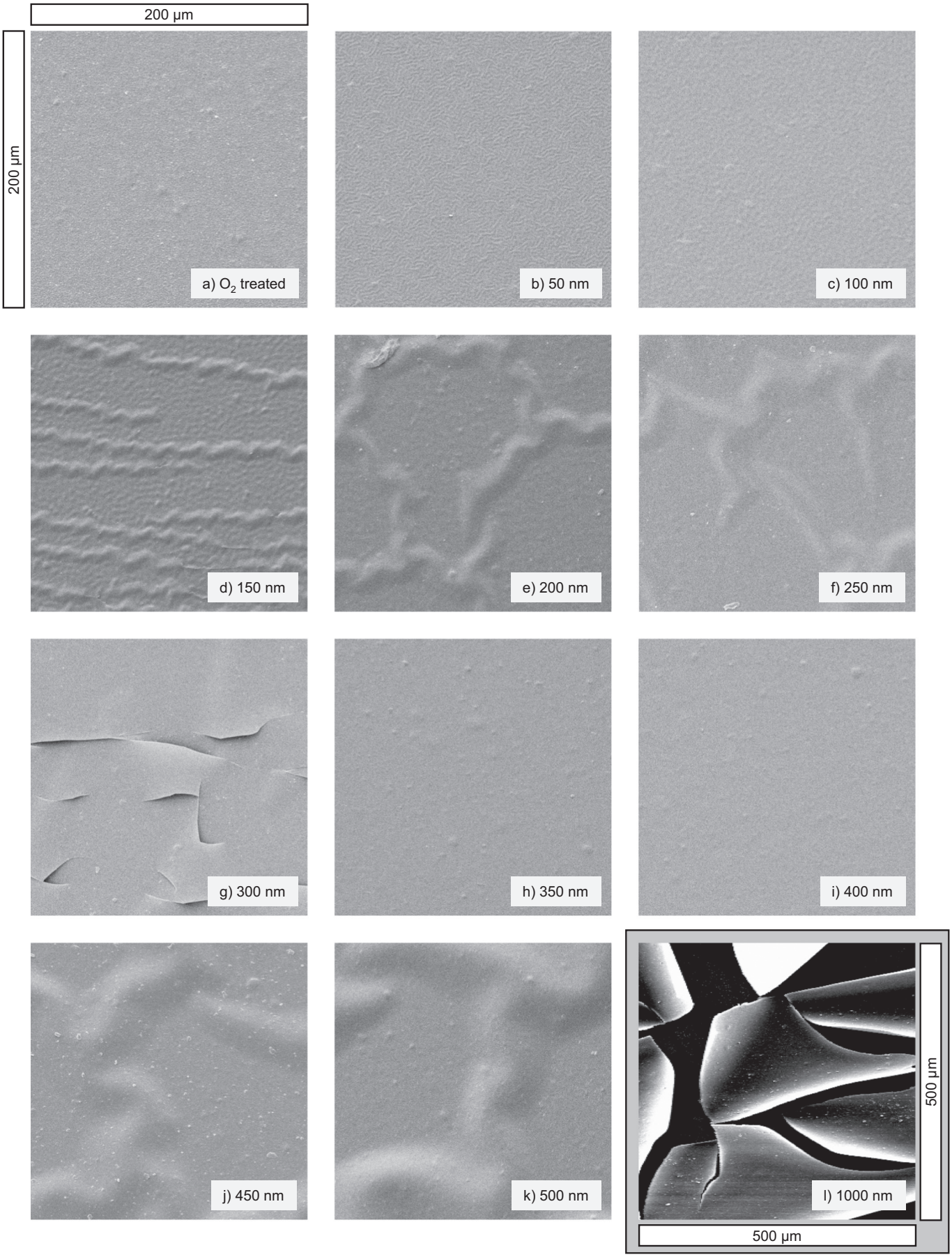

Fig. 1. SEM surface images of PLA samples coated with a:C-H layers of various thickness.

sp^2, sp^3 and C—O bonds in the full C1s peak were identified and evaluated. The results obtained were then plotted with Origin software to the corresponding layer thicknesses. Measurements were carried out at the XPS instrument (HE-SGM) at Helmholtz-Zentrum Berlin during the low alpha phase according to the previous section. The system and detector are described elsewhere [22].

3. Results and discussion

3.1. SEM image analysis

Fig. 1a shows the SEM image of an O_2 plasma treated PLA foil, which serves as reference here. Images of a-C:H coated samples are shown subsequently in ascending order (b to l). Compared to a raw resp. as delivered PLA foil (not shown here) the surface in Fig. 1a appears more pronounced and contrasted after the O_2-treatment, which is mainly assigned to the cleaning sputtering process. The application of O_2 plasma leads to a largely smooth sample surface with few scattered particles. These are assigned to the origin of remaining dust particles from ambient air or impurities caused already by the production or in-house processes. Fig. 1b shows a PLA sample with a 50 nm a-C:H coating on it. An overall uniform film was achieved, which remains unchanged up to 100 nm (Fig. 1c). With increasing thickness the carbon layer is still closed, but with strong visible crimps and ripples. This effect is called “telephone cord buckling” indicating stress release phenomena [24,25], as can be seen in Fig. 1d–f (150–250 nm) and again for j and k (450, 500 nm). In contrast Fig. 1g (300 nm) clearly shows a broken film. The cracks run through the entire film and show a broken surface. As the a-C:H layer thickness increases, at first a uniform film is repeatedly achieved with 350 and 400 nm layer thickness (h,i), which though starts to ripple and crimp again (j,k). Additionally, further film deposition leads to a peel off and roll up of the carbon film on the sample surface at the 1000 nm deposition (l).

Present examination shows a change in the adhesive properties of the carbon coated PLA films with increasing thickness of the a-C:H layer. In the first case of thin layers (50–100 nm, Fig. 1b,c), an apparently homogeneous and stable coating on the surface is achieved. Structures like bumps of the basic biopolymer are still visible. As the coating progresses, these structures are covered more and more by the deposited carbon layer. However, from 150 nm on cord buckling starts with an ongoing shedding of the layer. These emerging crimping structures grow and start to peel off more and more from the basic substrate, but without breaking the solid film (200, 250 nm, Fig. 1e,f). With increasing thickness, the layer finally breaks up (300 nm, Fig. 1g). If the C-deposition continues, the process repeats itself, first with re-smoothed layers (h,i), crimping once again (j,k) and later occurring a-C:H layer islands peeling off and rolling up at 1000 nm thickness (l).

This behavior can be explained by internal stress of the coating and substrate combination which is apparently proportional to the layer thickness. Reasons for the stress existence can be the following: different expansion resp. material coefficients of both materials (PLA, a-C:H), as well as an island formation of the a-C:H layer and an interaction of these islands with each other in early growth stages [26]. If the internal stress exceeds a critical value [5], the film starts to crimp resulting in the cord buckling effect [24,25], as can be seen with thicknesses from 150 nm (d). Due to the stress, the detached a-C:H layers begin to bulge more and more from the substrate, but the stability of the network ensures that the layer does not break open until 250 nm (f). If the stress continues to increase, however, the film breaks, as can be seen for the 300 nm layer (g). After an obviously first stress release at this point the process starts again with proceeding layer thickness. But if the film thickness is further increased, the film starts to peel off and rolls up (1000 nm). This repetitive behavior has already been observed by some of the authors for similar a-C:H coatings on polyhydroxybutyrate (PHB). They reported on the first coating defects at 450 nm carbon deposition and also a subsequent entire exfoliation of the layer from the PHB at 1000 nm [6].

Thus, it was possible to find layer thicknesses for PLA at which the film adheres stably after completion of the coating process (50, 100, 350, and 400 nm). At other thicknesses, there are still homogeneous and closed films identified on PLA, but they show stress phenomena as bulges etc. (150–250, 450, and 500 nm), that are subsequently released as cracks and complete layer failure at 300 and 1000 nm.

3.2. Surface wettability

The wettability of the present a-C:H surface depends on three factors: the resulting surface topography [27–29], surface chemical bonds [30–33] and different carbon hybridization states at the surface resp. their ratio [10,34,35]. For example, surface hydration reinforces the hydrophobic character. The saturation of free bonds by hydrogen forms strong C—H bonds, which inhibit the interaction between the top layer and a liquid (here: water) [30–32]. If an oxygenated surface is present, the O-groups lead to a higher water susceptibility [33]. An sp^3-rich surface has a reduced contact angle compared to sp^2-rich a-C:H layers, because of different carbon hybridization states [10,34,35]. Layers enriched in sp^3 have a strong covalent character resulting in a very high free surface energy compared to sp^2-rich layers as the later show a low polarity of their free bonds [10,11]. An increase of polarity leads to smaller contact angles and higher hydrophilicity [36].

The contact angles for PLA samples coated with different a-C:H thicknesses are presented in Fig. 2. With increasing layer thickness, the contact angle increases until it reaches a maximum at 200 nm. This indicates a continuous change in the sp^2/sp^3 ratio, which consequently leads to a change in free surface energy for the reason of different chemical structures resp. bonds on the surface as discussed before. For thin a-C:H layers until 200 nm an increasing hydrophobic behavior was found. At 250 nm the curve progress turns and the contact angle drops by more than 10°. In the further course the value seems to remain unchanged at around 72° until 350 nm before jumping again to a value of more than 86° at 400 nm. Here a second collapse occurs and values start to fluctuate, which can be attributed to the changing topography of the layer (cf. Fig. 1). Subsequently, the contact angles of the measured samples show large error bars (also for 200 nm), which is not surprising due to the cord buckling effects and finally broken surface of the a:C-H layer. As there is no longer a uniform surface and a statistical distribution of cracks, the contact angle measurements scatter a lot giving a large range of error bars. Therefore, the contact angles for these depositions are just presented for completeness.

3.3. DRIFT spectra

In order to determine differences in the chemical environment of raw and O_2 plasma treated PLA, DRIFT analysis was performed. Additionally, DRIFT measurements for all a-C:H thicknesses deposited on PLA were carried out to identify the specific C compositions. For the subsequently a-C:H coated samples, the O_2 plasma pretreated PLA was used as basic substrate and served as the reference spectra since the films were deposited on such pretreated material. DRIFT spectra are evaluated on the basics of infrared spectroscopy [21] and according to previous results of other groups and own observations [14,18,37–39]. Firstly a full overview (450–4100 cm^{-1}) for all samples was performed to check for main differences between the coated samples. For detailed analysis measurements in the interesting region, the C—H stretching area at 2800–3050 cm^{-1} was performed. In this area peaks for $=CH_2$ and $-CH_3$ are located [14,21,37,38].

In Fig. 3 the O_2 plasma treated PLA samples in respect to a raw PLA is shown. Compared to the raw polymer material the sp^2 CH olefinic vibrations from contaminations and small polymer fragments on the samples surfaces vanished (3027 respectively 3000 cm^{-1} [40]) after O_2 treatment resulting in a minimum at these positions. A strong absorbance peak at 2920 cm^{-1} which is assigned to the antisymmetric sp^3

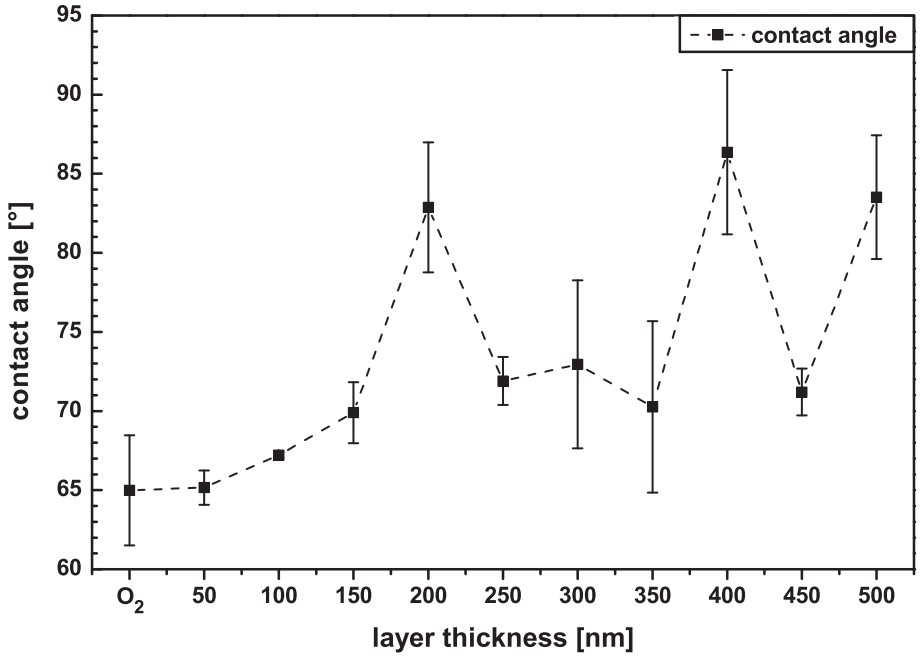

Fig. 2. Contact angle results for a:C-H coatings on PLA with increasing thickness. The coatings were applied to samples previously treated with an O_2 plasma. The dashed line only indicates a trend of the values.

CH_2 group indicates a successful uncovering of the polymer backbone. As a result the O_2 plasma activated sample surface contains a chemically different surface environment compared to the raw PLA.

In Fig. 3 a clear change from the raw PLA to the O_2 plasma treated one is visible. The raw PLA sample shows a peak at 2875 cm^{-1} which correlates with the sp^3 CH_3 binding. The hydrogen of the $-CH_3$ groups is attracted by the surface located oxygen groups creating free C dangling bonds on the emerging bare PLA surface. This peak disappears after the oxygen plasma treatment. Associated with the enhanced peak behavior at wavenumber 2920 cm^{-1} this confirms the loss of C bonded hydrogen due to O_2 plasma treatment resulting in a higher amount of sp^2 CH_2 bindings compared with the raw polymer.

Fig. 4 shows the DRIFT spectra in the range 2800–3050 cm^{-1} for stretching of vibrational modes of the a-C:H layers. From 50 to 100 nm a peak at about 3012 cm^{-1} appears related to the = CH_2 antisymmetric (a) vibration [14,37,38]. With a thicker coating, here starting with 150 nm, this peak moves to 3007 cm^{-1}. This backwards shift indicates a smaller carbon-hydrogen binding energy and therefore a larger carbon-hydrogen bond distance for the = CH_2 group. This behavior has already been demonstrated for such a-C:H coatings on PET [39] and POM [18]. The peaks at 2850 cm^{-1} and 2920 cm^{-1} belong to the symmetric (s) and antisymmetric (a) vibration of the sp^3 CH_2 group, respectively [14,37,38]. These signals mitigate with increasing a-C:H layer thickness and disappear completely until 150 nm. In contrast, a peak at 2950 cm^{-1} appears more pronounced and intensifies with higher depositions, which corresponds to the sp^2 = CH_2 symmetric (s) vibration [14,37,38].

With the ongoing coating process and the increase of a-C:H

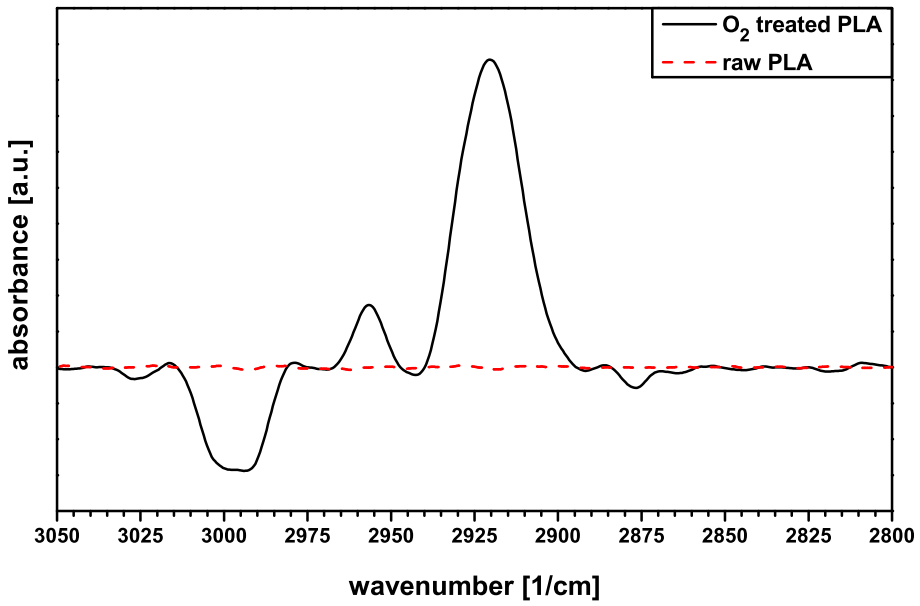

Fig. 3. Comparison of an O_2 treated PLA sample (solid line) to a raw PLA polymer background (dotted line).

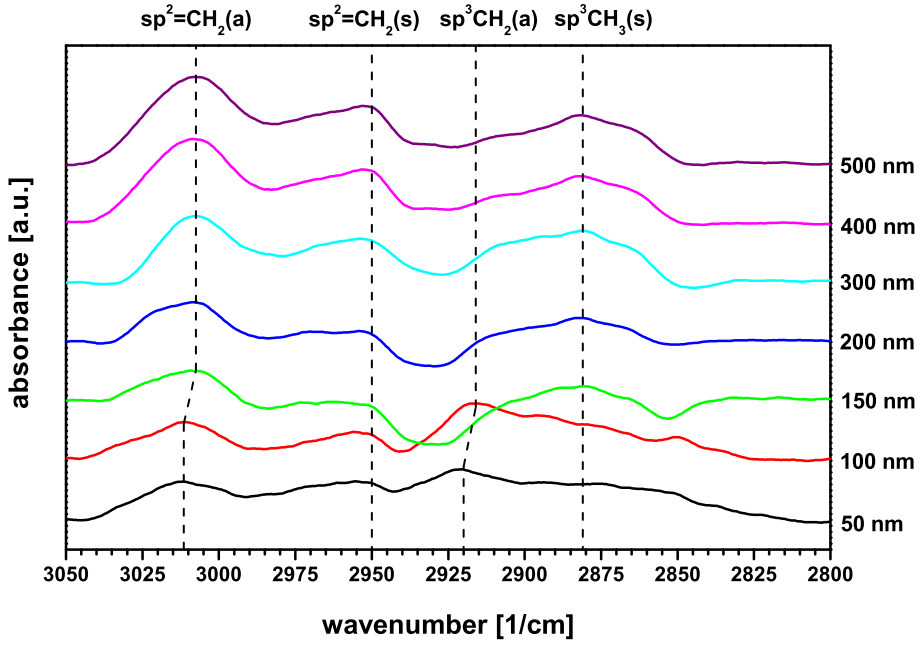

Fig. 4. DIRFT spectra of the analyzed PLA samples coated with a:C-H. The series is presented with increasing layer thickness and given in arbitrary units (a.u.). Layer intervals of 50 resp. 100 nm were chosen depending on changing effects in the spectra.

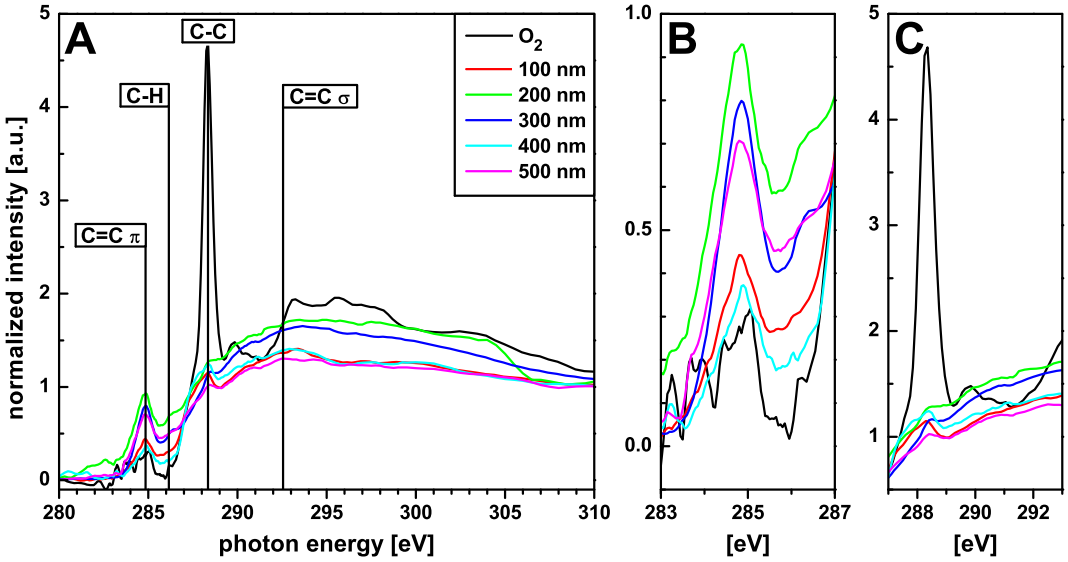

Fig. 5. A shows the full NEXAFS spectra of selected a:C-H coatings on the biopolymer PLA including the O_2 plasma treated PLA as reference. Figures **B** and **C** show detailed photon energy intervals for carbon relevant peaks: **B** 283.00 to 287.00 eV for the C═C π peak (284.85 eV) and the C−H peak (286.15 eV); **C** 287.00 to 293.00 eV for the C−C and C═C σ (288.15 eV and 292.58 eV).

thickness, several changes of the chemical composition take place in the layer. For a 50 nm layer thickness, peaks at 3012 cm^{-1} (sp^2 = CH_2 (a)) and 2920 cm^{-1} (sp^3 CH_2 (a)) are visible. The formation of new and shifting CH_2 groups is a strong indication for an interlayer formation [18,39]. The interlayer formation can be explained by three dominant subplantation processes [41]. First of all a non-specific etching of the entire surface area due to the several plasma species, second the insertion of C and H^+-ions into the sample, and last the adsorption of plasma radical species to form new bonds on the surface. According to the latest results of Catena et al. for comparable polymer substrates the interlayer formation process ends up at a layer thickness of around 50 nm [18,39]. In order to clarify the interlayer behavior for current PLA in detail, further investigations of the layer thickness between 0 and 50 nm in smaller intervals are necessary. As soon as = CH_2 bonds appear, the interlayer formation is more or less completed [39]. The CH_2 groups reveal a polymer-like a-C:H surface configuration while the formation of = CH_2 indicates sp^2 formations according to the cluster model [11]. Therefore it is concluded that the interlayer phase for present PLA is less than 50 nm of a-C:H deposition.

With further increase of a-C:H thickness, these signals become stronger. Additionally a peak at 2880 cm^{-1} shows up which is related to the sp^3 CH_3 (s) group. Here a little energy shift of 5 cm^{-1} has to be noted compared to the O_2 treated sample in Fig. 3. The presence of sp^3 bonded carbon indicates the formation of chain end-groups suggesting that some chains stop growing at this point within the a-C:H framework. With a thickness of 150 nm the sp^3 linked vibrational modes at 2850 cm^{-1} and 2920 cm^{-1} disappear in favor of a more sp^2 bonded a-C:H structure. A peak at 2950 cm^{-1} corresponding to sp^2 CH_2 (s)

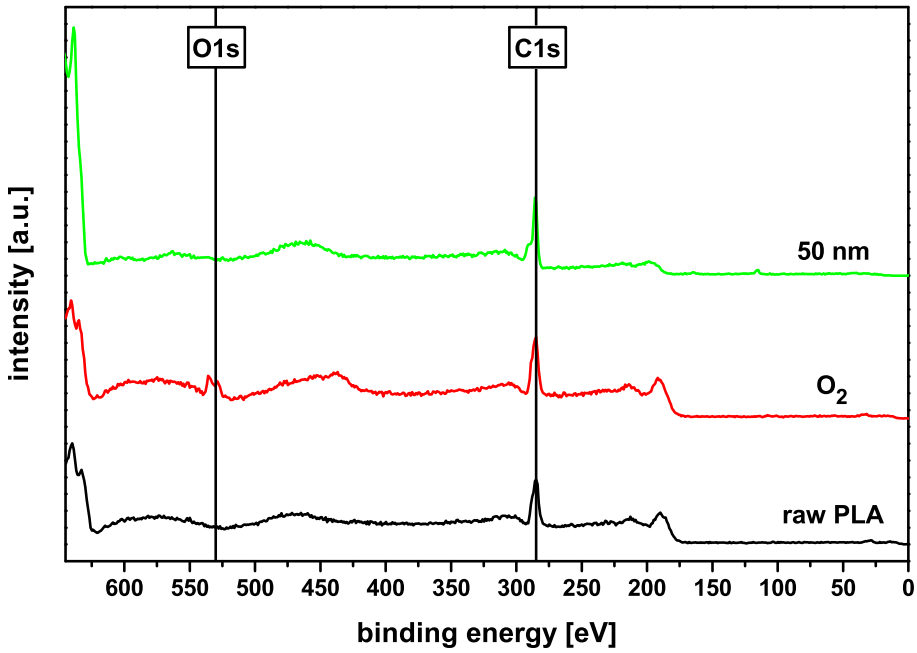

Fig. 6. XPS surveys for PLA: raw, O_2 treated and coated with an a:C-H layer exemplary for 50 nm. Differences for the O1s (around 532 eV) and the C1s (284.80 eV) are clearly visible.

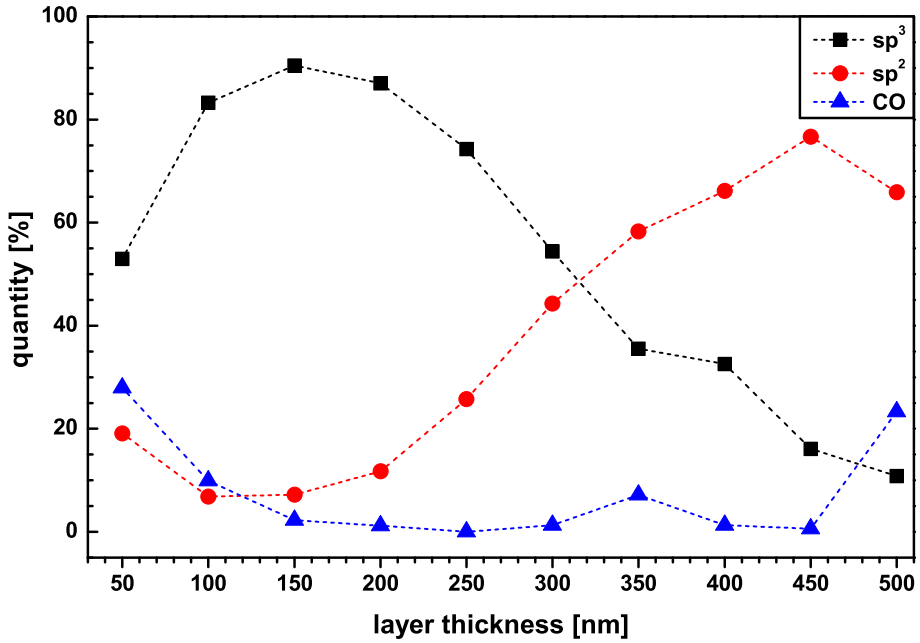

Fig. 7. Quantification of XPS spectra for PLA samples coated with a:C-H layers of various thickness. Circles present the specific amount of the sp^2 content, squares the sp^3 content and triangles the C—O content (dotted lines are just for better readability).

vibrational modes shows up. Additionally, until 500 nm the sp^2 linked vibrational modes at 2950 cm^{-1} and 3007 cm^{-1} intensify. The small sp^3 related peak at 2880 cm^{-1} also becomes slightly stronger with increasing film thickness. Overall, this shows that a more polymer-like structure of the a-C:H film is achieved. Starting with a layer thickness of 150 nm, the number of sp^3 bonds decreases in favor of sp^2 bonds. Additionally the increasing contact angles (Fig. 2) confirm this behavior.

3.4. NEXAFS spectra

The NEXAFS spectra of the O_2 plasma treated PLA together with various a-C:H layers on PLA (100, 200, 300, 400 and 500 nm) are shown in Fig. 5. The raw data of the recorded spectra are evaluated as described previously in section 2.5. The peak positions have been determined to C=C π (284.85 eV), C—H (286.15 eV), C—C (288.35 eV) and C=C σ (292.55 eV) [42–46]. If the PLA sample is treated with oxygen, the C—C peak at 288.35 becomes more pronounced in the NEXAFS examinations. The dominant bond after C-plasma treatment resulting from NEXAFS studies is the C=C π binding at an energy of 284.85 eV. All spectra are normalized to this value of the C=C π binding state. Therefore, the ratio of all other peaks is analyzed according to this C=C π signal. The ration of the C=C σ at 292.55 eV to the C=C π binding stays nearly constant. Exceptions can be found at a thickness of 100 nm and at 400/450 nm. Compared with the SEM

results (Fig. 1), the cord buckling effects occur immediately after these thicknesses, therefore the ratio of C═C σ/C═C π is assumed to indicate the beginning of the delamination of the carbon layer. At the same values the ratio of the C−C (288.35 eV) to C═C π increases significantly. The ratio of C−H (286.15 eV) to C═C π is nearly constant over the whole variation of a-C:H layer thickness.

The NEXAFS measurements support the results detected by CA and DRIFT. At 100 nm a-C:H the spectrum (Fig. 5) shows a strong sp^3 related signal at 288.35 eV and a comparatively small signal at 284.85 eV for the sp^2 binding (C═C π). With increasing thickness the sp^2 signal becomes stronger and a second sp^2 signal corresponding to the C═C σ bond occurs at 292.55 eV indicating a more polymer-like structure consisting mainly of sp^2 carbon double bonds. Only at 400 nm a strong sp^3 related peak at 288.35 eV is visible again. However, this behavior could not be confirmed by the previous DRIFT or following XPS measurements. Reasons for that may be the different penetration depth of the current methods as well as a non-homogeneous surface (cord buckling, peeling start etc.).

3.5. X-ray photoelectron spectroscopy

Fig. 6 shows the results of the XPS measurements for a raw PLA sample, one treated with the O_2 plasma and exemplary one with a a-C:H coating, here 50 nm. The data analysis was carried out as described in the experimental section. The peak positions have been determined through NIST database and the work of other groups [47–49]. The treatment with an O_2 plasma (red) increases the O1s peak at a binding energy of around 532 eV compared to the untreated sample (black). The shape of the C1s peak (284.80 eV) for both measurements indicates a strong C−O binding leading to an asymmetry on the left side of the peak (superposition of peaks). In accordance with DRIFT results the XPS spectra clearly show a change in the PLA polymer due to O_2 plasma treatment (cf. Fig. 3). The pre-activated O1s bonds react with the impinging species from the acetylene plasma to form the a:C-H coating and therefore disappear as demonstrated for the 50 nm thick layer (green). Also at this thickness a change for the C1s peak compared to the raw and O_2 plasma treated sample is detectable. As the signal for the C−O binding decreases, the peaks clearly separate. The profile of the C1s signal becomes sharper and individual peaks can be evaluated.

Carbon coatings of varying thicknesses on PLA samples compared to the amount of binding states are presented in Fig. 7. Therefore, the percentage shares of the sp^2, sp^3 and C−O binding of the C1s signal are plotted over the a-C:H layer thickness. For the first 300 nm of a-C:H layer thickness, the sp^3 binding rises and is clearly dominant. At a thickness of 150 nm nearly 90% of all C-bindings of the coated surface belong to sp^3. A sp^3-rich layer for thicknesses below 150 nm also correlates with the DRIFT data as presented in Fig. 4. Afterwards the sp^3 content decreases with increasing layer thickness until the sp^2 binding becomes dominant after 300 nm. This change of the dominant bond is accompanied by a breaking of the layer (cf. Fig. 1e). With a continuing rise of the layer thickness, the sp^2 content increases until it reaches its maximum at 450 nm and decreases later to 500 nm. The content of the C−O binding stays nearly the same over all analyzed layer thicknesses except for 50–100 nm showing a continuous decrease from a value nearly 30% to below 5% with increasing thickness and at 500 nm where it sharply steps up to more than 20%. One exception is the thickness of 350 nm, where the amount of the C−O binding increases slightly. This can also be seen with a slightly decreased CA (Fig. 2). The XPS data are clearly confirmed by the results of DRIFT and NEXAFS measurements. In the beginning sp^3 is the dominant bond and can be detected as such in all three detection methods, the signals decrease or mitigate with increasing layer thickness and let the sp^2 signal become the dominant signal in the further course.

4. Conclusions

The biopolymer PLA was coated with a:C-H layers in different thicknesses using an RF-PECVD acetylene plasma. The samples were analyzed with SEM, contact angle measurements, DRIFT spectroscopy, NEXAFS and XPS. The SEM images show a stable a:C-H layer on the investigated PLA samples, provided that thickness of the layer does not exceed 300 nm. A shift of the dominant binding from sp^3 to sp^2 indicates a pending stress relief in the layer resulting in cracking and an imminent layer failure. This was also demonstrated by the highly fluctuating contact angles. Not only the DRIFT investigations, but also both the NEXAFS and the XPS measurements revealed a changing chemical composition of the layer with increasing thickness. The sp^2 content rises as the layer thickens, also supported by the contact angles. The DRIFT investigations also showed a shift for the $=CH_2$ group, because of changing binding distances. This in turn underlines the changing chemical environment in the a-C:H layers. DRIFT measurements also indicated if there is an interlayer formation between the PLA polymer and a deposited a:C-H layer, it is already completed within the first 50 nm of layer thickness.

In summary, the deposition of a stable a:C-H layer on the biopolymer PLA is possible until a thickness of 300 nm and for the region of 350 nm to at least 450 nm. Before stress release occurs by forming cord buckling and later via cracks until complete delamination towards 1000 nm. A comprehensive analysis of the chemical environment in the present a-C:H layers was carried out and underlines the significant changing character of the layer with increasing layer thickness. Apart from small anomalies (e.g. the 400 nm in NEXAFS), the results for all methods are consistent and inline for the growth of the a-C:H layer described in this paper for PLA.

The bonding ratios of the carbon atoms depend not only on the plasma parameters selected, but also, as demonstrated here, on the layer thickness achieved. In concrete terms this means that the layer obtained can also be fabricated for a customized application via monitoring the layer thickness. This is possible because there is a change between the sp^3- or sp^2-bound, dominant carbon species in the present a-C:H coating process on PLA, which can be detected with various methods. Since this also causes a change in the properties of the applied layer, these can be controlled accordingly in this way.

Acknowledgements

The authors thank Dr. Heinz Busch (NTTF Coatings GmbH, Rheinbreitbach, Germany) for the industrial coating of the samples and Prof. Dr. Joachim Scholz (University of Koblenz-Landau, department of chemistry) for the DRIFT equipment. The authors also want to thank Dr. Alexei Nefedov from KIT (Karlsruhe Institute for Technology, Group: Chemistry of oxidic and organic interfaces; X-ray and Electron Spectroscopy at Interfaces) for beamtime support. We thank HZB for the allocation of synchrotron radiation beamtime. TS, LB and CF thankfully acknowledge the financial support by the Helmholtz-Zentrum Berlin (HZB), Germany.

References

[1] A.L. Andrady, M.A. Neal, Applications and societal benefits of plastics, Philos. Trans. R. Soc. B 364 (2009) 1977–1984, https://doi.org/10.1098/rstb.2008.0304.
[2] L. Sabbatini, Polymer Surface Characterization, De Gruyter, Berlin, Boston, 2014.
[3] P.G. Ryan, A brief history of marine litter research, in: M. Bergmann, L. Gutow, M. Klages (Eds.), Marine Anthropogenic Litter, Springer International Publishing, Cham, 2015, pp. 1–25.
[4] L.-T. Lim, R. Auras, M. Rubino, Processing technologies for poly(lactic acid), Prog. Polym. Sci. 33 (2008) 820–852, https://doi.org/10.1016/j.progpolymsci.2008.05.004.
[5] A. Grill, Plasma-deposited diamondlike carbon and related materials, IBM J. Res. Dev. 43 (1999) 147–162, https://doi.org/10.1147/rd.431.0147.
[6] M. Rohrbeck, S. Körsten, C.B. Fischer, S. Wehner, B. Kessler, Diamond-like carbon coating of a pure bioplastic foil, Thin Solid Films 545 (2013) 558–563, https://doi.org/10.1016/j.tsf.2013.07.028.

[7] M. Rohrbeck, C.B. Fischer, S. Wehner, J. Meier, W. Manz, DLC-coated pure bioplastic foil, Vak. Forsch. Prax. 26 (2014) 42–47, https://doi.org/10.1002/vipr.201400549.

[8] P. Couderc, Y. Catherine, Structure and physical properties of plasma-grown amorphous hydrogenated carbon films, Thin Solid Films 146 (1987) 93–107, https://doi.org/10.1016/0040-6090(87)90343-9.

[9] E. Mohagheghpour, M. Rajabi, R. Gholamipour, M.M. Larijani, S. Sheibani, Ion beam energy dependence of surface and structural properties of amorphous carbon films deposited by IBSD method on Ni–Cu alloy, J. Mater. Res. 32 (2017) 1258–1266, https://doi.org/10.1557/jmr.2017.43.

[10] R. Paul, S.N. Das, S. Dalui, R.N. Gayen, R.K. Roy, R. Bhar, A.K. Pal, Synthesis of DLC films with different sp^2/sp^3 ratios and their hydrophobic behavior, J. Phys. D. Appl. Phys. 41 (2008) 55309, , https://doi.org/10.1088/0022-3727/41/5/055309.

[11] J. Robertson, Diamond-like amorphous carbon, Mater. Sci. Eng. R 37 (2002) 129–281, https://doi.org/10.1016/S0927-796X(02)00005-0.

[12] S.-C. Lee, F.-C. Tai, C.-H. Wei, Correlation between sp^2/sp^3 ratio or hydrogen content and water contact angle in hydrogenated DLC film, Mater. Trans. 48 (2007) 2534–2538, https://doi.org/10.2320/matertrans.MER2007044.

[13] J. Robertson, Plasma deposition of diamond-like carbon, Jpn. J. Appl. Phys. 50 (2011) 01AF01, , https://doi.org/10.1143/JJAP.50.01AF01.

[14] P. Koidl, C. Wild, B. Dischler, J. Wagner, M. Ramsteiner, Plasma deposition, properties and structure of amorphous hydrogenated carbon films, Mater. Sci. Forum 52-53 (1990) 41–70, https://doi.org/10.4028/www.scientific.net/MSF.52-53.41.

[15] C.B. Fischer, M. Rohrbeck, S. Wehner, M. Richter, D. Schmeißer, Interlayer formation of diamond-like carbon coatings on industrial polyethylene: thickness dependent surface characterization by SEM, AFM and NEXAFS, Appl. Surf. Sci. 271 (2013) 381–389, https://doi.org/10.1016/j.apsusc.2013.01.210.

[16] A. Catena, S. Agnello, L.M. Rösken, H. Bergen, E. Recktenwald, F. Bernsmann, H. Busch, M. Cannas, F.M. Gelardi, B. Hahn, S. Wehner, C.B. Fischer, Characteristics of industrially manufactured amorphous hydrogenated carbon (a-C: H) depositions on high-density polyethylene, Carbon 96 (2016) 661–671, https://doi.org/10.1016/j.carbon.2015.09.101.

[17] A. Catena, T. McJunkin, S. Agnello, F.M. Gelardi, S. Wehner, C.B. Fischer, Surface morphology and grain analysis of successively industrially grown amorphous hydrogenated carbon films (a-C: H) on silicon, Appl. Surf. Sci. 347 (2015) 657–667, https://doi.org/10.1016/j.apsusc.2015.04.113.

[18] A. Catena, M.R. Kunze, S. Agnello, F.M. Gelardi, S. Wehner, C.B. Fischer, Amorphous hydrogenated carbon (a-C:H) depositions on polyoxymethylene: substrate influence on the characteristics of the developing coatings, Surf. Coat. Technol. 307 (2016) 658–665, https://doi.org/10.1016/j.surfcoat.2016.09.064.

[19] L. D'Souza, P. Devi, T. Kamat, C.G. Naik, Diffuse reflectance infrared Fourier transform spectroscopic (DRIFTS) investigation of E. coli, Staphylococcus aureus and Candida albicans, Indian J. Mar. Sci. 38 (2009) 45–51.

[20] T. Armaroli, T. Bécue, S. Gautier, Diffuse reflection infrared spectroscopy (drifts): application to the in situ analysis of catalysts, Oil Gas Sci. Technol. 59 (2004) 215–237, https://doi.org/10.2516/ogst:2004016.

[21] H. Günzler, H.-U. Gremlich, IR Spectroscopy: An Introduction, Wiley-VCH, Weinheim, 2002.

[22] A. Nefedov, C. Wöll, Advanced applications of NEXAFS spectroscopy for functionalized surfaces, in: G. Bracco, B. Holst (Eds.), Surface Science Techniques, Springer, Berlin, Heidelberg, 2013, pp. 277–303.

[23] B. Watts, L. Thomsen, P.C. Dastoor, Methods in carbon K-edge NEXAFS: experiment and analysis, J. Chem. Phys. 140 (2014) 105–120, https://doi.org/10.1016/j.elspec.2005.11.006.

[24] H. Mei, R. Huang, J.Y. Chung, C.M. Stafford, H.-H. Yu, Buckling modes of elastic thin films on elastic substrates, Appl. Phys. Lett. 90 (2007) 151902, , https://doi.org/10.1063/1.2720759.

[25] A.A. Volinsky, Experiments with in-situ thin film telephone cord buckling delamination propagation, Mater. Res. Soc. Symp. Proc. 749 (2002) 72, https://doi.org/10.1557/PROC-749-W10.7.

[26] C.A. Davis, A simple model for the formation of compressive stress in thin films by ion bombardment, Thin Solid Films 226 (1993) 30–34, https://doi.org/10.1016/0040-6090(93)90201-Y.

[27] W. Barthlott, C. Neinhuis, Purity of the sacred lotus, or escape from contamination in biological surfaces, Planta 202 (1997) 1–8, https://doi.org/10.1007/s004250050096.

[28] L. Feng, S. Li, Y. Li, H. Li, L. Zhang, J. Zhai, Y. Song, B. Liu, L. Jiang, D. Zhu, Superhydrophobic surfaces: from natural to artificial, Adv. Mater. 14 (2002) 1857–1860, https://doi.org/10.1002/adma.200290020.

[29] D. Banerjee, S. Mukherjee, K.K. Chattopadhyay, Controlling the surface topology and hence the hydrophobicity of amorphous carbon thin films, Carbon 48 (2010) 1025–1031, https://doi.org/10.1016/j.carbon.2009.11.021.

[30] L. Ostrovskaya, V. Perevertailo, V. Ralchenko, A. Dementjev, O. Loginova, Wettability and surface energy of oxidized and hydrogen plasma-treated diamond films, Diam. Relat. Mater. 11 (2002) 845–850, https://doi.org/10.1016/S0925-9635(01)00636-7.

[31] L.Y. Ostrovskaya, Studies of diamond and diamond-like film surfaces using XAES, AFM and wetting, Vacuum 68 (2002) 219–238, https://doi.org/10.1016/S0042-207X(02)00460-8.

[32] F. Piazza, G. Morell, Wettability of hydrogenated tetrahedral amorphous carbon, Diam. Relat. Mater. 18 (2009) 43–50, https://doi.org/10.1016/j.diamond.2008.09.023.

[33] B.K. Tay, D. Sheeja, S.P. Lau, J.X. Guo, Study of surface energy of tetrahedral amorphous carbon films modified in various gas plasma, Diam. Relat. Mater. 12 (2003) 2072–2076, https://doi.org/10.1016/S0925-9635(03)00192-4.

[34] Y. Zhou, B. Wang, X. Song, E. Li, G. Li, S. Zhao, H. Yan, Control over the wettability of amorphous carbon films in a large range from hydrophilicity to super-hydrophobicity, Appl. Surf. Sci. 253 (2006) 2690–2694, https://doi.org/10.1016/j.apsusc.2006.05.118.

[35] T. Werder, J.H. Walther, R.L. Jaffe, T. Halicioglu, P. Koumoutsakos, On the water−carbon interaction for use in molecular dynamics simulations of graphite and carbon nanotubes, J. Phys. Chem. B 107 (2003) 1345–1352, https://doi.org/10.1021/jp0268112.

[36] A. Bismarck, W. Brostow, R. Chiu, H.E. Hagg Lobland, K.K.C. Ho, Effects of surface plasma treatment on tribology of thermoplastic polymers, Polym. Eng. Sci. 48 (2008) 1971–1976, https://doi.org/10.1002/pen.21103.

[37] E. Tomasella, L. Thomas, M. Dubois, C. Meunier, Structural and mechanical properties of a-C:H thin films grown by RF-PECVD, Diam. Relat. Mater. 13 (2004) 1618–1624, https://doi.org/10.1016/j.diamond.2004.01.017.

[38] M. Veres, M. Koós, I. Pócsik, IR study of the formation process of polymeric hydrogenated amorphous carbon film, Diam. Relat. Mater. 11 (2002) 1110–1114, https://doi.org/10.1016/S0925-9635(02)00011-0.

[39] A. Catena, Q. Guo, M.R. Kunze, S. Agnello, F.M. Gelardi, S. Wehner, C.B. Fischer, Morphological and chemical evolution of gradually deposited diamond-like carbon films on polyethylene terephthalate: from subplantation processes to structural reorganization by intrinsic stress release phenomena, ACS Appl. Mater. Interfaces 8 (2016) 10636–10646, https://doi.org/10.1021/acsami.6b02113.

[40] C.N.R. Rao, Chemical Applications of Infrared Spectroscopy, Academic Press, New York-London, 1963.

[41] E. Neyts, A. Bogaerts, M.C.M. van de Sanden, Reaction mechanism and thin a-C:H film growth from low energy hydrocarbon radicals, J. Phys. Conf. Ser. 86 (2007) 12020, , https://doi.org/10.1088/1742-6596/86/1/012020.

[42] B. Brüster, C. Amozoqueño, P. Grysan, I. Peral, B. Watts, J.-M. Raquez, P. Dubois, F. Addiego, Resolving inclusion structure and deformation mechanisms in polylactide plasticized by reactive extrusion, Macromol. Mater. Eng. 302 (2017) 1700326, , https://doi.org/10.1002/mame.201700326.

[43] J. Stöhr, NEXAFS Spectroscopy, Springer Series in Surface Sciences, vol. 25, Springer, Berlin, Heidelberg, 1992.

[44] J. Díaz, S. Anders, X. Zhou, E.J. Moler, S.A. Kellar, Z. Hussain, Analysis of the π* and σ* bands of the x-ray absorption spectrum of amorphous carbon, Phys. Rev. B 64 (2001) 125204, , https://doi.org/10.1103/PhysRevB.64.125204.

[45] J. Diaz, O.R. Monteiro, Z. Hussain, Structure of amorphous carbon from near-edge and extended x-ray absorption spectroscopy, Phys. Rev. B 76 (2007) 094201, , https://doi.org/10.1103/PhysRevB.76.094201.

[46] O. Dhez, H. Ade, S. Urquhart, Calibrated NEXAFS spectra of some common polymers, J. Electron Spectrosc. Relat. Phenom. 128 (2003) 85–96, https://doi.org/10.1016/S0368-2048(02)00237-2.

[47] J.L. Solomon, R.J. Madix, J. Stöhr, Orientation and absolute coverage of benzene, aniline, and phenol on Ag(110) determined by NEXAFS and XPS, Surf. Sci. 255 (1991) 12–30, https://doi.org/10.1016/0039-6028(91)90008-G.

[48] F.C. Tai, S.C. Lee, C.H. Wei, S.L. Tyan, Correlation between I_D/I_G ratio from visible Raman spectra and sp^2/sp^3 ratio from XPS spectra of annealed hydrogenated DLC film, Mater. Trans. 47 (2006) 1847–1852, https://doi.org/10.2320/matertrans.47.1847.

[49] P.M. Dietrich, T. Horlacher, P.-L. Girard-Lauriault, T. Gross, A. Lippitz, H. Min, T. Wirth, R. Castelli, P.H. Seeberger, W.E.S. Unger, Adlayers of dimannoside thiols on gold: surface chemical analysis, Langmuir 27 (2011) 4808–4815, https://doi.org/10.1021/la104038q.

C Journal of Carbon Research

MDPI

Article

Changing Contents of Carbon Hybridizations in Amorphous Hydrogenated Carbon Layers (a-C:H) on Sustainable Polyhydroxybutyrate (PHB) Exhibit a Significant Deterioration in Stability, Depending on Thickness

Torben Schlebrowski [1], Lucas Beucher [1], Hadi Bazzi [2], Barbara Hahn [2], Stefan Wehner [1] and Christian B. Fischer [1,3,*,†]

[1] Department of Physics, University Koblenz-Landau, 56070 Koblenz, Germany
[2] Department of Material Analysis, RheinAhrCampus, University of Applied Sciences Koblenz, 53424 Remagen, Germany
[3] Materials Science and Nano-Engineering Department, Mohammed VI Polytechnic University, Ben Guerir 43150, Morocco
* Correspondence: chrbfischer@uni-koblenz.de; Tel.: +49-261-287-2345
† Dedicated to Professor Stefan Wehner on the occasion of his 50th birthday.

Received: 2 August 2019; Accepted: 26 August 2019; Published: 30 August 2019

Abstract: PHB is a biodegradable polymer based on renewable raw materials that could replace synthetic polymers in many applications. A big advantage is the resulting reduction of the waste problem, as well as the conservation of fossil resources. To arrange it for various applications, the surface is arranged by plasma-enhanced chemical vapor deposition (PECVD) with amorphous hydrogenated carbon layers (a-C:H). Here, on a 50 µm thick PHB-foil, a-C:H layers of different thicknesses (0–500 nm) were deposited in 50 nm steps. Surface topography was investigated by scanning electron microscopy (SEM), chemical composition by diffuse reflectance infrared Fourier transform (DRIFT) spectroscopy and wettability checked by contact angle. In addition, layers were examined by synchrotron supported X-ray photoelectron spectroscopy (XPS) and near edge X-ray absorption fine structure (NEXAFS), which revealed thickness dependent changes of the sp^2/sp^3 ratio. With increasing thickness, even the topography changes show internal, stress-induced phenomena. The results obtained provide a more detailed understanding of the predominantly inorganic a-C:H coatings on (bio)polymers via in situ growth.

Keywords: acetylene plasma; incremental a-C:H deposition; synchrotron based surface techniques; sp^2/sp^3 content evaluation; chemical environment survey; stress release phenomena

1. Introduction

A common feature of most polymers used in everyday life today is that they are based on crude oil. This inevitably causes a poor environmental impact, as these polymers are usually not (bio)degradable within a reasonable time. Due to the already high demand for plastics, which will increase rather than decrease, this will lead to a major disposal and raw material problem [1]. However, an adequate exchange of material is often not possible or appropriate, since polymers have some particularly advantageous properties: Formability, elasticity, low weight, wide working temperature range, chemical resistance and comparatively low cost [2,3]. Nevertheless, it needs to be mentioned that polymers cannot be used for every application, due to their poor mechanical properties, such as low hardness or insufficient resistance to surface abrasion [3]. This can be compensated by the deposition

of protective coatings, such as amorphous hydrogenated carbon (a-C:H) layers. Additionally, the material can be specifically functionalized for particular applications [4–11]. As a result, the range of applications of many polymers can be greatly expanded. Conversely, this leads to a further increase in use and drives the disposal and raw material problems further forward [1]. One possible approach to solving the raw material situation is to change from classic crude oil-based polymers to those that can be obtained from renewable raw materials. If these are also biodegradable, the problem of disposal could also be solved. A promising candidate for this is polyhydroxybutyrate (PHB), which can be obtained from renewable resources by fermentation processes and is biodegradable [12]. Although this also shares the poor properties of polymers, it can be modified and adapted for special applications by depositing an a-C:H layer [5].

Those a-C:H films are mostly applied by chemical vapor deposition (CVD). The layer deposition can be further enhanced by the use of RF plasma (radio frequency plasma-enhanced chemical vapor deposition; RF-PECVD) [4,13–16], which can also be used for non-conductive materials at low temperatures [5,13]. The layers consist of hydrogen and sp^2 (σ and π), as well as sp^3 hybridized interconnected carbons, where the sp^2 clusters are limited to short chains embedded in an sp^3 matrix of carbon and hydrogen [4,17,18]. The ratio of the carbon hybridizations, binding states and the hydrogen content can be controlled via the plasma parameter settings which determine the physical properties of the resulting layer [4,17,18]. If the deposited layer has a very high portion of sp^3 bonds, it is similar to diamond and has a high hardness [13]. In contrast, a large amount of sp^2 bonds leads to a more flexible, graphite-like layer with, e.g., electrical conductivity [13]. In addition, an influence of the existing bonding situation on the wettability of the surfaces is recognizable, which leads to a variation in contact angles [19].

The a-C:H coatings investigated in this study were applied to the biopolymer PHB by RF-PECVD using only acetylene plasma as the source for C and H. The surface morphology of the layers was inspected ex situ by scanning electron microscopy (SEM); the chemical composition of the obtained coatings by diffuse reflectance infrared Fourier transform (DRIFT) spectroscopy and synchrotron-based X-ray techniques (near edge X-ray absorption fine structure (NEXAFS) and X-ray photoelectron spectroscopy (XPS)). In addition, contact angle measurements were performed to investigate surface wettability.

2. Materials and Methods

2.1. Sample Preparation and Film Deposition

The PHB foils were purchased at industrial quality from Goodfellow (Bad Nauheim, Germany) with the dimensions 30 cm × 30 cm. After delivery, the 50 µm thick foils were cut to 10 cm × 10 cm samples and mounted on self-made aluminum holders specially manufactured for the coating process. PECVD was chosen for the plasma treatment in a high-vacuum chamber. As plasma source, a RF-controlled (13.65 MHz) Copra DN 400 (Copra DN 400, CCR GmbH, Troisdorf, Germany) was used. The coating process is described in detail elsewhere [5,20,21], but here only briefly: Sample holders were placed 275 mm in front of the plasma source. This direct alignment results in so-called r-type diamond-like carbon (DLC) coatings [20–23]. An initial oxygen plasma (10 min, 200 W, 1 Pa, 65 sccm/min) cleaned and activated the PHB surface for further coating. With subsequent exposure to acetylene plasma (107 W, 0.65 Pa, 65 sccm/min, deposition rate ca. 10 nm·min^{-1}), layer thicknesses of 0–500 nm in 50 nm steps were realized. Layer thicknesses above 500 nm were not feasible because the resulting layers were not stable, began to crack and then peeled off as the process progressed. This can be seen in the SEM section herein, as well as in previous work from our group [5]. In addition to the PHB samples, silicon wafers with partial cover by aluminum foil were placed on the holders to check the layer thicknesses obtained. The resulting layer edge could then be measured with a profilometer (Dektak 3, Veeco Instruments Inc., Plainview, NY, USA).

2.2. Analytical Techniques

The surface morphologies of the plasma treated PHB samples were examined with a scanning electron microscope (SEM515, Phillips, 7 kV, WD 20 mm). Since SEM investigations of polymers in particular are affected by charging effects caused by the electron beam, the samples were covered with a 7–10 nm thick conductive gold layer. In order to prove the accuracy of the investigations, measurements were carried out at least at three different points on each sample.

The surface wettability of the a-C:H layers was analyzed by a contact angle goniometer (OCA 15 plus, DataPhysics Instruments GmbH, Filderstadt, Germany). For this purpose, 1 µL drops of distilled water were applied to the samples in ambient conditions using the sessile drop technique. The resulting contact angles were measured and averaged at five different points of the entire sample to the left and right of each drop. This proves the homogeneity of the coating, ensures the accuracy of the values obtained and results in a representative value.

In order to obtain information about the chemical composition of the carbon atoms present in the a-C:H layers, infrared spectroscopic investigations were carried out. Due to the thin layers, DRIFT spectroscopy was chosen using a Shimadzu Fourier transform spectrometer (IRPrestige-21, Kyoto, Japan) equipped with the diffuse reflectance measuring apparatus DRS-8000 [24]. Measurements were performed at room temperature, under atmospheric pressure. Data was collected in two steps: First, a scan was performed over the entire spectral width (here 450–4000 cm^{-1}) with a resolution of 4 wavenumbers. This was repeated 100 times and spectra were averaged to compensate statistical noise. This was necessary to evaluate graduations in which regions of the applied a-C:H layers showed changes, depending on the layer thickness. The second step was a detailed measurement of the so-called C-H stretching zone in the range of 2800–3100 cm^{-1} containing vibrations of the different C-bonds [15,25]. Here a resolution of one wavenumber was chosen and the measurements were repeated 300 times and averaged. Step two was repeated at three different points on the sample to prove homogeneity of the sample and to ensure accuracy. For both steps the O_2 plasma treated PHB sample was used as reference, as each of the coated samples was first treated with an O_2 plasma. The subsequent evaluation of the spectra was performed with the commercial IR Solution—FTIR Control Software (software version 1.30, Shimadzu Corporation, Kyoto, Japan): First, a multipoint baseline fit of the spectra, followed by a subsequent smoothing was done (note: this only changes the appearance but not the information or peak positions).

For a detailed analysis of the chemical environment, NEXAFS in combination with XPS was performed. The measurements were accomplished at the beamline HE-SGM at the synchrotron source BESSY II in Berlin during the low-alpha phase. The detection system is described in detail elsewhere [26]. An additionally installed flood-gun is used to compensate charging effects caused by the radiation that can influence the measurements.

NEXAFS-spectra were recorded for the C- and the O-edge. The C-edge was repeated at a second point to control homogeneity of the layer and to ensure correctness of the results. Subsequently, the spectra obtained were normalized with the commercial Origin software and adapted to the decreasing ring current of the low alpha phase. The background noise was also compensated and a contamination correction of the grid with a previously measured gold edge was performed. The individual steps are reported in detail by Watts et al. [27]. After spectrum smoothing all spectra were analyzed by a self-written peak evaluation program and obtained results were plotted with Origin software.

XPS was applied for supporting analysis and for quantitative determination of different sp-bonding states. First, a survey spectrum over the full width of 0–700 eV was recorded for an overview of the elemental surface composition. For a more detailed analysis, both the O1s and the C1s peaks were recorded. The C1s peak was measured twice at different points to ensure homogeneity of the sample and measurement accuracy. The total C1s peak was analyzed with the commercial software CasaXPS to provide the proportions of sp^2, sp^3 and C–O bonds. Using Origin software, the results were presented according to the layer thickness.

3. Results and Discussion

3.1. SEM Image Analysis

Figure 1 shows representative SEM images for the different thicknesses of a-C:H layers on oxygen treated PHB samples. All images with increasing thickness starting with the O_2 plasma treated one in Figure 1a display a sample section of 200 µm × 200 µm, except for the 500 nm deposition in Figure 1k (it is a 100 µm × 100 µm detail).

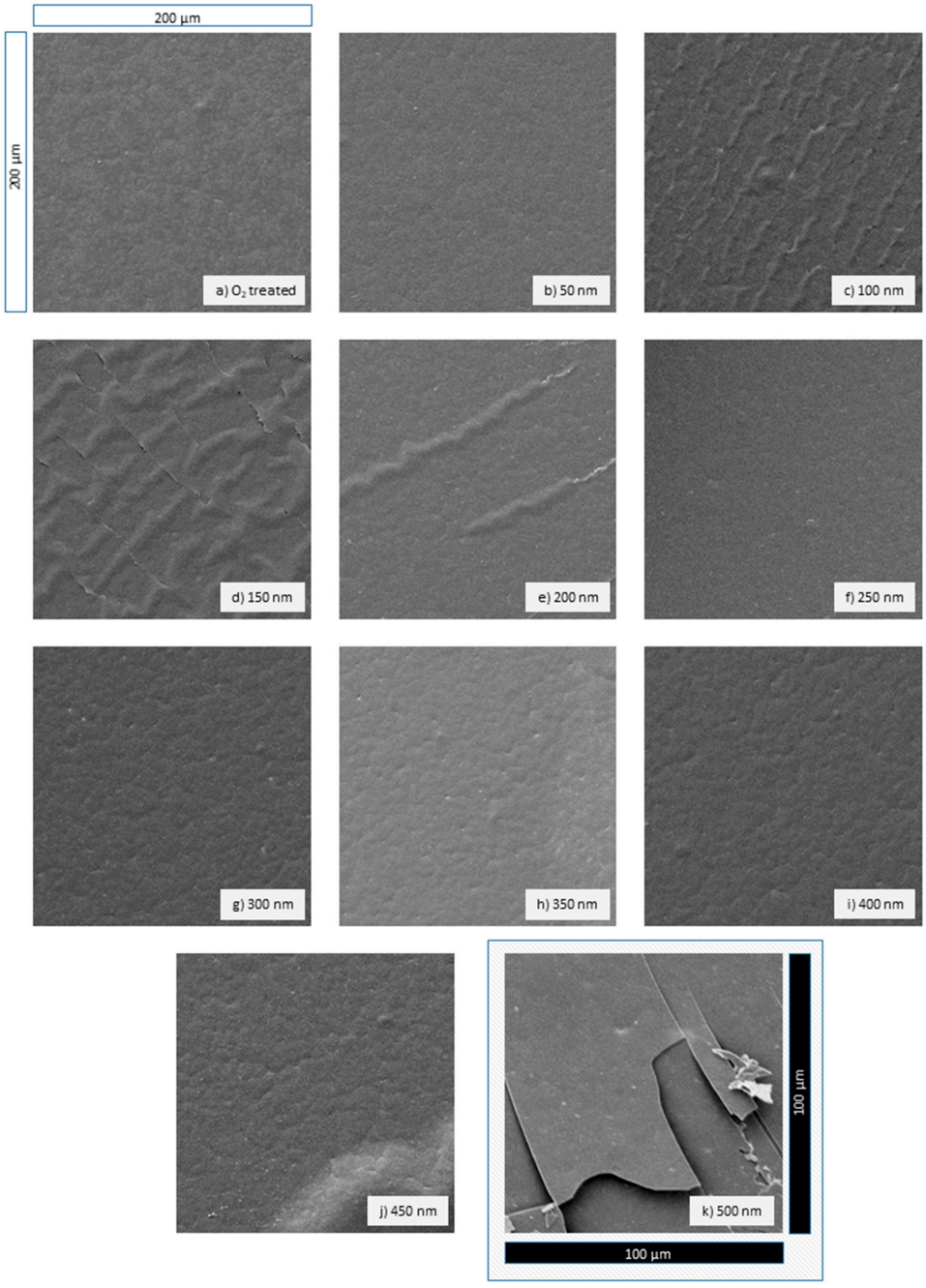

Figure 1. SEM images of PHB treated with O_2 plasma (**a**) and coated with different thicknesses of a-C:H layers. The series (**b**–**k**) shows the changing topography of a-C:H coating increasing in 50 nm steps.

Figure 1a shows PHB pretreated with O_2 plasma. The surface appears roughened by the plasma treatment and dirt is removed. The SEM analysis revealed layer thicknesses of stable and unstable a-C:H coatings on PHB. In the case of thin films (50 nm, Figure 1b), a homogeneous, stable a-C:H film is formed. The previously observable roughness for the O_2 plasma treated one (Figure 1a) decreases noticeably. With increasing layer thickness, the a-C:H film starts to delaminate and breaks open (100–200 nm, Figure 1c–e). First the carbon layer is still closed, but with strong visible crimps and ripples. This effect is called "telephone cord buckling" (and can be seen clearly in Figure 1d), indicating stress release phenomena [28,29]. At 200 nm (Figure 1e) the stress-related fractures in the carbon layer continue to increase. Afterwards a closed, homogeneous a-C:H layer is repeatedly formed on the PHB (250–400 nm, Figure 1f–i). Repeatedly, an emerging delamination is observable at a layer thickness of 450 nm (Figure 1j). With a layer thickness of 500 nm (Figure 1k), the deposited carbon film begins to tear open again and delaminate from the polymer.

The cracking and delamination of layers at 100–200 nm and 450–500 nm can be explained by internal stress. Reasons for this stress-related release are, e.g., different expansion coefficients of both materials (a-C:H layer and PHB substrate), as well as island formations of the a-C:H and their interaction with each other in the early growth stage [30]. The carbon layer on the material is stable until the stress exceeds a critical value and begins thereafter to delaminate. At first, the network can still hold the compound material together, but if the stress increases, the deposited layer begins to tear (Figure 1c–e,j,k).

3.2. *Surface Wettability by Contact Angles*

The surface wettability and the resulting contact angle depend in general, especially for the present a-C:H coatings, on several factors: The morphology of the surface [31–33], the existing chemical bonds [34–37] and different hybridization states of carbon on the surface [19,38,39]. The saturation of free bonds on the sample surface with hydrogen leads to the formation of strong C–H bonds which in turn inhibit a possible interaction between the sample surface and the applied liquid, herein water [34,36,37]. Consequently, hydrogenation of the surface leads to a more hydrophobic behavior. On the other hand, if the surface is oxidized or contains oxygen groups, it is more attractive for water [35]. Likewise, different carbon hybridization states lead to a change in the contact angle behavior at the sample surface [19,38,39]. An sp^3-rich surface has a reduced contact angle compared to a more sp^2-rich a-C:H layer, because of the different free surface energy. The low polarity of its free bonds for sp^2 hybridized carbon has a smaller surface energy compared to the covalent character of the sp^3 bonded carbon [13,19,40].

Figure 2 shows the contact angles obtained for the series of a-C:H layers of different thicknesses deposited on PHB. Additionally, the O_2 plasma cleaned PHB sample is shown which was used as a reference. The contact angle range obtained is between 65° and 80°. At 50 nm a-C:H, the lowest value of 66.5° is found, indicating a more sp^3 like hybridization of the carbon atoms. Furthermore, it shows a reduced content of oxygen-groups compared to the O_2 plasma activated sample. With increasing layer thickness, the contact angle increases until it reaches a maximum of 79.7° at 150 nm. Since the overall deposition process compared to the 50 nm sample has not been changed except for a longer coating time to get thicker layers, the hybridization states have to change with increasing layer thickness; the proportion of sp^2-hybridized carbon atoms increases. The contact angle measures also indicate surface roughening because of increasing error bars. At a layer thickness of 200 nm, the contact angle drops rapidly down to 72.1°, accompanied by a large error. Here, the a-C:H layer was broken up, presumably due to stress within the layer (see also Figure 1e, SEM section). As the a-C:H thickness increases to 250 nm the contact angle value decreases slightly. At a carbon thickness of 300 nm the value rises up again to 79.3°. Further along, the contact angles decrease again and remain nearly constant with a slight decrease of the higher layers.

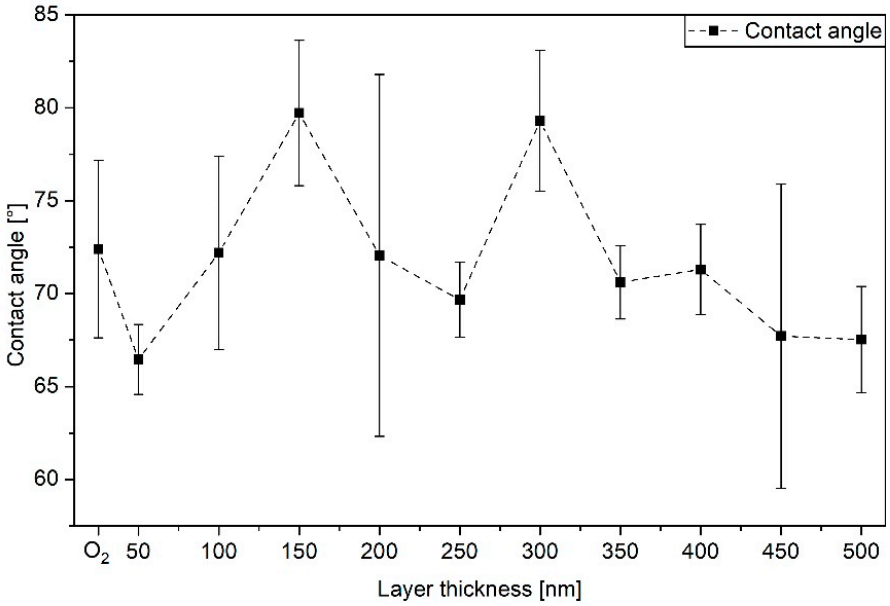

Figure 2. Contact angles of amorphous hydrogenated carbon (a-C:H) coatings of various thickness on previously O_2 plasma treated PHB samples (see first point). The dashed line is included to enhance visibility.

As lower contact angles indicate lower absolute sp^2 contents; both the 150 and 300 nm depositions exhibit comparatively high values that deviate clearly from the behavior of the surrounding samples. These high contact angles are either due to a very high sp^2 content, a strong hydrogenation of the surface or a change in the morphology. However, there is no evidence of such an increased proportion of sp^2-hybridized carbon atoms in these layers in the following analytical techniques, so that morphological effects (starting the partially visible delamination of the carbon layer) are concluded here, which are supported by the large errors. Cracks in the layer are also responsible for fluctuating contact angles, at a thickness of 200 and at a thickness of 450 nm each. Since there is no longer a uniform surface, the contact angle measurements here are very error-prone, which is also indicated by the large error bars. It is noticeable that at the beginning of the coating and the "new coating" after the instable thickness at 150 nm is accompanied by an increase in the contact angle, which suggests a larger but somehow delayed sp^2 content in the new, emerging layer.

3.3. DRIFT Spectroscopy

DRIFT spectroscopy was performed to examine the chemical composition and binding states of the PHB samples increasingly coated with a-C:H layers. First, the O_2 plasma treated sample was compared with the crude PHB to investigate the chemical activation of the samples by the oxygen plasma pretreatment. Subsequently, detailed DRIFT measurements were performed for all a-C:H coated samples to investigate layer thickness dependent differences in the chemical composition of the a-C:H layers. For the coated samples, O_2 plasma treated PHB was used as reference, since all carbon films were deposited on such pretreated PHB material. Figure 3 presents the corresponding spectra in ascending order plotted to arbitrary units (a.u.). The analysis of the DRIFT spectra was carried out on the basis of our own previous results, the work of other groups and known fundamental data [15,23,25,41–43]. In the range of 450 to 4100 cm^{-1} all samples were checked for chemical differences in the carbon coating first, before detailed analysis in the C–H stretching area between 2750–3150 cm^{-1} for the CH_2 and CH_3 groups followed [15,25,42,43].

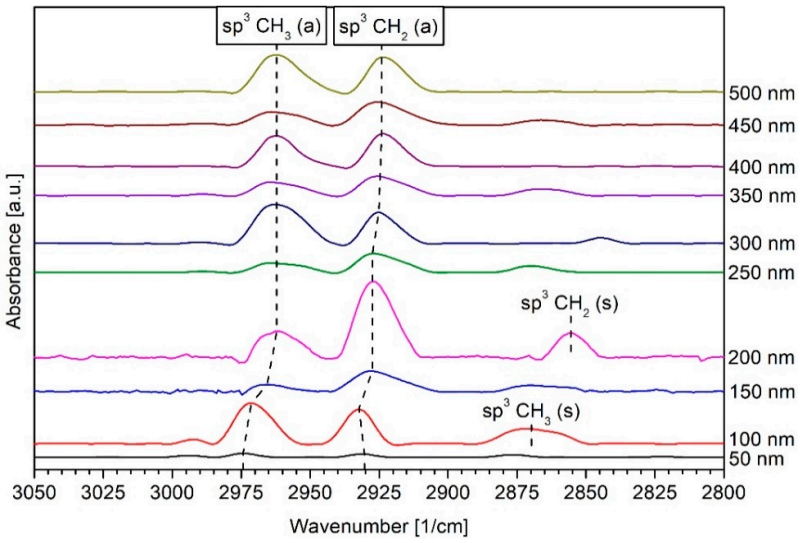

Figure 3. DIRFT spectra of the analyzed a-C:H layers with increasing thickness on PHB samples—substrate (indicated by changing colors with number labelling right next to it). The symmetrical (s) oscillations are only indicated for layer thicknesses with more pronounced intensity.

The formation of CH_2 groups at relatively small a-C:H depositions are an established proof for an interlayer formation between the polymeric substrate and the carbon coating [41]. So-called subplantation processes are a reasonable explanation for this behavior, which consists of three main reactions: (i) Surface etching with plasma species, (ii) insertion of C and H+ ions into the (sub)surface and (iii) surface absorption of plasma radicals to form new bonds. The interlayer formation stops at a layer thickness of around 50 nm and is considered complete as soon as the formation of $=CH_2$ bonds takes place [23,41]. Therefore, a possible interlayer phase for the present PHB is less than 50 nm. The CH_2 groups reveal a more polymer-like DLC surface configuration, while the formation of $=CH_2$ would indicate the sp^2 carbon bonds in line to the cluster model [13]. For a detailed examination of the process, further investigations with layer thicknesses between 0 and 50 nm are necessary, but are not in the focus of this study.

The strong sp^3 vibrations detected in the DRIFT spectra are also confirmed by XPS measurements (see later section). At 50 nm a-C:H, the sp^3 bond is the dominant one. When measuring samples with a layer thickness of 100 nm, these peaks are more pronounced. In addition, the dominant sp^3 CH_3 asymmetric (a) peak at 2971 cm^{-1} widens towards 2950 cm^{-1} on its right flank. This can be explained by an overlay with the sp^2 CH_2 symmetric (s) peak that is located at around 2950 cm^{-1} [42], which begins to form. Unfortunately, the two peaks could not be resolved separately, but the appearance of the sp^2 vibration is in accordance with the XPS results (see later section). Additionally, a broad peak at 2870 cm^{-1} associated to the sp^3 CH_3 (s) binding is visible [43]. At 150 nm a-C:H deposition, the formerly dominant sp^3 CH_3 (a) peak shifts to 2965 cm^{-1} and almost disappears. The sp^3 CH_3 (s) peak at 2870 cm^{-1} disappears nearly completely. The sp^3 CH_2 (a) peak at a wavenumber of 2932 cm^{-1} shifts to a value of 2927 cm^{-1} and dominates the spectrum. This shift-back of the frequency indicates a smaller carbon-hydrogen binding energy, and therefore a higher carbon-hydrogen binding distance for the CH_3 and CH_2 group [25].

With an a-C:H layer thickness of 200 nm, the sp^3 CH_3 (a) peak is again more pronounced. On the other hand, a peak appears at 2855 cm^{-1}, assigned to the sp^3 CH_2 (s) binding [42,44–46]. The sp^3 CH_2 (a) peak at 2927 cm^{-1} rises stronger and becomes the dominant one in the spectra. With 250 nm the spectrum changes again and is similar to the previous one for 150 nm. The sp^3 CH_2 (s) peak disappears and the sp^3 CH_3 (a) one decreases again. Additionally, the sp^3 CH_3 (s) peak at 2870 cm^{-1} appears again. The peak dominance is reversed by increasing the layer thickness to 300 nm a-C:H. The right flank,

which has formed due to the superposition with the sp^2 CH_2 (s) peak, is now falling more strongly, which is due to the fact that the sp^2 oscillation becomes weaker. At a layer thickness of 350 nm the spectrum is similar to 150 nm and 250 nm. With 400 nm of layer thickness, only two peaks are visible. Both the sp^3 CH_3 (a) peak at 2962 cm^{-1}, still overlaid with the sp^2 CH_2 (s) at 2950 cm^{-1} but nearly gone, and the sp^3 CH_2 (a) at 2924 cm^{-1}, are almost balanced. The spectrum for the 450 nm deposition is similar again to the ones of 150, 250 and 350 nm. The 500 nm spectrum corresponds to the spectrum for 400 nm layer thickness.

The similarities in the DRIFT spectra for 50, 150 and 250 nm depositions indicate that with a layer thickness larger than 250 nm a new layer growth of the carbon coating begins after an earlier layer failure. Additionally, the similarities between the 200 and 300 nm layer thickness and for 150, 250 and 350 nm and their respective changes in the chemical environment suggest a layer thickness region that changes repeatedly in its chemistry between bonding networks.

3.4. NEXAFS Results

In Figure 4 the NEXAFS spectra for raw PHB and an O_2 plasma treated one are shown. The spectra were processed as described in the experimental details. Both spectra do not differ significantly, except for a slightly higher intensity in the sample treated with O_2 and small variations in the fingerprint region. The fact that O_2 plasma—at least with respect to carbon bonds—has no changing properties, means it only serves herein to clean the sample surface of impurities. Based on the chemical structure of PHB, the dominant peak is the C–C bond.

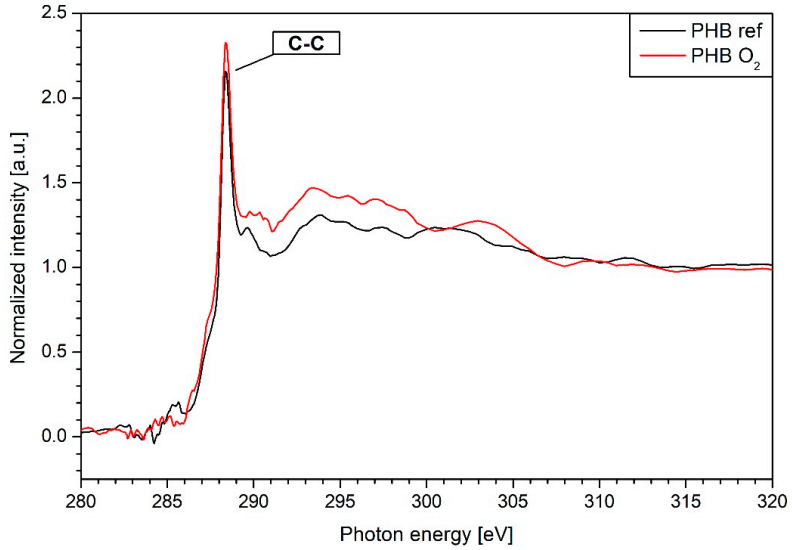

Figure 4. Near edge X-ray absorption fine structure (NEXAFS) spectra of a raw and untreated PHB (black) compared to an O_2 plasma treated one (red), which is used as the new reference for further analysis.

The obtained NEXAFS spectra for the series of a-C:H layers with various thickness (here: 100, 200, 300, 400 and 500 nm) are displayed in Figure 5. The peak positions have been determined to C=C π (284.85 eV), C002DH (286.15 eV), C–C (288.35 eV) and C=C σ (292.55 eV) [47–51]. The dominant binding resulting from NEXAFS studies is the C=C π binding at an energy of ~284.8 eV. For further analysis, all peaks for different binding states are normalized to the C=C π peak and its ratio to the other peaks is analyzed. The ratio of C=C σ to C=C π bonds remains almost constant at all time. There is a deviation from this factor at a layer thickness of 100 nm. Here, both the value of the ratio of C–C to C=C π and of C=C σ to C=C π make a jump, which can be attributed to a decrease in the proportion of

C=C π. The ratio is here nearly 1:1 each. The ratio of the C–H to C=C π is almost constant over the entire variation of the a-C:H layer thickness.

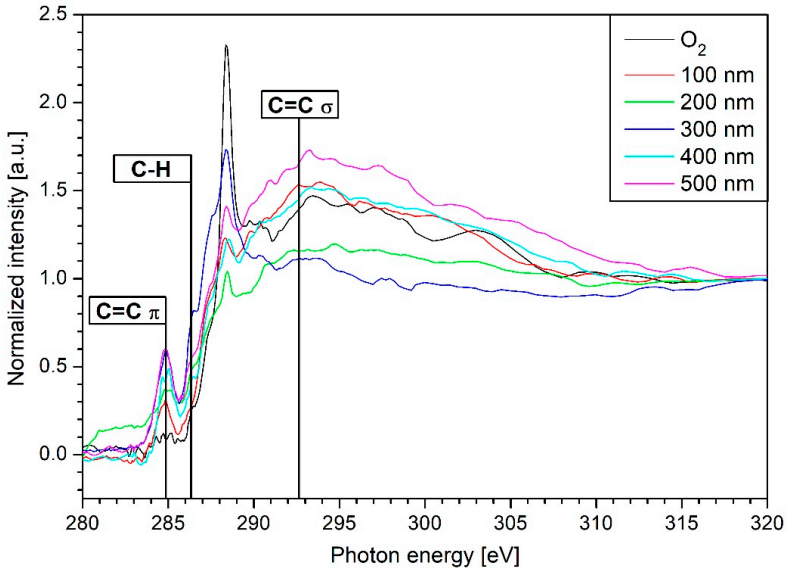

Figure 5. NEXAFS spectra of selected a-C:H layer thicknesses on PHB. Black is the reference sample, red a coating of 100 nm, green 200 nm, dark blue 300 nm, pale blue 400 nm and magenta 500 nm.

From a layer thickness of more than 400 nm, a further deviation of the ratio occurs. From here the C=C π bond increases steadily and the ratios of the three other bonds in relation to the C=C π decrease further. Therefore, with a layer thickness of 100 nm, the sp^2 bond is the dominant one. This continues even at 200 nm. With a layer thickness of 300 nm the sp^3 peak begins to dominate. At 400 nm, the sp^2 value determined during NEXAFS measurements increases again and the sp^3 content decreases. At 500 nm, the values measured for sp^2 are again the dominant ones.

The dominant sp^2 bond between 100 and 200 nm corresponds to the "cord buckling" visible in the SEM images. As the dominance of the sp^2 bonds increases from 100 to 200 nm, the deterioration of the a-C:H layers intensifies according to the SEM images. With the change from the sp^2 bond to the now stronger sp^3 bond, that effect disappears, and the layer seems homogeneous again. After repeated decrease of the dominance of the sp^3 bond and an increasing sp^2 content between 400 and 500 nm again, "cord buckling" and layer failure occurs. The NEXAFS data therefore indicates a layer failure or layer defect if the sp^3 bond loses its dominant position in favor of the sp^2 bond. The results found here are in line with the following XPS results.

3.5. XPS Results

Figure 6 shows the results of the XPS measurements for PHB raw, O_2 plasma treated and coated with 50 nm a-C:H. The analysis has been arranged according to the experimental details. The peak positions have been determined through the NIST database and work of other groups [52–54]. Contrary to the expectations, the O_2 plasma treatment on PHB decreases the O1s peak (532 eV) compared to the untreated sample. This may be due to degradation or removal of the carbonyl group in PHB, resulting in a dangling bond, and therefore a free carbon position. The C1s peak (284 eV) also changes and shows a more pronounced and sharper shape after the O_2 plasma treatment. The widening of the C1s peak to higher binding energies indicates additionally, the appearance of C–O binding. Applying the a-C:H layer changes the spectrum again. The O1s bonds are covered with an a-C:H layer and disappeared in the XPS survey. A shape change of the C1s peak compared to the raw and O_2 plasma treated sample is visible.

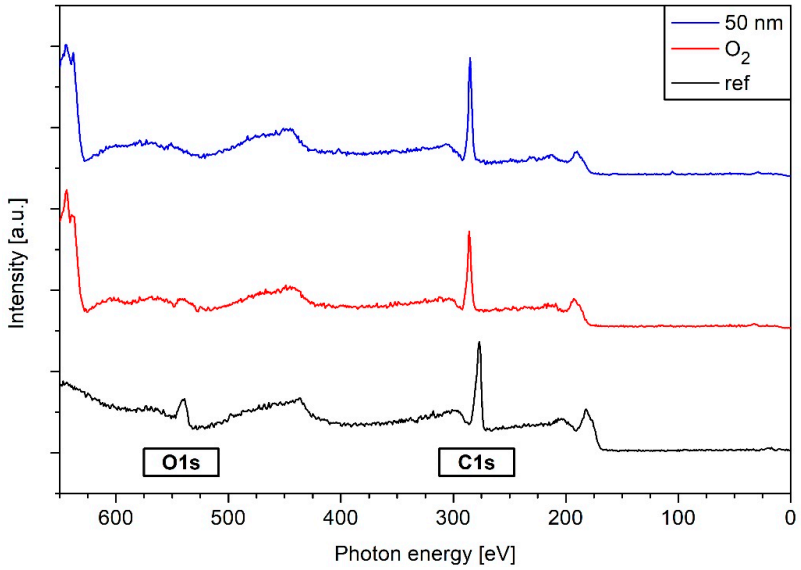

Figure 6. Full X-ray photoelectron spectroscopy (XPS) spectra of raw, O_2 treated and with a 50 nm a-C:H layer coated PHB. The disappearance for the O1s (532 eV) and shape changes in C1s (284 eV) are clearly visible.

Figure 7 shows the evaluated percentages for sp^2 and sp^3 binding of the C1s peak as a function of the increasing layer thickness. In the Supporting Information, the deconvolution of selected C1s peaks together with all obtained values can be found. At 50 nm the sp^3 bond is dominant, which is in accordance with the DRIFT results. With a layer thickness of 100 nm, this dominance changes in favor of the sp^2 bond. This remains the preferred bond type in the network until the layer thickness exceeds 200 nm. Both the DRIFT and the NEXAFS measurements confirmed this behavior of a growing sp^2 content. Thereafter, the situation changes again from the 250 nm a-C:H deposition and the sp^3 binding is repeatedly the favored one. As soon as the layer thickness exceeds 400 nm, there is another switch and the sp^2 bond is the preferred one in the network, which is in line to the findings confirmed by DRIFT and NEXAFS results.

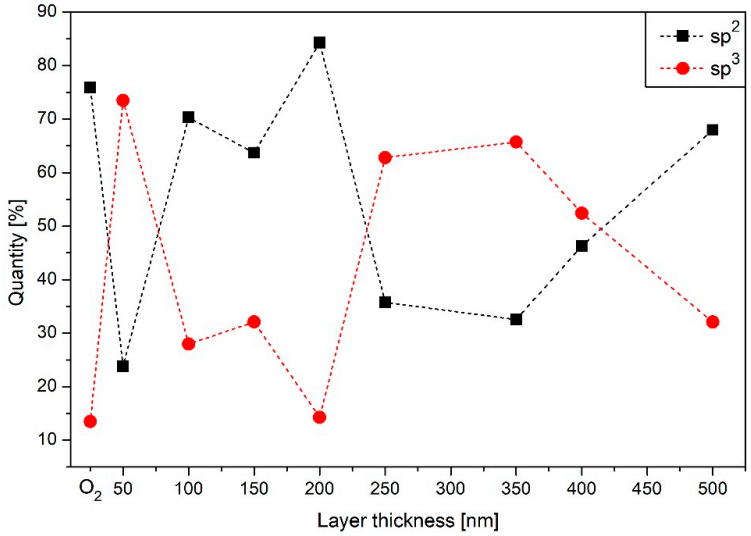

Figure 7. Results for the sp^2 (squares) and sp^3 (circles) from the XPS series for PHB coated with increasingly thick a-C:H layers. The dashed lines are included to enhance visibility.

The 500 nm XPS measurement is in contradiction to the DRIFT measurements. XPS shows a strong sp^2 content while the DRIFT results indicate dominant sp^3 binding. The XPS data is supported by the NEXAFS results which also show dominant sp^2 binding. A reason for the contradictory results of XPS/NEXAFS and DRIFT may be the different penetration depths of the techniques (a few nm compared to 10–20 nm, respectively). In addition, the sample surface is cracked or rather delaminated at 500 nm, which certainly influences the results.

It is noticeable that the change from sp^3 to sp^2 as the dominant bonding is accompanied by a delayed breakup of the layer from 100 to 150 nm (see Section 3.1 SEM Image Analysis). A shift from sp^2 to sp^3 as the dominant binding, in contrast, seems to have no effect on the stability of the applied a-C:H layer on the PHB substrate. This is in accordance with results obtained for a-C:H layers on the biopolymer polylactide acid (PLA) [55], although PLA did not show any delay in layer failure. Furthermore, the comparison of SEM images with XPS shows that a sp^2 dominated a-C:H layer on PHB is accompanied by "cord buckling" phenomena.

4. Conclusions

Layers of different a-C:H thicknesses were deposited on the biopolymer PHB using an acetylene plasma. The samples were analyzed with SEM, contact angle measurements, DRIFT spectroscopy, NEXAFS and XPS. Stable a-C:H layers on the examined PHB samples could be identified by SEM. Exceptions are the layers between 100 and 200 nm and thicknesses higher than 450 nm. This is in line to the highly fluctuating contact angles and their corresponding error bars. Not only the DRIFT investigation, but also both the NEXAFS and the XPS measurements, revealed a changing chemical composition of the layer with increasing thickness. In the beginning the sp^2 content increases as the layer thickens in accordance to the contact angles. In the DRIFT investigations also, a shift for the $=CH_2$ group was found, which indicates a changing binding distance and confirms a changing chemical environment in the presented layers. Furthermore, the DRIFT measurements showed that if there is an interlayer between the polymer and a-C:H layer, it is already completed before or by the 50 nm layer thickness. For a better understanding of the deposition process of a-C:H layers on PHB, this interlayer formation and its thickness needs to be analyzed, which is currently under investigation.

The results obtained with the current analytical techniques are largely consistent and present a nearly identical picture of the growth behavior of the a-C:H layers on PHB. Smaller deviations are caused, on the one hand by the different penetration depths of the measurement techniques, and on the other hand, by the stress-induced damaged surface. It has to be emphasized that a shift from sp^3 to sp^2 as the dominant carbon binding leads to a layer failure proven by SEM measurements due to stress release. This also corresponds to recent results for a-C:H layers on the biopolymer film polylactide acid (PLA). But in contrast to PLA, the layer failure for the presented a-C:H on PHB has a delay of roughly 100 nm film thickness, after the change from sp^3 to sp^2 as the dominant binding type. This occurs repeatedly after the turnaround at 100 and 400 nm.

The bonding ratios of the carbon atoms and the chemical environment depend not only on the applied plasma parameters, but also on the resulting a-C:H layer thickness. This means, similarly to recent results in our group for the biopolymer PLA, layers can also be customized for specific applications by checking the layer thickness of a-C:H on the present PHB. In summary, it is possible to deposit stable a-C:H layers with specific properties on the biopolymer PHB for most layer thicknesses up to 450 nm. A thickness dependent change between the sp^3 or sp^2 dominant carbon species in the present a-C:H coating process on PHB has been proven with various methods.

Author Contributions: Both T.S. and C.B.F. conceptualized the study and developed the related methodology. T.S. prepared the samples and performed the data evaluation, visualization and wrote the original draft. T.S. and C.B.F. reviewed and edited the manuscript. L.B. contributed in terms of contact angle acquisition. SEM related analyses were performed by H.B. and B.H. NEXAFS, XPS and DRIFT acquisition and evaluation was conducted by T.S. Both authors S.W. and C.B.F. contributed in terms of funding acquisition, project management, supervision and overall guidance in the study.

Funding: Funding for this work was provided by the German Research Foundation DFG (Deutsche Forschungsgemeinschaft) through the projects WE 4100/23-1 and FI 1802/14-1. T.S. and C.B.F. thankfully acknowledge the financial support by HZB.

Acknowledgments: The authors thank Heinz Busch (NTTF Coatings GmbH, Rheinbreitbach, Germany) for the industrial coating of the samples, and Joachim Scholz and Michael Kunze for the DRIFT equipment. The authors acknowledge the scientific collaborations between the Department of Physics of the University of Koblenz-Landau, and the Department of Chemistry of the University of Koblenz-Landau. The authors also want to thank Alexei Nefedov from KIT (Karlsruhe Institute for Technology, Group: Chemistry of oxidic and organic interfaces; X-ray and Electron Spectroscopy at Interfaces) for beamtime support. We thank the Helmholtz-Zentrum Berlin (HZB) for the allocation of synchrotron radiation.

Conflicts of Interest: The authors declare no conflict of interest.

References

1. Ryan, P.G. Brief History of Marine Litter Research. In *Book Marine Anthropogenic Litter*; Bergmann, M., Gutow, L., Klages, M.A., Eds.; Springer International Publishing: Cham, Germany, 2015; pp. 1–25.
2. Andrady, A.L.; Neal, M.A. Applications and societal benefits of plastics. *Philos. Trans. R. Soc. B Biol. Sci.* **2009**, *364*, 1977–1984. [CrossRef]
3. Sabbatini, L. *Polymer Surface Characterization*; De Gruyter: Berlin, Germany; Boston, MA, USA, 2014; ISBN 978-3110275087.
4. Grill, A. Plasma-deposited diamondlike carbon and related materials. *IBM J. Res. Dev.* **1999**, *43*, 147–162. [CrossRef]
5. Rohrbeck, M.; Körsten, S.; Fischer, C.B.; Wehner, S.; Kessler, B. Diamond-like carbon coating of a pure bioplastic foil. *Thin Solid Film.* **2013**, *545*, 558–563. [CrossRef]
6. Rohrbeck, M.; Fischer, C.; Wehner, S.; Meier, J.; Manz, W. DLC-coated pure bioplastic foil. *Vákuum Forsch. Und Prax.* **2014**, *26*, 42–47. [CrossRef]
7. Schink, C.; Catena, A.; Heintz, K.; Görls, H.; Beresko, C.; Ankerhold, G.; von der Au, M.; Meermann, B.; Van Malderen, S.J.M.; Vanhaecke, F.; et al. Attaching photochemically active ruthenium polypyridyl complex units to amorphous hydrogenated carbon (a-C:H) layers. *Adv. Mater. Interfaces* **2019**, *6*, 1801308. [CrossRef]
8. Bito, K.; Hasebe, T.; Maegawa, S.; Kitagawa, T.; Matsumoto, T.; Suzuki, T.; Hotta, A. Micropatterning of a 2-methacryloyloxyethyl phosphorylcholine polymer surface by hydrogenated amorphous carbon thin films for endothelialization and antithrombogenicity. *Acta Biomater.* **2019**, *87*, 187–196. [CrossRef] [PubMed]
9. Dufils, J.; Faverjon, F.; Héau, C.; Donnet, C.; Benayoun, S.; Valette, S. Evaluation of a variety of a-C:H coatings on PEEK for biomedical implants. *Surf. Coat. Technol.* **2017**, *313*, 96–106. [CrossRef]
10. Ishikawa, T.; Choi, J. The effect of microstructure on the tribological properties of a-C:H films. *Diam. Relat. Mater.* **2018**, *89*, 94–100. [CrossRef]
11. Ray, S.C.; Mukherjee, D.; Sarma, S.; Bhattacharya, G.; Mathur, A.; Roy, S.; McLaughlin, J. Functional diamond like carbon (DLC) coatings on polymer for improved gas barrier performance. *Diam. Relat. Mater.* **2017**, *80*, 59–63. [CrossRef]
12. Ahn, W.S.; Park, S.J.; Lee, S.Y. Production of Poly(3-Hydroxybutyrate) by Fed-Batch Culture of Recombinant Escherichia coli with a Highly Concentrated Whey Solution. *Appl. Environ. Microbiol.* **2000**, *66*, 3624–3627. [CrossRef]
13. Robertson, J. Diamond-like amorphous carbon. *Mater. Sci. Eng. R Rep.* **2002**, *37*, 129–281. [CrossRef]
14. Robertson, J. Plasma Deposition of Diamond-Like Carbon. *Jpn. J. Appl. Phys.* **2011**, *50*, 01AF01-1–01AF01-8. [CrossRef]
15. Koidl, P.; Wild, C.; Dischler, B.; Wagner, J.; Ramsteiner, M. Plasma Deposition, Properties and Structure of Amorphous Hydrogenated Carbon Films. *Mater. Sci. Forum.* **1990**, *52*, 41–70. [CrossRef]
16. Aldeeb, M.A.; Morgan, N.; Abouelsayed, A.; Amin, K.M.; Hassaballa, S.; Hassablla, S. Correlation of acetylene plasma discharge environment and the optical and electronic properties of the hydrogenated amorphous carbon films. *Diam. Relat. Mater.* **2019**, *96*, 74–84. [CrossRef]
17. Grill, A. Diamond-like carbon coatings as biocompatible materials—An overview. *Diam. Relat. Mater.* **2003**, *12*, 166–170. [CrossRef]
18. Couderc, P.; Catherine, Y. Structure and physical properties of plasma-grown amorphous hydrogenated carbon films. *Thin Solid Film.* **1987**, *146*, 93–107. [CrossRef]

19. Paul, R.; Das, S.N.; Dalui, S.; Gayen, R.N.; Roy, R.K.; Bhar, R.; Pal, A.K.; Das, S. Synthesis of DLC films with different sp^2/sp^3 ratios and their hydrophobic behaviour. *J. Phys. D Appl. Phys.* **2008**, *41*, 1–7. [CrossRef]
20. Fischer, C.B.; Rohrbeck, M.; Wehner, S.; Richter, M.; Schmeißer, D. Interlayer formation of diamond-like carbon coatings on industrial polyethylene. *Appl. Surf. Sci.* **2013**, *271*, 381–389. [CrossRef]
21. Catena, A.; McJunkin, T.; Agnello, S.; Gelardi, F.M.; Wehner, S.; Fischer, C.B. Surface morphology and grain analysis of successively industrially grown amorphous hydrogenated carbon films (a-C:H) on silicon. *Appl. Surf. Sci.* **2015**, *347*, 657–667. [CrossRef]
22. Catena, A.; Agnello, S.; Rösken, L.M.; Bergen, H.; Recktenwald, E.; Bernsmann, F.; Busch, H.; Cannas, M.; Gelardi, F.M.; Hahn, B.; et al. Characteristics of industrially manufactured amorphous hydrogenated carbon (a-C:H) depositions on high-density polyethylene. *Carbon* **2016**, *96*, 661–671. [CrossRef]
23. Catena, A.; Kunze, M.R.; Agnello, S.; Gelardi, F.M.; Wehner, S.; Fischer, C.B. Amorphous hydrogenated carbon (a-C:H) depositions on polyoxymethylene: Substrate influence on the characteristics of the developing coatings. *Surf. Coat. Technol.* **2016**, *307*, 658–665. [CrossRef]
24. Armaroli, T.; Bécue, T.; Gautier, S. Diffuse Reflection Infrared Spectroscopy (Drifts). *Oil Gas Sci. Technol.* **2004**, *59*, 215–237. [CrossRef]
25. Günzler, H.; Gremlich, H.U. *IR Spectroscopy: An Introduction*; Wiley-VCH: Weinheim, Germany, 2002.
26. Nefedov, A.; Wöll, C. Advanced Applications of NEXAFS Spectroscopy for Functionalized Surfaces. In *Book Surface Science Techniques*; Bracco, G., Holst, B., Eds.; Springer: Berlin/Heidelberg, Germany, 2013; pp. 277–303.
27. Watts, B.; Thomsen, L.; Dastoor, P.C. Methods in carbon K-edge NEXAFS: Experiment and Analysis. *J. Chem. Phys.* **2014**, *140*, 105–120. [CrossRef]
28. Mei, H.; Huang, R.; Chung, J.Y.; Stafford, C.M.; Yu, H.H. Buckling modes of elastic thin films on elastic substrates. *Appl. Phys. Lett.* **2007**, *90*, 151902. [CrossRef]
29. Volinsky, A.A. Experiments with in-situ thin film telephone cord buckling delamination propagation. *MRS Proc.* **2002**, *749*. [CrossRef]
30. Davis, C.A. A simple model for the formation of compressive stress in thin films by ion bombardment. *Thin Solid Film.* **1993**, *226*, 30–34. [CrossRef]
31. Banerjee, D.; Mukherjee, S.; Chattopadhyay, K. Controlling the surface topology and hence the hydrophobicity of amorphous carbon thin films. *Carbon* **2010**, *48*, 1025–1031. [CrossRef]
32. Feng, L.; Li, S.; Li, Y.; Li, H.; Zhang, L.; Zhai, J.; Song, Y.; Liu, B.; Jiang, L.; Zhu, D. Super-Hydrophobic Surfaces. *Adv. Mater.* **2002**, *14*, 1857–1860. [CrossRef]
33. Barthlott, W.; Neinhuis, C. Purity of the sacred lotus, or escape from contamination in biological surfaces. *Planta* **1997**, *202*, 1–8. [CrossRef]
34. Piazza, F.; Morell, G. Wettability of hydrogenated tetrahedral amorphous carbon. *Diam. Relat. Mater.* **2009**, *18*, 43–50. [CrossRef]
35. Tay, B.K.; Sheeja, D.; Lau, S.P.; Guo, J. Study of surface energy of tetrahedral amorphous carbon films modified in various gas plasma. *Diam. Relat. Mater.* **2003**, *12*, 2072–2076. [CrossRef]
36. Ostrovskaya, L.; Perevertailo, V.; Ralchenko, V.; Dementjev, A.; Loginova, O. Wettability and surface energy of oxidized and hydrogen plasma-treated diamond films. *Diam. Relat. Mater.* **2002**, *11*, 845–850. [CrossRef]
37. Ostrovskaya, L. Studies of diamond and diamond-like film surfaces using XAES, AFM and wetting. *Vacuum* **2002**, *68*, 219–238. [CrossRef]
38. Werder, T.; Walther, J.H.; Jaffe, R.L.; Halicioglu, T.; Koumoutsakos, P. On the Water-Carbon Interaction for Use in Molecular Dynamics Simulations of Graphite and Carbon Nanotubes. *J. Phys. Chem. B* **2003**, *107*, 1345–1352. [CrossRef]
39. Zhou, Y.; Wang, B.; Song, X.; Li, E.; Li, G.; Zhao, S.; Yan, H. Control over the wettability of amorphous carbon films in a large range from hydrophilicity to super-hydrophobicity. *Appl. Surf. Sci.* **2006**, *253*, 2690–2694. [CrossRef]
40. Bismarck, A.; Brostow, W.; Chiu, R.; Lobland, H.E.H.; Ho, K.K. Effects of surface plasma treatment on tribology of thermoplastic polymers. *Polym. Eng. Sci.* **2008**, *48*, 1971–1976. [CrossRef]
41. Catena, A.; Guo, Q.; Kunze, M.R.; Agnello, S.; Gelardi, F.M.; Wehner, S.; Fischer, C.B. Morphological and Chemical Evolution of Gradually Deposited Diamond-Like Carbon Films on Polyethylene Terephthalate: From Subplantation Processes to Structural Reorganization by Intrinsic Stress Release Phenomena. *ACS Appl. Mater. Interfaces* **2016**, *8*, 10636–10646. [CrossRef]

42. Tomasella, E.; Thomas, L.; Dubois, M.; Meunier, C. Structural and mechanical properties of a-C. *Diam. Relat. Mater.* **2004**, *13*, 1618–1624. [CrossRef]
43. Veres, M.; Koos, M.; Pócsik, I. IR study of the formation process of polymeric hydrogenated amorphous carbon film. *Diam. Relat. Mater.* **2002**, *11*, 1110–1114. [CrossRef]
44. Ristein, J.; Stief, R.T.; Ley, L.; Beyer, W. A comparative analysis of a-C:H by infrared spectroscopy and mass selected thermal effusion. *J. Appl. Phys.* **1998**, *84*, 3836–3847. [CrossRef]
45. Flett, M.S.C. *Characteristic Frequencies of Chemical Groups in the Infrared*, 1st ed.; Elsevier Publishing Co.: Amsterdam, The Netherlands; London, UK; New York, NY, USA, 1963.
46. Rao, C.N.R. *Chemical Applications of Infrared Spectroscopy*, 1st ed.; Academic Press: New York, NY, USA; London, UK, 1963.
47. Brüster, B.; Amozoqueño, C.; Grysan, P.; Peral, I.; Watts, B.; Raquez, J.-M.; Dubois, P.; Addiego, F. Resolving Inclusion Structure and Deformation Mechanisms in Polylactide Plasticized by Reactive Extrusion. *Macromol. Mater. Eng.* **2017**, *302*, 1700326. [CrossRef]
48. Stöhr, J. *NEXAFS Spectroscopy*; Springer Series in Surface Sciences 25; Springer: Berlin/Heidelberg, Germany, 1992.
49. Díaz, J.; Anders, S.; Zhou, X.; Moler, E.J.; Kellar, S.A.; Hussain, Z. Analysis of the π^* and σ^* bands of the x-ray absorption spectrum of amorphous carbon. *Phys. Rev. B* **2001**, *64*, 125204. [CrossRef]
50. Diaz, J.; Monteiro, O.R.; Hussain, Z. Structure of amorphous carbon from near-edge and extended x-ray absorption spectroscopy. *Phys. Rev. B* **2007**, *76*, 094201. [CrossRef]
51. Dhez, O.; Ade, H.; Urquhart, S.; Urquhart, S. Calibrated NEXAFS spectra of some common polymers. *J. Electron Spectrosc. Relat. Phenom.* **2003**, *128*, 85–96. [CrossRef]
52. Solomon, J.; Madix, R.; Stôhr, J. Orientation and absolute coverage of benzene, aniline, and phenol on Ag(110) determined by NEXAFS and XPS. *Surf. Sci.* **1991**, *255*, 12–30. [CrossRef]
53. Tai, F.C.; Lee, S.C.; Wei, C.H.; Tyan, S.L. Correlation between ID/G Ratio from Visible Raman Spectra and sp^2/sp^3 Ratio from XPS Spectra of Annealed Hydrogenated DLC Film. *Mater. Trans.* **2006**, *47*, 1847–1852. [CrossRef]
54. Dietrich, P.M.; Horlacher, T.; Girard-Lauriault, P.L.; Gross, T.; Lippitz, A.; Min, H.; Wirth, T.; Castelli, R.; Seeberger, P.H.; Unger, W.E.S. Adlayers of Dimannoside Thiols on Gold: Surface Chemical Analysis. *Langmuir* **2011**, *27*, 4808–4815. [CrossRef]
55. Schlebrowski, T.; Beucher, L.; Bazzi, H.; Hahn, B.; Wehner, S.; Fischer, C. Prediction of a-C:H layer failure on industrial relevant biopolymer polylactide acide (PLA) foils based on the sp^2/sp^3 ratio. *Surf. Coat. Technol.* **2019**, *368*, 79–87. [CrossRef]

materials

MDPI

Article

Refinement of Sustainable Polybutylene Adipate Terephthalate (PBAT) with Amorphous Hydrogenated Carbon Films (a-C:H) Revealing Film Instabilities Influenced by a Thickness-Dependent Change of sp^2/sp^3 Ratio

Torben Schlebrowski [1], Halima Acharchi [2], Barbara Hahn [2], Stefan Wehner [1] and Christian B. Fischer [1,3,*]

[1] Department of Physics, University Koblenz-Landau, 56070 Koblenz, Germany; schlebrowski@uni-koblenz.de (T.S.); wehner@uni-koblenz.de (S.W.), chrbfischer@uni-koblenz.de (C.F.)
[2] Department of Material Analysis, University of Applied Sciences Koblenz—RheinAhr Campus, 53424 Remagen, Germany; halima-87@hotmail.de (H.A.); hahn@hs-koblenz.de (B.H.)
[3] Materials Science, Energy and Nano-engineering Department, Mohammed VI Polytechnic University, Ben Guerir 43150, Morocco
* Correspondence: chrbfischer@uni-koblenz.de; Tel.: +49-261-287-2345

Received: 16 December 2019; Accepted: 25 February 2020; Published: 28 February 2020

Abstract: The increasing use of polymers is related to a growing disposal problem. Switching to biodegradable polymers such as polybutylene adipate terephthalate (PBAT) is a feasible possibility, but after industrial production of commercially available material PBAT is not suitable for every application. Therefore, surface refinements with amorphous hydrogenated carbon films (a-C:H) produced by plasma-assisted chemical vapor deposition (PE-CVD) changing the top layer characteristics are used. Here, 50 µm-thick PBAT films are coated with a-C:H layers up to 500 nm in 50 nm steps. The top surface sp^2/sp^3 bonding ratios are analyzed by X-ray photoelectron spectroscopy (XPS) and near-edge X-ray absorption fine structure (NEXAFS) both synchrotron-based. In addition, measurements using diffuse reflectance infrared Fourier transform spectroscopy (DRIFT) were performed for detailed chemical composition. Surface topography was analyzed by scanning electron microscopy (SEM) and the surface wettability by contact angle measurements. With increasing a-C:H layer thickness not only does the topography change but also the sp^2 to sp^3 ratio, which in combination indicates internal stress-induced phenomena. The results obtained provide a more detailed understanding of the mostly inorganic a-C:H coatings on the biodegradable organic polymer PBAT via in situ growth and stepwise height-dependent analysis.

Keywords: RF-PECVD; acetylene plasma; synchrotron based surface analytical techniques; chemical composition of uppermost layers; stress release phenomena

1. Introduction

Plastics are now being used in many areas of modern life. Specialized areas of applications are the packaging industry, agriculture and even medical technology. This is made possible by their formability, elasticity, low weight and good chemical resistance [1,2]. Limiting factors of the untreated polymers are their low hardness, low abrasion resistance or poor mechanical properties, which considerably restrict their usability [2]. Another intrinsic problem of common polymers is their poor to impossible compostability and the large amount of waste they generate. This clearly has a negative impact on the environment [3]. Possible alternatives are biodegradable polymers like polybutylene adipate terephthalate (PBAT), which is a flexible, fast-degrading material [4].

In order to further adapt this biopolymeric material to certain applications, they are often improved with amorphous hydrogenated carbon (a-C:H) layers [5–7]. The carbon in these layers is π- and σ- hybridized for sp^2 as well as sp^3. The sp^2 clusters are limited to short chains embedded in a sp^3 matrix containing carbon and hydrogen [5,8]. The properties of the resulting layers strongly depend on this sp^2 to sp^3 ratio and hydrogen (H) content. This ratio as well as the H-content can be adjusted by the chosen plasma parameters [5,8–10]. Another possibility is the variation of the layer thickness keeping constant plasma parameters [11,12]. Thus, it is possible to obtain the desired layer properties such as high hardness with high electrical resistance (a sp^3 dominated, diamond-like layer) or a soft, electrically conductive layer (predominantly sp^2 hybridized carbon, graphite-like layer) [13].

The precursor gas for the plasma operation also contributes to the sp^2/sp^3 hybridization ratio of the carbon atoms deposited on the polymer and crosslinked. The change in the hybridization ratio also leads to a chemically different behavior of the resulting layers, which is reflected, for example, in their surface wettability [14]. Thus, the obtained layer can be adapted to the required application by varying the hybridization of the carbon. The most common method for depositing such a-C:H layers is chemical vapor deposition (CVD). This can be additionally supported by the use of high-frequency controlled plasmas (radio frequency plasma-enhanced chemical vapor deposition; RF-PECVD) [5,13,15,16]. The RF-PECVD process has the advantage that it operates at low temperatures and can also coat non-conductive substrates [7,13].

The present study investigates the variation dependence of the carbon hybridization of a:C-H layers by their thickness applied on biodegradable polymer PBAT. The carbonaceous layers were produced by RF-PECVD with acetylene plasma. Ex-situ scanning electron microscopy (SEM) was performed to investigate the surface morphology of these deposited carbon layers. The chemical composition of the resulting layers was analyzed by diffusive reflectance infrared Fourier transform (DRIFT) and the surface-sensitive X-ray techniques near-edge X-ray absorption fine structure (NEXAFS) and X-ray photoelectron spectroscopy (XPS). In addition, contact angle measurements (CA) were performed to evaluate the relationship between the sp^2/sp^3 ratio and macroscopic physical aspects.

2. Materials and Methods

2.1. Sample Preparation and Deposition of a-C:H Layers

For the coating, films of polybutylene adipate terephthalate (PBAT; industrial quality, Lackner Ventures and Consulting GmbH, Vienna, Austria) were cut into pieces with a size of 10 cm x 10 cm and fixed on vacuum-compatible, self-manufactured aluminum sample holders of similar dimensions and placed in a high-vacuum chamber. The chamber in which the coatings were performed was equipped with a high-frequency (RF, 13.65 MHz) plasma source (Copra DN 400, CCR GmbH, Troisdorf, Germany) [17]. To activate and clean the sample surface, all samples were pretreated with an oxygen plasma (RT, pressure 1 Pa, flux 65 sccm/min, power 200 W, plasma time 10 min) before carbon coating [18–21]. After oxygen plasma treatment, the PBAT samples were exposed to acetylene plasma (RT, pressure 0.65 Pa, flux 65 sccm/min, power 107 W) [18–21]. Within these parameters the plasma was operated in H-mode. The temperature of the films never exceeded 40 °C at any time during plasma treatment [21]. By varying the coating time, different a-C:H layer thicknesses of 50–500 nm were realized in 50 nm steps. The deposition rate was about 10 nm/min and is approximately constant over time [21]. A smaller variation was present during the initial growth. During the coating process, the samples were positioned at a distance of 275 mm in front of the plasma source [21], resulting in a r-type diamond-like carbon (DLC) coating [18–20]. This is a more hard and flexible coating due to a higher degree of cross-linked sp^3 carbon centers in the coating caused by a high amount of subplantation processes [21]. In addition, silicon wafers (Silicon Materials, Kaufering, Germany), half covered with aluminia foil, were mounted on the aluminum sample holders, to determine the thickness of the applied layer using a profilometer (Dektak 3, Veeco Instruments Inc., Plainview, NY, USA).

2.2. Surface Topography and Wettability

Scanning electron microscopy (SEM515, Phillips, 7 kV, WD 20 mm, FEI Company, Amsterdam, The Netherlands) and contact angle measurements were performed to check the surface condition. In order to avoid charging effects and sample damage due to low conductivity, a ca. 7–10 nm thick gold layer was sputtered onto the samples prior to measurement conducted at least at three different points on the entire sample. This ensured reproducibility and reliability that the data obtained was correct.

Contact angle measurements are a macroscopic technique checking the surface wettability of the various samples. The measurements were carried out using the sessile drop technique on a contact angle goniometer (OCA15EC, Dataphysics Instruments GmbH, Filderstadt, Germany) at room temperature and in ambient air. A dispensing needle deposited a drop of high-performance liquid chromatography (HPLC) grade water (CHEMSOLUTE®, Th. Geyer GmbH & Co. KG, Renningen, Germany) with a volume of 1 µl on the sample surface. Subsequently, the contact angles of the droplets with the surface are measured on the left and right side. Measurements were repeated on at least five different locations on each sample surface to verify homogeneity and for the purpose of averaging.

2.3. Chemical Composition

To analyze the binding states and chemical composition of carbon atoms DRIFT, XPS, and NEXAFS measurements were performed. The XPS and NEXAFS data were collected at the beamline HE-SGM at the synchrotron source BESSY II, Helmholtz-Zentrum Berlin, Germany during the low alpha phase. The beamline system and detector are described elsewhere [22]. In addition, the system is equipped with a floodgun to prevent charge induced effects on the sample surface. For the XPS measurements, a full survey spectrum (700 eV–0 eV) was first recorded to determine the total chemical composition. Subsequently, the C1s peak was examined at a minimum of two different sample locations, to analyze the different binding states of the carbon atoms. The set of multiple and repeating measurements was performed to check reproducibility and evaluate the homogeneity and stability of a-C:H layers. Additionally, the O1s peak was measured separately to check its presence or absence. The C1s spectra were analyzed by the commercially available software CasaXPS (software version 2.3.18, Casa Software Ltd., Teignmouth, United Kingdom). Thereby proportions of sp^2, sp^3 and C-O bonds in the full C1s peak were identified and evaluated. The results obtained were then plotted with Origin software to the corresponding layer thicknesses.

In NEXAFS investigations, both the C- and O-edge of the samples were recorded. In order to support the correctness of the measurements, the C-edge was recorded also at a minimum of two locations. The NEXAFS measurements were performed in partial electron yield (PEY). Due to the counter voltage, not all electrons emerging from the material reach the measurement electronics and the measurement is more surface sensitive [22]. All the spectra were collected at a photon incidence angle of 55° (''magic angle''). The spectra C K-edges obtained were evaluated using the commercial software Origin. For this purpose, the spectra were first normalized and then adapted to the decreasing ring current, which is present at the BESSY experimental station during the low alpha phase. Subsequently, a correction of possible contamination of the grid by a previously measured gold edge was carried out. The individual steps are summarized by Watts et al. and described elsewhere [23]. Following this, a further analysis was carried out with a self-written peak evaluation program and plotting by Origin 8.1 software. The O K-edge measurements were only used to verify the presence of oxygen and were not evaluated further.

Further analysis of the chemical composition was performed with DRIFT measurements. A Shimadzu Fourier transform spectrometer (IRPrestige-21, Shimadzu, Kyoto, Japan) equipped with the diffuse reflectance measuring apparatus DRS-8000 (Shimadzu, Kyoto, Japan) was used at ambient conditions [24,25]. Two different spectra were recorded: first, the entire spectrum of 500–4000 cm^{-1} (resolution: 4 wavenumbers, 100 repetitions) to find the focus for the thickness-dependent sections of the spectrum. Second a detailed measurement for the most relevant spectral range of 2800–3100 cm^{-1}, the C-H stretching region [16,26]. Here, measurements were performed with a resolution of 1

wavenumber and 300 repetitions. Both measurements were repeated at three different locations to ensure surface homogeneity. The overall reference for a-C:H data analysis and measurements itself was an O_2 plasma-cleaned PBAT sample. The spectral analysis was done with the commercial IR Solution–FTIR Control Software (software version 1.30, Shimadzu Corporation, Kyoto, Japan). Firstly, multipoint baseline insertion with the integrated manipulation tool followed by a software integrated smoothing manipulation (only changes graph appearance but not the information).

3. Results and Discussion

3.1. Condition of a-C:H Layers

Figure 1 shows the image of pure (1a), O_2 plasma treated (1b) and a-C:H coated PBAT foil samples (1c–l). The images of the a-C:H coated samples are shown subsequently in ascending order.

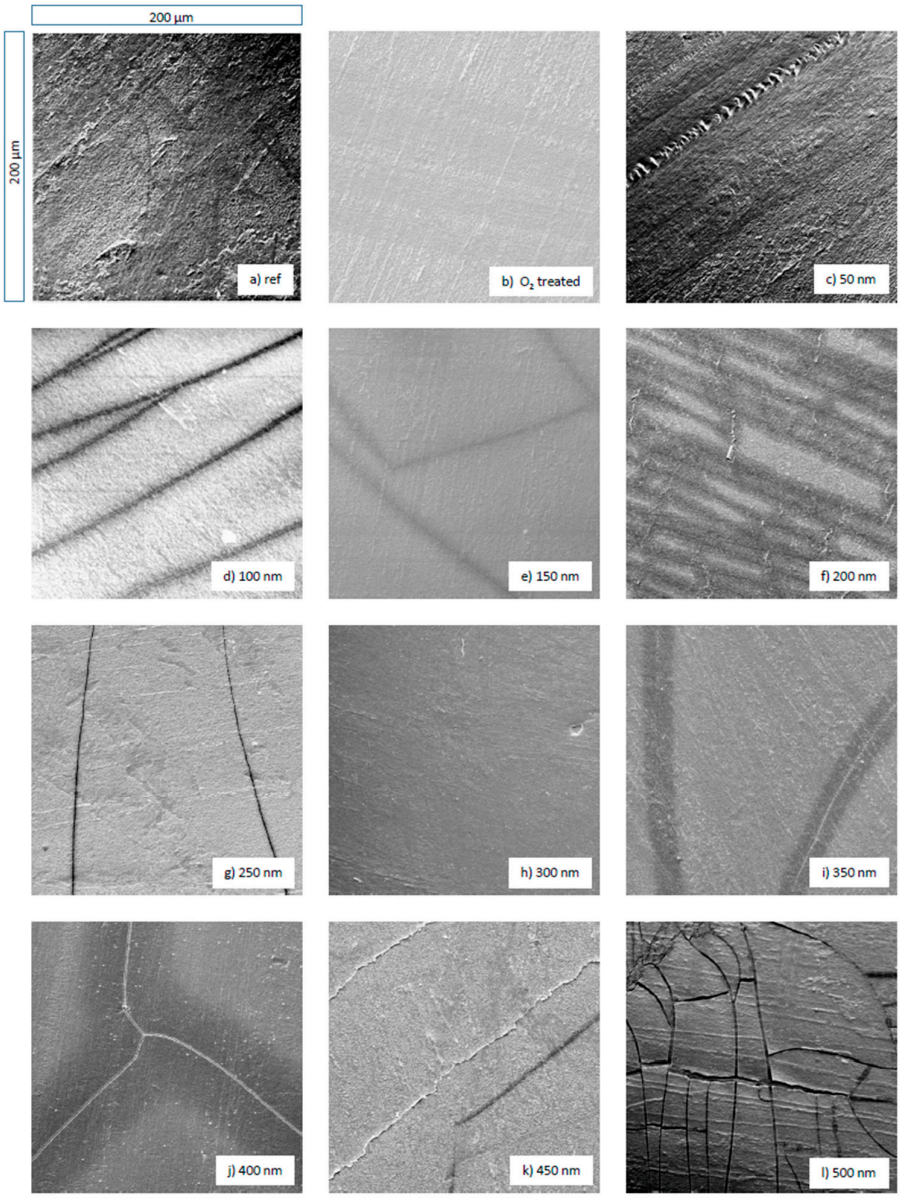

Figure 1. Scanning electron microscope (SEM) images of polybutylene adipate terephthalate (PBAT): (**a**) untreated reference sample, (**b**) treated with O_2 plasma and (**c**)–(**l**) coated with a-C:H layers. The series from (**c**)–(**l**) shows the changes in topography of an increasing a-C:H coating in 50 nm steps up to 500 nm.

A comparison of the O_2-treated sample (1b) with the raw polymer (1a) shows that the previously present impurities have been removed. The surface also appears less roughened and accented. This is mainly due to the sputtering effect by the plasma. The application of O_2 plasma leads to overall smoothing with only a few particles visible. Possible sources of these particles are remnants from the production and coating processes or dust particles from the ambient air during storage and transport of the films. In addition, parallel, vein-like granulate structures at the surface are visible. These were already existent in the raw polymer, but are now much more pronounced. In parallel, dark, line shaped areas are visible, which cut and interrupt these granulate structures. In the course of the SEM measurements, these lines are present on most images (except for 50, 300 and 500 nm). These are most likely due to a break-up of the gold film applied to the samples for the SEM measurements.

For the 50 nm a-C:H coated sample there is a closed film on the surface. The granulate structures are emphasized and also the dark areas are visible. This behavior continues up to a layer thickness of 150 nm. The layer remains homogeneous and appears stable. The granulate structures also remain visible. At 200 nm there are smaller fractures in the layer, but these are only locally limited. With increasing layer thickness the layer is still closed and appears homogeneous again. Furthermore, the granulate structures and black areas are present. With a layer thickness of 450 nm the layer starts to crack again until the layer breaks up completely and destructive layer failure occurs at a a-C:H thickness of 500 nm. It is noticeable that the cord buckling effect [27,28] that has been present on polylactide acide (PLA) and polyhydroxybutyrate (PHB) samples [11,12] coated in the same manner as the PBAT samples only occurs to some extent at 450 nm. This is an indication of good adhesion of the layer on the polymer and consequently for a more pronounced interlayer [17,19].

The break-up of the layer at the thicknesses of 200 nm and 450–500 nm can be explained by the residual stress of the coating and substrate combination, which is apparently proportional to the layer thickness. Reasons for the existence of this stress are different coefficients of expansion or material coefficients of both materials (PBAT and a-C:H layer) and processes during the coating like the so-called island formation of the a-C:H layer and an interaction of these islands with each other in early growth phases [29]. If the residual stress exceeds a critical value, the layer begins to break [5]. Up to this point, the layer on the polymer is stable and adheres well without the presence of the cord-buckling effects (only rudimentarily at 450 nm).

This results in layer thicknesses at which the layer adheres stably to the PBAT after completion of the coating process. Film thickness below 400 nm provides homogeneous and closed layers. An exception is the layer for 200 nm, at which slight local layer failures occur. Higher layer thicknesses lead to a stress-induced layer fracture of the applied layers. Whether closed, homogeneous layers can be restored with increasing thickness and this must be clarified with further measurement campaigns.

Three factors determine the surface wettability and thus the resulting contact angle for the a-C:H coatings investigated here: the morphology of the surface [30–32], the existing chemical bonds [33–36], and various hybridization states of carbon on the surface [10,37,38]. Consequently, contact angle measurements provide information on the structural and chemical properties of the current surface. For example, an oxidized surface leads to an increased attractiveness of water due to the formation of oxygenated groups [36]. However, if the free bonds on the surface are saturated with hydrogen, the strong C–H bonds prevent further interaction between the water applied for the measurement and the sample surface [33–35]. The behavior is more hydrophobic compared to a less hydrogenated surface. Various carbon hybridization states also lead to a change in the contact angle behavior at the sample surface [10,37,38]. For a sp^3 dominated surface, the surface energy is very high due to its strongly covalent character compared to a sp^2 wetted surface, which has a low polarity of its bonds [10,13]. This leads to a reduced contact angle for sp^3 rich surfaces, since an increase in polarity results in smaller contact angles and higher hydrophilicity [39].

In Figure 2 the contact angle results for PBAT samples coated with a-C:H layers of different thickness are displayed. The reference measurement is the O_2 plasma-treated sample, since all samples were treated with O_2 plasma prior to the carbon coating. Overall, the error bars obtained during the measurements are relatively large due to the original wavy structure of the PBAT films.

Due to this wave structure, the contact angles can only be evaluated with regard to the chemical structure, as measurements of surface roughness are not possible. However, a trend can be identified: With the application of a 50 nm a-C:H layer, the contact angle drops from 64° to 52° indicating a higher proportion of sp^3 bonds. With increasing film thickness the contact angles are in an interval of 51–53°, which keeps constant up to 200 nm. From 250 nm on, the contact angle increases steadily until it reaches a maximum at 300 nm. This change in the contact angle is accompanied by a change in the surface free energy, which is explained by different chemical structures and bonds as discussed before. The proportion of sp^2 bonds increases at the expense of the sp^3 ones and leads to an increasing contact angle. Up to a layer thickness of 350 nm a-C:H, the values of the contact angles are between 56° and 61° until they drop down to a value of 50° at the 400 nm layer. A renewed restructuring of the carbon network towards sp^3-dominated surfaces is responsible for this, which is also confirmed later by XPS measurements. With a further increase to 450 and 500 nm, the contact angle quickly increases again to 64° and 61°, respectively. In this region, a layer failure also occurs in accordance with the SEM measurements (compare Figure 1k,l).

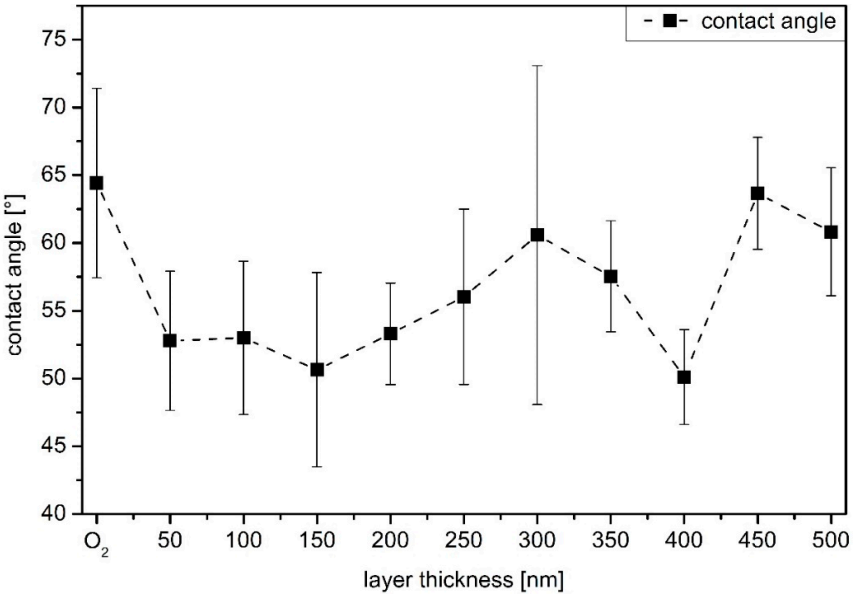

Figure 2. Contact angle results for the O_2 plasma cleaned and a-C:H coatings on PBAT previously treated by O_2 plasma with increasing thickness (the dashed line only indicates a trend of the values).

3.2. Chemical Composition of the Sample Surface

XPS measurements were performed to analyze the chemical composition and especially the carbon hybridization of the sample surface. Figure 3 shows the results of the XPS measurements for a raw PBAT sample, one treated with the O_2 plasma and an exemplary one with a 50 nm a-C:H coating. The data analysis was carried out as described in the experimental section. The peak positions were determined through the NIST database and compared to literature [40–42].

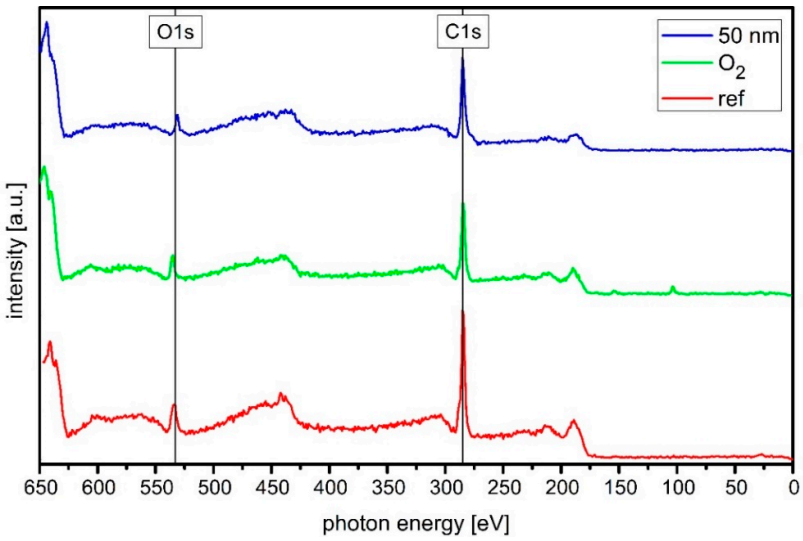

Figure 3. Full X-ray photoelectron spectroscopy (XPS) spectra of raw (red), O_2 treated (green) and 50 nm a-C:H layer coated PBAT sample (blue). The intensity variation of the oxygen peak as well as the shape of the C1s peak significantly changes as the treatment of the polymer surface progresses.

First, the untreated PBAT reference sample (red) is applied. If this sample is treated with an O_2 plasma (green), the shape of the C1s peak changes (285 eV). The peak side becomes more symmetrical and less pronounced, which indicates reduced C–O bondings. This bond is also superimposed within the C1s peak. It is noticeable that the C KLL peaks (~440 eV) disappear with the O_2 plasma treatment. If a 50 nm a-C:H layer (blue) is applied to the previously O_2 treated sample, the acetylene plasma species will react with the prior activated O1s (approx. 533 eV) bonds present on the sample. This initiates and forms the a-C:H layer. The O1s peak is reduced in the XPS survey compared to the O_2 plasma-treated sample. In addition, the C1s peak has become more symmetrical and the C–O peak it contains has almost disappeared. Both plasma treatments thus cause a significant change in the shape of the C1s peak.

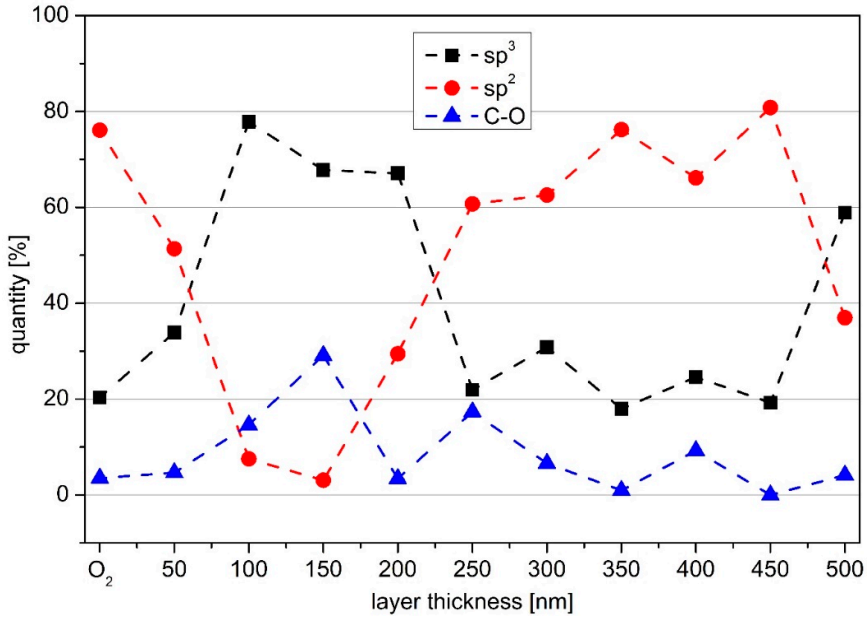

Figure 4. Results for the deconvoluted X-ray photoelectron spectroscopy (XPS) spectra for PBAT. The percentages for the amount of sp^3 (squares), sp^2 (circles), and C–O bond (triangles) for coatings with increasing a-C:H layer thickness are shown (dashed lines are only included for clarity).

Figure 4 shows the XPS results for the series of a-C:H layers applied to the previously O_2 plasma-treated PBAT, which is also included as reference. The percentages of the sp^2 and sp^3 bonds in the C1s peak were determined from XPS and their quantity plotted according to the layer thickness. For the evaluation of the data the C–O and the C=O peak were determined separately, but were plotted and discussed together as C–O in Figure 4. The individual deconvoluted spectra of the C1s peaks are attached as supplementary information SI (available online at www.mdpi.com/xxx/si). In the range of 50–200 nm the sp^3 bond is dominant. An initially sp^3-dominated growth of the a-C:H layer on polymer samples has already been observed on other materials such as PLA and PHB [11,12]. The dominance of the sp^3 bond is in line with the contact angle measurements. With a layer thickness of 250 nm, the dominant bond changes from sp^3 to sp^2. This change has also been observed for other materials, even if the turning point varies depending on the material. If the layer thickness continues to increase, the proportion of sp^2 bonds in the uppermost layers of the film also increases. The system achieves a maximum amount of sp^2 bonds at 450 nm. From 500 nm, the sp^3 bonds increase again and dominate. The C–O bond is variable in the first 300 nm, and reaches a maximum at 150 nm to decrease thereafter again. From 300 nm it remains more or less constantly low below 5 %.

A comparison of the results from the XPS with those from the SEM shows that the changes in the dominant bond are related to failures in the applied a-C:H layers. As the sp^3 content of the carbon bonds increases, the rigid network of sp^3 bonds creates stress in the layer and increases together with the bond content [43,44]. C. A. Davis introduced a model for stress generation in such layers [29]. One way to relax the network is to introduce energy through thermal spikes into the network [29]. The other possibility is to break the bonds by too much stress. The layer failure that occurs in the SEM images is most likely caused by such bond break-up. The offset between layer failure and maximum sp^3 content could be due to a good bond between polymer/layer and a resulting delay until the whole network is riddled with such cracks and the break is visible. The extremely high sp^3 bond content could also be responsible for the high oxygen content in the 100–200 nm layer thickness range. Immediately after coating, the vacuum chamber was vented with ambient air. The high sp^3 content on the surface implies a high degree of stress. Due to the mechanical stress during removal of the samples or due to the time needed for discharge of the stress during storage/transport, the bonds on the surface can be broken. As this happens in ambient air, the oxygen contained in the sample can occupy the now free dangling bonds and as a consequence a high proportion of oxygen is obtained in the following ex situ surface-sensitive measurements. The relaxation of the network as presented by Davis [29] combined with a stress release due to layer failure could be responsible for a rising sp^2 content after a layer thickness of 200 nm. For the layer failure at 500 nm no oxygen saturation takes place. With an increase of the layer from 200 to 250 nm, the sp^3/sp^2 ratio drops to a value below one. At a layer thickness of 200 nm, the sp^3 is dominant. This changes around 250 nm and the sp^2 one dominates accompanied by the occurrence of slight breaks and minor cracks, but the applied layer remains stable on the sample.

The second change in dominant bonds takes place from 450 to 500 nm. Here the sp^3 alternates with the sp^2 as the dominant bond. Once again, this is accompanied by a layer failure, this time right at the change of the bond ratio. At a layer thickness of 500 nm, a strong layer failure is clearly visible. It is noticeable that the layer does not detach from the substrate and rolls up, but remains firmly attached to it. This is an indication of an accentuated interlayer between substrate and a-C:H layer, so that the layer stays on the substrate despite layer failure. The XPS measurements show no change in the oxygen content of the sample, so no oxygen saturation takes place. A possible explanation is the time when the layer failure occurs on the samples. If the stress in the layer is that high, and layer failure takes place during the plasma process, the free bonds are probably saturated by hydrogen or carbon again, as oxygen is not available here. If the stress only leads to coating failure during ventilation or the mechanical load during sampling, the sample is already under ambient air and oxygen can occupy the now free bonds. Up to a layer thickness of 350 nm, the results of the contact angle are in line to the XPS results. However, it would be expected that the contact angles would remain strong up to a value of 450 nm and then drop rapidly, as the sp^3 content from here on is much higher than before. The reason for this difference cannot be stated precisely, but the layer failure (increased surface roughness) and the wavy structure of the original PBAT film are reasonable possibilities.

The results found here only partly correspond to those of a-C:H layers on both biopolymers PLA and PHB [11,12], which were coated simultaneously in the same process. Here the layer failure is a consequence of the change from sp^3 to sp^2 as dominant bond. The change from sp^2 to sp^3 has no influence. In addition, the layer breaks only after the change of binding, so that the change of binding is an indication for an early layer failure. In the case of PBAT, however, there is a small layer failure followed by a change of the dominant binding from sp^3 to sp^2, so that the layer failure is an indication for the binding change. The change from sp^2 to sp^3 as dominant bond, as it is present at 450 nm layer thickness, leads to a strong layer failure. For other materials, this direction of change for the dominant bond was without consequence [11,12], so it could be additionally a substrate effect. It is possible that the layer failure at 450 nm is due to the bond change from sp^3 to sp^2 at 250 nm, only that it occurs with a strong delay of 200 nm layer thickness. Similar findings have already been made for PHB [12]. However, the break-up of the layer at 200 nm would then also be due to a late reaction of the layer to such a change. For this purpose, the layer thickness range of 10–50 nm would have to be examined more closely to determine whether such a change of a dominant bond is present and if an interlayer can be located [45].

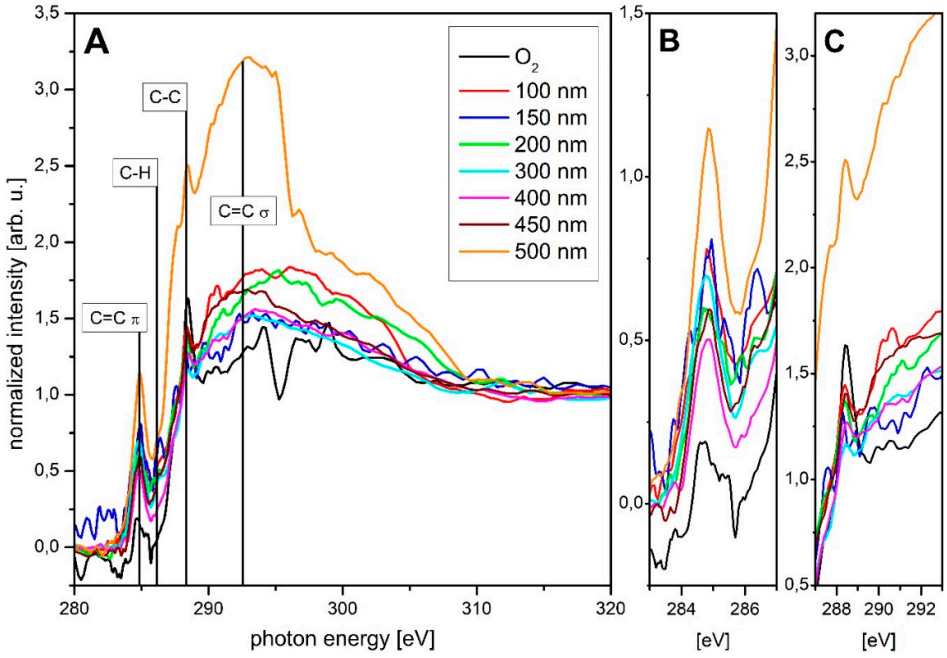

Figure 5. C K-edge near-edge X-ray absorption fine structure (NEXAFS) spectra of an O_2 treated PBAT sample as well as a-C:H coated PBAT with presented layer thicknesses of 100-500 nm in 100 nm steps. Figure **A** displays full spectra, **B** and **C** zooms for 283 eV to 287 eV and 287 eV to 293 eV.

Figure 5 shows the spectra of the C K-edge NEXAFS analysis. For a better overview, only the layer thicknesses of 0–500 nm are applied in 100 nm steps. Exceptions are the layer thicknesses of 150 nm and 450 nm. An overview of all NEXAFS C K-edge spectra is given in the supplementary information SI (available online at www.mdpi.com/xxx/si). The analysis was performed as described in the experimental details. The positions of the peaks analyzed here were determined as follows: C=C π (284.85 eV), C–H (286.15 eV), C–C (288.35 eV) and C=C σ (292.55 eV) [46–50]. Although the region from 290 to 310 eV also represents the C–C bond, only the peak at 288.35 eV was specifically discussed, as this is the most pronounced for this bond type. The peak also changes with closed, thick layers, so it is not (only) due to the basic PBAT structure. Considering the penetration depth of the very surface-sensitive PEY NEXAFS measurement, changes here are only due to changes in the chemical composition of the layer. A thickness-dependent peak change has already been observed and discussed for other polymers (e.g., PLA, PHB), even if a substrate effect is visible [11,12]. In the following, these peaks and their course will be examined in detail. The application of an a-C:H layer up to 100 nm thickness shows the increase of the C–C peak. The peak for the C=C π binding increases,

while the C=C σ binding is less pronounced and almost disappears as the surrounding signals increase. However, its height remains almost unchanged and it broadens a little. Overall, the peak is therefore stronger. An existing C–H peak remains weak but constant. With the application of a 150 nm layer, the C–C peak, which represents the sp^3 bond, decreases while the C=C π bond becomes more dominant. This is consistent with the results obtained in XPS, where a decrease of the sp^3 and an increase of the sp^2 content occurs at this layer thickness and the C–H peak becomes more pronounced. With a layer thickness of 200 nm, the peak of the C–C bond grows again, while the C=C π peak weakens again. The C–H peak and the C=C σ peak are emphasized more strongly again, the surrounding signals of the C=C σ peak decrease and the peak becomes more narrow. The C=C σ peak thus decreases just like the C=C π peak. When thickness exceeds, the C–C peak decreases rapidly and the C=C π peak increases until it begins to weaken again after reaching a layer thickness of 400 nm. This behavior continues with increasing layer thickness. With a thickness of 450 nm, the C–C peak increases again and becomes more accentuated. The other peaks (C=C σ and C–H) are very weak and undefined over the entire measurements. Thus, the measurement data obtained in NEXAFS are in accordance with those obtained in XPS over wide ranges and thus confirm these measurements. Differences in the results of the respective measuring methods are, however, clearly visible in some places and probably partly traceable to the different penetration depths, especially since the NEXAFS measurements are very surface sensitive due to the use of PEY and the XPS measurements that have a comparatively higher penetration depth. The XPS measurements were performed at a larger number of spots than the NEXAFS measurements due to the shorter duration of individual measurements and provide the same results over the sample surface. The NEXAFS measurements themselves also provide similar results at different measuring points. Differences in the respective results are, therefore, not due to singular events on the surface, but rather to the different penetration depths already mentioned. In order to analyze the chemical structure of the a-C:H layers more precisely, DRIFT measurements were performed. For the analysis of the films, an O_2-treated sample was taken as reference, since all a-C:H coated samples were previously treated with O_2 plasma. The spectra obtained with DRIFT were evaluated on the basis of infrared spectroscopy [26] and previous results [16,19,20,51,52]. The following steps were performed: first a full overview (450–4100 cm^{-1}) was taken to check in which regions the samples differ. Subsequently, detailed measurements of the C–H stretching region, which is in the range 2800–3050 cm^{-1}, were arranged to allocate the $=CH_x$ and $-CH_x$ bonds [16,26,51,52]. The spectra obtained during these measurements are plotted in Figure 6 in ascending order according to the thickness of the layer.

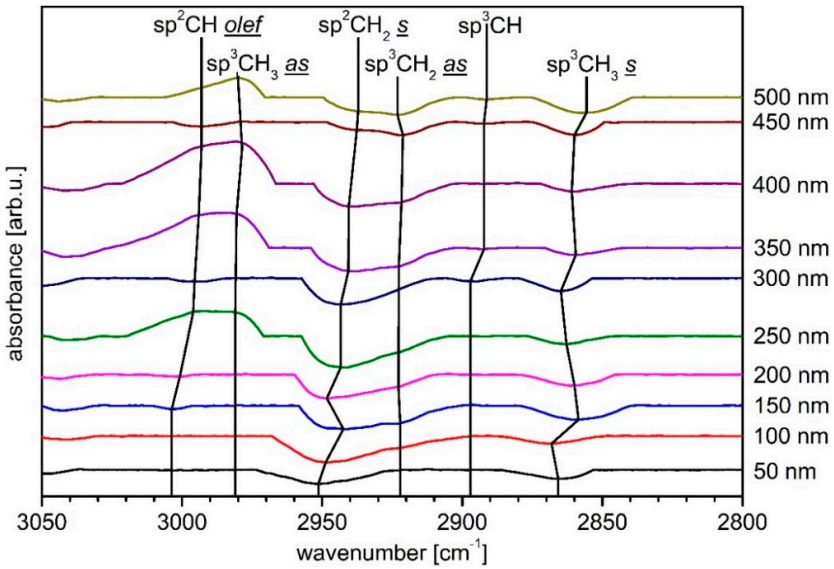

Figure 6. Diffuse reflectance infrared Fourier transform spectroscopy (DRIFT) spectra of the analyzed a-C:H layers with increasing thickness on PBAT. The rising layer thickness is indicated by changing colors with number labelling right next to it.

The sample coated with 50 nm a-C:H has only two absorption peaks. Firstly, the sp^2CH_2 symmetrical peak at a wavenumber of 2951 cm^{-1} and the sp^3CH_3 symmetrical peak at 2866 cm^{-1} [51]. Both peaks are clearly visible. The formation of new and shifting CH_2 groups is a strong indication for an interlayer formation [19,20]. The interlayer formation can be explained by three dominant subplantation processes [53]. A non-specific etching of the entire surface area due to the several plasma species, the insertion of C and H^+-ions into the sample, and the adsorption of plasma radical species to form new bonds on the surface. According to the latest results of Catena et al. for comparable polymer substrates, the interlayer formation process ends up at a layer thickness of around 50 nm [19,20]. If the layer thickness increases to 100 nm, a third peak appears at a wavenumber of 2920 cm^{-1}. This peak can be assigned to the asymmetric sp^3CH_2 [51]. This peak is, notwithstanding, only weakly formed. The other two peaks are retained. The sp^2CH_2 symmetric peak undergoes a shift to lower wavenumbers with increasing layer thickness, which indicates a changing distance of the C–H bond [26]. This changing bond length is already known for a-C:H layers on other polymers [11,12,18,20]. If the layer thickness rises to 150 nm, a small peak appears at 3003 cm^{-1} which can be associated with the sp^2CH olefins [52]. A layer thickness of 200 nm results in a short backshift, which is reversed with increasing layer thickness.

If the layer thickness continues to increase, the sp^2CH_2 symmetrical peak is increasingly emphasized. At 250 nm, this peak is very pronounced. Here, two further peaks become visible, but they overlap each other. In addition, these peaks are formed in such a way that these bonds are less present compared to the O_2 plasma-treated PBAT sample. They are 2980 cm^{-1} and 2995 cm^{-1} and are linked to the sp^3CH_3 asymmetric [51] bond and the shifted sp^2CH olefin bond [52]. The reduction in sp^3 bonds corresponds to the results obtained in XPS. When a layer thickness of 300 nm is reached, the peaks appearing at 250 nm almost disappear again. Only the sp^2CH olefin peak is weakly visible, this time as absorption peak. In addition, a peak at 2897 cm^{-1} is visible, which can be assigned to the sp^3CH bond [52]. With a 350 nm a-C:H layer, the sp^3CH_3 appears asymmetrically and the sp^2CH olefin peak again, but again not as absorption peak, and the sp^3CH_2 asymmetric peak appears again. Both the sp^3CH peak and the sp^3CH_3 symmetric peak shift to smaller wavenumbers. It is noticeable that the peaks belonging to the sp^3 bonds are weaker here. This behavior continues with increasing layer thickness and is consistent with the XPS measurements, which predict the lowest fraction of sp^3 bonds here.

With a layer thickness of 450 nm, the sp^3CH_3 symmetric peak is more pronounced again together with the sp^3CH_2 as peak. The overlapping sp^2CH olefin and sp^3CH_3 asymmetric peaks become here absorption peaks. In addition, the sp^2CH_2 symmetric peak is only weakly emphasized. This also corresponds to the XPS measurements, which predict a reduction of the sp^2 and an increase of the sp^3 content at this layer thickness. At 500 nm the sp^3 bonds are even stronger. It should be mentioned that the sp^3CH_3 symmetric peak shifted to lower wavenumbers and the sp^3CH_2 asymmetric peak to higher. While the sp^3CH_3 symmetric peak continues to strengthen, the sp^3CH_3 asymmetric peak also becomes visible again. However, its orientation once again indicates a weakening of this bond compared to the O_2 plasma-treated sample. Altogether, the strengthening of the sp^3 bonds is again consistent with the results obtained in XPS, which predict the sp^3 bond as the dominant ones. The peaks belonging to the sp^2 bonds have almost disappeared here.

In summary, the results obtained with DRIFT support those from XPS and NEXAFS. In addition, the DRIFT measurements provide more detailed information on how precisely the carbons are bound. A large number of shifts in the wavenumbers associated with the bond lengths show a steady change in the chemical bond ratios when depositing the a-C:H layers on PBAT, which depends on the thicknesses of the applied layers.

4. Conclusions

Using a RF-PECVD process and acetylene as precursor gas, the biodegradable polymer PBAT was coated with a-C:H layers of different thicknesses. The resulting samples were analyzed with SEM, by contact angle measurements and, furthermore, DRIFT spectroscopy, NEXAFS and XPS in order to establish their chemical composition. SEM analysis revealed that stable a-C:H layers can be

achieved on PBAT if the thickness does not exceed 200 nm. Thereafter, the dominating bond situation changes from sp^3 to sp^2. The layer is ruptured by the high stresses in the layer associated with the emerging sp^3 bond. The damage itself seems to be only superficial and insignificant. Also in the DRIFT measurements a sp^2 peak is formed at 250 nm, which supports the change from sp^3 again to sp^2 as dominant bond. Supporting NEXAFS and XPS data additionally confirm the changing chemical composition of the layer with increasing thickness. The DRIFT investigation is underlined by the fact that a large number of shifts in wavenumbers belonging to different bonds correspond to fluctuating bond lengths and, therefore, reveal a changing chemical environment in the a-C:H layers. In the further course, the layer growth remains stable until the layer thickness reaches 450 nm. At this point the dominant bond also changes, this time from sp^2 to more sp^3.

In summary, the deposition of a stable a:C-H layer on biodegradable PBAT is possible up to a thickness of 150 nm and for the range between 250 nm to at least 400 nm. However, complete delamination of the film does not occur. Despite some tearing, the layer remains adherent to the polymer. A comprehensive analysis of the chemical composition by using synchrotron-based XPS and NEXAFS in combination with DRIFT was performed for the present carbon layers and underlines a significant changing character for the layers with increasing deposition height. Apart from minor deviations, the results of the three techniques used for the chemical analysis of the coating are consistent. The stable adhesion of the a-C:H layers despite breakage of the layer underlines the formation of a distinct interlayer between the polymer and the a-C:H layer.

The analyses carried out and presented here show that the bonding ratios of the carbon atoms depend not only on the plasma parameters selected, but also on the layer thickness achieved. It follows that it is also possible to adapt the layer obtained to the selected applications (e.g., hydrophilic, -phobic) by monitoring the layer thickness. This is possible because there is a layer thickness-dependent change between the sp^3- or sp^2-bound dominant carbon types in the present a-C:H coating process on PBAT. Since the properties of the applied layer also change as a result of the change in the bonding ratio, these can be controlled accordingly in this way.

Supplementary Materials: The following are available online at www.mdpi.com/xxx/si.

Author Contributions: T.S. and C.F. conceptualized the study, developed and organized the related procedures. T.S. prepared the samples and performed the data evaluation, visualization and wrote the original draft. T.S. and C.F. reviewed and edited the manuscript. H.A. and B.H. contributed in terms of SEM-related analyses. NEXAFS, XPS and DRIFT acquisition and evaluation was conducted by T.S. Both authors S.W. and C.F. contributed in terms of funding acquisition, project management, supervision and overall guidance in the study. All authors have read and agreed to the published version of the manuscript.

Funding: T.S., S.W. and C.F. gratefully acknowledge the financial support provided by the German Research Foundation DFG (Deutsche Forschungsgemeinschaft) through the project WE 4100/23-1 and FI 1802/14-1. T.S. and C.F. thankfully acknowledge the financial support by HZB.

Acknowledgments: The authors thank Dr. Heinz Busch (NTTF Coatings GmbH, Rheinbreitbach, Germany) for the industrial coating of the samples and Prof. Dr. Joachim Scholz (University of Koblenz-Landau, department of chemistry) for the DRIFT equipment. The authors also want to thank Dr. Alexei Nefedov from KIT (Karlsruhe Institute for Technology, Group: Chemistry of oxidic and organic interfaces; X-ray and Electron Spectroscopy at Interfaces) for beamtime support and PD. DI Dr. M. Lackner (Lackner Ventures and Consulting GmbH, Austria) for the kind support of PBAT films used in the experiments. We thank HZB for the allocation of synchrotron radiation beamtime.

Conflicts of Interest: The authors declare no conflict of interest.

References

1. Andrady, A.L.; Neal, M.A. Applications and societal benefits of plastics. *Philos. Trans. R. Soc. B Biol. Sci.* **2009**, *364*, 1977–1984.
2. Sabbatini, L. *Polymer Surface Characterization*; De Gruyter: Boston, MA, USA, 2014.
3. Ryan, P.G. Brief History of Marine Litter Research. In *Book Marine Anthropogenic Litter*; Bergmann, M., Gutow, L., Klages, M.A., Eds.; Springer: Berlin/Heidelberg, Germany, 2015.

4. Witt, U.; Einig, T.; Yamamoto, M.; Kleeberg, I.; Deckwer, W.D.; Müller, R.J. Biodegradation of aliphatic–aromatic copolyesters: Evaluation of the final biodegradability and ecotoxicological impact of degradation intermediates. *Chemosphere* **2001**, *44*, 289–299.
5. Grill, A. Plasma-deposited diamondlike carbon and related materials. *IBM J. Res. Dev.* **1999**, *43*, 147–162.
6. Rohrbeck, M.; Fischer, C.; Wehner, S.; Meier, J.; Manz, W. DLC-coated pure bioplastic foil. *Vakuum Forsch. Prax.* **2014**, *26*, 42–47.
7. Rohrbeck, M.; Körsten, S.; Fischer, C.B.; Wehner, S.; Kessler, B. Diamond-like carbon coating of a pure bioplastic foil. *Thin Solid Film.* **2013**, *545*, 558–563.
8. Couderc, P.; Catherine, Y. Structure and physical properties of plasma-grown amorphous hydrogenated carbon films. *Thin Solid Film.* **1987**, *146*, 93–107.
9. Mohagheghpour, E.; Rajabi, M.; Gholamipour, R.; Larijani, M.M.; Sheibani, S. Ion beam energy dependence of surface and structural properties of amorphous carbon films deposited by IBSD method on Ni–Cu alloy. *J. Mater. Res.* **2017**, *32*, 1258–1266.
10. Paul, R.; Das, S.N.; Dalui, S.; Gayen, R.N.; Roy, R.K.; Bhar, R.; Pal, A.K.; Das, S. Synthesis of DLC films with different sp^2/sp^3 ratios and their hydrophobic behaviour. *J. Phys. D Appl. Phys.* **2008**, *41*, 1–7.
11. Schlebrowski, T.; Beucher, L.; Bazzi, H.; Hahn, B.; Wehner, S.; Fischer, C.B. Prediction of a-C: H layer failure on industrial relevant biopolymer polylactide acide (PLA) foils based on the sp^2/sp^3 ratio. *Surf. Coat. Technol.* **2019**, *368*, 79–87.
12. Schlebrowski, T.; Beucher, L.; Bazzi, H.; Hahn, B.; Wehner, S.; Fischer, C.B. Changing Contents of Carbon Hybridizations in Amorphous Hydrogenated Carbon Layers (a-C: H) on Sustainable Polyhydroxybutyrate (PHB) Exhibit a Significant Deterioration in Stability, Depending on Thickness. *C J. Carbon Res.* **2019**, *5*, 1–14.
13. Robertson, J. Diamond-like amorphous carbon. *Mater. Sci. Eng. R Rep.* **2002**, *37*, 129–281.
14. Lee, S.C.; Tai, F.C.; Wei, C.H. Correlation between sp^2/sp^3 ratio or hydrogen content and water contact angle in hydrogenated DLC film. *Mater. Trans.* **2007**, *48*, 2534–2538.
15. Robertson, J. Plasma Deposition of Diamond-Like Carbon. *Jpn. J. Appl. Phys.* **2011**, *50*, 1–8.
16. Koidl, P.; Wild, C.; Dischler, B.; Wagner, J.; Ramsteiner, M. Plasma Deposition, Properties and Structure of Amorphous Hydrogenated Carbon Films. *Mater. Sci. Forum.* **1990**, *52*, 41–70.
17. Fischer, C.B.; Rohrbeck, M.; Wehner, S.; Richter, M.; Schmeißer, D. Interlayer formation of diamond-like carbon coatings on industrial polyethylene. *Appl. Surf. Sci.* **2013**, *271*, 381–389.
18. Catena, A.; Agnello, S.; Rösken, L.M.; Bergen, H.; Recktenwald, E.; Bernsmann, F.; Busch, H.; Cannas, M.; Gelardi, F.M.; Hahn, B.; et al. Characteristics of industrially manufactured amorphous hydrogenated carbon (a-C: H) depositions on high-density polyethylene. *Carbon* **2016**, *96*, 661–671.
19. Catena, A.; Guo, Q.; Kunze, M.R.; Agnello, S.; Gelardi, F.M.; Wehner, S.; Fischer, C.B. Morphological and Chemical Evolution of Gradually Deposited Diamond-Like Carbon Films on Polyethylene Terephthalate: From Subplantation Processes to Structural Reorganization by Intrinsic Stress Release Phenomena. *ACS Appl. Mater. Interfaces* **2016**, *8*, 10636–10646.
20. Catena, A.; Kunze, M.R.; Agnello, S.; Gelardi, F.M.; Wehner, S.; Fischer, C.B. Amorphous hydrogenated carbon (a-C: H) depositions on polyoxymethylene: Substrate influence on the characteristics of the developing coatings. *Surf. Coat. Technol.* **2016**, *307*, 658–665.
21. Catena, A.; McJunkin, T.; Agnello, S.; Gelardi, F.M.; Wehner, S.; Fischer, C.B. Surface morphology and grain analysis of successively industrially grown amorphous hydrogenated carbon films (a-C:H) on silicon. *Appl. Surf. Sci.* **2015**, *347*, 657–667.
22. Nefedov, A.; Wöll, C. Advanced Applications of NEXAFS Spectroscopy for Functionalized Surfaces. In *Book Surface Science Techniques*; Bracco, G., Holst, B., Eds.; Springer: Berlin/Heidelberg, Germany, 2013.
23. Watts, B.; Thomsen, L.; Dastoor, P.C. Methods in carbon K-edge NEXAFS: Experiment and Analysis. *J. Chem. Phys.* **2014**, *140*, 105–120.
24. Armaroli, T.; Bécue, T.; Gautier, S. Diffuse Reflection Infrared Spectroscopy (Drifts). *Oil Gas Sci. Technol.* **2004**, *59*, 215–237.
25. D'Souza, L.; Devi, P.; Kamat, T.; Naik, C.G. Diffuse reflectance infrared fourier transform spectroscopic (DRIFTS) investigation of E.coli, Staphylococcus aureus and Candida albicans. *Indian J. Mar. Sci.* **2009**, *38*, 45–51.
26. Günzler, H.; Gremlich, H.U. *IR Spectroscopy: An. Introduction*; Wiley-VCH: Weinheim, Germany, 2002.

27. Mei, H.; Huang, R.; Chung, J.Y.; Stafford, C.M.; Yu, H.H. Buckling modes of elastic thin films on elastic substrates. *Appl. Phys. Lett.* **2007**, *90*, 151902.
28. Volinsky, A.A. Experiments with in-situ thin film telephone cord buckling delamination propagation. *MRS Proc.* **2002**, *749*, 1–6.
29. Davis, C.A. A simple model for the formation of compressive stress in thin films by ion bombardment. *Thin Solid Film.* **1993**, *226*, 30–34.
30. Banerjee, D.; Mukherjee, S.; Chattopadhyay, K. Controlling the surface topology and hence the hydrophobicity of amorphous carbon thin films. *Carbon* **2010**, *48*, 1025–1031.
31. Feng, L.; Li, S.; Li, Y.; Li, H.; Zhang, L.; Zhai, J.; Song, Y.; Liu, B.; Jiang, L.; Zhu, D. Super-Hydrophobic Surfaces. *Adv. Mater.* **2002**, *14*, 1857–1860.
32. Barthlott, W.; Neinhuis, C. Purity of the sacred lotus, or escape from contamination in biological surfaces. *Planta* **1997**, *202*, 1–8.
33. Ostrovskaya, L.; Perevertailo, V.; Ralchenko, V.; Dementjev, A.; Loginova, O. Wettability and surface energy of oxidized and hydrogen plasma-treated diamond films. *Diam. Relat. Mater.* **2002**, *11*, 845–850.
34. Ostrovskaya, L. Studies of diamond and diamond-like film surfaces using XAES, AFM and wetting. *Vacuum* **2002**, *68*, 219–238.
35. Piazza, F.; Morell, G. Wettability of hydrogenated tetrahedral amorphous carbon. *Diam. Relat. Mater.* **2009**, *18*, 43–50.
36. Tay, B.K.; Sheeja, D.; Lau, S.P.; Guo, J. Study of surface energy of tetrahedral amorphous carbon films modified in various gas plasma. *Diam. Relat. Mater.* **2003**, *12*, 2072–2076.
37. Werder, T.; Walther, J.H.; Jaffe, R.L.; Halicioglu, T.; Koumoutsakos, P. On the Water-Carbon Interaction for Use in Molecular Dynamics Simulations of Graphite and Carbon Nanotubes. *J. Phys. Chem. B* **2003**, *107*, 1345–1352.
38. Zhou, Y.; Wang, B.; Song, X.; Li, E.; Li, G.; Zhao, S.; Yan, H. Control over the wettability of amorphous carbon films in a large range from hydrophilicity to super-hydrophobicity. *Appl. Surf. Sci.* **2006**, *253*, 2690–2694.
39. Bismarck, A.; Brostow, W.; Chiu, R.; Lobland, H.E.H.; Ho, K.K. Effects of surface plasma treatment on tribology of thermoplastic polymers. *Polym. Eng. Sci.* **2008**, *48*, 1971–1976.
40. Dietrich, P.M.; Horlacher, T.; Girard-Lauriault, P.L.; Gross, T.; Lippitz, A.; Min, H.; Wirth, T.; Castelli, R.; Seeberger, P.H.; Unger, W.E.S. Adlayers of Dimannoside Thiols on Gold: Surface Chemical Analysis. *Langmuir* **2011**, *27*, 4808–4815.
41. Solomon, J.; Madix, R.; Stöhr, J. Orientation and absolute coverage of benzene, aniline, and phenol on Ag (110) determined by NEXAFS and XPS. *Surf. Sci.* **1991**, *255*, 12–30.
42. Tai, F.C.; Lee, S.C.; Wei, C.H.; Tyan, S.L. Correlation between I_D/I_G Ratio from Visible Raman Spectra and sp^2/sp^3 Ratio from XPS Spectra of Annealed Hydrogenated DLC Film. *Mater. Trans.* **2006**, *47*, 1847–1852.
43. Lacerda, R.G.; Marques, F.C. Hard hydrogenated carbon films with low stress. *Appl. Phys. Lett.* **1998**, *73*, 617–619.
44. Marques, F.C.; Lacerda, R.G.; Odo, G.Y.; Lepienski, C.M. On the hardness of a-C: H films prepared by methane plasma decomposition *Thin Solid Film.* **1998**, *332*, 113–117.
45. Schlebrowski, T.; Rouabeh, W.; Wehner, S.; Fischer, C.B. Specifying the interlayer turning point and dehydrogenation in a-C:H layers plasma deposited on high-density polyethylene with X-ray synchrotron techniques. *Thin Solid Film.* **2019**, *691*, 1–6.
46. Brüster, B.; Amozoqueño, C.; Grysan, P.; Peral, I.; Watts, B.; Raquez, J.-M.; Dubois, P.; Addiego, F. Resolving Inclusion Structure and Deformation Mechanisms in Polylactide Plasticized by Reactive Extrusion. *Macromol. Mater. Eng.* **2017**, *302*, 1700326.
47. Diaz, J.; Monteiro, O.R.; Hussain, Z. Structure of amorphous carbon from near-edge and extended x-ray absorption spectroscopy. *Phys. Rev. B* **2007**, *76*, 094201.
48. Díaz, J.; Anders, S.; Zhou, X.; Moler, E.J.; Kellar, S.A.; Hussain, Z. Analysis of theπ^*andσ^*bands of the x-ray absorption spectrum of amorphous carbon. *Phys. Rev. B* **2001**, *64*, 125204.
49. Dhez, O.; Ade, H.; Urquhart, S.; Urquhart, S. Calibrated NEXAFS spectra of some common polymers. *J. Electron. Spectrosc. Relat. Phenom.* **2003**, *128*, 85–96.
50. Stöhr, J. *NEXAFS Spectroscopy*; Springer: Berlin/Heidelberg, Germany, 1992.
51. Tomasella, E.; Thomas, L.; Dubois, M.; Meunier, C. Structural and mechanical properties of a-C. *Diam. Relat. Mater.* **2004**, *13*, 1618–1624.

52. Veres, M.; Koos, M.; Pócsik, I. IR study of the formation process of polymeric hydrogenated amorphous carbon film. *Diam. Relat. Mater.* **2002**, *11*, 1110–1114.
53. Neyts, E.; Bogaerts, A.; van de Sanden, M.C.M. Reaction mechanism and thin a-C: H film growth from low energy hydrocarbon radicals. *J. Phys. Conf. Ser.* **2007**, *86*, 12020.

Thin Solid Films 691 (2019) 137617

Contents lists available at ScienceDirect

Thin Solid Films

journal homepage: www.elsevier.com/locate/tsf

Specifying the interlayer turning point and dehydrogenation in a-C:H layers plasma deposited on high-density polyethylene with X-ray synchrotron techniques

T. Schlebrowski[a], W. Rouabeh[a,b], S. Wehner[a], C.B. Fischer[a,c,*]

[a] Department of Physics, University Koblenz-Landau, 56070 Koblenz, Germany
[b] Department of Chemistry, University Koblenz-Landau, 56070 Koblenz, Germany
[c] Materials Science and Nano-engineering Department, Mohammed VI Polytechnic University, 43150 Ben Guerir, Morocco

ARTICLE INFO

Keywords:
sp^2/sp^3 ratio
Industrial plasma coating
Thin films
X-ray photoelectron spectroscopy
Near-edge X-ray absorption fine structure
Diffuse reflectance infrared Fourier transform spectroscopy

ABSTRACT

High-density polyethylene (HDPE) samples were coated with amorphous carbon layers (a-C:H) increasing in thickness from nm to μm using an radio frequency plasma source. The deposited layers were examined in detail by synchrotron based X-ray photoelectron spectroscopy (XPS) and near edge X-ray absorption fine structure spectroscopy (NEXAFS) to determine the binding states of the carbon atoms to each other and their status in the network. Particular attention was paid to coatings between 500 and 1500 nm, where dehydrogenation of the a-C:H layer occurs, and to thin depositions from 0 to 50 nm to specify the interlayer turning point from the polymer to the pure a-C:H network equivalent to the end point of a mixed phase. Since this is decisive for the adhesion of the carbon layer to the polymer, this area was additionally investigated by means of diffuse reflectance infrared Fourier transform (DRIFT) spectroscopy. Herein the dimension of the interlayer between a-C:H layers on HDPE could be consistently narrowed to a thickness of more than 30 nm and less than 40 nm in all methods, as later the a-C:H network is appearing. The dehydrogenation process in the growing a-C:H layer was also confirmed, leading to a decrease in the sp^3 respectively increase in sp^2 bonds.

1. Introduction

Plastic materials are indispensable and are used today in many technical aspects of everyday life. This is ensured by their malleability, chemical resistance, elasticity, low weight and low cost [1]. However, they also have poor characteristics, such as low hardness or poor mechanical properties, which limit their applications [1]. A common way to improve their surface properties is to apply thin amorphous carbon layers upon the raw material [2,3]. The advantages of these coatings are their high hardness, increased abrasion resistance, reduced adhesion and biocompatibility [4-6]. They are also used in the food processing industry due to their excellent gas barrier properties [7]. These films consist of a mixture of carbon atoms with sp, sp^2 and sp^3 hybridizations and different contents of hydrogen [8,9]. The properties of the coated material depend very much on the specific ratio of sp^2 and sp^3 as well as on the hydrogen content. This mainly determines the density of the film, its hardness, surface roughness and its electrical properties [8-11].

These a-C:H layers for plastics are mostly realized by the radio frequency plasma-enhanced chemical vapor deposition technique [3,10], as these ensure that the temperature of the coated substrate remains low and that it can also be used for insulating substrates [6,8]. One common polymer is high-density polyethylene (HDPE) with a simple CH_2 chain. This material is used in a variety of applications in everyday life such as packaging foils or bottles and even in the medical field as implants [4,12]. In this context a-C:H layers are used to improve the gas diffusion barrier properties or the antibacterial properties on polymers [13,14].

In this study, a comprehensive series of a-C:H coatings with increasing thickness are investigated with synchrotron based spectroscopy techniques. Indicative results revealing interlayer behavior have been earlier presented by Catena et al. [15]. Here pursuing and detailed facts for a-C:H layers on HDPE are presented. Of special interest is firstly the transition point from the organic substrate towards the more inorganic network of the carbon layer. Therefore, sample series with small intervals of 10 and later 50 nm have been realized. Secondly with longer deposition times respectively thicker layers dehydrogenation was revealed [15], which is additionally investigated by its sp^2/sp^3

* Corresponding author.
E-mail address: chrbfischer@uni-koblenz.de (C.B. Fischer).

https://doi.org/10.1016/j.tsf.2019.137617
Received 4 April 2019; Received in revised form 5 September 2019; Accepted 4 October 2019
Available online 07 October 2019

ratio. The X-ray synchrotron based techniques used are photoelectron spectroscopy (XPS) and near edge X-ray absorption fine structure (NEXAFS). Together with diffuse reflectance infrared Fourier transform (DRIFT) analysis and the hybridization ratio of the carbon the turning point of the interlayer towards the a-C:H network is located within few nm.

2. Experimental details

2.1. Sample preparation and film deposition

HDPE plates (thickness 1 mm) have been obtained in industrial quality (Goodfellow GmbH, Bad Nauheim, Germany), stamped to circular pieces with a diameter of 10 mm and positioned on vacuum suitable alumina sample holders. a-C:H coatings with thicknesses from 10–2000 nm were deposited on HDPE. Special attention was paid to the region of 10–50 nm, since the formation of the interlayer between the a-C:H layer and the HDPE polymer is expected here. The thickness was increased in small steps of 10 nm. The layer thickness range from 0–50 nm is referred to in this publication as thin layers. Layer thicknesses exceeding 500 nm are referred to as thick layers. The coating process has been performed through a radio frequency (13.56 MHz) plasma-enhanced chemical vapor deposition process in a high vacuum chamber. The RF-driven plasma source (Copra DN 400, CCR GmbH, Troisdorf, Germany), sample cleaning with isopropanol (10 min, ultrasonic-bath) and subsequent oxygen plasma (10 min) and the coating process itself with C_2H_2 including plasma parameters as well as gas flow and coating geometry are described in detail elsewhere [3,11,15,16]. The coating time was varied to maintain different film thicknesses (deposition rate 10 nm min^{-1}). The samples to be coated were directly aligned to the plasma resulting in an r-type a-C:H coating [15,16]. In order to detect the coating thickness, silicon wafer (Silicon Materials, Kaufering, Germany) half covered with alumina foil, have been mounted additionally on the aluminum sample holders. This enabled the applied layer thickness to be determined with the aid of a profilometer (Dektak 3, Veeco Instruments Inc., Plainview, NY, USA) on Si resp. the aliquot of deposited a-C:H on the polymer sample.

2.2. X-ray photoelectron spectroscopy (XPS)

XPS measures were carried out at the beamline HE-SGM at the Berlin electron storage ring BESSY II during the low alpha phase. XPS is used to determine the chemical environment of the samples top surface as its analytical detection depth is around 10 nm. At first, spectra were measured over the full spectral range of 700 to 0 eV. Subsequently, the C1s peak was measured with high resolution in duplicate at different locations of the sample coating to ensure homogeneity. Furthermore, the O1s peak was measured separately. For the evaluation the C1s signal, deconvoluted peaks were analyzed with the commercially available software CasaXPS (software version 2.3.18, Casa Software Ltd. United Kingdom). Thereby the proportion of sp^2, sp^3 and C—O bonds in the full C1s peak could be determined. The full system and used detector is described elsewhere [17]. A tunable floodgun was used to reduce charging effects on the sample caused by the irradiation with the beam.

2.3. Near edge X-ray absorption fine structure (NEXAFS)

The surface of the samples was examined additionally by NEXAFS spectroscopy for their C and O composition. The measurement system is described in detail elsewhere [17]. The system is equipped with a tunable floodgun as described above. Measurements of the C-edge were repeated at a second location to ensure reproducibility. Applying an in-house developed script (Origin 8.1 G), the spectra were initially normalized and adapted to the decreasing ring current. Also a correction of the background noise was carried out. Finally, an adaptation to a gold edge was performed to correct the soiling of the grid. The enhanced spectra were then smoothed and analyzed by an in-house developed peak evaluation program. The obtained ratios of the various bonds normalized to the C=C π bond were subsequently plotted with Origin.

2.4. Diffuse reflectance infrared Fourier transform (DRIFT) spectroscopy

Infrared investigations of the coated samples were performed with diffuse reflectance for infrared Fourier transform (DRIFT) spectroscopy. A Shimadzu Fourier transform spectrometer (IR Prestige-21, Kyoto, Japan) equipped with the diffuse reflectance measuring apparatus DRS-8000 was used in ambient air and at room temperature [18]. At first, an entire spectrum (500–4000 cm^{-1}) with a resolution of 4 wave numbers and 100 repetitions was recorded. With the help of the full spectra later detailed measurements with a higher resolution of one wavenumber and an average of 300 repetitions were performed for the most relevant spectral range of 2800–3100 cm^{-1}, the C—H stretching region [10,19]. The measurements were done on three different spots on the samples to prove layer homogeneity and measurement correctness. The O_2-plasma cleaned HDPE sample was used as reference for the following DRIFT measurements of a-C:H coated samples. The spectral analysis was done with the commercial IR Solution - FTIR Control Software (software version 1.30, Shimadzu Corporation, Kyoto, Japan). The applied protocol just briefly: multipoint baseline insertion via the integrated manipulation tool and fine-tuning with software integrated smoothing manipulation (These manipulations only change the appearance of the graph but not the information contained).

3. Results and discussion

XPS results presented in Fig. 1A and B and Table 1 show the data obtained for the sp^2 and sp^3 binding as a function of the layer thickness. The peak positions have been determined by NIST database and the work of other groups [20-22]. For a better overview, the measurements in Fig. 1 were separated into two groups: **A)** thicknesses from 0–200 nm including reference (ref) and oxygen-treated ($0 = O_2$) and **B)** the results for the 200–2000 nm. This grouping for the smaller steps is used to study interlayer formation, which is a mixed phase of the a-C:H layer and the raw material. It has been shown to be present for e.g. HDPE or polyethylene terephthalate [3,15,23]. Fig. 1A shows the data for the thin layers. For the raw sample around 40% of sp^2 bonds are detected instead of a pure sp^3 content, therefore an obvious contamination of the raw polymer is visible. This could be due to olefins from the manufacturing process or softeners detaching from the polymer over time. After the O_2-plasma treatment these sp^2 bonded carbons have disappeared. The O_2-plasma treated sample is used as new reference with a layer thickness of 0 nm since every sample is treated identically with O_2 plasma before the carbon layer deposition. In the range from 10 nm to 20 nm layer thickness there is a very strong increase of the sp^2 content. From 20 nm to 30 nm there is a short decrease of the sp^2 content in order to grow almost constantly later on. This could be a clear indication for the turning point around this thickness and the end of the interlayer formation leading to a change in the layer deposition process. With a thickness of 200 nm, the layer has the lowest measured proportion of sp^3 bonds respectively highest for sp^2.

Fig. 1B shows that with the application of a layer of 500 nm the sp^3 content of the layer increases strongly, which is in strong contrast to the previous course. Afterwards the growing to a more sp^2 bonded carbon film continues. From 500 to 1500 nm layer thickness the sp^2 bond is increasing again. This correlates with earlier results of this group. Between 500 and 1500 nm a dehydrogenation takes place. This results in a rehybridization of the carbon atom orbitals. The sp^3 bonded carbon changes into sp^2 hybridized carbon clusters. Also the coalescence phenomenon of merging grains on the surface takes place in this region as proven recently by some of the authors [15]. As the layer thickness increases, the sp^2 bond becomes more dominant for the applied a-C:H

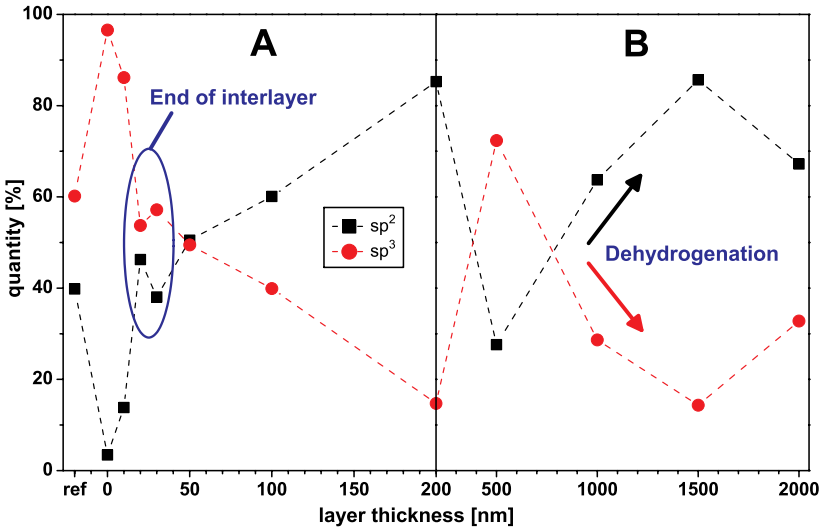

Fig. 1. XPS results for sp^2 and sp^3 content of HDPE samples coated with a-C:H layers of various thickness: **A**) thin layers from raw (ref) and O_2 cleaned material (0) to 200 nm and **B**) thicker layers up to 2000 nm. The black squares are the quantity of the sp^2 content and the red dots the sp^3 content (lines only illustrate a trend).

Table 1
Summary of sp^2 and sp^3 content from XPS results for increasing thickness.

layer thickness [nm]	Content [%] sp^2	sp^3
ref	40	60
O_2	3	97
10	14	86
20	46	54
30	38	57
50	50	50
100	60	40
200	85	15
500	28	72
1000	64	29
1500	86	14
2000	67	33

layer. This growing dehydrogenation lasts up to the layer thickness of 1500 nm. After that, the sp^2 content turns and decreases again slightly.

The NEXAFS measurements are presented separately in Fig. 2 (thin layers) and Fig. 3 (thicker layers) for better clarity. The selected sections are the O_2-plasma treated sample as a new reference and the layer thicknesses of 0 to 50 nm in Fig. 2a–f. With this the investigation of the interlayer formation and its turning point is more obvious.

The layer thicknesses of 100–2000 nm are shown in Fig. 3. In the following, the three typical main bonds C−C (288.35 eV), C−H (286.15 eV) and C=C σ (292.55 eV) are investigated in relation to the C=C π (284.85 eV) bond [24-27]. Up to a layer thickness of 30 nm, there is a continuous increase in all three bond types compared to the C=C π bond. With a layer thickness of 30 nm, the C=C π bond decreases, which supports the similar findings in the XPS measurements. At a layer thickness of 40 nm, the C=C π bond increases abruptly and the ratio of the other three bonds decreases as compared to the C=C π bond. The change in the behavior of layer growth that occurs here can be traced back to the finalization of the interlayer formation. After this turning point the normal growth of the a-C:H layer starts.

The dimension of the interlayer strongly depends on the substrate. In some cases, such as HDPE, it is very well developed, which results in good interlocking between the a-C:H layer and the basic material. With other materials on the other hand e.g. polyoxymethylene it is almost non-existent and the layer easily detaches [16]. The composition of the interlayer is most likely a mixture of the a-C:H layer and the specific substrate material. The content of substrate residues in the interlayer also influences its final surface properties. Therefore, the resulting bonding ratios are strongly dependent on the substrate on which the a-C:H layer is applied and known as substrate effect [28].

From 50 nm there is a steady increase in the C−H bond up to a thickness of 200 nm while the C=C π bond also increases. The C−H bond continues to grow until it reaches its maximum at 1000 nm, at which point it steadily decreases again. The following impression results for NEXAFS measures with thick layers: With a layer growth from 200 nm to 500 nm, the proportion of C−C bonds increases strongly at the expense of the C=C π bond. This could already be seen in XPS. If the layer is 1000 nm thick, this process is initially continued in the NEXAFS measurements. However, there is also an increase in C=C σ bonds. As the layer continues to grow, both the C−C and C−H bonds decrease, while the C=C σ bond continues to increase. By dehydrogenation of the layer C−H single bonds are broken and double bonds are formed. Additionally C−C bonds are broken and rearranged. The C−C and C−H bonds decrease in relation to the C=C π and C=C σ bonds. When the 2000 nm layer thickness is reached, C−C and C−H bonds are relatively negligible, while the proportion of C double bonds increases sharply. This means that the layers with a higher layer thickness have a high sp^2 content with a very dominant C=C π bond. This can be attributed to the formation of the aforementioned sp^2 clusters and is in line with the XPS findings, although the dehydrogenation in NEXAFS was found to be slightly delayed, this may be due to the different penetration depths of the different techniques. These findings are in line with the results obtained from previous studies with different techniques [3,15] and support furthermore the occurrence of dehydrogenation which happens with increasing layer thickness as well as the presence of the interlayer and its dimension.

To further investigate the formation of the interlayer and localize the turning point with its corresponding chemical structure, the deposited layers were additionally examined with DRIFT for their chemical composition. Samples with a layer thickness up to 100 nm were analyzed by DRIFT spectroscopy. An O_2-plasma treated HDPE sample was used as a background sample for the measurements, since an oxygen plasma was used for every sample to clean and activate the surface before the a-C:H layer was applied. DRIFT spectra are evaluated on the basics of infrared spectroscopy [19] and according to previous results of other groups and own observations [10,16,23,29,30,31]. The peaks for the $=CH_2$ and $-CH_3$ carbon bonds are in the C−H stretching area at 2800–3500 cm^{-1} [10,19,29,30].

However, the results obtained with DRIFT do not correspond to those achieved with X-ray spectroscopy. In these investigations only the sp^3 CH_2 oscillations (both symmetrical and asymmetrical) could be

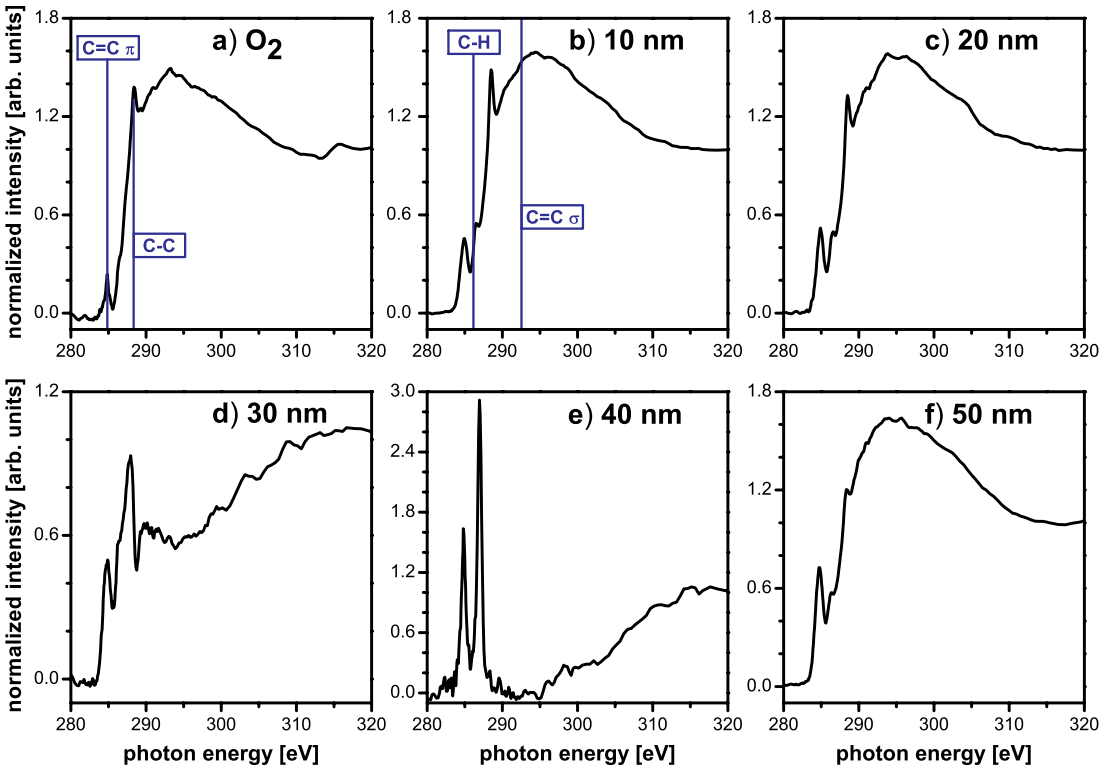

Fig. 2. NEXAFS spectra for O_2 (0 nm) to 50 nm as individual plots. From 2 b) to 2 d) the turning point for the end of the interlayer is obvious by the significant spectral change.

detected (Fig. 4).

For both oscillations a shift forward as well as a shift-back of the corresponding wave numbers is visible. At the beginning the peak for the asymmetric oscillation is 2927 cm^{-1} and the peak for the symmetric oscillation is 2854 cm^{-1} for the 10 nm a-C:H layer [10,29,30]. On thickness increased to 20 nm, both oscillations result in a shift of eleven wave numbers back to 2916 cm^{-1} and 2843 cm^{-1}, respectively. This backwards shift indicates a smaller carbon-hydrogen binding energy and therefore a larger carbon-hydrogen bond distance for the $=CH_2$ group [19]. In addition, the peaks become more pronounced with increasing layer thickness. As the layer thickness continues, a shift back occurs, which is completed at 40 nm layer thickness. Here the observed peaks lie again on their original measured position.

As the thickness of the layer continues to increase, there is only a very small shift of 5 cm^{-1} towards smaller wave numbers. At 50 nm the peaks have their strongest characteristics and decrease in their intensity towards the 100 nm layer thickness. Considering the greater penetration depth of the IR investigations, this corresponds to the behavior of the sp^3 bonds resulting from X-ray spectroscopic investigations.

The extreme shift of the oscillations in the measurements for thin film thicknesses, which shifts back to its original value at 40 nm, is noticeable. This can also be an indication for the completion of

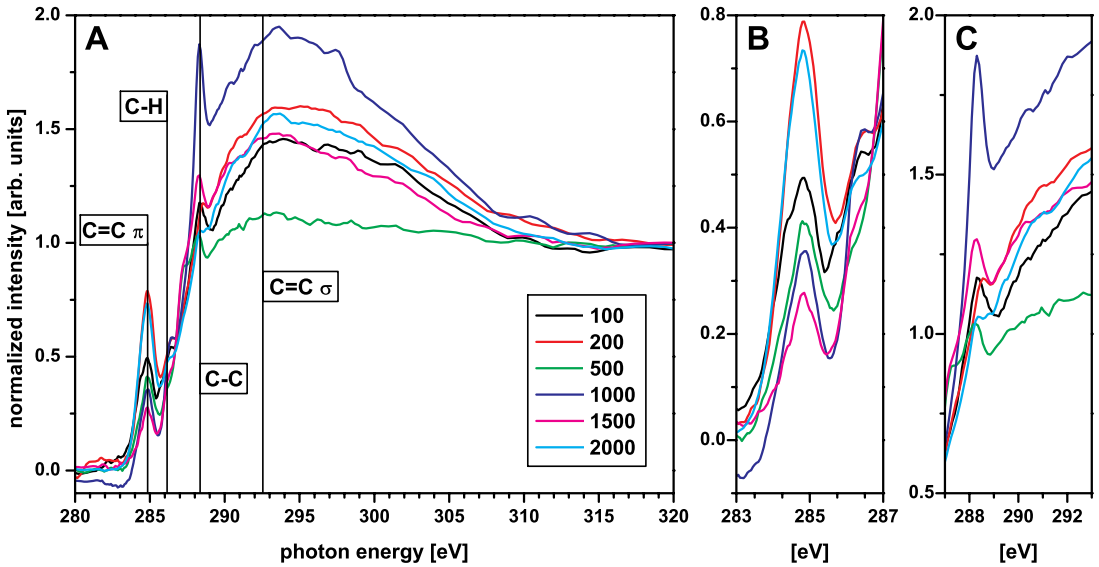

Fig. 3. NEXAFS spectra for the a-C:H layer thickness 100 nm (black), 200 nm (red), 500 nm (green), 1000 nm (blue), 1500 nm (magenta), and 2000 nm (yellow) on HDPE. Figure **A** shows the full spectrum, **B** and **C** zoom magnifications of the region of 283 eV to 287 eV and 287 eV to 293 eV.

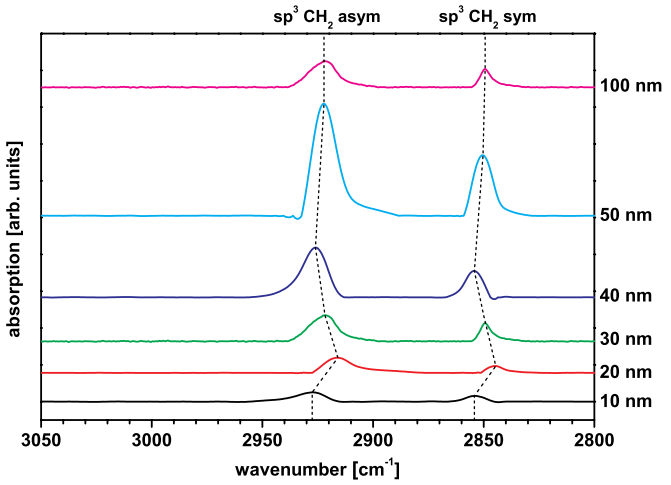

Fig. 4. DRIFT spectra of HDPE samples coated with a-C:H layers of different thickness from 10 up to 100 nm showing sp^3 CH_2 asymmetric and symmetric peaks.

interlayer formation. The chemical environment of the obtained layer during the formation of the interlayer is different due to the mixed phase of the a-C:H layer with the polymer than in the further process of the coating. Therefore, there is also an indication for an interlayer here, which forms at the beginning of the coating of HDPE with an a-C:H layer and is completed again at a layer thickness of 40 nm as the turning point.

In Fig. 5 the absorption curves obtained by diffuse reflectance infrared Fourier transform (DRIFT) spectroscopy for the a-C:H layers in the range from 100 nm to 2000 nm deposited on commercial HDPE are plotted. As for the thin layers, the so-called C—H stretching region between 2800 cm^{-1} and 3050 cm^{-1} is considered and an O_2-plasma treated sample served as the reference. Here, too, it is noticeable that only absorption peaks for the sp^3 CH_2 symmetric and asymmetric oscillation could be measured. If the a-C:H layer thickness is increased from 100 nm to 500 nm, both peaks perform a slight shift to lower wave numbers, which is again due to a variation of the bond length.

If the layer thickness increases to 1000 nm, two major changes can be observed: on the one hand, both peaks show a large shift-back to higher wavenumbers indicating a changing chemical composition of the layer. On the other hand, the absorption peaks change their orientation

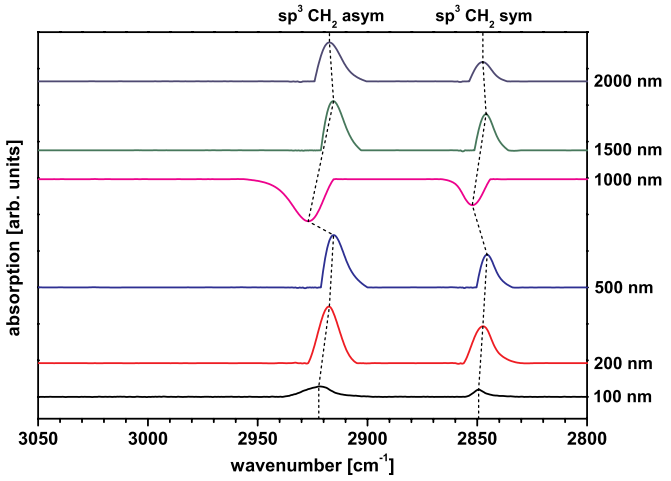

Fig. 5. DRIFT spectra of HDPE samples coated with a-C:H layers of different thickness from 100 up to 2000 nm showing the sp^3 CH_2 asymmetric and symmetric peaks. The 100 nm result is added for comparison with the thin layers (Fig. 4).

to negative. This means for the binding ratio that in comparison to the uncoated, O_2-plasma activated HDPE reference sample there are significantly less sp^3 bonds present. The dehydrogenation of the deposited a-C:H layer can also be seen here: sp^3 bonds are broken, the hydrogen bound there is removed and sp^2 bonds are created, which are again not sufficiently visible in these DRIFT measurements. The discrepancy between the DRIFT and the XPS and NEXAFS measurements is again visible here. While the dehydrogenation there also extends over the 1500 nm sample, it is only visible here at the 1000 nm layer thickness. However, the 1500 nm layer thickness shows DRIFT results which are comparable with the 500 nm layer thickness.

The discrepancy between the XPS/NEXAFS and the DRIFT measurements could be due to the different penetration depths. In addition, the DRIFT measurements of the HDPE and the coated HDPE samples show some problems such as the absence of sp^2 absorption peaks, which could also be responsible for the deviations.

4. Conclusion

In addition to previous data from atomic force microscopy, Raman spectroscopy and contact angle measurements, explicit surface sensitive, synchrotron based X-ray spectroscopic investigations with XPS and NEXAFS as well as complementary infrared spectroscopic investigations were performed in this study for a precise specification of the a-C:H layer obtained chemical composition. This is indispensable to understand the formation and growth of the a-C:H layers on polymers. With this knowledge it will be possible to customize these carbon layers for specific applications. Furthermore, the current investigation focused on two areas: In the range of thin layers from 10 nm to about 100 nm to investigate the interlayer formation between the raw material and the applied a-C:H layer. Secondly in thicker layers up to 2000 nm to examine further the dehydrogenation process of the increasing a-C:H layer by X-ray spectroscopy and DRIFT measurements on the top surface. The results obtained indicate the completion of interlayer formation at an a-C:H layer thickness of about 40 nm. There is a clear change in the binding ratios according to NEXAFS measurements. The XPS data shows a change from more sp^3 bound carbon atoms to a sp^2 enhanced structure of the applied layer and in the DRIFT spectra a shift back occurs at 40 nm.

The dehydrogenation process in the increasing a-C:H layers could also be confirmed. With XPS it seems to get started after a layer thickness of 500 nm, in the DRIFT and NEXAFS spectra significantly from a layer thickness of 1000 nm. In sum this leads again to a reduced sp^3 content and a correspondingly high proportion of sp^2 bonds in the thicker a-C:H layers, although the ratio after the interlayer completion and ongoing depositions were reversed accordingly. The application of surface sensitive techniques as XPS, NEXAFS and DRIFT made it possible to more precisely specify the dimension of the interlayer from a-C:H layers on commercially available HDPE. The turning point is located at a thickness of 40 nm where the interlayer formation is completed and the normal growth of the a-C:H layer starts.

Acknowledgements

The authors thank Dr. Heinz Busch and Dr. Falk Bernsmann (NTTF Coatings GmbH, Rheinbreitbach, Germany) for the industrial coating of the samples and Prof. Dr. Joachim Scholz (University of Koblenz-Landau, department of chemistry) for the DRIFT equipment. The authors also want to thank Dr. Alexei Nefedov from KIT (Karlsruhe Institute for Technology, Group: Chemistry of oxidic and organic interfaces; X-ray and Electron Spectroscopy at Interfaces) for beamtime support. We thank HZB for the allocation of synchrotron radiation beamtime. TS, WR and CF thankfully acknowledge the financial support by the Helmholtz-Zentrum Berlin (HZB).

References

[1] L. Sabbatini, Polymer Surface Characterization, De Gruyter, Berlin, Boston, 2014.
[2] A. Grill, Diamond-like carbon coatings as biocompatible materials—an overview, Diam. Relat. Mater. 12 (2003) 166–170, https://doi.org/10.1016/S0925-9635(03)00018-9.
[3] C.B. Fischer, M. Rohrbeck, S. Wehner, M. Richter, D. Schmeißer, Interlayer formation of diamond-like carbon coatings on industrial polyethylene, Appl. Surf. Sci. 271 (2013) 381–389, https://doi.org/10.1016/j.apsusc.2013.01.210.
[4] R.K. Roy, K.-.R. Lee, Biomedical applications of diamond-like carbon coatings: a review, J. Biomed. Mater. Res. Part B: Appl. Biomater. 83B (2007) 72–84, https://doi.org/10.1002/jbm.b.30768.
[5] M. Rohrbeck, C.B. Fischer, S. Wehner, J. Meier, W. Manz, DLC-coated pure bioplastic foil, Vak. Forsch. Prax. 26 (2014) 42–47, https://doi.org/10.1002/vipr.201400549.
[6] M. Rohrbeck, S. Körsten, C.B. Fischer, S. Wehner, B. Kessler, Diamond-like carbon coating of a pure bioplastic foil, Thin Solid Films 545 (2013) 558–563, https://doi.org/10.1016/j.tsf.2013.07.028.
[7] Y. Tachimoto, M. Noborisaka, A. Shirakura, C. Kuroyanagi, T. Suzuki, Gas barrier properties of diamond-like carbon films synthesized by using remote type microwave plasma CVD under sub-ambient atmospheric pressure, J. Phys.: Conf. Ser. 417 (2013) 012043, , https://doi.org/10.1088/1742-6596/417/1/012043.
[8] J. Robertson, Diamond-like amorphous carbon, Mater. Sci. Eng. R 37 (2002) 129–281, https://doi.org/10.1016/S0927-796X(02)00005-0.
[9] J. Robertson, Plasma deposition of diamond-like carbon, Jpn. J. Appl. Phys. 50 (2011), https://doi.org/10.1143/JJAP.50.01AF01 01AF01.
[10] P. Koidl, C. Wild, B. Dischler, J. Wagner, M. Ramsteiner, Plasma deposition, properties and structure of amorphous hydrogenated carbon films, Mater. Sci. Forum 52-53 (1991) 41–70, https://doi.org/10.4028/www.scientific.net/MSF.52-53.41.
[11] A. Catena, T. McJunkin, S. Agnello, F.M. Gelardi, S. Wehner, C.B. Fischer, Surface morphology and grain analysis of successively industrially grown amorphous hydrogenated carbon films (a-C: H) on silicon, Appl. Surf. Sci. 347 (2015) 657–667, https://doi.org/10.1016/j.apsusc.2015.04.113.
[12] T. Hasebe, A. Hotta, H. Kodama, A. Kamijo, K. Takahashi, T. Suzuki, Recent advances in diamond-like carbon films in the medical and food packing fields, New Diam. Front. Carbon Technol. 17 (2007) 263-79.
[13] T. Hoshida, D. Tsubone, K. Takada, H. Kodama, T. Hasebe, A. Kamijo, T. Suzuki, A. Hotta, Controlling the adhesion between diamond-like carbon (DLC) film and high-density polyethylene (HDPE) substrate, Surf. Coat. Technol. 202 (2007) 1089–1093, https://doi.org/10.1016/j.surfcoat.2007.07.087.
[14] J. Wang, N. Huang, C.J. Pan, S.C.H. Kwok, P. Yang, Y.X. Leng, J.Y. Chen, H. Sun, G.J. Wan, Z.Y. Liu, P.K. Chu, Bacterial repellence from polyethylene terephthalate surface modified by acetylene plasma immersion ion implantation–deposition, Surf. Coat. Technol. 186 (2004) 299–304, https://doi.org/10.1016/j.surfcoat.2004.02.046.
[15] A. Catena, S. Agnello, L.M. Rösken, H. Bergen, E. Recktenwald, F. Bernsmann, H. Busch, M. Cannas, F.M. Gelardi, B. Hahn, S. Wehner, C.B. Fischer, Characteristics of industrially manufactured amorphous hydrogenated carbon (a-C:H) depositions on high-density polyethylene, Carbon 96 (2016) 661–671, https://doi.org/10.1016/j.carbon.2015.09.101.
[16] A. Catena, M.R. Kunze, S. Agnello, F.M. Gelardi, S. Wehner, C.B. Fischer, Amorphous hydrogenated carbon (a-C:H) deposigtions on polyoxymethylene: substrate influence on the characteristics of the developing coatings, Surf. Coat. Technol. 307 (2016) 658–665, https://doi.org/10.1016/j.surfcoat.2016.09.064.
[17] A. Nefedov, C. Wöll, Advanced applications of nexafs spectroscopy for functionalized surfaces, in: G. Bracco, B. Holst (Eds.), Surface Science Techniques, Springer, Berlin Heidelberg, Berlin, Heidelberg, 2013, pp. 277–303.
[18] T. Armaroli, T. Bécue, S. Gautier, Diffuse reflection infrared spectroscopy (Drifts), Oil Gas Sci. Technol. 59 (2004) 215–237, https://doi.org/10.2516/ogst:2004016.
[19] H. Günzler, H.-.U. Gremlich, IR Spectroscopy: an Introduction, Wiley-vch, Weinheim, 2002http://www.loc.gov/catdir/description/wiley033/2002283667.html.
[20] J.L. Solomon, R.J. Madix, J. Stöhr, Orientation and absolute coverage of benzene, aniline, and phenol on Ag(110) determined by NEXAFS and XPS, Surf. Sci. 255 (1991) 12–30, https://doi.org/10.1016/0039-6028(91)90008-G.
[21] F.C. Tai, S.C. Lee, C.H. Wei, S.L. Tyan, Correlation between ID/IG ratio from visible raman spectra and sp2/sp3 ratio from XPS spectra of annealed hydrogenated DLC film, Mater. Trans. 47 (2006) 1847–1852, https://doi.org/10.2320/matertrans.47.1847.
[22] P.M. Dietrich, T. Horlacher, P.-.L. Girard-Lauriault, T. Gross, A. Lippitz, H. Min, T. Wirth, R. Castelli, P.H. Seeberger, W.E.S. Unger, Adlayers of dimannoside thiols on gold: surface chemical analysis, Langmuir 27 (2011) 4808–4815, https://doi.org/10.1021/la104038q.
[23] A. Catena, Q. Guo, M.R. Kunze, S. Agnello, F.M. Gelardi, S. Wehner, C.B. Fischer, Morphological and chemical evolution of gradually deposited diamond-like carbon films on polyethylene terephthalate: from subplantation processes to structural reorganization by intrinsic stress release phenomena, ACS Appl. Mater. Interfaces 8 (2016) 10636–10646, https://doi.org/10.1021/acsami.6b02113.
[24] J. Stöhr, NEXAFS Spectroscopy; Springer Series in Surface Sciences 25, Springer, Berlin, Heidelberg, 1992.
[25] J. Diaz, O.R. Monteiro, Z. Hussain, Structure of amorphous carbon from near-edge and extended x-ray absorption spectroscopy, Phys. Rev. B 76 (2001) 125204, , https://doi.org/10.1103/PhysRevB.76.0125204.
[26] J. Díaz, S. Anders, X. Zhou, E.J. Moler, S.A. Kellar, Z. Hussain, Analysis of the π^* and σ^* bands of the near absorption spectrum of amorphous carbon, Phys. Rev. B 64 (2007) 094201, , https://doi.org/10.1103/PhysRevB.64.094201.
[27] O. Dhez, H. Ade, S. Urquhart, Calibrated NEXAFS spectra of some common polymers, J. Electron. Spectrosc. Relat. Phenom. 128 (2003) 85–96, https://doi.org/10.1016/S0368-2048(02)00237-2.
[28] I. Ahmad, S.S. Roy, M.A. Rahman, T.I.T. Okpalugo, P.D. Maguire, J.A. McLaughlin, Substrate effects on the microstructure of hydrogenated amorphous carbon films, Curr. Appl. Phys. 9 (2009) 937–942, https://doi.org/10.1016/j.cap.2008.09.006.
[29] E. Tomasella, L. Thomas, M. Dubois, C. Meunier, Structural and mechanical properties of a-C, Diam. Relat. Mater. 13 (2004) 1618–1624, https://doi.org/10.1016/j.diamond.2004.01.017.
[30] M. Veres, M. Koós, I. Pócsik, IR study of the formation process of polymeric hydrogenated amorphous carbon film, Diam. Relat. Mater. 11 (2002) 1110–1114, https://doi.org/10.1016/S0925-9635(02)00011-0.
[31] T. Schlebrowski, L. Beucher, H. Bazzi, B. Hahn, S. Wehner, C.B. Fischer, Prediction of a-C:H layer failure on industrial relevant biopolymer polylactide acide (PLA) foils based on the sp^2/sp^3 ratio, Surf. Coat. Tech. 368 (2019) 79–87, https://doi.org/10.1016/j.surfcoat.2019.03.069.

Diamond & Related Materials

Influence of cellulose microfiber reinforcement for polyvinyl alcohol on the layer growth of plasma-deposited a-C:H

--Manuscript Draft--

Manuscript Number:	
Article Type:	Research Paper
Section/Category:	Tetrahedral Amorphous and Other Diamond-Like Carbons
Keywords:	cellulose microfibers based polymer composite; plasma-enhanced chemical vapour deposition (PECVD); sp2/sp3 content evaluation; surface morphology; synchrotron based spectroscopy; wettability
Corresponding Author:	Christian B. Fischer University Koblenz-Landau Koblenz, Germany
First Author:	Torben Schlebrowski
Order of Authors:	Torben Schlebrowski
	Zineb Kassab
	Mounir El Achaby
	Stefan Wehner
	Christian B. Fischer
Manuscript Region of Origin:	Europe
Abstract:	Pure polyvinyl alcohol (PVA) and PVA reinforced with cellulose microfibers (PVA/CMF) composite films were coated with amorphous carbon layers (a-C:H, 50 and 100 nm thick) using radio frequency plasma enhanced chemical vapour deposition (RF-PECVD). The effects of cellulose microfibers on the polymer coatability were investigated. Deposited carbon layers were characterized surface morphologically by ex-situ atomic force microscopy (AFM). In addition, surface wettability was checked by contact angle (CA) measurements. The chemical composition was analysed by surface sensitive synchrotron X-ray based techniques (near edge X-ray absorption fine structure (NEXAFS) and X-ray photoelectron spectroscopy (XPS)) and diffuse reflectance infrared Fourier transform spectroscopy (DRIFT).
Suggested Reviewers:	Tom Lindfors, Prof. PhD Åbo Akademi University Tom.Lindfors@abo.fi Expert in composite materials concerning thin carbon (graphene) films and their properties.
	Yongxin Wang, Prof. PhD Ningbo Institute of Industrial Technology Chinese Academy of Sciences yxwang@nimte.ac.cn He is expert in microstructure analytics and tribology of especially CVD generated coatings.
	Andreas Markwitz, PhD The Institute of Geological & Nuclear Sciences Limited A.Markwitz@gns.cri.nz He is expert in nanomaterials analysis and deposition of thin films.

University Koblenz-Landau · Department of Physics · D - 56070 Koblenz

To

Elsevier

Diamond and Related Materials

Editorial board

University Koblenz-Landau
Department of Physics
Prof. (UM6P) Dr. Christian Fischer
Universitätsstraße 1
56070 Koblenz, Germany

Telefon +49261 287 2345
Telefax +49261 287 100 2345
E-Mail chrbfischer@uni-koblenz.de

June 5, 2020

Manuscript submission for consideration as full paper

Dear Prof. Dr. Ken Haenen,

Dear editorial board,

With this letter, we are submitting an original research manuscript entitled:

"Influence of cellulose microfiber reinforcement for polyvinyl alcohol on the layer growth of plasma-deposited a-C:H"

In the presented work a-C:H coatings of 50 and 100 nm were successfully deposited by plasma-enhanced chemical vapor deposition (PECVD) on the biocompatible, non-toxic and biodegradable polymer poly vinyl alcohol (PVA) by using acetylene. Additionally the PVA was used as composite reinforced with naturally derived cellulose microfibers (PVA/CMF) and compared to the pristine polymer material. Here especially the top surface of both PVA types is analyzed with several methods including synchrotron based techniques (at the synchrotron facility BESSYII, Berlin, Germany): topography by atomic force microscopy (AFM), chemical composition by diffuse reflectance infrared Fourier transform (DRIFT), X-ray photoelectron spectroscopy (XPS) and near edge X-ray absorption fine structure (NEXAFS), and wettability by contact angle.

The biocompatible, non-toxic and biodegradable PVA is a possible alternative to conventional plastics. Its intrinsic properties can be improved by adding fillers, like here naturally derived fibers, but its surface characteristics for functional applications are somehow limited. This subject is of great relevance since carbon coatings like diamond-like carbon (DLC) or amorphous hydrogenated carbon (a-C:H) on polymers are strongly considered as antibacterial coverings in medical or health care, as abrasive wear protection in automotive industry but also for the packaging industry etc. as these coatings change the environmental behaviors of the polymers with suitable and designable surface functionalization. Therefore, it is very important to know the detailed morphology and chemical composition of deposited carbon films on diverse polymers and if there is an effect, when additives/fillers are used to improve their characteristics. This understanding will result in the production of suitable carbon coatings tailored to various applications.

Highlights of the current paper are:

- Effective coating of PVA and PVA/CMF with stable a-C:H films
- Topmost chemical composition of sp^3/sp^2 changes with thickness and basic material
- Effects of cellulose microfibers (CMF) on the resulting surface characteristics are investigated
- Substrate effects detectable due to used CMF fillers

The manuscript contains original data clearly demonstrating that surface changes occur between PVA and the composite PVA/CMF when coated with thin a-C:H layers revealing substrate effects of the used filler material. We were able to identify significant changes in the chemical composition of the respective surfaces and for the increasing thickness.

=> **Prime novelty statement**

Amorphous carbon layers (a-C:H) were successfully deposited on polyvinyl alcohol (PVA) and cellulose microfiber (CMF) reinforced PVA. Differences in the chemical composition of deposited carbon layers (sp^2/sp^3) were detected with synchrotron based techniques in combination with changes in their morphology and wettability showing clear substrate effects when used with microfiber reinforcement.

In summary, we are convinced that these findings are very interesting for the diamond (-like carbon) community esp. material scientists and researchers using plasma deposition methods for processing thin films on polymeric materials. Therefore, we consider “Diamond and Related Materials” for the most suitable journal to publish our research work. We would appreciate if you agree on this and hope for a sympathetic reception.

All references mentioned in the reference list are cited in the text, and vice versa. Additionally they are adjusted to the journal style and journal abbreviations were checked according to CASSI.

The manuscript is spell and grammar checked.

There are no existing previous or concurrent submissions of the current manuscript send to other publishers.

Declarations of interest: none

Best regards

Christian Fischer

Highlights

- Effective coating of PVA and PVA/CMF with stable a-C:H films
- Topmost chemical composition of sp^3/sp^2 changes with thickness and basic material
- Effects of cellulose microfibers (CMF) on the resulting surface characteristics are investigated
- Substrate effects detectable due to used CMF fillers

Graphical Abstract

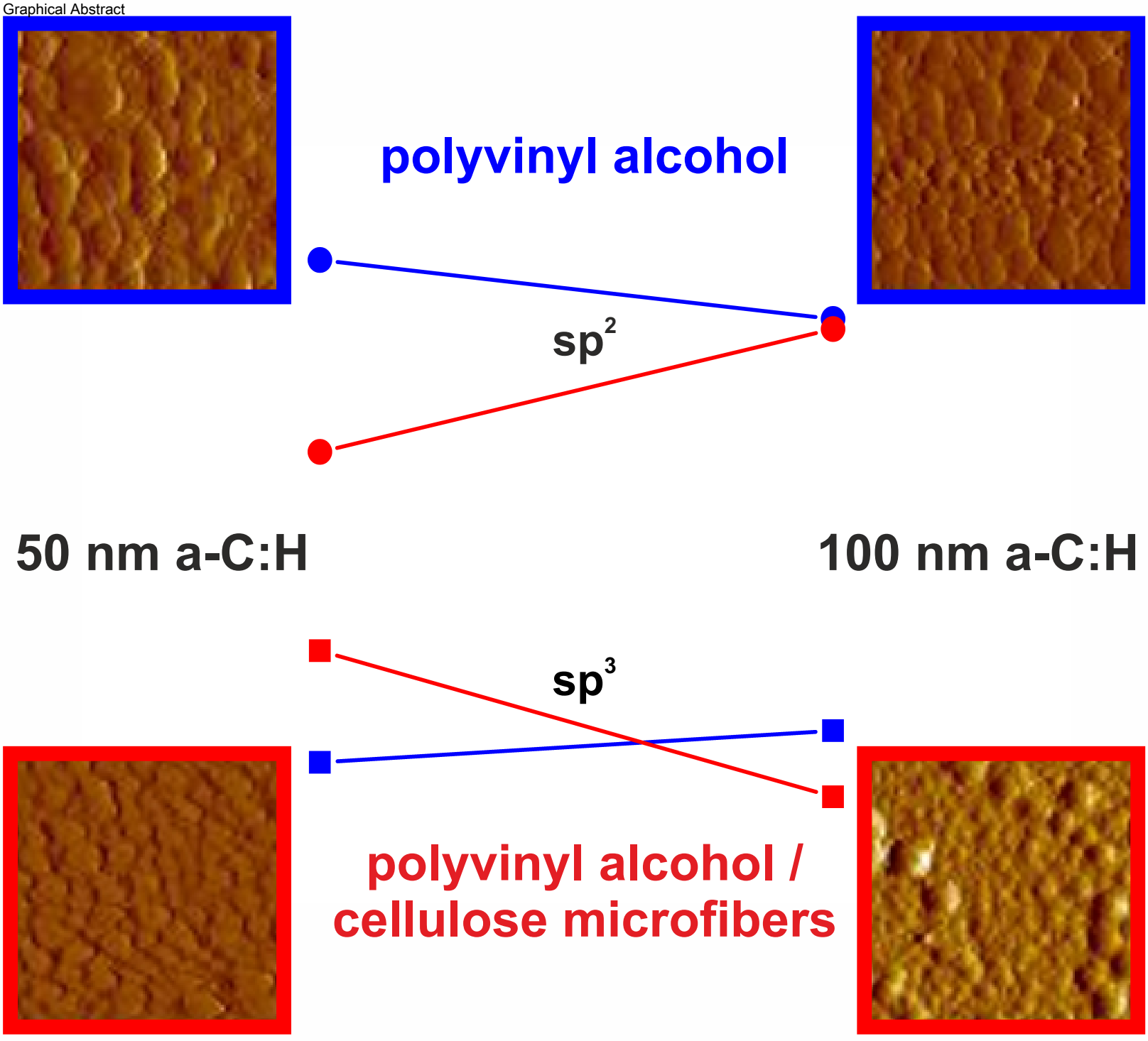

Influence of cellulose microfiber reinforcement for polyvinyl alcohol on the layer growth of plasma-deposited a-C:H

Torben Schlebrowski[1], Zineb Kassab[2,3], Mounir El Achaby[2], Stefan Wehner[1], Christian B. Fischer[1,2]*

[1] Department of Physics, University Koblenz-Landau, 56070 Koblenz, Germany

[2] Materials Science, Energy and Nano-engineering Department, Mohammed VI Polytechnic University, 43150 Ben Guerir, Morocco

[3] Laboratoire d'Ingénierie et Matériaux (LIMAT), Faculté des Sciences Ben M'sik, Université Hassan II de Casablanca, B.P.7955, Casablanca, Morocco

* E-mail: chrbfischer@uni-koblenz.de

Abstract

Pure polyvinyl alcohol (PVA) and PVA reinforced with cellulose microfibers (PVA/CMF) composite films were coated with amorphous carbon layers (a-C:H, 50 and 100 nm thick) using radio frequency plasma enhanced chemical vapour deposition (RF-PECVD). The effects of cellulose microfibers on the polymer coatability were investigated. Deposited carbon layers were characterized surface morphologically by ex-situ atomic force microscopy (AFM). In addition, surface wettability was checked by contact angle (CA) measurements. The chemical composition was analysed by surface sensitive synchrotron X-ray based techniques (near edge X-ray absorption fine structure (NEXAFS) and X-ray photoelectron spectroscopy (XPS)) and diffuse reflectance infrared Fourier transform spectroscopy (DRIFT).

Keywords

cellulose microfibers based polymer composite; plasma-enhanced chemical vapour deposition (PECVD); sp^2/sp^3 content evaluation; surface morphology; synchrotron based spectroscopy; wettability

1 Introduction

Biodegradable polymer-based composite materials reinforced with naturally derived fillers, especially cellulose, are becoming increasingly important due to their interesting properties and diverse applications [1–5]. Polyvinyl alcohol (PVA) is a biocompatible, non-toxic and biodegradable synthetic polymer with good film-forming properties, high crystallinity, flexibility, good chemical stability, and water-solubility [6–9]. Owing to the presence of hydroxyl groups on its macromolecular chains, PVA can promote the formation of hydrogen bonds with cellulosic functional groups. Therefore, the incorporation of cellulosic charge within PVA matrix is suitable to achieve enhanced properties [3,4]. Nevertheless, these materials still have certain disadvantages of surface properties such as low hardness and low abrasion resistance, which limit their applications [10,11].

A frequently used method to modify the surface properties of polymers is the application of hydrogenated amorphous carbon (a-C:H) layers. Here, the carbon is π and σ bound containing sp^2 as well as sp^3 clustered connections. The sp^2 clusters are limited to short chains embedded in a sp^3 matrix of carbon and hydrogen. The physical properties of the surfaces can be controlled by varying the plasma parameters, the gas used and the amount of hydrogen atoms in the plasma that crosslink the subsurface of the layer [12–16]. The resulting ratio of sp^2 to sp^3 hybridized carbons directly determines the properties of the layer. Diamond-like properties such as high hardness, chemical inertness or high electrical resistance are caused by a high sp^3 to sp^2 ratio [12]. If the sp^3 to sp^2 ratio is reduced, a graphite-like layer is obtained which is less robust and has improved electrical conductivity [12]. The change in chemical composition affects the overall wettability resp. contact angle behaviour of the deposited carbon layer. In addition, the layer thickness also determines the ratio of sp^2 to sp^3 as reported for several polymers and biopolymers [11,17–21].

A widely used process for depositing such a-C:H layers is chemical vapour deposition (CVD), which can be additionally supported by the use of radio frequency induced plasma (RF-

PECVD) [12,16,19,22]. The RF-PECVD process has the advantage that it operates at low temperatures and can also coat non-conductive substrates [12,17].

In the present study, a-C:H layers of 50 and 100 nm are realized on pure and with cellulose microfibers reinforced PVA (PVA/CMF) using the RF-PECVD technique and acetylene plasma as carbon source. The aim is to investigate how the fibre affects the basic coatability of the polymer and whether the resulting layers differ significantly. The surface morphology of deposited carbon layers was investigated ex-situ by atomic force microscopy (AFM). Diffuse Reflectance Infrared Fourier Transform (DRIFT) and surface sensitive synchrotron X-ray based techniques as near edge X-ray absorption fine structure (NEXAFS) and X-ray photoelectron spectroscopy (XPS) were used to study their chemical composition. In addition, contact angle measurements (CA) were performed to evaluate the relationship between sp^2/sp^3 ratios on a macroscopic scale.

2 Experimental Section

2.1 Samples preparation

Cellulose microfibers (CMF), neat PVA and 5 wt% CMF reinforced PVA (PVA/CMF) films were prepared as described in our previous work [9]. Briefly, CMF were extracted from ground Juncus plant stems using prewashed with distilled water, alkali-treatment with 4 wt% NaOH solution followed by bleaching treatment with a solution made up of equal parts (v:v) of acetate buffer (pH 4.8) (27 g NaOH and 75 mL glacial acetic acid, diluted to 1 L of distilled water) and aqueous sodium chlorite (1.7 wt% NaClO2 in water). Resulting in CMF with an average microfiber diameter of 3.5 ± 1.3 µm and a crystallinity index of 75 %. The solvent-casting method was used for the preparation of neat PVA and CMF reinforced PVA (PVA/CMF) composite films. Thus, PVA powder was dissolved in distilled water; meanwhile, an aqueous suspension containing the desired amount of CMF 5 wt% of CMF was prepared and ultrasonicated for 5 min and added to PVA solution, resulting in 5 wt% CMF filled PVA

mixture. The obtained mixture was mixed for 30 min at room temperature, then poured onto Petri dishes and air-dried in laboratory hood at room temperature for 72 h to evaporate the water. Neat PVA film was also prepared according to the same process but without the addition of CMF.

2.2 Coating process

For the coating of the samples, PVA and PVA/CMF samples were fixed on a vacuum-suitable aluminium sample holder and placed in a high-vacuum chamber. The coating in the process chamber is realized with a high frequency (HF, 13.65 MHz) plasma source (Copra DN 400, CCR GmbH, Troisdorf, Germany) [22]. For the activation and cleaning of the sample surface, all samples were pretreated with an O_2 plasma (RT, pressure 1 Pa, flux 65 sccm/min, power 200 W, active plasma duration 10 min) before carbon coating [11,18–21,23,24]. After the O_2 plasma treatment, the polymer samples were treated with an C_2H_2 plasma (RT, pressure 0.65 Pa, flux 65 sccm/min, power 107 W) resulting in the a-C:H layers [18,19,23,24]. The deposition rate is about 10 nm/min and approximately constant over time [23]. A smaller variation is present during the initial growth. No external BIAS was applied for the process, but a SELF-BIAS of -20 V (average value) develops on the sample during the coating process. In previous studies by Kleinen et al. with the setup used here, ion energies between 15 eV and 25 eV and current densities between 0.1 and 0.2 were determined $\mu A\ cm^{-1}$ [17,25,26]. The entire process is described in detail elsewhere [25,26]. By doubling the coating time from 5 to 10 minutes two different a-C:H layer thicknesses of 50 nm and 100 nm can be achieved. The distance between plasma source and samples was kept at 275 mm during the entire plasma process [23]. By placing the sample surface directly in front of the plasma source, r-type DLC coating was obtained [18,19,24], which has a higher degree of cross-linked sp^3 carbon centres caused by a high number of subplantation processes present in the coating [23]. The coating parameters also ensure that the temperature of the substrate never exceeds 40°C and that all effects are not

caused by melting of the substrate [18]. In order to be able to determine the coating thickness afterwards, additional silicon wafers (Silicon Materials, Kaufering, Germany), one half of each one was covered with aluminia foil, were mounted on the aluminum sample holders. The thickness of the applied layer was determined with a profilometer (Dektak 3, Veeco Instruments Inc., Plainview, NY, USA).

2.3 Surface topography and wettability

The surface topography of the samples was examined by Atomic Force Microscopy (AFM, Omicron nanoTechnology GmbH, Taunusstein, Germany). The AFM was operated in contact mode with standard silicon nitride PNP-TR cantilevers (NanoAndMore GmbH, Wetzlar, Germany) at RT and ambient air conditions. To avoid tip sample convolution and tip blend the tips were regularly checked with cellulose acetate replica (Pelco, calibration specimen for atomic force microscopy, 607-AFM) of a 2.160 lines/mm waffle pattern diffraction grating. The measuring range was 5 µm × 5 µm. All measurements were performed atat least three different positions on the samples to ensure that the measurements were performed correctly and that no image errors occurred.

To investigate the surface wettability of the different samples, contact angle measurements were performed. Therefore, the sessile drop technique was performed on a contact angle goniometer (OCA15EC, Dataphysics Instruments GmbH, Filderstadt, Germany) at room temperature and in ambient air. A dosing needle deposits a drop of water of HPLC quality (CHEMSOLUTE®) with a volume of 1 µl on the sample surface. Afterwards the contact angles left and right of the drops are measured. The measurements were repeated at least at five different locations on each sample surface to check the homogeneity and to determine the mean value.

2.4 Chemical composition

To investigate the binding states and chemical composition of the carbon layers, both infrared based DRIFT spectroscopy and X-ray based techniques XPS- and NEXAFS were used. The XPS and NEXAFS data were collected at the beamline HE-SGM at Helmholtz-Zentrum Berlin during the low-alpha phase. The beamline system and the detector are described elsewhere [27]. Additionally, the system is equipped with a floodgun to prevent charge-induced effects on the sample surface.

Diffuse Reflectance Infrared Fourier Transform (DRIFT) measurements were performed to measure the chemical surface properties. A Shimadzu Fourier transform spectrometer (IRPrestige-21, Kyoto, Japan) equipped with the DRS-8000 diffuse reflectance instrument was used in ambient air at ambient temperature [28,29]. Two different spectra were recorded: First, the full spectrum from 500-4000 cm^{-1} (resolution: 4 wave numbers, 100 repetitions) to evaluate the thickness-dependent influence on the chemical surface structure. Subsequently, a detailed measurement for the most relevant spectral range of 2800-3100 cm^{-1}, the C-H-streching-region [30,31] was performed with a resolution of 1 wave number and 300 repetitions. Both measurements were repeated at least at three different positions on the sample surface to ensure surface homogeneity. The overall reference for the analysis of the a-C:H data and the measurements themselves is the raw polymer PVA or PVA/CMF, each treated with O_2 plasma. The spectral analysis was performed with the commercial IR-Solution - FTIR Control Software (software version 1.30, Shimadzu Corporation, Kyoto, Japan). First a multipoint baseline was inserted with the integrated manipulation tool, followed by a software integrated smoothing manipulation (changes only the appearance of the graph, but not the information).

For the XPS measurements, a complete measurement spectrum (700 eV - 0 eV) was first recorded to get an overview of the entire chemical composition of the surface. In order to analyse the different bonding states of the carbon atoms, the C1s peak was examined at least at two different sample sites. These repeated measurements were performed to check the reproducibility and to evaluate the homogeneity and stability of the a-C:H layers. The C1s

spectra were analysed with the commercially available software CasaXPS (software version 2.3.18, Casa Software Ltd., United Kingdom). The percentages of sp^2, sp^3, C-O and C=O bonds in the entire C1s peak were identified and evaluated. The results obtained were then applied to the corresponding layer thicknesses using Origin 8.1 software.

In the NEXAFS series, both the C K- and O K-edges of the samples were recorded. The C-edge was also recorded at a minimum of two locations to assist in the accuracy of the measurements. The O-edges were used to detect the presence or absence of oxygen on the sample surface. All measurements have been performed in the "magic angle" at a photon incidence angle of 55° with the partial electron yield (PEY). In PEY, a counter voltage is applied and not all electrons emerging from the material can reach the measurement electronics. Therefore the measurement is more surface sensitive [27]. The spectra obtained from the C K-edges were analysed using the commercial Origin software. For this purpose, the spectra were first normalized and then adjusted to the decreasing ring current present at the BESSY experimental station during the low-alpha phase (100 mA decay mode). A correction for possible contamination of the grating by a previously measured gold edge was then performed. The individual steps were summarized in the paper by Watts et al. and described in detail elsewhere [32]. A further analysis was then performed using a self-written peak evaluation program and the Origin 8.1 software.

3 Results and Discussion

3.1 Morphology

The upper line in **Figure 1** of the AFM measurements show a relatively smooth, homogeneous surface for the untreated PVA. The most prominent structure visible for the PVA reference sample (Figure 1a) are some roundish, particle-like structures protruding from the material surface. These particles may be pellets of the raw polymer that have not completely merged with the surrounding material during the production process. If the material is O_2 plasma treated, a strong restructuring of the surface is visible (Figure 1b). The formerly smooth surface

is now covered with small craters, which is due to the roughening of the material by the plasma. These craters are also visible on the particles previously visible on the surface. With the deposition of a 50 nm a-C:H layer (Figure 1c), a homogeneous surface coating is visible. This layer consists of a grain-like structure forming a closed film. The diameter of these grains is about 150 nm. The visibility of this grain-like structure indicates the completion of the interlayer phase [10,22,24], since normal layer growth is taking place afterwards, as explained by Smith [33]. The interlayer is a mixture phase between the material and the applied layer. After it is completed, the normal a-C:H film growth starts and grains begin to form [22]. Some single grains, which are one level higher and are a little larger, are visible. When the thickness of the layer increases to 100 nm (Figure 1d), the surface appearance of the layer is similar to that of the 50 nm sample.

<Figure 1 here>

The bottom line of Figure 1 shows the AFM measurements for PVA/CMF samples. The surface of the reference sample (Figure 1e) looks somehow a little more corrugated than for the pure PVA samples. In addition, the particle-like structures as visible in Figure 1a are not present. With the O_2 plasma treatment of the PVA/CMF (Figure 1f), the surface is also more roughened here. However, there is no crater structure visible over the entire surface, but rather a fibrous structure, which is revealed here. If a 50 nm a-C:H layer is applied to the sample (Figure 1g), a homogeneous layer is formed here as well, which consists of a closed grain-like structure. The grain structure does not look as round as the unreinforced PVA, but the size of the grain-like components is the same for both materials. Also, as already visible with PVA, PVA/CMF shows some larger grains, which seem to be located a level higher. When the layer thickness reaches 100 nm (Figure 1h), the layer no longer consists of a closed, coarse grain-like layer, but appears much more homogeneous between the grains. A closer look shows that this homogeneous

surface consists of a very fine, granular layer. A comparison of the AFM images for PVA and the PVA/CMF shows that the surface structure of both materials is different and that the a-C:H layer grows with slight differences. The visible bigger grains for both materials at a film thickness of 50 nm is an indication for a completed interlayer between the basic material and the a-C:H layer. Similar behaviour have already been found on different materials [19,23,24].

3.2 **Surface wettability**

Figure 2 shows the contact angles determined for PVA and PVA/CMF samples. As before, measurement series were performed for untreated reference samples, the O_2 plasma treated ones and the coatings of 50 and 100 nm a-C:H.

<Figure 2 here>

Three factors are significantly involved in the wettability of surfaces: The interaction of surface chemical bonds [34–37], the different carbon hybridization states on the surface [38–40] and thirdly the different surface topographies [41–43]. Hydrogenation of the surface enhances the hydrophobic character, since dangling bonds are saturated by hydrogen and strong C-H bonds are formed. This leads to a weaker interaction between film and water [35–37]. If, on the other hand, the surface is oxygenated, the surface becomes more reactive with water, since oxygen-containing functional groups are formed on the surface [34]. A surface rich in sp^2 hybridized carbon shows a higher contact angle than a surface rich in sp^3 due to different surface free energies [38–40]. The surface free energy of an sp^3 dominated surface shows only weak polarity of the dangling bonds compared to an sp^2 hybridized surface due to its strongly covalent character [13,38].

Figure 2A shows the measurements for the PVA samples. The raw PVA has a contact angle of 75° and is therefore more hydrophilic. If the PVA is treated with an oxygen plasma, the contact

angle decreases to 32°, which is due to the strong oxygenation of the surface bonds. If a 50 nm thick a-C:H layer is applied to the PVA, the contact angle changes only imperceptibly to a slightly higher value. Additionally, the error bar increases, which is due to a rougher surface. With increasing the layer thickness to 100 nm, the contact angle again increases slightly, but the error of the measurement increases as well, indicating a rougher surface in line with the AFM topography.

The obtained contact angles for the PVA/CMF samples are shown in Figure 2B. The contact angle of the raw polymer is 59°, which is noticeably smaller than that for PVA itself. When the PVA/CMF is exposed to an oxygen plasma, the contact angle decreases to 32° and thus more or less the same value as the O_2 treated pure PVA. Here too, oxygenation of the surface bonds is responsible for the decay. With a layer thickness of 50 nm, the contact angle further drops to only 25°, but here again at the expense of a larger error. The further decrease of the contact angle is completely different to the a-C:H coated PVA and indicates a different (chemical) structure of the carbon layer on the CMF reinforced PVA. With a layer thickness of 100 nm the contact angle increases strongly and reaches a value of 66°, which is probably due to a more sp^3 hybridized surface. The finer graining of the surface visible in AFM, which makes the layer much more homogeneous, is also partly responsible for this change in the contact angle and the smaller error bar compared to the untreated PVA material. Again, the PVA/CMF behaves differently than the PVA. The layer, which was applied to the two different materials simultaneously in the same plasma, has a different character. Nevertheless, both systems show an overall hydrophilic behaviour.

3.3 **Chemical composition**

The chemical analysis of the surface composition was performed by XPS, NEXAFS and DRIFT measurements. First, the results of the XPS measurements are presented and interpreted, which are shown in **Figure 3**. The data analysis was carried out as described in the experimental

section. The peak positions have been confirmed by NIST database and the work of other groups [44–46].

<Figure 3 here>

Figure 3A shows the measurements for the PVA. As a raw polymer, most of its carbons are sp^2 hybridized and only a small part is sp^3 bound. The high sp^2 and low oxygen content is surprising. It is possible that more monomer chains of the original polymer are present at the surface, in which sp^2 bound carbon is contained. The low oxygen content could be traceable to an overlap of oxygen by carbon. With oxygen plasma treatment the hybridization of the carbon hardly changes, the sp^2 and sp^3 contents decrease only slightly in favour of a growing C-O content due to the oxidization of the polymer surface. This higher C-O content can also be clearly seen in the contact angle measurements, where the contact angle with the O_2 treatment drops sharply. If a 50 nm thick a-C:H layer is deposited on the material, the number of sp^2 bonded carbons increases to more than 85%, while the sp^3 bonded and C-O bonds decrease considerably. Therefore, the applied a-C:H layer is dominated by sp^2 bonded carbon. Comparing the results with the contact angle measurements, the contact angle also increases slightly. If the film thickness is increased to 100 nm, the proportion of sp^2 hybridized carbon drops to 77% while the proportion of sp^3 bonds increases slightly to 18%. With increasing plasma treatment duration of the surface and thus also increasing layer thickness, the proportion of sp^3 bonds in the carbon network of the layer begins to increase, which is due to a comparatively longer bombardment with (high-energy) ions [16].

The course of the PVA/CMF samples, which is shown in Figure 3B, is different from the PVA. The raw polymer shows a high sp^3 content of 66%, which explains the low contact angle of only 59° compared to the PVA. The proportion of sp^2 bonds is about 26%. This proportion is possibly traceable to the CMF fibres. With O_2 plasma treatment, both the proportion of sp^2 and

sp^3 hybridized carbons decrease in favour of C-O and C=O bonding. The XPS measurement proves the oxygenation of the surface, which was already suspected by the decrease of the contact angle. By applying a 50 nm a-C:H layer, the sp^2 bond becomes the dominant one on the surface. This has already been observed in the PVA samples, even though the coated PVA/CMF has only 58% of the sp^2 bond. The comparatively higher proportion of sp^3 bonds is probably due to the interlayer, which consists of a mixed phase of applied a-C:H layer and base material (which is strongly dominated by sp^3). As the thickness of the layer increases to 100 nm, the proportion of sp^2 bonds increases further and reaches 75%, while sp^3 bonds drop to 8%. This increase is responsible for the rising value in contact angle measurements. It is noticeable that the proportions of sp^2 bound carbon for 100 nm a-C:H correspond to PVA as well as to the reinforced PVA/CMF and are about 75% for both.

The XPS measurements show a clear difference in the chemical structures between raw PVA and PVA/CMF. The deposited layer shows different hybridization states for the respective basic polymer and composite and also in the further course of the coating they behave differently. The 50 nm layers applied to the two polymers differ strongly in their carbon bonds. Since the PVA/CMF raw material was more strongly sp^3 bonded than the PVA, there is relatively more carbon sp^3 bonded in the mixed phase of the layer and PVA/CMF, since the raw polymer is also incorporated in this phase. The fact that these sp^3 bonds are still visible at 50 nm suggests that at least the PVA/CMF has a distinct interlayer of not much less than 50 nm, since the penetration depth of the XPS is only a few nm. The PVA, on the other hand, has a strongly sp^2 dominated 50 nm a-C:H layer, since the raw material, which is brought into the interlayer here, is strongly sp^2 dominated. Since the a-C:H layer remains dominated by sp^2 in the further course of the coating process, it is difficult to draw conclusions about the thickness of the interlayer. By applying a 100 nm a-C:H layer the two layer systems are converging. While on the PVA a-C:H coating the sp^2 fraction decreases in favour of the sp^3 one, the sp^2 hybridization increases with the application of a thicker layer on PVA/CMF. For both systems, the 100 nm layer thus have

similar properties: a largely (75%) sp^2 bonded and thus relatively soft layer, even if the systems differ greatly for the 50 nm a-C:H layers. The influence of the fiber reinforcement on the deposited a-C:H layer seems to decrease even with relatively thin layers.

Figure 4 displays the NEXAFS measurements; Figure 4A for PVA and 4B for PVA/CMF. The peak positions have been determined to C=C π (284.85 eV), C-H (286.15 eV), C-C (288.35 eV) and C=C σ (292.55 eV) [47–51]. For the PVA samples (Figure 4A), the reference shows only a small proportion of sp^2 bonds (C=C), contrary to the XPS measurements. For the O_2 plasma treated PVA, the C=C π peak and the peak associated with the C-C bond weaken a little. If an a-C:H layer of 50 nm is deposited on the PVA, a dominant C=C π peak is formed and the C=C σ peak decreases slightly. The sp^3 fraction also decreases slightly. With a further increase of the layer thickness this trend continues in favour of a stronger C=C π bond. This is in contrast to the measurements with the XPS, where the sp^3 bond increased slightly, but this may also be due to the different penetration depth.

The results for the NEXAFS measurements of PVA/CMF samples are shown in Figure 4B. The C-H peak is well formed for the raw polymer, a C=C π peak is hardly present. The C=C σ peak is also weak but visible. The double bonds associated with sp^2 hybridization are probably due to the CMF content. With O_2 plasma treatment, the C=C π peak is hardly noticeable, the C=C σ is comparatively broadened and more emphasized by the surrounding bonds, while the C-H peak is more pronounced. With the application of a 50 nm thick a-C:H layer, a strong C=C π peak is formed, the C=C σ peak decreases slightly, the proportion of the C-H peak decreases strongly. This corresponds to the measurements obtained in XPS. If the layer thickness is increased to 100 nm, there are no changes in the NEXAFS measurements which is in contrast to the XPS measurements obtained, where the sp^2 content increases and the sp^3 content is strongly reduced. The differences obtained in the XPS and NEXAFS measurements are a result of the different penetration depth of the two measurement techniques.

<Figure 4 here>

For additional surface evaluation of the chemical composition DRIFT measurements are recorded and discussed. For the subsequently a-C:H coated samples, the O_2 plasma treated PVA (resp. PVA/CMF) was used as basic substrate and served as the reference spectra, since each a-C:H layer was deposited on such pre-treated material. DRIFT spectra are evaluated on the basics of infrared spectroscopy [31] and according to previous results of other groups and own observations [18,24,30,52,53].

<Figure 5 here>

Firstly, a full overview (450-4100 cm^{-1}) for all samples was performed to check for main differences between the coated samples. For detailed analysis measurements in the interesting region, the C-H stretching area at 2800-3050 cm^{-1} was performed [31]. In this area peaks for $=CH_2$ and $–CH_3$ are located [30,31,52,53]. It is noticeable that the DRIFT measurements do not correspond to the X-ray spectroscopic methods. Only the sp^3 oscillations could be detected in the measurements, the sp^2 oscillations could not be detected. This problem has already occurred for other a-C:H coated polymers [10]. For the coated PVA and PVA/CMF samples, only the two oscillations of the sp^3CH_2 as (asymmetric) at 2939 cm^{-1} [52,53] and the sp^3CH bond at 2903 cm^{-1} [52] could be detected. The presence of $=CH_2$ oscillations indicates that an interlayer present between the material and the a-C:H layer is completed [24]. Based on the DRIFT measurements compared to earlier results [24], it can therefore be concluded to take less than 50 nm.

In **Figure 5**A the results for the PVA measurements are shown. As the thickness of the layer increases from 50 nm to 100 nm, there is a shift in sp^3CH_2 as vibration to a wavenumber of 2936 cm^{-1}. This shift to lower wavenumbers indicates a smaller carbon-hydrogen binding

energy and therefore a larger carbon-hydrogen bond distance for the $=CH_2$ group [31]. This behaviour has already been demonstrated for such a-C:H coatings on several (bio-)polymers [11,18,20,21,24]. Furthermore, both sp^3 binding peaks were more pronounced. This is in line with the results from the XPS measurements.

The results of the PVA/CMF measurements are shown in Figure 5B. Here again, the same shift back of the sp^3CH_2 as oscillation occurs, which could already be determined for the PVA. The only noticeable difference to the a-C:H coated PVA is in the shape of the two sp^3 peaks at 100 nm film thickness. In the step from 50 nm to 100 nm the sp^3CH_2 as peak seems to weaken, while the sp^3CH peak is much more pronounced compared to the results for the coated PVA.

4 Conclusion

Pure polyvinyl alcohol (PVA) and PVA reinforced with cellulose microfibers (PVA/CMF) were coated with a-C:H layers in order to compare how a modification of the base material affects the basic coatability and growth of the a-C:H layer. For the coating an RF PE-CVD plasma with acetylene precursor was used. Subsequently, the layers obtained were examined by AFM and contact angle measurements for their surface properties and by XPS, NEXAFS and DRIFT measurements for their chemical composition. Layer thicknesses of up to 100 nm a-C:H were realized, which also adhered stably to the material. The AFM measurements show a similar growth pattern of the layers on both materials, but the resulting grain-like structure of the 100 nm layer is finer for the PVA/CMF. This is also noticeable in the different contact angles changing from 35° for pure PVA to 67° for PVA/CMF. The presence of pronounced grains in AFM measurements of the 50 nm a-C:H layer thickness for both materials indicates a previous completion of the interlayer. After the completion of the mixed phase between polymer and a-C:H layer the normal a-C:H layer growth takes place. This is also confirmed by the DRIFT measurements, since $=CH_2$ bonds are already present at 50 nm, which only form when the interlayer is completed.

The XPS measurements show large differences in the hybridization of carbon for the reference samples of the PVA as well as the enhanced PVA samples. The influence of the CMF fibres is clearly visible for the raw polymer as well as the O_2 treated samples. Both materials are similar in respect to the fact that the applied layer is sp^2 dominated at 50 nm layer thickness, even if its proportion is significantly lower for the enhanced PVA. The higher proportion of sp^3 bonds here is probably due to base material present in the interlayer phase. As the thickness of the layer increases to 100 nm, the sp^2 fraction for the enhanced PVA increases, while it decreases in the normal PVA in favour of a stronger sp^3 fraction. It is noticeable that at 100 nm a-C:H layer thickness about 75% sp^2 bound carbon is present for both materials. The NEXAFS measurements do not show any major differences for the respective 50 and 100 nm coatings of the different base materials. Due to the shift of the measured peak positions, the DRIFT measurements prove a film thickness dependent change of the chemical structure with increasing film thickness.

Overall, the reinforcement of PVA with CMF fibres does not lead to too much variation for the resulting coatings, which are stable for both materials and the applied layer thicknesses. The measurements for the 50 nm samples differ chemically, which is due to the different interlayer phase through the different base materials. At 100 nm layer thickness the systems approach each other, the influence of the fibres is, at least chemically, only limited to the initial growth. The surface roughness of the AFM images differs between the two systems, but this is due to the relatively thin layer of 100 nm, which cannot yet compensate for differences in the surface condition of the two substrates. Additionally, the contact angle differs due to different surface roughness for the pure and reinforced PVA. Further measurements of thinner coatings would provide information about the different initial growth of the layer. Thicker layers must also be analysed to check whether and how the modification of the base material affects the applied layers and their stability.

Acknowledgement

The authors thank Dr. Heinz Busch (NTTF Coatings GmbH, Rheinbreitbach, Germany) for the possibility of industrial coating of the samples and Prof. Dr. Joachim Scholz (University of Koblenz-Landau, department of chemistry) for the DRIFT equipment. The authors also want to thank Dr. Alexei Nefedov from KIT (Karlsruhe Institute for Technology, Group: Chemistry of oxidic and organic interfaces; X-ray and Electron Spectroscopy at Interfaces) for beamtime support. We thank HZB for the allocation of synchrotron radiation beamtime. The authors thankfully acknowledge the financial support by the Helmholtz-Zentrum Berlin (HZB), Germany. The financial assistance of the Office Chérifien des Phosphates (OCP S.A.) in the Moroccan Kingdom toward this research is hereby acknowledged. Additionally, the authors gratefully acknowledge the financial support provided by DAAD funds within the framework of German-Arab Transformation Partnership 2018 and 2019, Program line 2, DAAD Project ID: 57448234 and 57514023, and the German Research Foundation (DFG) for funding this work within the projects WE 4100/23-1 and FI 1802/14-1.

Figure captions

FIGURE 1 AFM images for PVA (upper line **a**-**d**) and PVA/CMF (bottom line **e**-**h**) from left to right: reference, O_2 plasma treated, with 50 nm and 100 nm a-C:H coating. The magnification below each image has a side length of 1 μm each.

FIGURE 2 Contact angle results for both polymer types: **2A** for PVA and **2B** for PVA/CMF. Measurements for the raw polymer, the O_2 plasma treated and two coatings (50 nm and 100 nm a-C:H) are shown (the lines only indicate a trend). The grey box indicates the O_2 plasma pretreatment of the raw polymer. The O_2 sample represents a layer thickness of 0 nm.

FIGURE 3 XPS measurements for PVA in **A** and PVA/CMF in **B**. Measurements are shown for the raw polymer, O_2 plasma treated, plasma coated samples of 50 nm and 100 nm a-C:H (the dashed lines only indicate a trend). For every sample the sp^3 (black triangles), sp^2 (red squares), C-O (green circles) and C=O (blue stars) content has been determined. The grey box indicates the O_2 plasma pretreatment of the raw polymer. The O_2 sample represents a layer thickness of 0 nm.

FIGURE 4 NEXAFS measurements for PVA in **A** and PVA/CMF in **B**. Black is the respective raw polymer, red the O_2 plasma treated, green the 50 nm a-C:H and magenta the 100 nm coated sample.

FIGURE 5 DIRFT spectra of the analysed PVA and PVA/CMF samples coated with a:C-H. The measurements are presented with increasing layer thickness and given in arbitrary units (arb.u.). Layer thicknesses of 50 nm (black) and 100 nm (red) a-C:H are shown.

References

[1] H.A. Silvério, W.P. Flauzino Neto, N.O. Dantas, D. Pasquini, Extraction and characterization of cellulose nanocrystals from corncob for application as reinforcing agent in nanocomposites, Industrial Crops and Products 44 (2013) 427–436. https://doi.org/10.1016/j.indcrop.2012.10.014.

[2] J. Sapkota, M. Jorfi, C. Weder, E.J. Foster, Reinforcing Poly(ethylene) with Cellulose Nanocrystals, Macromol. Rapid Commun. (2014). https://doi.org/10.1002/marc.201400382.

[3] Z. Kassab, F. Aziz, H. Hannache, H. Ben Youcef, M. El Achaby, Improved mechanical properties of k-carrageenan-based nanocomposite films reinforced with cellulose nanocrystals, Int. J. Biol. Macromol. 123 (2019) 1248–1256. https://doi.org/10.1016/j.ijbiomac.2018.12.030.

[4] Z. Kassab, H. Ben youcef, H. Hannache, M. El Achaby, Isolation of Cellulose Nanocrystals from Various Lignocellulosic Materials: Physico-chemical characterization and Application in Polymer Composites Development, Materials Today: Proceedings 13 (2019) 964–973. https://doi.org/10.1016/j.matpr.2019.04.061.

[5] M. El Achaby, Z. Kassab, A. Aboulkas, C. Gaillard, A. Barakat, Reuse of red algae waste for the production of cellulose nanocrystals and its application in polymer nanocomposites, Int. J. Biol. Macromol. 106 (2018) 681–691. https://doi.org/10.1016/j.ijbiomac.2017.08.067.

[6] B. Poyraz, A. Tozluoğlu, Z. Candan, A. Demir, M. Yavuz, Influence of PVA and silica on chemical, thermo-mechanical and electrical properties of Celluclast-treated nanofibrillated cellulose composites, Int. J. Biol. Macromol. 104 (2017) 384–392. https://doi.org/10.1016/j.ijbiomac.2017.06.018.

[7] S. Singh, K.K. Gaikwad, Y.S. Lee, Antimicrobial and antioxidant properties of polyvinyl alcohol bio composite films containing seaweed extracted cellulose nano-crystal and basil leaves extract, Int. J. Biol. Macromol. 107 (2018) 1879–1887. https://doi.org/10.1016/j.ijbiomac.2017.10.057.

[8] Z. Kassab, A. Boujemaoui, H. Ben Youcef, A. Hajlane, H. Hannache, M. El Achaby, Production of cellulose nanofibrils from alfa fibers and its nanoreinforcement potential in polymer nanocomposites, Cellulose 26 (2019) 9567–9581. https://doi.org/10.1007/s10570-019-02767-5.

[9] Z. Kassab, S. Mansouri, Y. Tamraoui, H. Sehaqui, H. Hannache, A.E.K. Qaiss, M. El Achaby, Identifying Juncus plant as viable source for the production of micro- and nano-cellulose fibers: Application for PVA composite materials development, Industrial Crops and Products 144 (2020) 112035. https://doi.org/10.1016/j.indcrop.2019.112035.

[10] T. Schlebrowski, W. Rouabeh, S. Wehner, C.B. Fischer, Specifying the interlayer turning point and dehydrogenation in a-C:H layers plasma deposited on high-density polyethylene with X-ray synchrotron techniques, Thin Solid Films 691 (2019) 137617. https://doi.org/10.1016/j.tsf.2019.137617.

[11] T. Schlebrowski, H. Acharchi, B. Hahn, S. Wehner, C.B. Fischer, Refinement of Sustainable Polybutylene Adipate Terephthalate (PBAT) with Amorphous Hydrogenated Carbon Films (a-C:H) Revealing Film Instabilities Influenced by a Thickness-Dependent Change of sp2/sp3 Ratio, Materials 13 (2020) 1077. https://doi.org/10.3390/ma13051077.

[12] J. Robertson, Plasma Deposition of Diamond-Like Carbon, Jpn. J. Appl. Phys. 50 (2011) 01AF01. https://doi.org/10.1143/JJAP.50.01AF01.

[13] J. Robertson, Diamond-like amorphous carbon, Materials Science and Engineering: R: Reports 37 (2002) 129–281. https://doi.org/10.1016/S0927-796X(02)00005-0.

[14] S.-C. Lee, F.-C. Tai, C.-H. Wei, Correlation between **sp^2/sp^3** Ratio or Hydrogen Content and Water Contact Angle in Hydrogenated DLC Film, Mater. Trans. 48 (2007) 2534–2538. https://doi.org/10.2320/matertrans.MER2007044.

[15] E. Mohagheghpour, M. Rajabi, R. Gholamipour, M.M. Larijani, S. Sheibani, Ion beam energy dependence of surface and structural properties of amorphous carbon films deposited by IBSD method on Ni–Cu alloy, J. Mater. Res. 32 (2017) 1258–1266. https://doi.org/10.1557/jmr.2017.43.

[16] A. Grill, Plasma-deposited diamondlike carbon and related materials, IBM J. Res. & Dev. 43 (1999) 147–162. https://doi.org/10.1147/rd.431.0147.

[17] M. Rohrbeck, S. Körsten, C.B. Fischer, S. Wehner, B. Kessler, Diamond-like carbon coating of a pure bioplastic foil, Thin Solid Films 545 (2013) 558–563. https://doi.org/10.1016/j.tsf.2013.07.028.

[18] A. Catena, M.R. Kunze, S. Agnello, F.M. Gelardi, S. Wehner, C.B. Fischer, Amorphous hydrogenated carbon (a-C:H) depositions on polyoxymethylene: Substrate influence on the characteristics of the developing coatings, Surface and Coatings Technology 307 (2016) 658–665. https://doi.org/10.1016/j.surfcoat.2016.09.064.

[19] A. Catena, S. Agnello, L.M. Rösken, H. Bergen, E. Recktenwald, F. Bernsmann, H. Busch, M. Cannas, F.M. Gelardi, B. Hahn, S. Wehner, C.B. Fischer, Characteristics of industrially manufactured amorphous hydrogenated carbon (a-C:H) depositions on high-density polyethylene, Carbon 96 (2016) 661–671. https://doi.org/10.1016/j.carbon.2015.09.101.

[20] T. Schlebrowski, L. Beucher, H. Bazzi, B. Hahn, S. Wehner, C.B. Fischer, Changing Contents of Carbon Hybridizations in Amorphous Hydrogenated Carbon Layers (a-C:H) on Sustainable Polyhydroxybutyrate (PHB) Exhibit a Significant Deterioration in Stability, Depending on Thickness, C 5 (2019) 52. https://doi.org/10.3390/c5030052.

[21] T. Schlebrowski, L. Beucher, H. Bazzi, B. Hahn, S. Wehner, C.B. Fischer, Prediction of a-C:H layer failure on industrial relevant biopolymer polylactide acide (PLA) foils based on the sp2/sp3 ratio, Surface and Coatings Technology 368 (2019) 79–87. https://doi.org/10.1016/j.surfcoat.2019.03.069.

[22] C.B. Fischer, M. Rohrbeck, S. Wehner, M. Richter, D. Schmeißer, Interlayer formation of diamond-like carbon coatings on industrial polyethylene: Thickness dependent surface characterization by SEM, AFM and NEXAFS, Applied Surface Science 271 (2013) 381–389. https://doi.org/10.1016/j.apsusc.2013.01.210.

[23] A. Catena, T. McJunkin, S. Agnello, F.M. Gelardi, S. Wehner, C.B. Fischer, Surface morphology and grain analysis of successively industrially grown amorphous hydrogenated carbon films (a-C:H) on silicon, Applied Surface Science 347 (2015) 657–667. https://doi.org/10.1016/j.apsusc.2015.04.113.

[24] A. Catena, Q. Guo, M.R. Kunze, S. Agnello, F.M. Gelardi, S. Wehner, C.B. Fischer, Morphological and Chemical Evolution of Gradually Deposited Diamond-Like Carbon Films on Polyethylene Terephthalate: From Subplantation Processes to Structural Reorganization by Intrinsic Stress Release Phenomena, ACS Appl. Mater. Interfaces 8 (2016) 10636–10646. https://doi.org/10.1021/acsami.6b02113.

[25] L. Kleinen, U. Böde, K. Schenk, H. Busch, J. Bradenahl, S.C. Müller, B. Hillebrands, N. Laube, Amorphous Carbon Coatings Inhibit Crystalline Biofilm Formation on Urological Implants, Plasma Process. Polym. 4 (2007) S386-S391. https://doi.org/10.1002/ppap.200731005.

[26] L. Kleinen, U. Böde, N. Laube, Ex-vivo investigations on the friction behavior of amorphous carbon coated ureteral stents, Diamond and Related Materials 17 (2008) 1746–1750. https://doi.org/10.1016/j.diamond.2008.01.099.

[27] A. Nefedov, C. Wöll, Advanced Applications of NEXAFS Spectroscopy for Functionalized Surfaces, in: G. Bracco, B. Holst (Eds.), Surface Science Techniques, Springer Berlin Heidelberg, Berlin, Heidelberg, 2013, pp. 277–303.

[28] T. Armaroli, T. Bécue, S. Gautier, Diffuse Reflection Infrared Spectroscopy (Drifts): Application to the in Situ Analysis of Catalysts, Oil & Gas Science and Technology - Rev. IFP 59 (2004) 215–237. https://doi.org/10.2516/ogst:2004016.

[29] L. D'Souza, P. Devi, T. Kamat, C.G. Naik, Diffuse reflectance infrared fourier transform spectroscopic (DRIFTS) investigation of E.coli, Staphylococcus aureus and Candida albicans, Indian J. Mar. Sci (2009) 45–51.

[30] P. Koidl, C. Wild, B. Dischler, J. Wagner, M. Ramsteiner, Plasma Deposition, Properties and Structure of Amorphous Hydrogenated Carbon Films, MSF 52-53 (1991) 41–70. https://doi.org/10.4028/www.scientific.net/MSF.52-53.41.

[31] H. Günzler, H.-U. Gremlich, IR spectroscopy: An introduction, Wiley-VCH, Weinheim, 2002.

[32] B. Watts, L. Thomsen, P.C. Dastoor, Methods in carbon K-edge NEXAFS: Experiment and analysis, Journal of Electron Spectroscopy and Related Phenomena 151 (2006) 105–120. https://doi.org/10.1016/j.elspec.2005.11.006.

[33] D.L. Smith, Thin-film deposition: Principles and practice, Internat. ed., McGraw-Hill, Boston, Mass., 1995.

[34] B.K. Tay, D. Sheeja, S.P. Lau, J.X. Guo, Study of surface energy of tetrahedral amorphous carbon films modified in various gas plasma, Diamond and Related Materials 12 (2003) 2072–2076. https://doi.org/10.1016/S0925-9635(03)00192-4.

[35] F. Piazza, G. Morell, Wettability of hydrogenated tetrahedral amorphous carbon, Diamond and Related Materials 18 (2009) 43–50. https://doi.org/10.1016/j.diamond.2008.09.023.

[36] L.Y. Ostrovskaya, Studies of diamond and diamond-like film surfaces using XAES, AFM and wetting, Vacuum 68 (2002) 219–238. https://doi.org/10.1016/S0042-207X(02)00460-8.

[37] L. Ostrovskaya, V. Perevertailo, V. Ralchenko, A. Dementjev, O. Loginova, Wettability and surface energy of oxidized and hydrogen plasma-treated diamond films, Diamond and Related Materials 11 (2002) 845–850. https://doi.org/10.1016/S0925-9635(01)00636-7.

[38] R. Paul, S.N. Das, S. Dalui, R.N. Gayen, R.K. Roy, R. Bhar, A.K. Pal, Synthesis of DLC films with different sp2/sp3 ratios and their hydrophobic behaviour, J. Phys. D: Appl. Phys. 41 (2008) 55309. https://doi.org/10.1088/0022-3727/41/5/055309.

[39] T. Werder, J.H. Walther, R.L. Jaffe, T. Halicioglu, P. Koumoutsakos, On the Water−Carbon Interaction for Use in Molecular Dynamics Simulations of Graphite and Carbon Nanotubes, J. Phys. Chem. B 107 (2003) 1345–1352. https://doi.org/10.1021/jp0268112.

[40] Y. Zhou, B. Wang, X. Song, E. Li, G. Li, S. Zhao, H. Yan, Control over the wettability of amorphous carbon films in a large range from hydrophilicity to super-hydrophobicity, Applied Surface Science 253 (2006) 2690–2694. https://doi.org/10.1016/j.apsusc.2006.05.118.

[41] L. Feng, S. Li, Y. Li, H. Li, L. Zhang, J. Zhai, Y. Song, B. Liu, L. Jiang, D. Zhu, Super-Hydrophobic Surfaces: From Natural to Artificial, Adv. Mater. 14 (2002) 1857–1860. https://doi.org/10.1002/adma.200290020.

[42] W. Barthlott, C. Neinhuis, Purity of the sacred lotus, or escape from contamination in biological surfaces, Planta 202 (1997) 1–8. https://doi.org/10.1007/s004250050096.

[43] D. Banerjee, S. Mukherjee, K.K. Chattopadhyay, Controlling the surface topology and hence the hydrophobicity of amorphous carbon thin films, Carbon 48 (2010) 1025–1031. https://doi.org/10.1016/j.carbon.2009.11.021.

[44] F.C. Tai, S.C. Lee, C.H. Wei, S.L. Tyan, Correlation between *ID*/*IG* Ratio from Visible Raman Spectra and sp2/sp3 Ratio from XPS Spectra of Annealed Hydrogenated DLC Film, Mater. Trans. 47 (2006) 1847–1852. https://doi.org/10.2320/matertrans.47.1847.

[45] J.L. Solomon, R.J. Madix, J. Stöhr, Orientation and absolute coverage of benzene, aniline, and phenol on Ag(110) determined by NEXAFS and XPS, Surface Science 255 (1991) 12–30. https://doi.org/10.1016/0039-6028(91)90008-G.

[46] P.M. Dietrich, T. Horlacher, P.-L. Girard-Lauriault, T. Gross, A. Lippitz, H. Min, T. Wirth, R. Castelli, P.H. Seeberger, W.E.S. Unger, Adlayers of dimannoside thiols on gold: surface chemical analysis, Langmuir 27 (2011) 4808–4815. https://doi.org/10.1021/la104038q.

[47] J. Stöhr, NEXAFS spectroscopy, second. print, Springer, Berlin, 2003.

[48] J. Díaz, S. Anders, X. Zhou, E.J. Moler, S.A. Kellar, Z. Hussain, Analysis of the π* and σ* bands of the x-ray absorption spectrum of amorphous carbon, J. Phys. D: Appl. Phys. 64 (2001) 17. https://doi.org/10.1103/PhysRevB.64.125204.

[49] J. Diaz, O.R. Monteiro, Z. Hussain, Structure of amorphous carbon from near-edge and extended x-ray absorption spectroscopy, Phys. Rev. B 76 (2007) 388. https://doi.org/10.1103/PhysRevB.76.094201.

[50] O. Dhez, H. Ade, S.G. Urquhart, Calibrated NEXAFS spectra of some common polymers, Journal of Electron Spectroscopy and Related Phenomena 128 (2003) 85–96. https://doi.org/10.1016/S0368-2048(02)00237-2.

[51] B. Brüster, C. Amozoqueño, P. Grysan, I. Peral, B. Watts, J.-M. Raquez, P. Dubois, F. Addiego, Resolving Inclusion Structure and Deformation Mechanisms in Polylactide Plasticized by Reactive Extrusion, Macromol. Mater. Eng. 302 (2017) 1700326. https://doi.org/10.1002/mame.201700326.

[52] M. Veres, M. Koós, I. Pócsik, IR study of the formation process of polymeric hydrogenated amorphous carbon film, Diamond and Related Materials 11 (2002) 1110–1114. https://doi.org/10.1016/S0925-9635(02)00011-0.

[53] E. Tomasella, L. Thomas, M. Dubois, C. Meunier, Structural and mechanical properties of a-C:H thin films grown by RF-PECVD, Diamond and Related Materials 13 (2004) 1618–1624. https://doi.org/10.1016/j.diamond.2004.01.017.

Figure 1

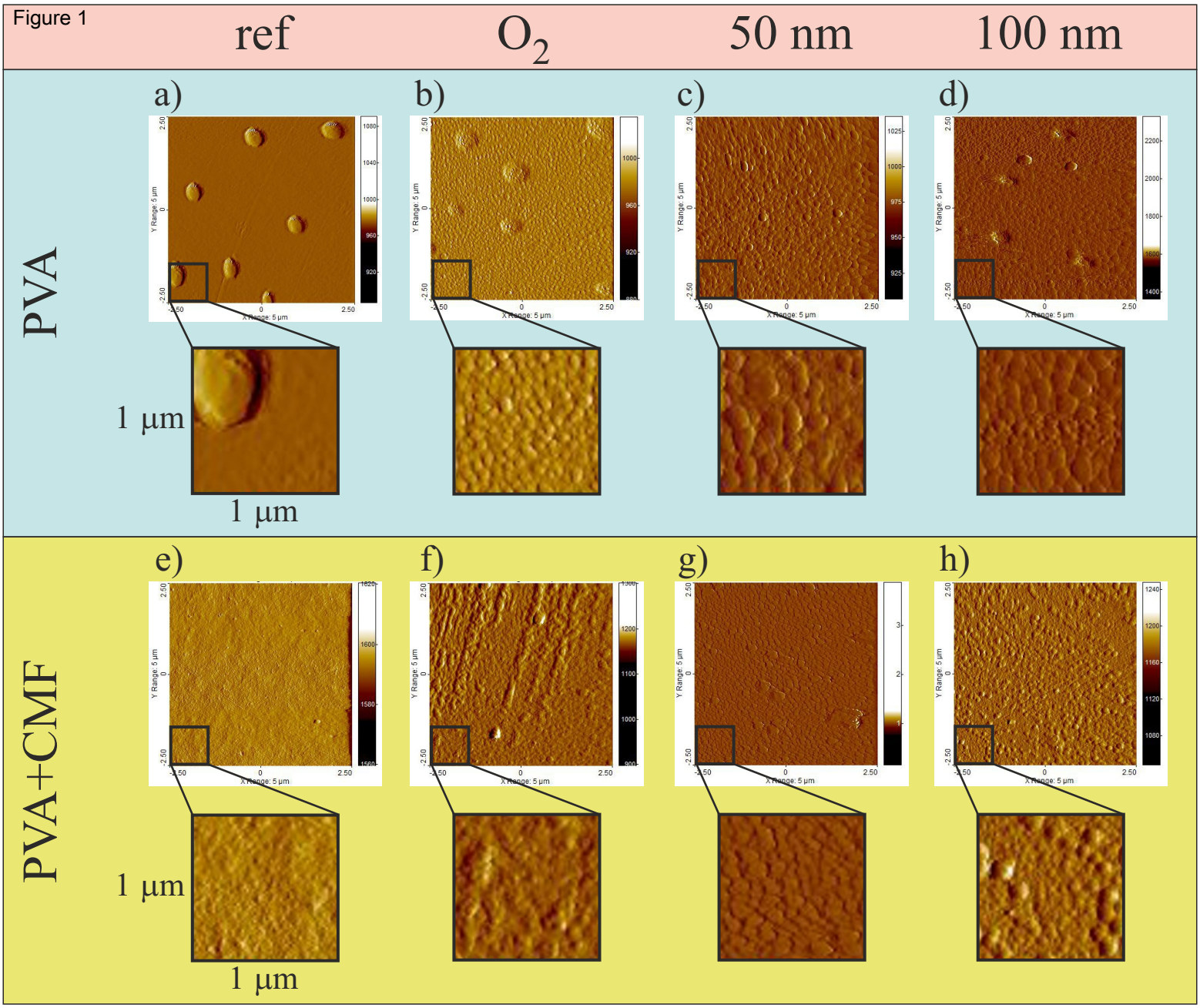

Figure 2

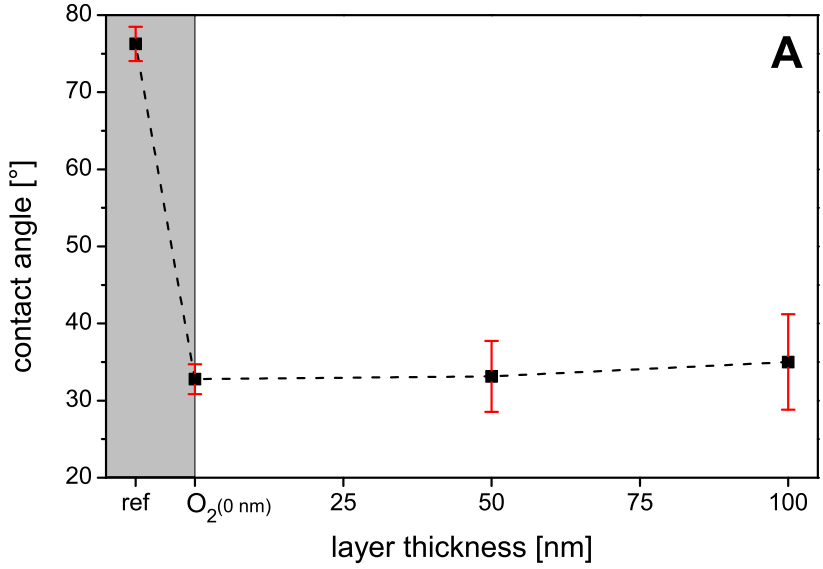
A
contact angle [°]
80
70
60
50
40
30
20
ref
O2(0 nm)
25
50
75
100
layer thickness [nm]

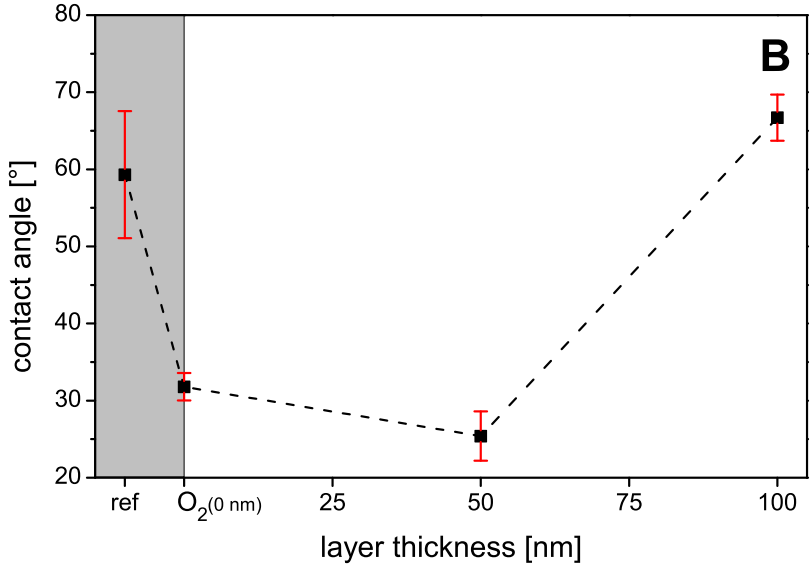
B
contact angle [°]
80
70
60
50
40
30
20
ref
O2(0 nm)
25
50
75
100
layer thickness [nm]

Figure 3

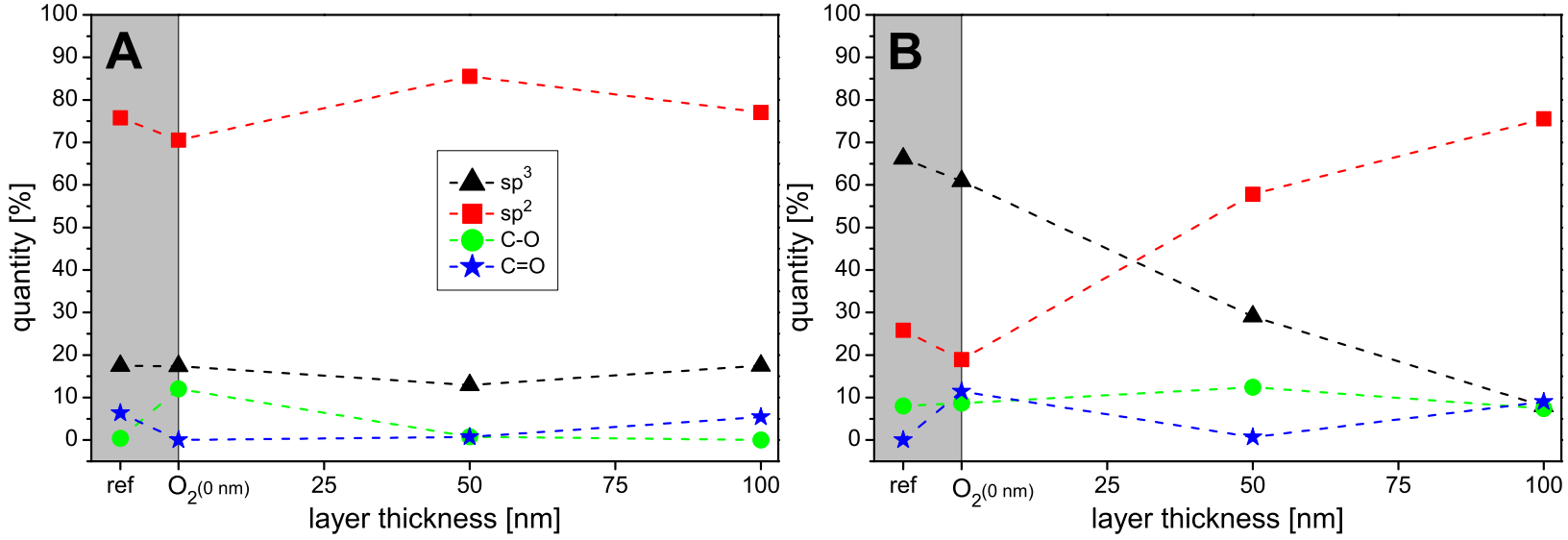
A
B
quantity [%]
layer thickness [nm]
ref
O2(0 nm)
25
50
75
100
sp3
sp2
C-O
C=O

Figure 4

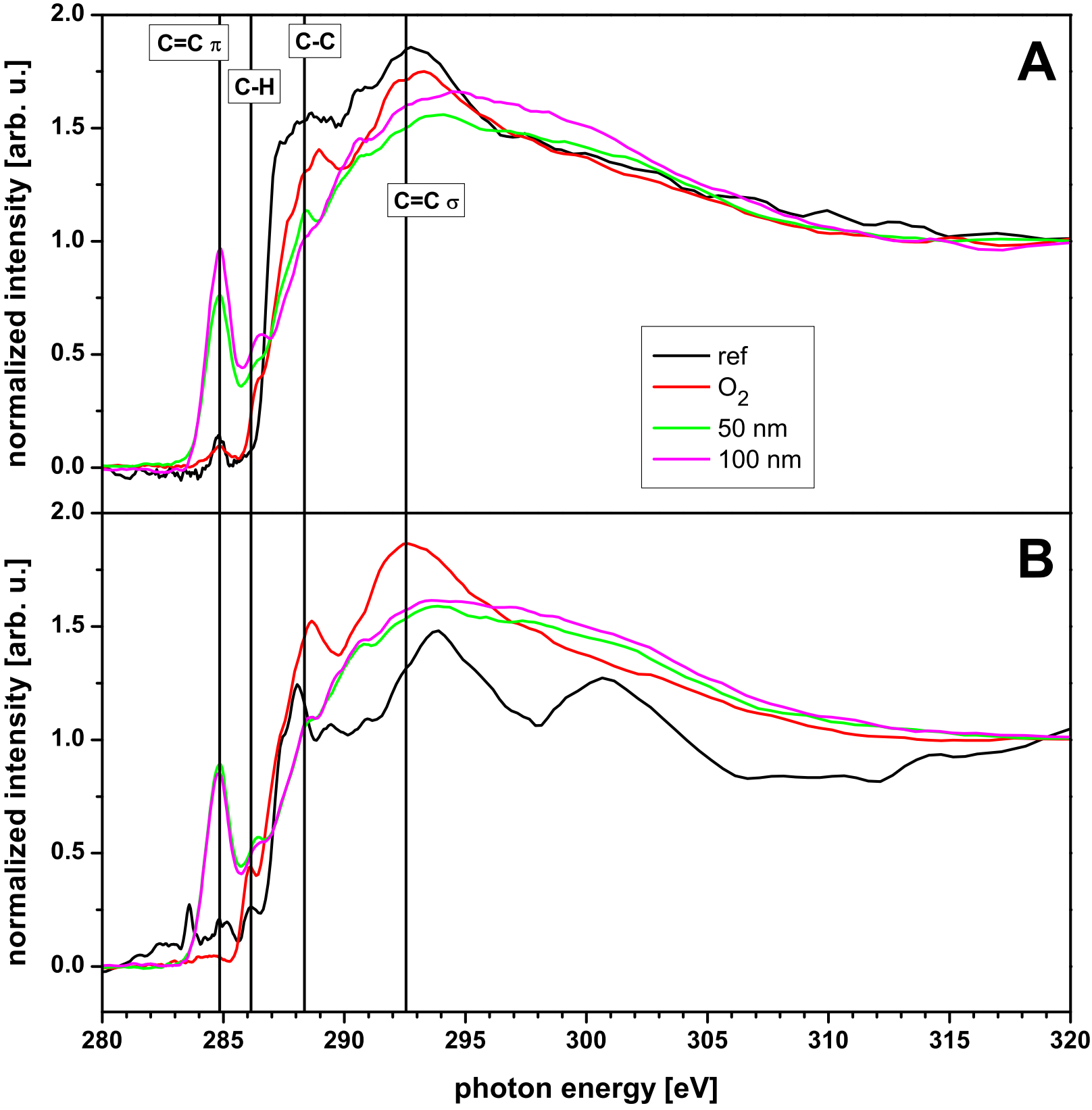
A
B
C=C π
C-H
C-C
C=C σ
ref
O2
50 nm
100 nm
normalized intensity [arb. u.]
normalized intensity [arb. u.]
photon energy [eV]
2.0
1.5
1.0
0.5
0.0
280
285
290
295
300
305
310
315
320

Figure 5

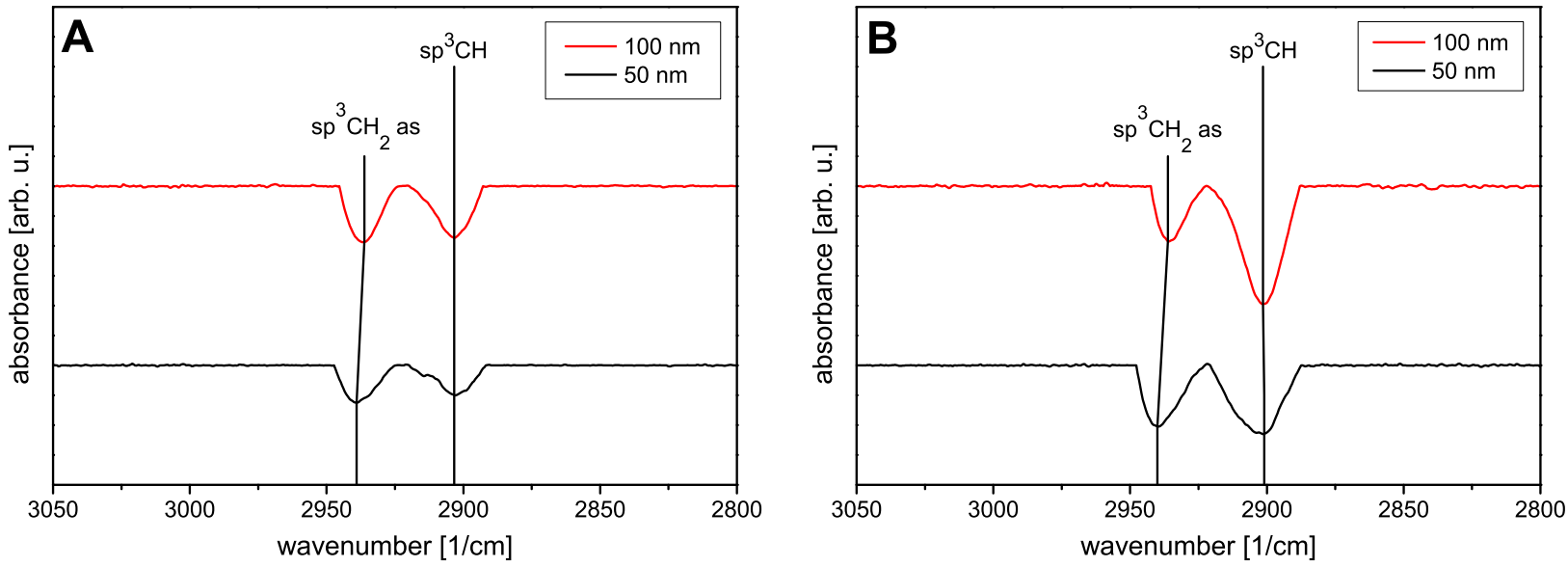
A
B
100 nm
50 nm
sp3CH
sp3CH2 as
absorbance [arb. u.]
wavenumber [1/cm]
3050
3000
2950
2900
2850
2800

Declaration of interests

☒ The authors declare that they have no known competing financial interests or personal relationships that could have appeared to influence the work reported in this paper.

☐The authors declare the following financial interests/personal relationships which may be considered as potential competing interests:

Amorphous carbon layers (a-C:H) were successfully deposited on polyvinyl alcohol (PVA) and cellulose microfiber (CMF) reinforced PVA. Differences in the chemical composition of deposited carbon layers (sp^2/sp^3) were detected with synchrotron based techniques in combination with changes in their morphology and wettability showing clear substrate effects when used with microfiber reinforcement.